

3033

JNCASR
Acc
No. - 3033
LIBRARY

Library copy.

JNCASR
620.189 2 P02

3033

**CHARGE ORDERING AND RELATED PHENOMENA IN
RARE EARTH MANGANATES (PART 1) AND METAL
NANOPARTICLES AND THEIR ASSEMBLIES (PART 2)**

A Thesis

Submitted for the Degree of

Doctor of Philosophy

By

K. VIJAYA SARATHY



TO

MANIPAL ACADEMY OF HIGHER EDUCATION

THROUGH

JAWAHARLAL NEHRU CENTRE FOR ADVANCED SCIENTIFIC

RESEARCH, BANGALORE-560 064, INDIA

FEBRUARY 2002

JNCASR

189 2 P02



3033

Dedication

कुरु भुङ्क्ष्व च कर्म निजं नियतं
हरिपादविनम्रधिया सततं ।
हरिरेव परो हरिरेव गुरुः
हरिरेव जगत्पितृमातृगतिः ॥

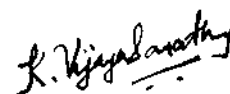
620.189 2

P02

STATEMENT

I hereby declare that the matter embodied in this thesis entitled "Charge ordering and related phenomena in rare earth manganates (Part 1) and Metal nanoparticles and their assemblies (Part 2)" is the result of the investigations carried out by me in the Chemistry and Physics of Materials Unit, Jawaharlal Nehru Centre for Advanced Scientific Research, Jakkur, Bangalore, India under the supervision of Prof. C. N. R. Rao.

In keeping with general practice of reporting observations, due acknowledgement has been made whenever the work described has been based on the findings of the other investigators. Any omission, which might have occurred by oversight or error of judgement, is regretted.



K. VIJAYA SARATHY



**JAWAHARLAL NEHRU CENTRE FOR
ADVANCED SCIENTIFIC RESEARCH**

JAKKUR CAMPUS, JAKKUR P.O.
BANGALORE 560 064, INDIA

4, February, 2002

CERTIFICATE

Certified that the work described in the thesis is the result of investigations carried out by Mr. K. Vijaya Sarathy in the Chemistry and Physics of Materials Unit, Jawaharlal Nehru Centre for Advanced Scientific Research, Jakkur, Bangalore, under my supervision.


Prof. C. N. R. Rao

ACKNOWLEDGEMENTS

I would like to place on record my respect as well as gratitude to my teacher, Prof. C. N. R. Rao. Not only has he guided my research activities but also helped me develop. Over the years I realize his sheer presence gives me untold enthusiasm and a zeal to reach further. One striking aspect that is unique only to him, is his mammoth knowledge coupled with his legendary speed; a sight that is obvious in all the activities he pursues. I consider myself as among the privileged few who have had the unique opportunity to be under his tutelage. I am grateful for the opportunities he has provided me.

I take this opportunity to thank Professors V. Krishnan, S. Chandrasekaran and S. Ramasesha for all their help and timely guidance on various occasions. I also thank the academic section in particular Dr. Madhusudhan for all the help delivered.

I would like to thank all my course teachers in IISc, in particular Prof. J. Gopalkrishan, Prof. T. N. Guru Row, Prof. S. Chandrashekar, Prof. D. D. Sarma and all others for their guidance.

In my JNCASR campus, I would foremost thank Prof. G. U. Kulkarni who not only introduced me to the area of colloids and surface science but also assisted me in various other activities. I thank Dr. A. R. Raju who has helped me acquiring a working knowledge of various equipment that I have utilised in the course of my research work. I also thank Prof. K. S. Narayan with whom I

worked for a brief stint and was introduced to various optical methods. I have collaborated with all these Professors in the course of my Ph.D.

I would like to thank my course teachers – Dr. Shobhana Narsimhan, Prof. Natarajan and Dr. Chandrabhas. I would like to mention a special thanks to Dr. Umesh for he has been very kind and supportive to me. I have also had many fruitful discussions with Dr. Swapan Pati. Lastly I thank Dr. Balasubramaniam for the computer facilities.

I thank my collaborators Dr. Ram Seshadri, Dr. White, Gargi, Anthony, Vinmathi, Sachin, John, Sudheendra, Yadav, Sreeraj and Nitai. I thank Dr. Govindaraj for not only providing a helping hand but also for making my stay lively. I thank my friends, C. P., N. V, Ash, Kavitha, Saroj, Shobhana, Pattu, Inguva, Murgavel, Sheebha, Prasad, Vaidhya, Vijayalakshmi, Neena, Sarika, Manoj, Biru, Padmanabhan, Veni, Sagar, Manju, Kripa, Anupama, Neeraj, Gopalan, Amitava, Pushpa, Julius, Jeo, Basha all others who have kept me smiling all the way through. I thank all the technical staff in particular Srinath, Srinivas, Basavaraj, Anil and Vasu.

I would also like to thank Mr. Nagaraja Rao and all the office staff for all the help rendered. And lastly I thank my innumerable friends, in particular Srinivas, Harish, Satish, Shrikant, Nagaraj, Kp, Vidya, Gopal, Anil, Anand, and the rest of the gang. I also thank my parents for having been patient with me in all my endeavours.

CONTENTS

STATEMENT	i
CERTIFICATE	ii
ACKNOWLEDGEMENTS	iii
PREFACE	ix
Part 1	
CHARGE ORDERING AND RELATED PHENOMENA IN RARE EARTH MANGANATES	
SUMMARY	1
1.1 AN OVERVIEW OF THE RARE EARTH MANGANATES	5
1.1.1 Structural aspects of rare earth manganates	8
1.1.2 Electronic properties of the manganates	13
1.1.3 Phase diagrams and terminology	17
1.1.4 Charge ordering process	24
1.1.5 Some important results reported in the literature	29
1.2 SCOPE OF THE PRESENT INVESTIGATION	67
1.2.1 A comparative study of the hole- and the electron-doped rare earth manganates	67
1.2.2 Hopping conduction mechanism in charge ordered rare earth manganates, $\text{Ln}_{1-x}\text{Ca}_x\text{MnO}_3$ (Ln = rare earth)	71

1.2.3	A- versus CE-type antiferromagnetism in $\text{Pr}_{0.5-x}\text{Nd}_x\text{Sr}_{0.5}\text{MnO}_3$	73
1.2.4	Layered manganates	73
1.3	EXPERIMENTAL	75
1.3.1	Synthesis	75
1.3.2	Characterisation and measurements	79
1.4	RESULTS AND DISCUSSION	84
1.4.1	A study of the electron-hole asymmetry in rare earth manganates	84
1.4.2	Thin films of $\text{Pr}_{0.6}\text{Ca}_{0.4}\text{MnO}_3$ and $\text{Pr}_{0.4}\text{Ca}_{0.6}\text{MnO}_3$	123
1.4.3	Electronic structure calculations	132
1.4.4	Hopping conduction in charge ordered rare earth manganates	140
1.4.5	A- versus CE-type antiferromagnetism in $\text{Pr}_{0.5-x}\text{Nd}_x\text{Sr}_{0.5}\text{MnO}_3$	158
1.4.6	Layered manganates	163
	REFERENCES	168

Part 2

METAL NANOPARTICLES AND THEIR CRYSTALLINE ARRAYS

SUMMARY	179
2.1 AN OVERVIEW OF METAL NANOPARTICLES AND THEIR ARRAYS	182
2.1.1 Synthesis of metal colloids	184

2.1.2 SAMs and nanoparticle arrays	191
2.1.3 Properties of self-assembled arrays	199
2.1.4 Applications	204
2.2 SCOPE OF THE PRESENT INVESTIGATIONS	210
2.2.1 Synthesis and characterization of metal colloids by the polyol process	210
2.2.2 Nanocrystalline arrays of metal nanoparticles	211
2.2.3 Metal nanoparticle superlattice	212
2.2.4 Polymer blends of Au nanoparticles	213
2.3 EXPERIMENTAL	215
2.3.1 Preparation of submicron- and nanoparticles of noble metals	215
2.3.2 Thiol derivatization of metal hydrosols	215
2.3.3 Superlattices of metal and metal-semiconductor nanoparticles	222
2.3.4 Au-polyoctylthiophene blends	223
2.3.5 Characterization	225
2.4 RESULTS AND DISCUSSION	228
2.4.1 Metal colloids by the polyol process	228
2.4.2 Two-dimensional arrays of metal nanoparticles capped by alkanethiols	236
2.4.3 Superlattices of metal nanoparticles	256

2.4.4 Au nanoparticle-polymer blends	280
REFERENCES	293

PREFACE

The thesis contains two parts. The first part deals with charge ordering and related phenomena in rare earth manganates and the second part with metal nanoparticles and their crystalline arrays.

Part 1 of the thesis mainly addresses the problem of electron-hole asymmetry in rare earth manganates of the general formula, $\text{Ln}_{1-x}\text{A}_x\text{MnO}_3$ (Ln = rare earth, A = alkaline earth). Comparative studies of $\text{Pr}_{1-x}\text{Ca}_x\text{MnO}_3$ with $x = 0.36$ and 0.64 have been carried out with respect to structure as well as effects of doping, magnetic fields and substitution in the Mn-site. The results show the electron-doped manganate ($x = 0.64$) to be distinctly different from the hole-doped composition ($x = 0.36$) in its properties. Unlike in the hole-doped composition, it is not possible to induce ferromagnetism and metallicity in the electron-doped manganate. Increasing the Mn-O-Mn angle as in $\text{La}_{0.33}\text{Ca}_{0.33}\text{Sr}_{0.34}\text{MnO}_3$ does not give rise to a ferromagnetic metallic state. The conduction mechanism in the charge ordered regime of the rare earth manganates have been examined in detail. The hole-doped compositions follow the variable range hopping mechanism whereas it is not so evident in electron-doped composition. Evolution of A-type and CE-type ordering in $\text{Pr}_{0.5-x}\text{Nd}_x\text{Sr}_{0.5}\text{MnO}_3$ has also been studied. Possible occurrence of charge ordering in

the layered manganate of Ruddlesden-Popper series ($n=1$) $\text{Nd}_{0.5}\text{Ca}_{1.5}\text{MnO}_4$ has been explored.

Part 2 deals with the synthesis of sub-micron and nanosized metal particles by the polyol method as well as the preparation of two-dimensional crystalline arrays of Au, Ag and Pt nanoparticles. The arrays have been characterized by various techniques. Three-dimensional superlattices of metal nanoparticles arrays have been prepared by layer-by-layer deposition. Interaction of Au nanoparticles with polyoctylthiophene has been studied by employing a variety of techniques.

PART 1

CHARGE ORDERING AND RELATED PROPERTIES OF

RARE EARTH MANGANATES

Summary

This part of the thesis presents the essential results of the investigations of charge ordering and related phenomena in hole-doped and electron-doped manganate systems of the type $\text{Ln}_{1-x}\text{A}_x\text{MnO}_3$ (Ln = rare earth, A = alkaline earth) carried out by the candidate.

Properties of hole-doped $\text{Pr}_{0.64}\text{Ca}_{0.36}\text{MnO}_3$ and electron-doped $\text{Pr}_{0.36}\text{Ca}_{0.64}\text{MnO}_3$ have been investigated by x-ray diffraction, magnetisation, d.c. electrical resistivity and magnetoresistive measurements. On comparing the results we find significant differences. While both $\text{Pr}_{0.64}\text{Ca}_{0.36}\text{MnO}_3$ and $\text{Pr}_{0.36}\text{Ca}_{0.64}\text{MnO}_3$ are charge ordered (CO) with charge ordering temperatures of ~ 220 K and ~ 265 K respectively, the charge ordered state can be destroyed by applying a high magnetic field or doping the Mn-site by Cr^{3+} or Ru^{4+} ions. The CO state of $\text{Pr}_{0.36}\text{Ca}_{0.64}\text{MnO}_3$ on the other hand, is unaffected by these perturbations. We have also doped the Mn-site in these materials with Cr^{3+} and Ru^{4+} ions and found that in electron doped materials, the ferromagnetic metallic (FMM) state cannot be induced, even on the application of high magnetic fields.

Rietveld analysis showed the Mn-O-Mn angle in electron-doped composition to be significantly below 180° . Keeping this in mind, we have synthesised $\text{La}_{0.33}\text{Ca}_{0.33}\text{Sr}_{0.34}\text{MnO}_3$ where the Mn-O-Mn angle was confirmed to be close to 180° by rietveld analysis. Significantly, we found that the material was not ferromagnetic down to low temperatures and did not exhibit colossal magnetoresistance as well. In addition, doping this material with $\text{Cr}^{3+}/\text{Ru}^{4+}$ revealed that the FMM state could not be attained in this electron-doped composition. This result marks the important difference between the two different regions of the electronic phase diagram *a la* electron-hole asymmetry. Unlike in $\text{Pr}_{0.36}\text{Ca}_{0.64}\text{MnO}_3$, doping by $\text{Cr}^{3+}/\text{Ru}^{4+}$ in $\text{Pr}_{0.5}\text{Ca}_{0.5}\text{MnO}_3$ and $\text{Pr}_{0.5}\text{Sr}_{0.5}\text{MnO}_3$ results in the FMM state, the dopant concentration being as low as 3%.

Thin films of both hole-doped $\text{Pr}_{0.6}\text{Ca}_{0.4}\text{MnO}_3$ and electron-doped $\text{Pr}_{0.4}\text{Ca}_{0.6}\text{MnO}_3$ have been prepared and effect of doping by Cr^{3+} and Ru^{4+} ions has been carried out on these systems. The hole-doped films show behavior as the bulk samples. However in the case of the electron-doped films, we see a drop in resistivity at low temperatures, but the FMM state could not be induced. The only similarity between the films of these two manganate compositions is in the electric fields on the resistivity.

The above studies show the unique nature of electron-doped rare earth manganates and the presence of electron-hole asymmetry in these systems. We

have examined the EPR spectra of $\text{Pr}_{0.36}\text{Ca}_{0.64}\text{MnO}_3$ to see whether it differs from that of $\text{Pr}_{0.64}\text{Ca}_{0.36}\text{MnO}_3$. The g-value falls with respect to temperature in electron-doped systems below the charge ordering temperature unlike in the hole-doped composition where it increases. We have performed LMTO calculations to shed some light. The low density of electrons in $\text{Pr}_{0.4}\text{Ca}_{0.6}\text{MnO}_3$ near the Fermi-level has suggested to us the possibility of a Mott-Hubbard type gap.

The nature of electrical conduction in the manganates of the type $\text{Ln}_{0.5}\text{Ca}_{0.5}\text{MnO}_3$ (Ln = Gd, Nd), in both single crystalline and polycrystalline samples, has been examined. The various mechanisms explored are Arrhenius behavior, polaron hopping behavior and variable range hopping (VRH) in these systems. In $\text{La}_{0.7}\text{Ca}_{0.3}\text{MnO}_3$ the nature of hopping in the insulating state is described by small polaronic hopping. We have investigated the possibility of adiabatic and nonadiabatic and bipolaronic hopping mechanisms in $\text{Ln}_{0.5}\text{Ca}_{0.5}\text{MnO}_3$. We have carried out similar investigations on hole-doped $\text{Pr}_{0.6}\text{Ca}_{0.4}\text{MnO}_3$ and electron-doped $\text{Pr}_{0.4}\text{Ca}_{0.6}\text{MnO}_3$. Our studies reveal that the VRH mechanism is dominant in the hole-doped regime whereas it is not so evident in the electron-doped regime. A.c conductivity measurements have been carried out on these samples. In the case of electron-doped composition, we find unusually high value of exponent 's'.

The nature of antiferromagnetic ordering in $\text{Pr}_{0.5}\text{Sr}_{0.5}\text{MnO}_3$ is of A-type whereas in $\text{Nd}_{0.5}\text{Sr}_{0.5}\text{MnO}_3$ it is CE-type. Accordingly, the latter is charge-ordered whereas the former is not, even though the radii of Pr^{3+} are comparable to Nd^{3+} . We have investigated the nature of the transition in $\text{Pr}_{0.5-x}\text{Nd}_x\text{Sr}_{0.5}\text{MnO}_3$ solid solutions. It is found that at $x=0.2$, there is a change from $I4/mcm$ to $Imma$ indicating change of spin ordering from A-type to CE-type.

Lastly, we have investigated for the presence of charge ordering in layered manganate of $\text{Nd}_{0.5}\text{Ca}_{1.5}\text{MnO}_4$ (Ruddlesden-Popper type). In $\text{Nd}_{0.5}\text{Sr}_{1.5}\text{MnO}_4$, which has larger A-site radii, no charge ordering has been observed. We have also found similar observations in measurements of single crystals of this material.

Papers related to this work have appeared in *Solid. State. Commun* (2000), *Chem. Mater.* (2001) and *J. Chem. Phys. Solids* (2001). Another paper will soon appear in *Solid State Sci.* (2002).

CHARGE ORDERING AND RELATED PROPERTIES OF RARE EARTH MANGANATES

1.1 AN OVERVIEW OF THE RARE EARTH MANGANATES

In transition metal oxides, where the metal cation exists in more than one valence state, it is often found that below a particular temperature, electron hopping between the cations become highly unfavorable and therefore localizes the charges to specific lattice sites. As a consequence, an abrupt increase is observed in the resistivity. This is also often accompanied by a change in the crystal symmetry and the magnetic structure as well. This phenomena is called charge ordering and the temperature at which the ordering sets in is called the charge ordering temperature, T_{CO} [1-4].

Historically, charge ordering was first observed in magnetite, Fe_3O_4 [5,6]. Iron exists in two valence states in this spinel structure, as Fe^{2+} and Fe^{3+} and can be represented as $Fe^{3+}[Fe^{2+},Fe^{3+}]O_4$. At room temperature the ground state is insulating and ferrimagnetic ($T_N=858K$). At around 120K ($=T_V$), a two-fold decrease is seen in the conductivity data as depicted in Fig. 1. 1. This is known in the literature as the Verwey transition and was first observed by Verwey in 1939 [5]. Structurally, the metal cation exists in two different sites; one-third of it is tetrahedrally coordinated (A-site) to the oxygen atoms and the remaining two-thirds are octahedrally coordinated (B-site) similarly. The spins of A- and B-

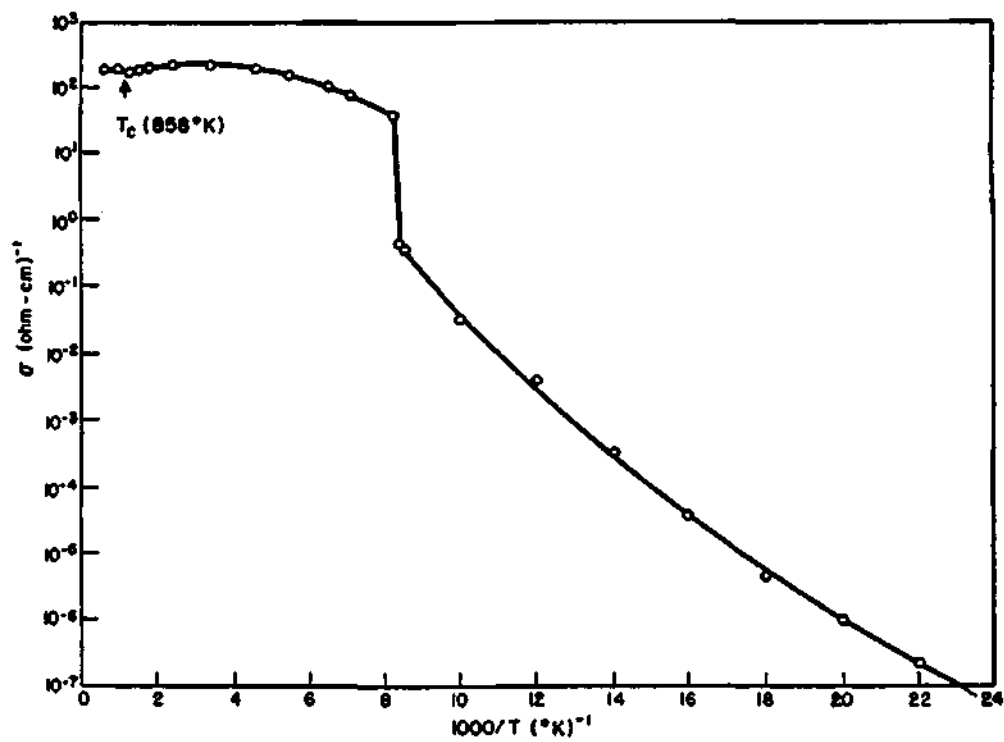


Fig. 1. 1. The charge ordering phenomena as observed in the conductivity measurement of Fe_3O_4 [6].

sublattices are antiparallel to each giving rise to ferrimagnetism. The electrical conduction takes place along the B-plane and below T_V , the Fe^{2+} and Fe^{3+} cations in this plane gets ordered [6-9]. However recently, this understanding with respect to the charge ordering process is under scrutiny with findings of ordering on the tetrahedral sites as well [10,11].

From the literature, one finds that a majority of the materials exhibiting charge ordering behavior are the rare earth manganates of the formula, $Ln_{1-x}A_xMnO_3$ [Ln = rare earths La, Pr, Nd etc, A = alkaline earths Ca, Sr] where the valency of manganese ions vary between 3+ and 4+ depending on the relative mole fractions of Ln and A ions. However charge ordering is also observed in other systems such as $La_{1-x}Sr_xFeO_3$, $La_{2-x}Sr_xNiO_4$, $La_{1-x}Sr_{1+x}MnO_4$ and $LiMn_2O_4$ albeit often in a narrow window of composition. A brief description of charge ordering in some of these compounds will be given before embarking to see it richly in the rare earth manganates.

$La_{1-x}Sr_xFeO_3$ is seen to exhibit charge ordering at $T_{CO} = 210$ K at the compositional value of $x = 0.66$ [12,13]. An interesting feature of this material is that antiferromagnetism also sets in simultaneously i.e., $T_N = T_{CO}$. Employing the charge neutrality principle, iron should exist as Fe^{3+} and Fe^{4+} . However by Mossbauer spectroscopy, it is seen that Fe^{4+} disproportionates into Fe^{3+} and Fe^{5+} in the ratio of 2:1. The ordering therefore arises from Fe^{3+} and Fe^{5+} and this is

confirmed by electron and neutron diffraction studies. This ordered structure is depicted in Fig. 1. 2.

Charge ordering is also observed in $\text{La}_{2-x}\text{Sr}_x\text{NiO}_{4+y}$ for values of $p(=x+2y)$ given by $0 < p < 0.7$ [14,15]. The presence of both charge and spin modulation in this material has led to its intense investigation [16]. Doping of Sr in the parent compound LaNiO_4 results in formation of holes which cooperatively orders with the spins on the Ni sites. As a typical example, for $p = 0.3$ ($x = 0.3$, $y = 0$), charge ordering is seen at 240 K, while the material remains antiferromagnetic. This is an example where the ordering of spins drive the system to be charge ordered. In Fig. 1. 3, resistivity curves depict the charge ordering phenomena in a single crystal of $\text{La}_{1.67}\text{Sr}_{0.33}\text{NiO}_4$ in two different orientations with respect to c -axis [16].

As a final example, LiMn_2O_4 shows charge ordering at $T_{\text{CO}} = 290$ K and is accompanied by a phase transition from cubic to tetragonal symmetry of its spinel structure. At lower temperature (65 K), it exhibits a complex magnetic behavior [17,18].

1.1.1 Structural aspects of rare earth manganates

Rare-earth manganates of the general formula $\text{Ln}_{1-x}\text{Ca}_x\text{MnO}_3$ crystallize in the perovskite structure, in which Mn-atoms occupy the vertices and constitute

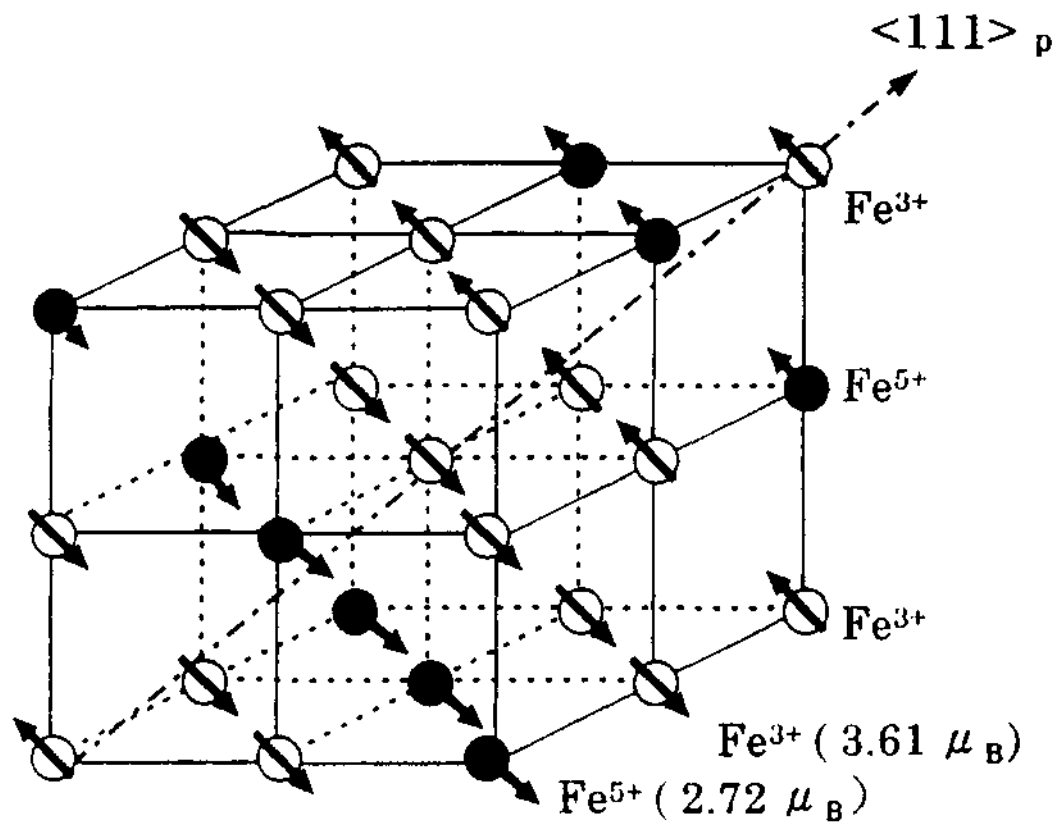


Fig. 1. 2. Charge ordering accompanied by spin ordering as seen in the composition $\text{La}_{0.33}\text{Sr}_{0.67}\text{FeO}_3$ [4].

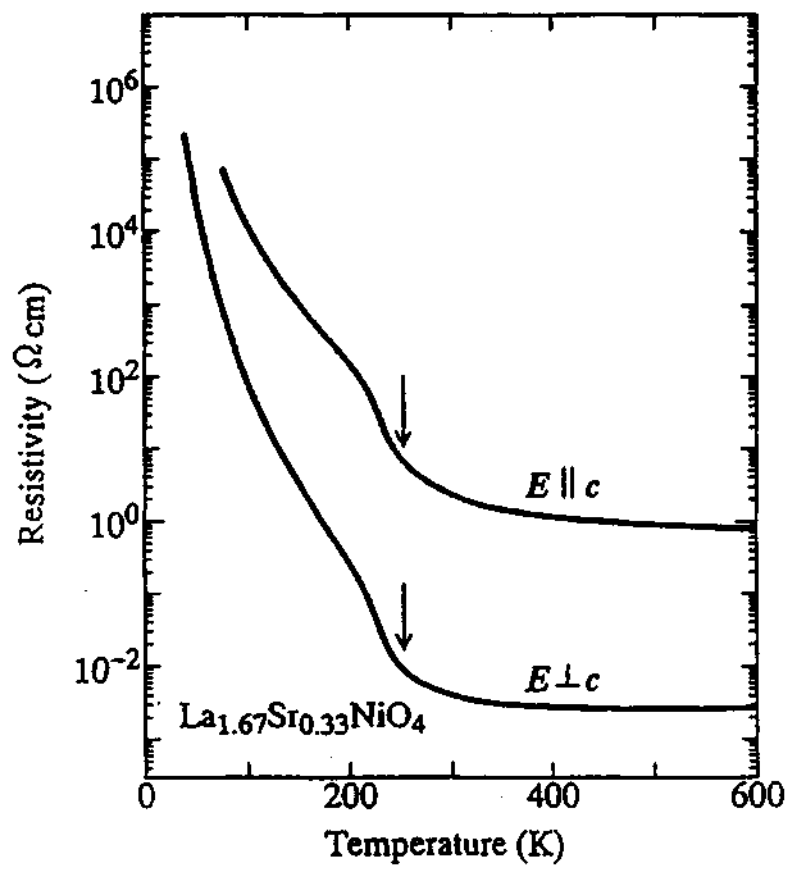


Fig. 1. 3. Single crystal of $\text{La}_{1.67}\text{Sr}_{0.33}\text{NiO}_4$ showing anisotropy in the charge ordering process [16].

the B-site, the oxygen atoms lie along the edges and the rare earth/alkaline earth occupies the central A-site. In an alternative description, this can be viewed akin to the FCC structure where the vertices are occupied by the rare earth/alkaline earth atoms and the centre of each face is occupied by the oxygen atoms. With the Mn atom lying in the centre, this connects ensemble to form the $\text{MnO}_{6/2}$ octahedra. The structure of a cubic perovskite is shown in Fig. 1. 4. It is viewed both as a ball-stick framework and as connected octahedra. In rare-earth manganate compositions, a majority of them are seen to adopt orthorhombic, rhombohedral or tetragonal space groups. This deviation from the ideal cubic symmetry is the consequence of size-mismatch of the A-site cation and also due to Jahn-teller (JT) distortion as a consequence of the Mn^{3+} ion. The Mn^{3+} ion which is a d^3 system ($t_{2g}^3 e_g^1$) undergoes JT distortion which works to lift the degeneracy of the e_g orbital and in doing so, the Mn—O distance along a particular direction (say z) changes. This process is diagrammatically [19] shown in Fig. 1. 5.

Deviation from the "ideal" cubic perovskite is measured in terms of the tolerance factor. Mathematically, it is given by

$$\Gamma = \frac{(r_A + r_O)}{\sqrt{2}(r_B + r_O)}$$

where, r_A , r_B and r_O represent the ionic radii of the A, B and O ions. The tolerance factor is actually a measure of the relative mismatch between the AO and BO_2

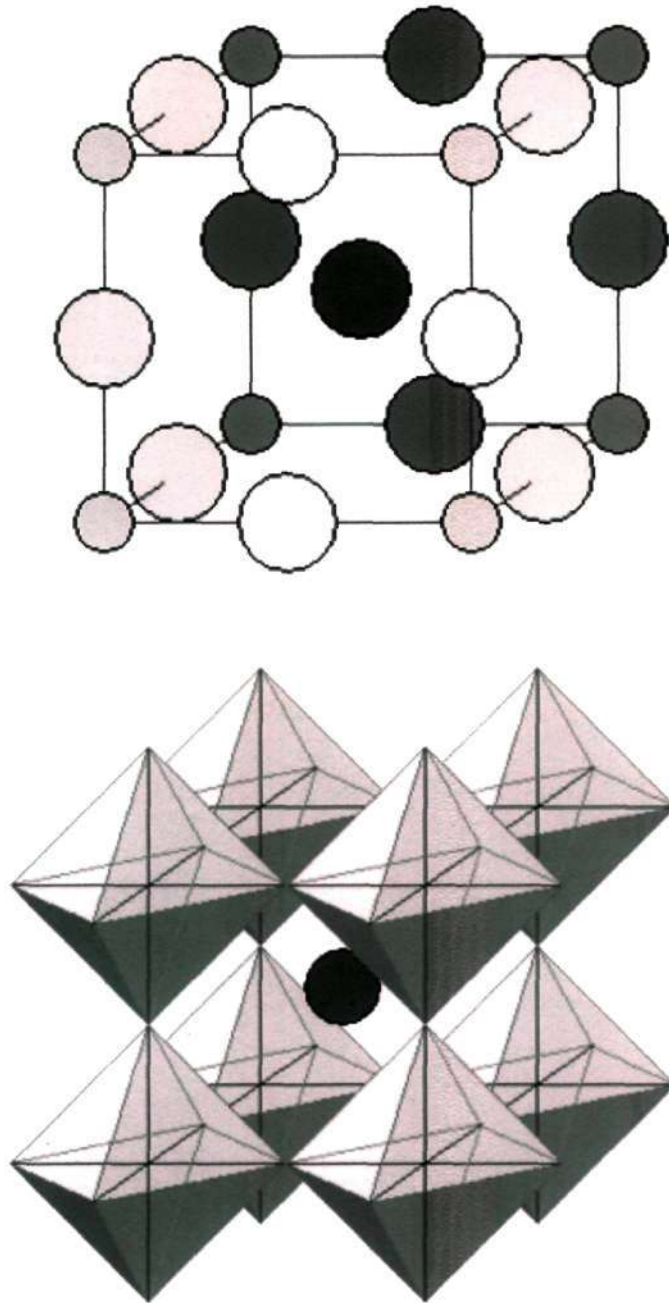


Fig. 1. 4. Cubic perovskite structure (ABO_3) shown by employing stick-ball configuration and connected octahedra. In the centre of the cube is the A-atom, along the centre of the edges lies the oxygen atoms and the corners are occupied by B-atoms.

planes which can be viewed as stacked one above another. When $\Gamma = 1$, the ideal cubic perovskite is said to be realized. Structures with $\Gamma < 1$ can be accomplished by the rotation of the B—O—B bond through an angle $180-\varphi$. For example, when such rotations are about the [110] axis of the cubic symmetry, orthorhombic $Pbmm$ (the so called $GdFeO_3$ type distortion) space group is obtained (Fig. 1. 6). The value of tolerance factor here is less than 0.96. If such a rotation is about the [111] axis, a rhombohedral $R\bar{3}c$ space group is realized where $0.96 < \Gamma < 1$. This ability to accommodate $\Gamma < 1$ values while retaining the perovskite structure, allows extensive cationic substitutions in both the A- and B-sites.

1.1.2 Electronic properties of the manganates

Before looking into the different electronic features of rare earth manganates, an overview of the orbital energetics is useful. The 3d orbitals of Mn-atom lie in the same energy scale of the oxygen 2p and these orbitals overlap. The filled bands constituting the bonding orbitals are predominantly 2p in its character and are separated from the antibonding orbitals by a large energy gap (~ 6 eV). The empty 5d states of the rare earth atoms lie well within the antibonding region [20]. The 4f levels are characterized by large intraatomic, electron-electron coulomb repulsion interactions (> 5 eV) and are highly localized and lie well below the Fermi-level (E_F) [21]. Therefore, the band near E_F is mainly O2p and Mn3d in character. The extent of overlap between these

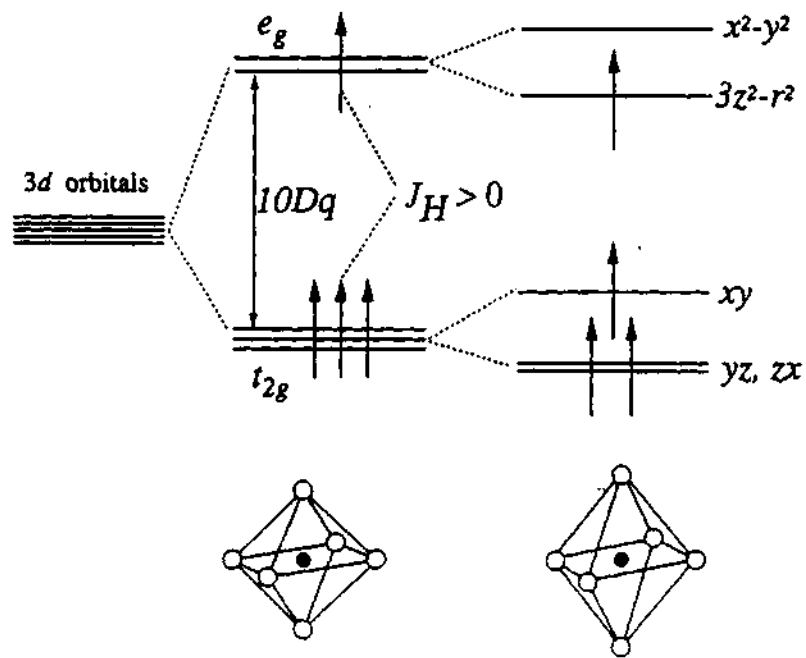


Fig. 1. 5. Jahn-Teller distortion of the d -levels of the Mn^{3+} ion ($t_{2g}^3 e_g^1$) leading to elongation of the octahedra in the z -direction [19].

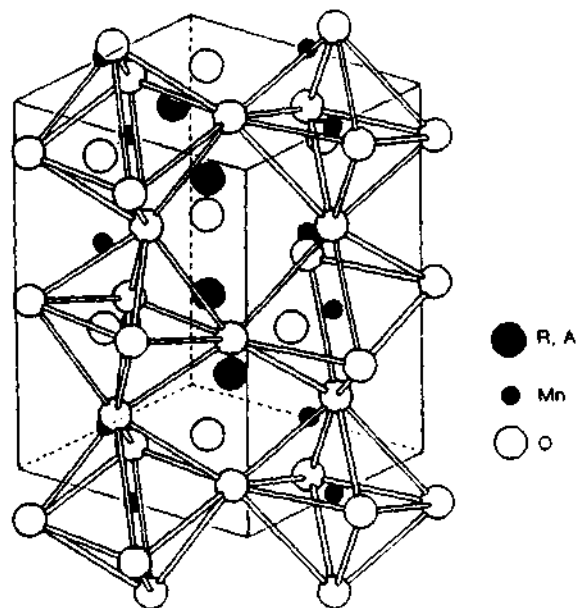


Fig. 1. 6. Orthorhombic distortion in a manganese perovskite.

orbitals is dependent on their separation as well as the angle subtended by the Mn—O—Mn bond. The properties of the material not only depend on the length and the angle but also on the ratio of Mn³⁺/Mn⁴⁺, which in itself is dependent on the occupancy of the A-site substitution. Therefore, tuning of the Mn³⁺/Mn⁴⁺ ratio gives rise to a variety of electronic properties.

It is seen that two of the most commonly observed features in these materials are the presence of ferromagnetism-metallicity and antiferromagnetism-insulating behaviour. In order to understand this, the aid of the double-exchange and the superexchange mechanism is necessary. A concise description pertaining to each of these mechanisms is given below.

(a) *Double exchange mechanism*

In the perovskite structure, the manganese ion is in an octahedral environment surrounded by oxygen atoms and due to crystal-field symmetry, the *d*-orbitals are split into lower *t*_{2g} levels and upper *e*_g levels. The valence state of manganese as mentioned earlier is in either the 3+ or the 4+ state corresponding to the electronic configuration $t_{2g}^3 e_g^1$ (*S* = 2) and $t_{2g}^3 e_g^0$ (*S* = 3/2). The Mn³⁺ ion is however a Jahn-Teller ion and therefore the degeneracy of the *e*_g states is lifted. The *e*_g orbital (say 3z²-r²) are lowered in energy to such an extent that the spin (*S* = 1/2) couples with the spin of the *t*_{2g} level (*S* = 3/2). This intra-site spin coupling is referred to as the Hund coupling (*J*_H). The energetics of the

d-orbital splitting due to crystal field (Δ_{Dq}) is around 1 eV whereas the on-site Hund coupling J_H is around 2-3 eV. The t_{2g} levels which lie lower are less hybridized than the e_g levels. The electrons in the t_{2g} levels are therefore localized whereas the e_g electrons tend to be itinerant. This mobility of the electrons against the backdrop of the spin interaction is governed by the intersite hopping amplitude term t_{ij} , where i,j correspond to indices of neighboring atoms. Mutual repulsion or electron correlation effects (as they are referred to) characterize the electrons in the *d*-orbitals as a consequence of Hund's rule. This repulsion therefore inhibits the electrons jumping onto the neighboring sites. The ratio J_H/t_{ij} is used to measure the strength of this correlation interaction versus the hopping term. The hopping amplitude t_{ij} is given by the Anderson-Hasegawa [22] relation;

$$t_{ij} = t_{ij}^0 \left[\cos\left(\frac{\theta_{ij}}{2}\right) \right]$$

where θ_{ij} is the measure of the relative angle between neighboring atoms. This is shown in Fig. 1. 7. It can be seen from the equation that the hopping amplitude is maximized when $\theta_{ij} = 0$, corresponding to alignment of the t_{2g} spins. This hopping process is favoured only if the neighbouring e_g orbital is empty i.e., corresponding to a Mn^{4+} ion. This corresponds to the interaction where spins have to be aligned to give rise to conduction and consequently the ferromagnetic behavior [22,24]. The process of electron-hopping takes place with the electron

jumping from a Mn^{3+} site to the intervening oxygen atom, and from there to the adjacent Mn^{4+} site leading to a double-exchange process.

(b) Superexchange mechanism

Consider the case where $\text{Mn}^{3+}-\text{O}-\text{Mn}^{3+}$, i.e., two adjacent e_g orbitals with an intervening orbital of oxygen. Hopping is highly unfavorable due to electron correlation effects. The only way the system can stabilize itself is to align the spins on the e_g orbitals in an antiparallel fashion resulting in an antiferromagnetic behaviour. In the octahedral environment, the e_g orbital x^2-y^2 (say) aligns itself parallel to the 2p orbital (180°) and the electrons couple antiferromagnetically as shown in Fig. 1. 8. This correlation interaction giving rise to the antiferromagnetic insulating behavior is known as the superexchange mechanism [25,26]. The 180° antiferromagnetic interaction occurs in more than one ways. In Fig. 1. 9, the different arrangements of spins are shown, each giving rise to the net antiferromagnetic behavior. Other types of superexchange interaction exist in which orbitals interact via an angle of 90° giving rise to ferromagnetic-insulating state.

1.1.3 Phase diagrams and terminology

A glance at the literature involving rare earth perovskite manganates of the type $\text{Ln}_{1-x}\text{A}_x\text{MnO}_3$ reveals the richness and intricacy between the electronic,

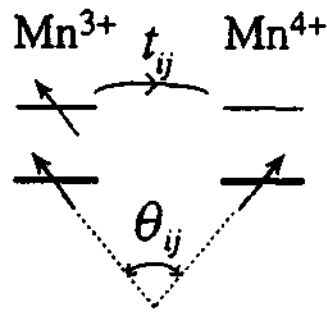


Fig. 1. 7. The angle between the t_{2g} spins as described in the double exchange process [19].

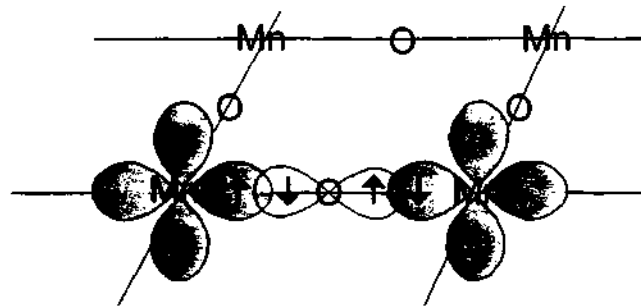


Fig. 1. 8. The superexchange interaction between Mn ($d_{x^2-y^2}$) and O($2p_x$) orbital (view is along the xz plane)

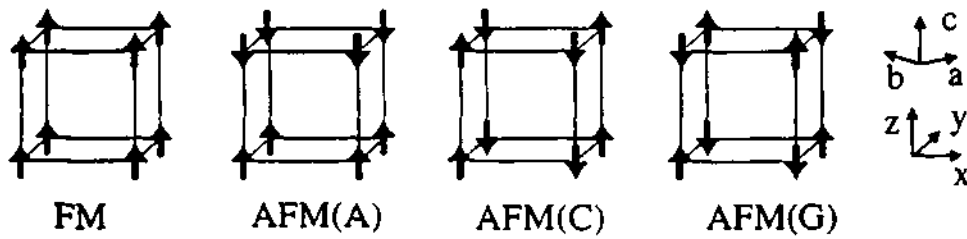


Fig. 1. 9. Antiferromagnetic interactions (AFM) achieved in a variety of ways by the superexchange interaction [4].

magnetic and structural properties of these systems. In order to explore charge ordering and accompanying phenomena in different families of rare earth manganates, it is worthwhile to inspect the phase diagrams of these. For this purpose, phase diagrams from rare earths La, Nd and Pr and alkaline earths Ca and Sr forming the families of $\text{La}_{1-x}\text{Ca}_x\text{MnO}_3$, $\text{Pr}_{1-x}\text{Ca}_x\text{MnO}_3$, $\text{La}_{1-x}\text{Sr}_x\text{MnO}_3$, $\text{Nd}_{1-x}\text{Sr}_x\text{MnO}_3$ and $\text{Pr}_{1-x}\text{Sr}_x\text{MnO}_3$ have been chosen and displayed in Fig. 1. 10.

A glance at the different families reveals certain general features common to all. For example when $x > 0.5$ i.e., in the electron doped regime, charge ordering seems to be clearly favored as evidenced in the case of $\text{La}_{1-x}\text{Ca}_x\text{MnO}_3$, $\text{Nd}_{1-x}\text{Sr}_x\text{MnO}_3$ and $\text{Pr}_{1-x}\text{Ca}_x\text{MnO}_3$. Simultaneously in the hole doped regime when $x < 0.5$, one sees the onset of ferromagnetism except in the case of $\text{Pr}_{1-x}\text{Ca}_x\text{MnO}_3$ where it is observed not till $x = 0.3$. Thus one observes a clear demarcation between the electron- and the hole-doped regimes resulting in an electron-hole asymmetry.

The subtlety involving the factors governing charge ordering is clearly brought out in the case study of $\text{Pr}_{1-x}\text{Sr}_x\text{MnO}_3$ and $\text{Nd}_{1-x}\text{Sr}_x\text{MnO}_3$ family. The general features in both these phase diagrams greatly resemble each other; however $\text{Nd}_{1-x}\text{Sr}_x\text{MnO}_3$ is charge ordered (for $x > 0.5$) whereas $\text{Pr}_{1-x}\text{Sr}_x\text{MnO}_3$ does not exhibit charge ordering in all of the composition range, even though the radii of both Pr and Nd are nearly the same. It is noticed that if Ca is employed in

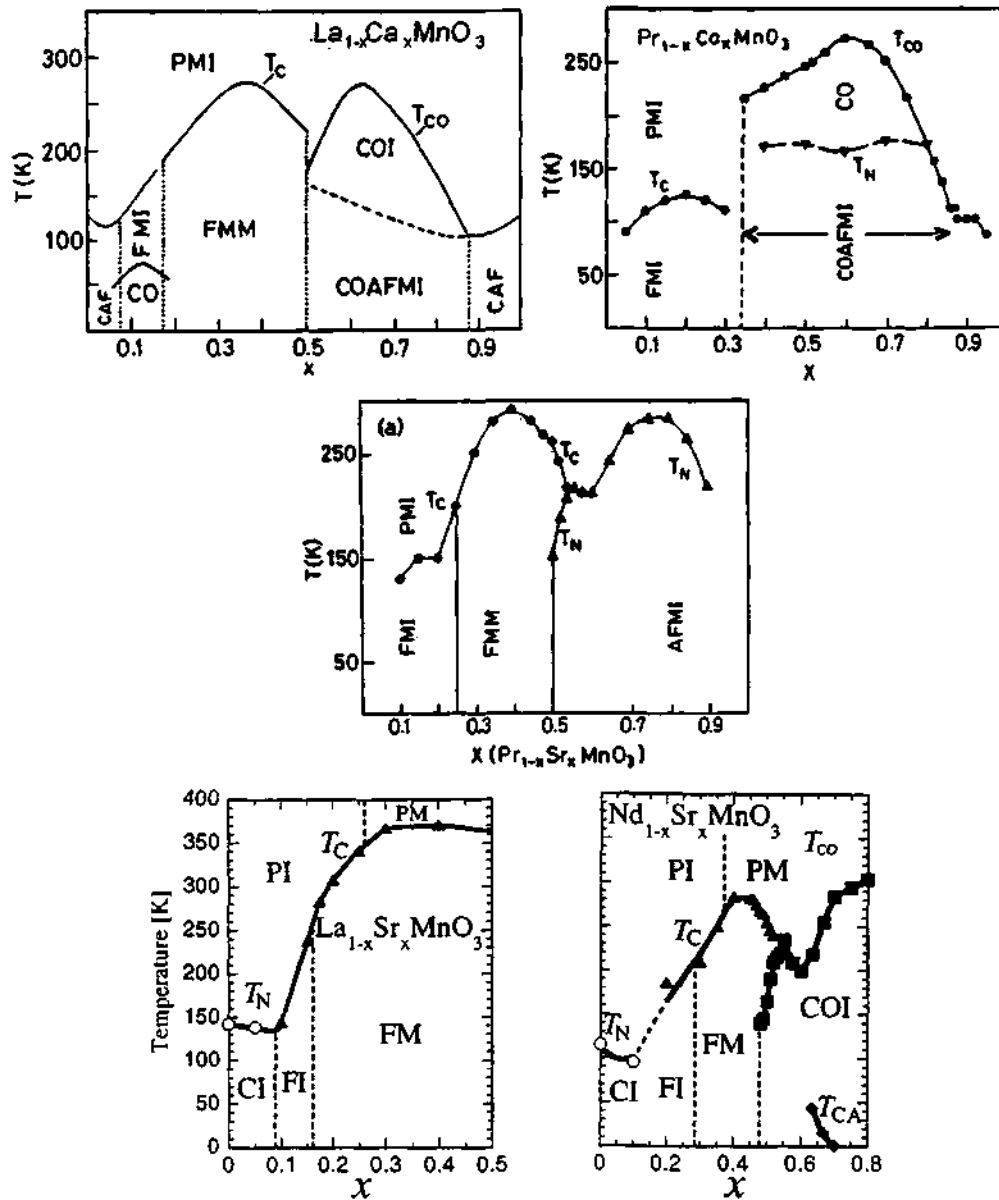


Fig. 1. 10. Phase diagrams of a few rare-earth manganates [2,4]. The description of the legends are: CO(\equiv C) - charge ordering; P (\equiv PM) - paramagnetic; I - insulator; F(\equiv FM) - Ferromagnetic; AFM - antiferromagnetic; CAF(\equiv CA) - canted antiferromagnetic; T_c - Curie temperature; T_N - Neel temperature; T_{co} - Charge ordering temperature.

place of Sr, then this distinction completely disappears and the phase diagram therefore for $\text{Nd}_{1-x}\text{Ca}_x\text{MnO}_3$ (not shown) reads exactly like that of $\text{Pr}_{1-x}\text{Ca}_x\text{MnO}_3$. On the other hand, $\text{La}_{1-x}\text{Ca}_x\text{MnO}_3$ shows charge ordering for $x < 0.5$ whereas $\text{La}_{1-x}\text{Sr}_x\text{MnO}_3$ does not exhibit it. Various factors governing charge ordering and the related phenomena will be described later by taking specific examples.

Before proceeding any further, it is important to look into the essential aspects and the associated terms frequently employed in the literature reports. For this purpose, two specific examples will be sought. The composition LaMnO_3 is chosen as the first candidate where the valency of Mn is $3+$ ($t_{2g}^3 e_g^1$). The second candidate is CaMnO_3 involving only the alkaline earth calcium, where manganese is in $4+$ state ($t_{2g}^3 e_g^0$). In LaMnO_3 where upon the doping of Ca in the A-site (La - site), results in the valency of Mn to change from $3+$ to $4+$ in order to maintain charge neutrality. This process in essence corresponds to the creation of holes, provided the doping concentration is maintained in the regime $x < 0.5$. Appropriately these compositions are said to be hole-doped and consequently whenever $x > 0.5$ i.e., corresponding to the doping of lanthanum in the calcium rich compound, the compositions are referred to as being electron-doped. At the phase boundary i.e., $x = 0.5$, the compositions are said to be "maximum hole-doped" corresponding in this example to the composition $\text{La}_{0.5}\text{Ca}_{0.5}\text{MnO}_3$. Now let us look into some of the electronic features exhibited by these systems.

The ground state electronic property of LaMnO_3 is that of a paramagnetic insulator (PMI) and adopts the structure of a orthorhombic perovskite. At temperatures below 150 K, it exhibits antiferromagnetism and is classified as an A-type antiferromagnet [27]. In this class, ferromagnetic planes containing Mn^{3+} ions are stacked antiparallel to each other along the c -axis resulting in the observed antiferromagnetic behavior [28,29]. However the interesting feature is not that of the spin arrangement, but the presence of ordering among the d -orbital $3x^2-r^2$ (or $3y^2-r^2$) of the manganese ions. This d -orbital orders in a particular manner as depicted in Fig. 1. 11. In addition to these orderings present, the system exhibits a collective Jahn-Teller (JT) distortion due to the presence of Mn^{3+} ions. This material is not charge ordered even though spin and orbital orderings are present. A common feature in rare-earth manganates exhibiting A-type antiferromagnetism is that there is always a certain electron transfer along the ferromagnetic ab -planes which prevents the process of charge ordering [92]. Consider on the other hand, the case of CaMnO_3 , where manganese exists only in the 4+ state. However Mn^{4+} (d^3 system) is not a JT ion and consequently the structure is that of a cubic perovskite. Ordering is seen to be confined only to spins leading to antiferromagnetism. The nature of antiferromagnetism is however not of the A-type but of the G-type where adjacent spins are antiparallel to each other as shown in Fig. 1. 9. No orbital ordering is observed and neither is charge ordering. Now let us consider $\text{La}_{0.5}\text{Ca}_{0.5}\text{MnO}_3$. It exhibits ferromagnetism

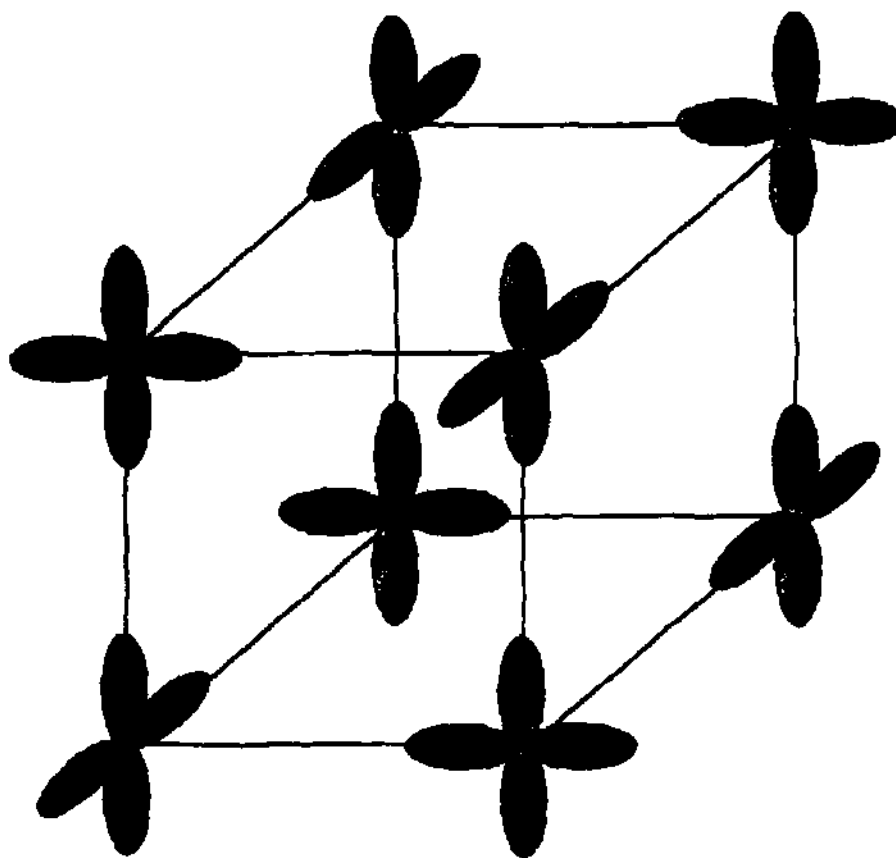


Fig. 1. 11. Orbital ordering involving the orbital $d_{x^2-y^2}$ in LaMnO_3 [4].

($T_C = 225$ K), followed by an antiferromagnetic charge-ordering process ($T_N = 225$ K = T_{CO}). Thus there is a series of complex transitions seen. The consequence of charge ordering is seen as bond length variation, wherein the Mn—O bond along *ab*-plane bond length is 1.92 Å and along the *c*-axis, it is 2.07 Å.

From the examples employed above, we observe that the relative amounts of Mn³⁺ and Mn⁴⁺ ions give rise to a variety of behavior. In a later section of this introduction we shall see that their spatial arrangement in the crystal structure as well as the relative angle between neighbouring Mn sites play a crucial role in determining the various properties exhibited by the material. In the next section, charge ordering and related processes will be dealt in detail.

1.1.4 Charge ordering process

Charge ordering (CO) is affected by a number of factors. These include the presence of impurity dopants such as Cr³⁺ and Ru⁴⁺ in the Mn-site, the variation of the radius of the A-site cation, oxygen stoichiometry, ¹⁸O isotopic substitution and the presence of external influences such as electric and magnetic fields. The effects of some of these on the charge ordered state is so drastic that it is completely destroyed. In most cases it induces an insulator-metal transition in the system. In this context, another phenomenon that is observed is the colossal magnetoresistance (CMR). This occurs as a result of the application of a magnetic

field on the insulating state in these materials. By magnetoresistance, one measures of the relative change in the resistivity of the material on the application of a magnetic field on it and is given by;

$$\text{MR} = \left[\frac{\delta\rho}{\rho(0)} \right] = \frac{[\rho(H) - \rho(0)]}{\rho(0)}$$

where $\rho(H)$ and $\rho(0)$ are the resistivity of the material in the presence and the absence of a magnetic field H , at a given particular temperature. When the resistivity of the material increases on the application of a magnetic field, the magnetoresistance is said to be positive and when it is vice-versa, it is called negative magnetoresistance. Metals and all semiconductors exhibit MR of a few percent and in other materials such as bimetallic layers of Fe/Cr [30,31], the MR is much higher (10-40%). This is termed as giant magnetoresistance (GMR). However, in rare earth perovskite manganates, the MR encountered is almost 100% and therefore goes by the name of colossal magnetoresistance (CMR) [33-37]. The importance of materials that exhibit CMR lies in its potential ability to serve as candidates for storage media in the electronic industry [38]. The quest for these materials in the past led to the detailed investigation of the rare earth manganates. This in turn led to the discovery of charge ordering and other related phenomena. As an example of a charge ordered material in rare earth manganates, consider $\text{Pr}_{0.7}\text{Ca}_{0.3}\text{MnO}_3$. This exhibits T_{CO} at ~ 200 K [39] and is a CMR material. At 100 K and an applied field of 7T, the drop in resistivity is 1000 fold from $10^4 \Omega\cdot\text{cm}$ to $10 \Omega\cdot\text{cm}$ accompanied by an I-M transition [40]. This is

shown in Fig. 1. 12a. It is noticed that in materials exhibiting ferromagnetism such as $\text{La}_{0.7}\text{Ca}_{0.3}\text{MnO}_3$ [41], the CMR is maximum near T_C (see Fig. 1. 12b). In this case, magnetoresistance of the order of 80% is observed at ~ 252 K for a field of 6T [19]. In order to understand this important phenomena, often the double-exchange (DE) mechanism is invoked as it abets to understand it in a simple manner. Consider the diagrammatic sketch in Fig. 1. 13. In the ferromagnetic metallic state, conduction takes place by hopping of the e_g hole between adjacent Mn ions. However, above T_C , the spins become "disoriented" and the hopping is therefore greatly reduced as given by t_{ij} (see Sec. 1.1.2). Therefore in the vicinity of T_C in the insulating state, even on applying a low magnetic field, the spins orient parallel to each other which thereby facilitates electron transfer ($\theta \rightarrow 0^\circ$; $t_{ij} \rightarrow \max$). Thus, near T_C , the resistivity falls drastically and the MR observed is a maximum. However, in reality the situation is more complicated. It however serves as a intuitive guideline in its understanding. In the case of charge ordered materials, it should be noted that it is not always possible to destroy it by the application of a magnetic field. An example is the case of the charge ordered state in $\text{Y}_{0.5}\text{Ca}_{0.5}\text{MnO}_3$. It is so robust that no melting has been seen hitherto [42]. A look into these details concerning charge ordering and the various factors affecting it in different families are discussed below. Before moving on, an important point to be noted is that the CMR effect has been observed in only the hole doped regime. In reports claiming to observe the CMR effect in electron

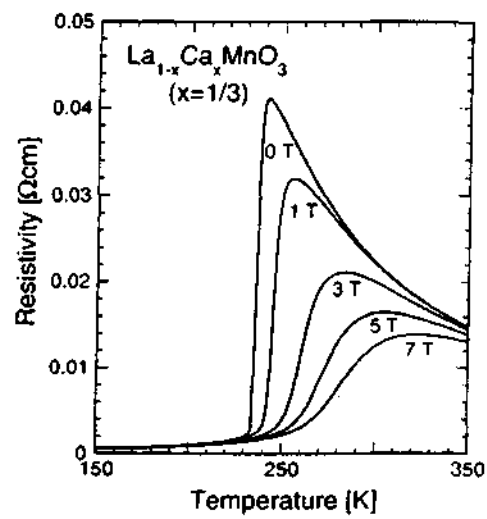
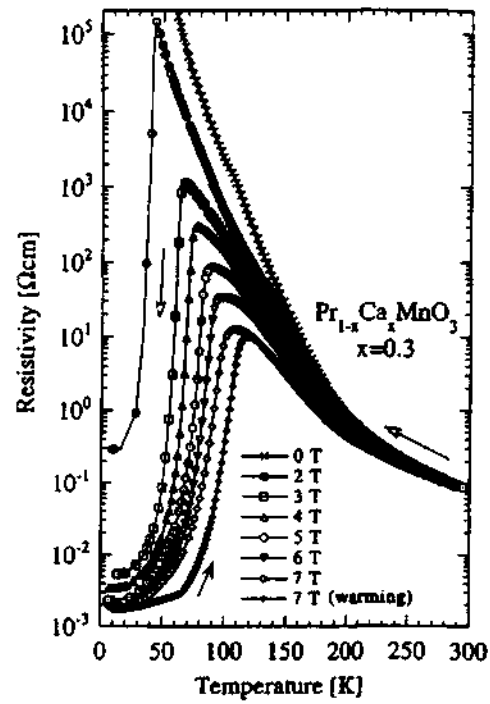
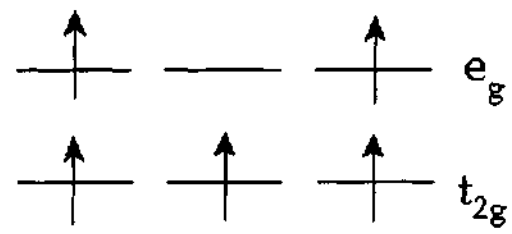
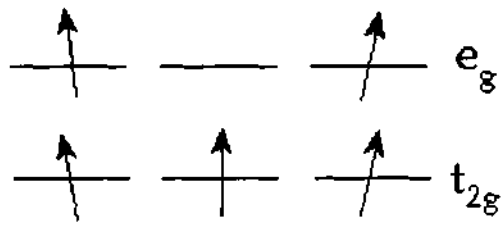


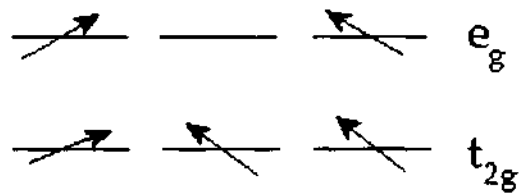
Fig. 1. 12. Magnetoresistance effect in $\text{Pr}_{0.7}\text{Ca}_{0.3}\text{MnO}_3$ and $\text{La}_{0.7}\text{Ca}_{0.3}\text{MnO}_3$ as a function of magnetic field [4,19].



(a) $T \ll T_c$



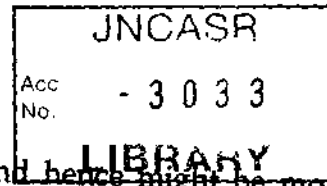
(b) $T \sim T_c$



(c) $T \gg T_c$

Fig. 1. 13. The CMR effect explained on the basis of double-exchange (DE) alone.

Just below T_c in the highly insulating regime, the field required to align the spins is low and this consequently maximizes the hopping amplitude.



doped regimes, the actual drop is only 10-100 fold and hence might be more appropriate to call it as the GMR effect [43,44].

1.1.5 Some important results reported in the literature

It is clear from the phase diagrams that charge ordering occurs over the widest range of composition in $\text{Pr}_{1-x}\text{Ca}_x\text{MnO}_3$ followed by $\text{Nd}_{1-x}\text{Sr}_x\text{MnO}_3$ and $\text{La}_{1-x}\text{Ca}_x\text{MnO}_3$. In the present section, a few of the prominent results featured in the literature will be discussed.

The crystal structure adopted by most of the charge ordered systems are seen to be orthorhombic; *Pbnm* as in $\text{Pr}_{0.6}\text{Ca}_{0.4}\text{MnO}_3$ and $\text{La}_{0.5}\text{Ca}_{0.5}\text{MnO}_3$ [45,46] and *Imma* in $\text{Nd}_{0.5}\text{Sr}_{0.5}\text{MnO}_3$ [47,48] etc at room temperature. Therefore, the tolerance factor is $\Gamma < 0.96$ and consequently the Mn—O—Mn bond angles are sufficiently deviated away from 180° . Due to this, the one-electron e_g band width is greatly narrowed and this favours charge ordering. The charge ordering process is observed experimentally by numerous techniques. In diffraction studies, it is seen directly by the appearance of superlattice spots at low angles. As an example, in $\text{Pr}_{0.7}\text{Ca}_{0.3}\text{MnO}_3$ composition, charge ordering is established with the help of neutron-diffraction technique, which appears as superlattice spots at ~ 200 K [49]. However, these are not easily detected in polycrystalline samples due to grain boundary formation. In these cases they are more easily

620.189 2

PO2

confirmed by resistivity and magnetization measurements which clearly show anomalies at temperatures corresponding to the onset of the charge ordered state. In Fig. 1. 14 the resistivity data of single crystals of $\text{Pr}_{1-x}\text{Ca}_x\text{MnO}_3$ for $x = 0.4$ and 0.35 are shown [50]. Also shown are the MR effects due to magnetic fields of 6 and 12T. The zero field data of both the compositions are seen to be insulating, wherein the charge ordering process occurs between 220-230 K. Magnetization measurements reveal antiferromagnetic behavior and it sets in below T_{CO} . In addition it is accompanied by orbital ordering. Thus charge ordering drives spin and orbital ordering. It is observed that charge ordering process is greatly stabilized when the band filling value coincides with a rational number of the periodicity of the lattice i.e., commensurate charge ordering takes place. It is therefore, maximized in the $x = 0.5$ composition where the $\text{Mn}^{3+}/\text{Mn}^{4+}$ ratio is 1:1 and consequently there is one "e_g hole" per two Mn ions. Thus commensurate ordering is seen in $\text{Nd}_{0.5}\text{Sr}_{0.5}\text{MnO}_3$. However, the nature of the charge ordering process is different in this material. It goes from a ferromagnetic metallic state to an antiferromagnetic charge ordered insulating state. Thus spin ordering drives charge ordering in this material. The resistivity and magnetization of this compound are shown in Fig. 1. 15. Both $\text{Nd}_{0.5}\text{Sr}_{0.5}\text{MnO}_3$ and all charge-ordered members of $\text{Pr}_{1-x}\text{Ca}_x\text{MnO}_3$ family exhibit the CE-type ordering in which spin, charge and orbital ordering is seen. This is seen in Fig. 1. 16 for $\text{Nd}_{0.5}\text{Sr}_{0.5}\text{MnO}_3$. This kind of ordering takes place because of the particular arrangement of the $\text{MnO}_{6/2}$ octahedra. Due to corner sharing arrangement, displacement of the

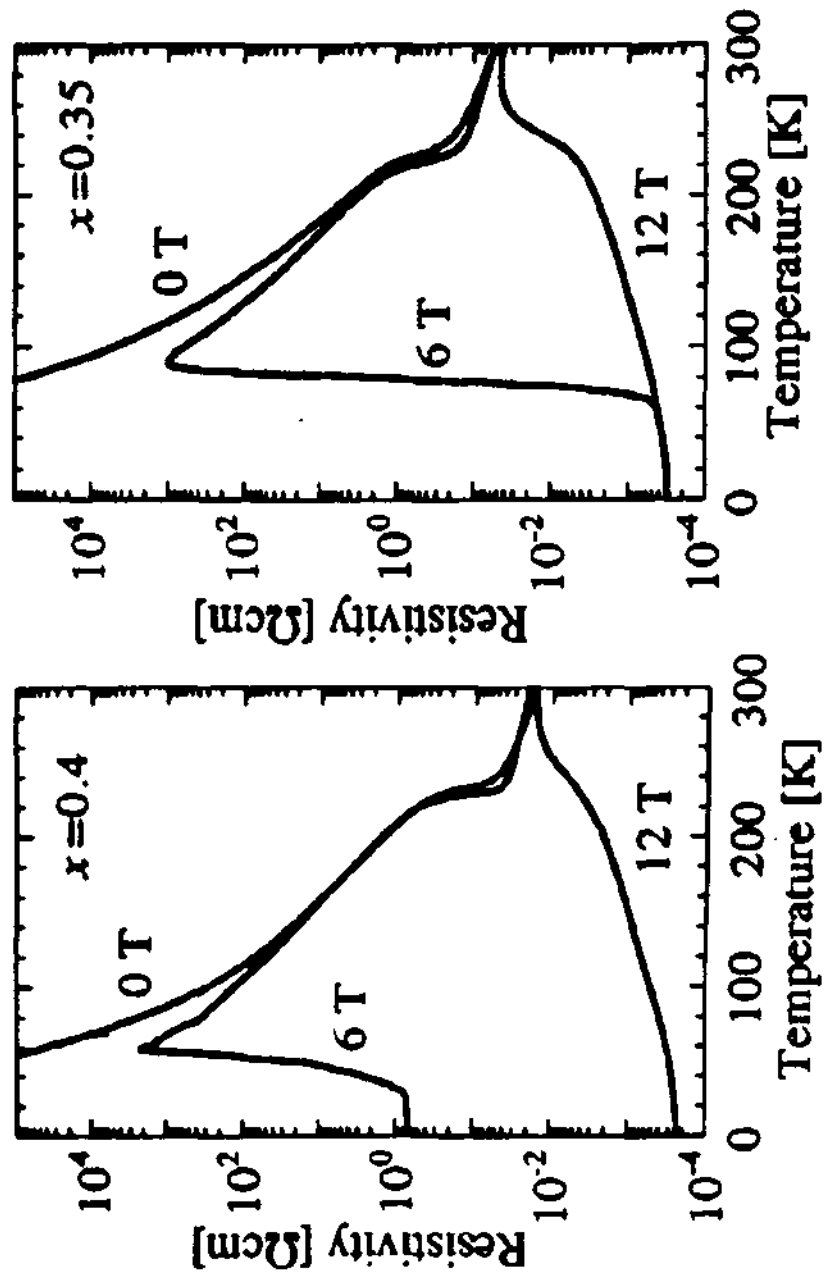


Fig. 1. 14. Resistivity data of $\text{Pr}_{1-x}\text{Ca}_x\text{MnO}_3$ ($x=4, 0.35$) showing charge ordering.

Also shown is the I-M transition obtained with 6 and 12T [50].

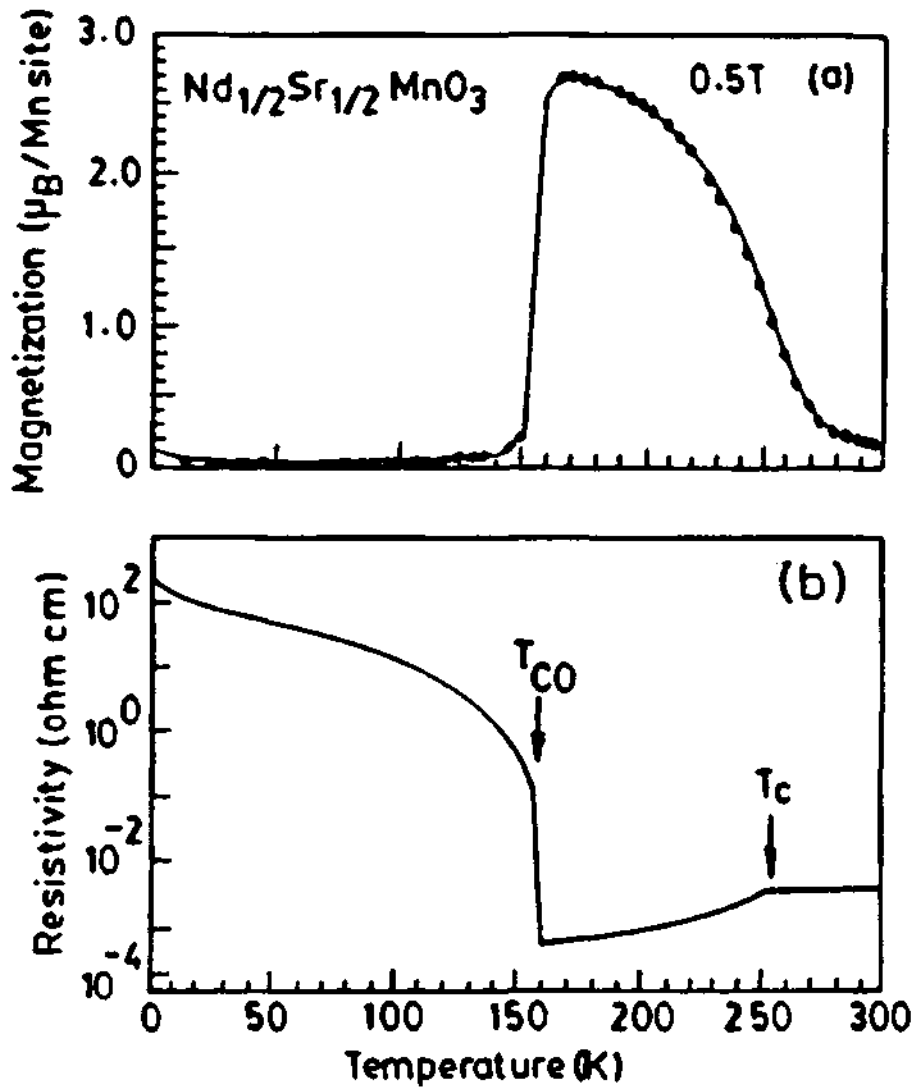


Fig. 1. 15. Magnetization and resistivity of $\text{Nd}_{0.5}\text{Sr}_{0.5}\text{MnO}_3$ [1].

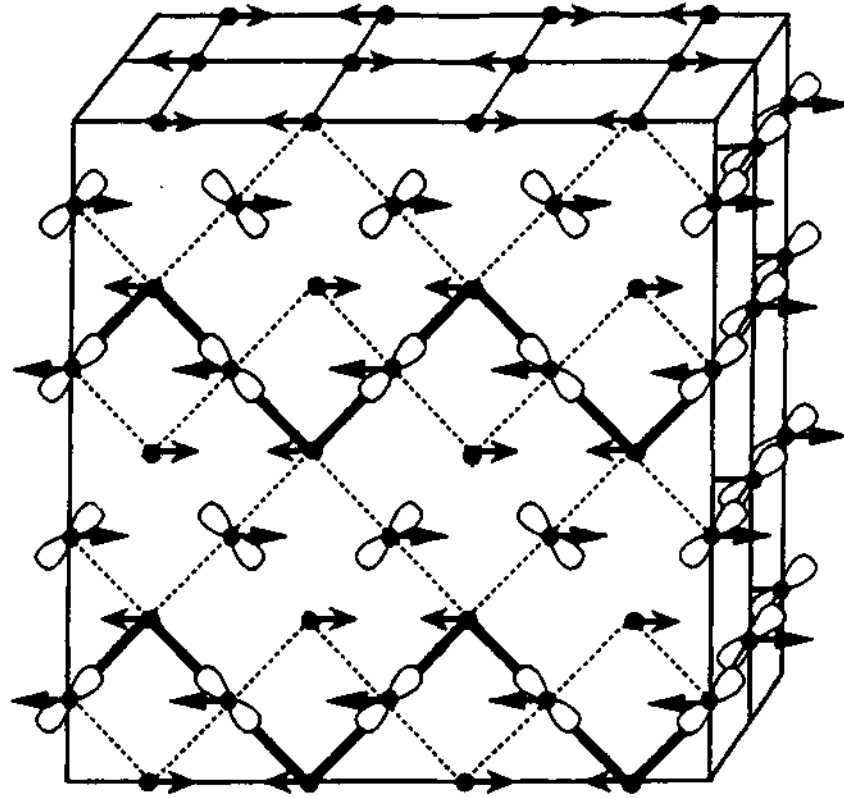


Fig. 1. 16. CE-type ordering as seen in $\text{Nd}_{0.5}\text{Sr}_{0.5}\text{MnO}_3$ (ab -plane facing) [47].

oxygen anion at one end induces the occupation of the opposite orbitals of the adjacent Mn ions. Thus orbitals get ordered in an "antiferro" arrangement in addition to the spin ordering present.

The application of magnetic field on the charge ordered compositions of $\text{Pr}_{1-x}\text{Ca}_x\text{MnO}_3$ ($x = 0.4, 0.35$) induces an I-M transition. This is true in the case of charge ordered $\text{Nd}_{0.5}\text{Sr}_{0.5}\text{MnO}_3$ also; only a smaller field is required [47]. A distinctive feature of the I-M transition in the case of $\text{Pr}_{1-x}\text{Ca}_x\text{MnO}_3$ ($x = 0.3, 0.35, 0.4$ and 0.5) family is that the transition temperature always occurs around 100 K. An interesting observation is made in the case of $\text{Pr}_{0.5}\text{Ca}_{0.5}\text{MnO}_3$. As shown in Fig. 1. 17 [50], it seems that the metallic state observed in the high temperature region (> 160 K), give way to charge ordering again. This feature is unique to this composition and not observed in other $x = 0.5$ systems. The quantification of I-M transition done by recording isothermal MRs also show interesting features. An example is that of $\text{Pr}_{0.65}\text{Ca}_{0.35}\text{MnO}_3$ where it reveals hysteresis behavior as shown in Fig. 1. 18 [50]. At 175 K, the charge ordered state melts at a field of ~ 11 T during the increasing cycle (open triangle) of the magnetic field. However, the CO state is regained at a lower field of ~ 10 T on the decreasing field cycle (closed triangle). When similar measurements are carried out at $T=4.2$ K, one sees the drop in resistivity due to charge order melting to be a huge 10^{11} times at an applied ~ 6 T (increasing cycle). However, the insulating charge ordered state is not recovered at all. This hysteresis features are not unique to $\text{Pr}_{1-x}\text{Ca}_x\text{MnO}_3$

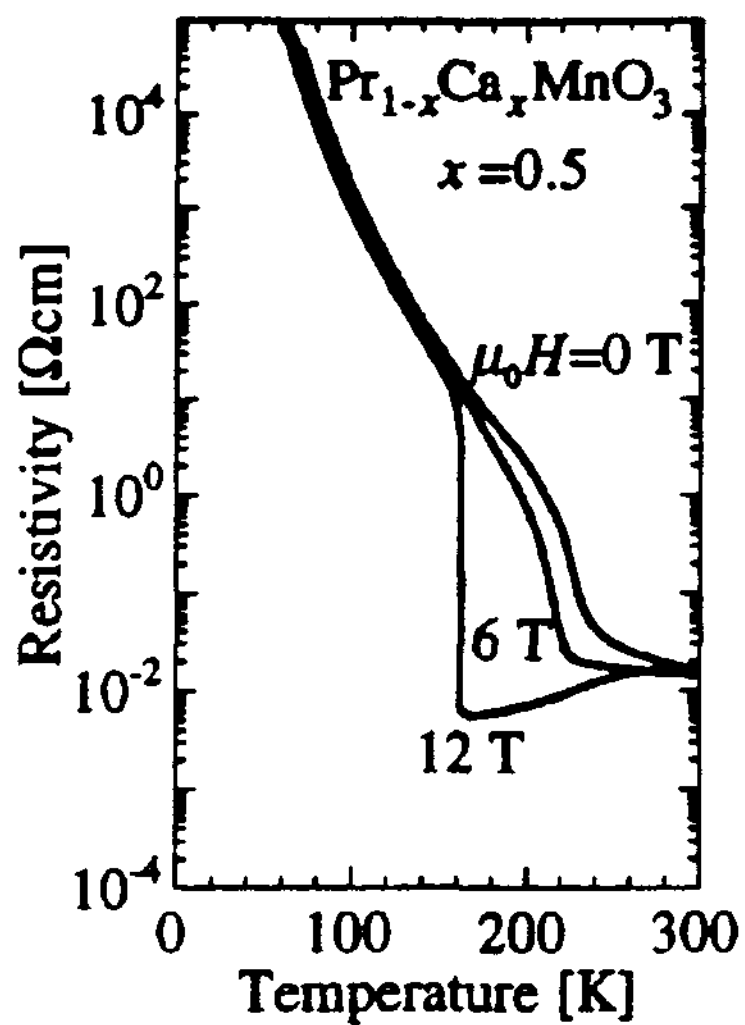


Fig. 1. 17. Resistivity data of a single crystal of $\text{Pr}_{0.5}\text{Ca}_{0.5}\text{MnO}_3$ showing re-entrant charge ordering after an I-M transition due to the application of 12T magnetic field [50].

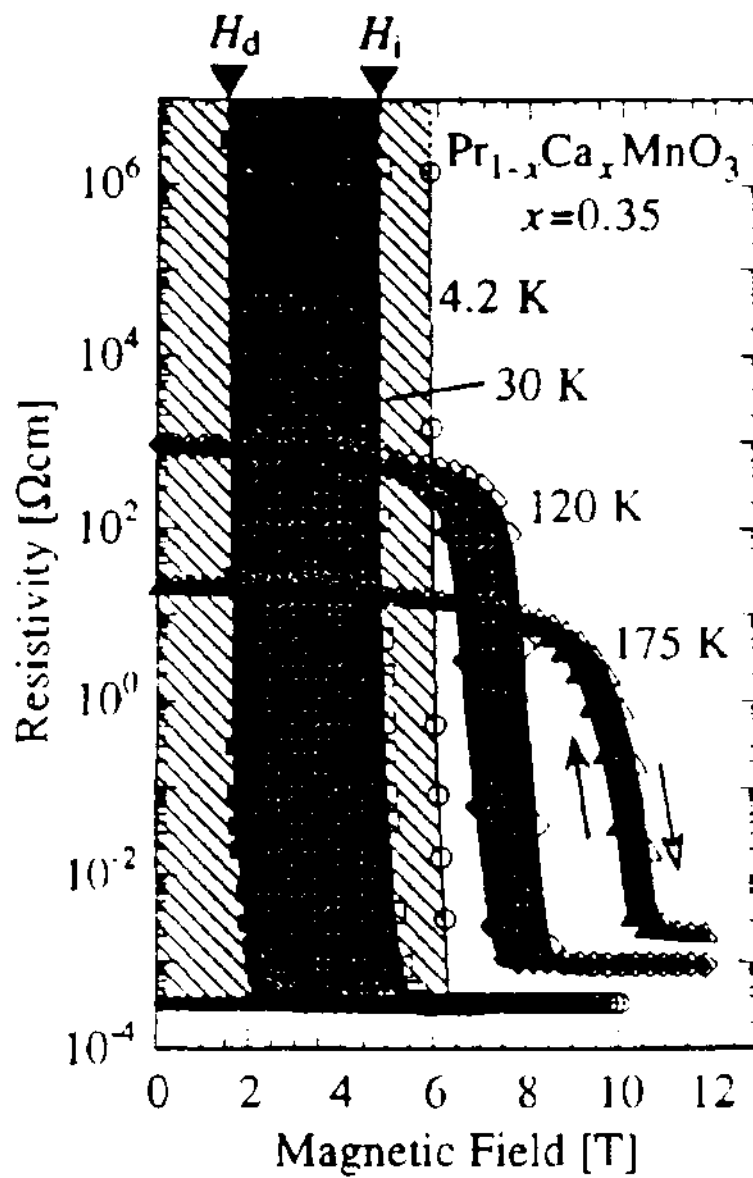


Fig. 1. 18. Isothermal magnetoresistance curves for $\text{Pr}_{0.65}\text{Ca}_{0.35}\text{MnO}_3$ showing hysteresis behaviour [50].

family and are also seen in the case of $\text{Nd}_{0.5}\text{Sr}_{0.5}\text{MnO}_3$ albeit to a lower extent (shown in Fig. 1. 19). Usually these features are represented with H-T curves, where the hatched portions show the hysteresis regions. In Fig. 1. 20 the hysteresis features are shown for a variety of charge ordered systems at $x = 0.5$ composition [51].

Charge ordering and associated phenomena has been probed by a number of techniques; important among them are optical and tunneling measurements. Optical spectroscopy is useful to probe the nature of electronic structure and is also helpful in understanding I-M transitions. In the reflectance spectroscopy technique, the reflectance $R(\omega)$ is obtained as function of frequency at various temperatures. Kramer-Kronig (KK) transformation is performed to obtain the optical conductivity, $\sigma(\omega)$. In the case of $\text{Pr}_{1-x}\text{Ca}_x\text{MnO}_3$ ($x = 0.4$) near normal incidence reflectivity measurements has revealed the anisotropy in the electronic structure, with respect to the CO state. The conductivity data obtained above and below the charge-ordering temperature ($T_{\text{CO}} = 235$ K) at 293 and 10 K respectively is shown in Fig. 1. 21. It clearly reflects the anisotropy encountered in the conduction process [52]. Baring the initial spiky features near 0.06 eV (optical phonon modes), the conductivity largely deviates at $T=10$ K ($T < T_{\text{CO}}$), along two different crystal axes. This variation is largely due to the difference in the ordering pattern of charge, spin and orbitals in the crystal. The charge ordering gap estimated to be ~ 0.2 eV, is actually comparable to that observed in

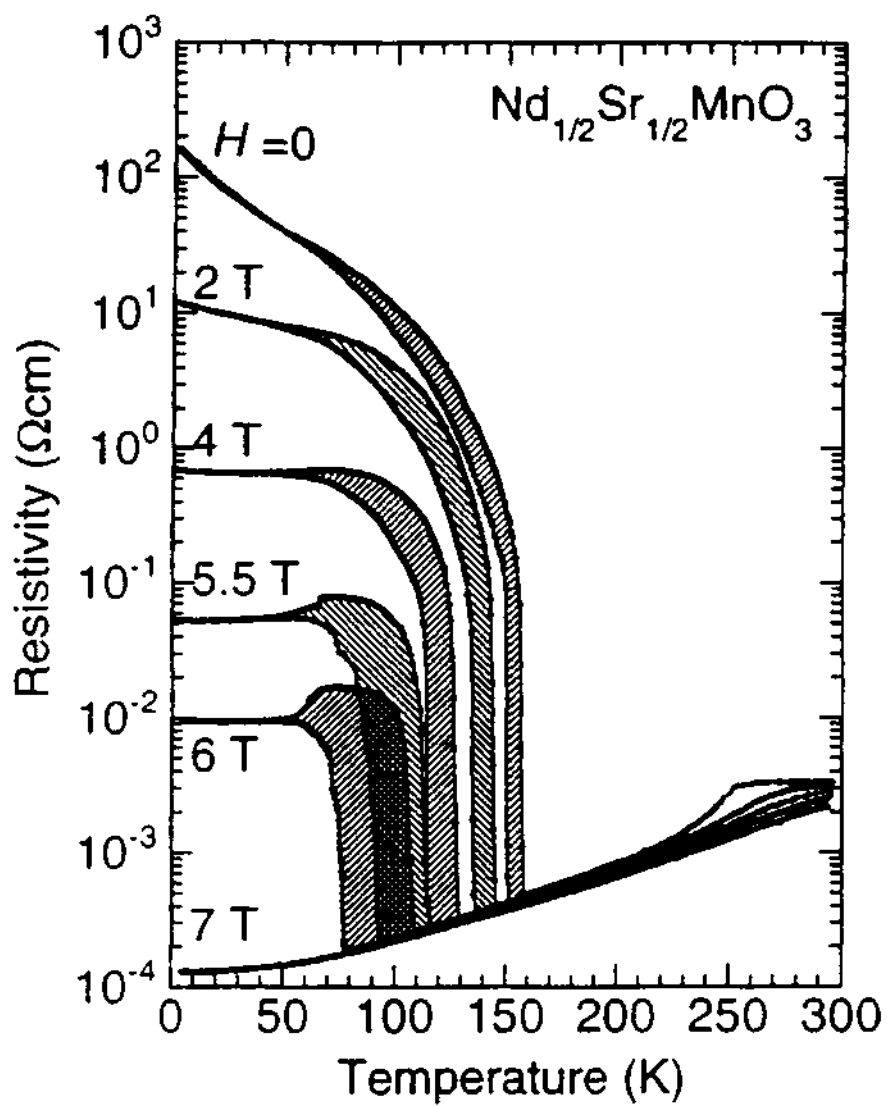


Fig. 1. 19. Variation in the resistivity data of $\text{Nd}_{0.5}\text{Sr}_{0.5}\text{MnO}_3$ under different magnetic fields showing hysteresis behavior [47].

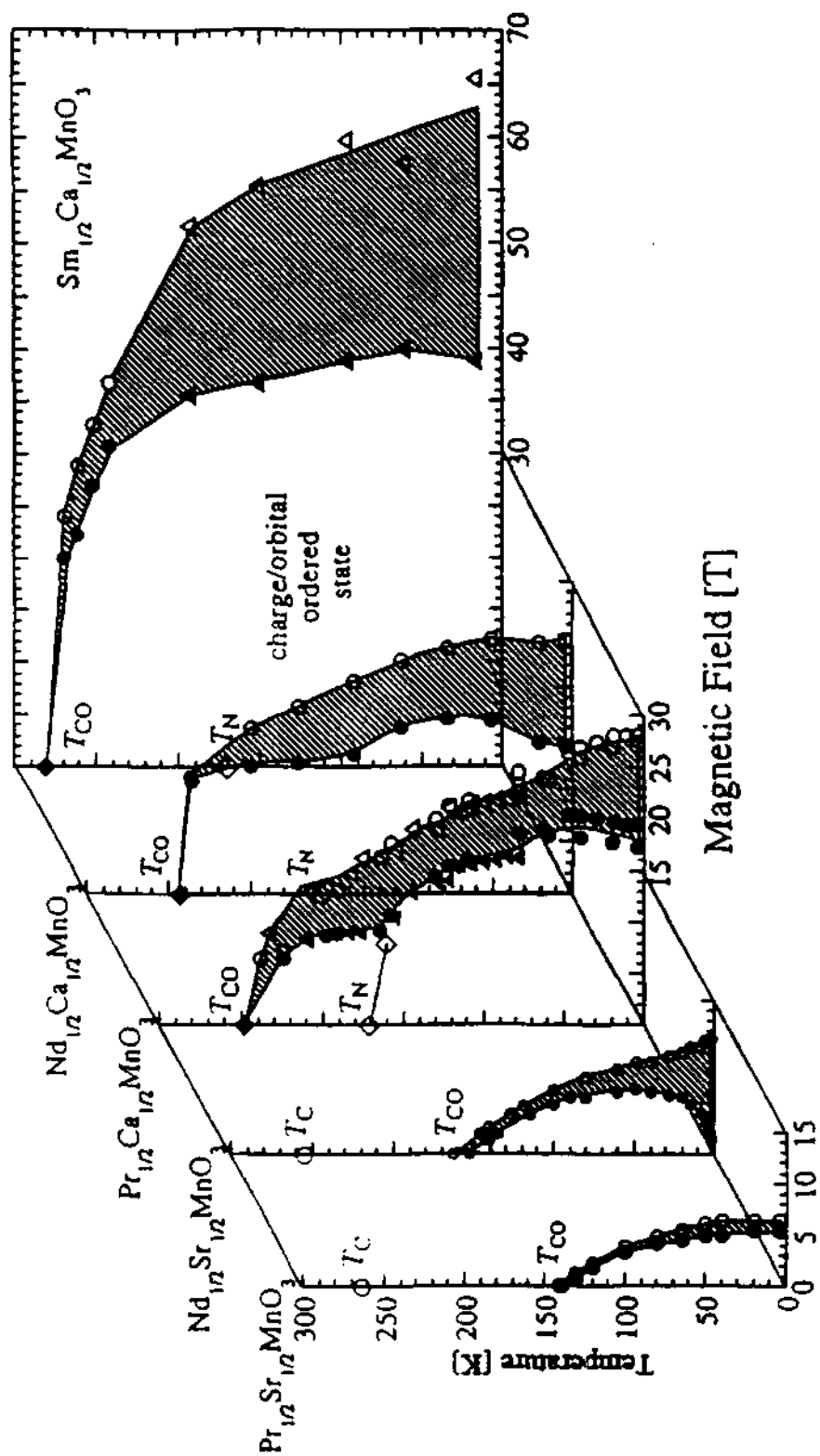


Fig. 1. 20. H-T curves for $\text{Ln}_{0.5}\text{Ca}_{0.5}\text{MnO}_3$ systems showing hysteresis in all of the systems [51].

other rare earth families and also in Fe_3O_4 (~ 0.14 eV) [53] and $\text{La}_{2-x}\text{Sr}_x\text{NiO}_4$ (~ 0.24 eV) [54]. With the aid of reflectivity measurements, the collapse of the charge ordered state is also clearly seen as shown in Fig. 1. 22a for $T=30$ K. Till a magnetic field of 6T, the material is still seen to be insulating as observed with the low reflectance value. Gradually increasing the magnetic field to 7T and the reflectivity increases and somewhere in between, shoots to metallic values-an indication on the onset of I-M transition. An important note is with respect to the magnitude of the charge ordered gap. By scanning tunneling spectroscopy measurements (STS) for $\text{Nd}_{0.5}\text{Sr}_{0.5}\text{MnO}_3$ [54] the CO gap has been observed to be 0.25 eV (shown in Fig. 1. 23), which compares reasonably well with optical conductivity measurements. However, from photoemission experiments, the measured gap has been estimated to be 0.1 eV [55] which is somewhat lower.

One of the factors that the charge ordering process is extremely sensitive is the effective size of the A-site cation. This plays a vital role in determining the properties of the material and affects the I-M transition (T_M) and the ferromagnetic temperature, (T_C), as well. For example, increasing the average radius of the cation $\langle r_A \rangle$ (defined by $\sum x_i r_i$ where x_i and r_i are the mole fraction and radii of the particular cationic species), increases the T_C value, whereas for T_{CO} it is seen to decrease. These effects can be understood in the larger framework of the DE mechanism, where change of the bond angle due to variation of the central A-site cation leads to tilt of the $\text{MnO}_{6/2}$ octahedra which

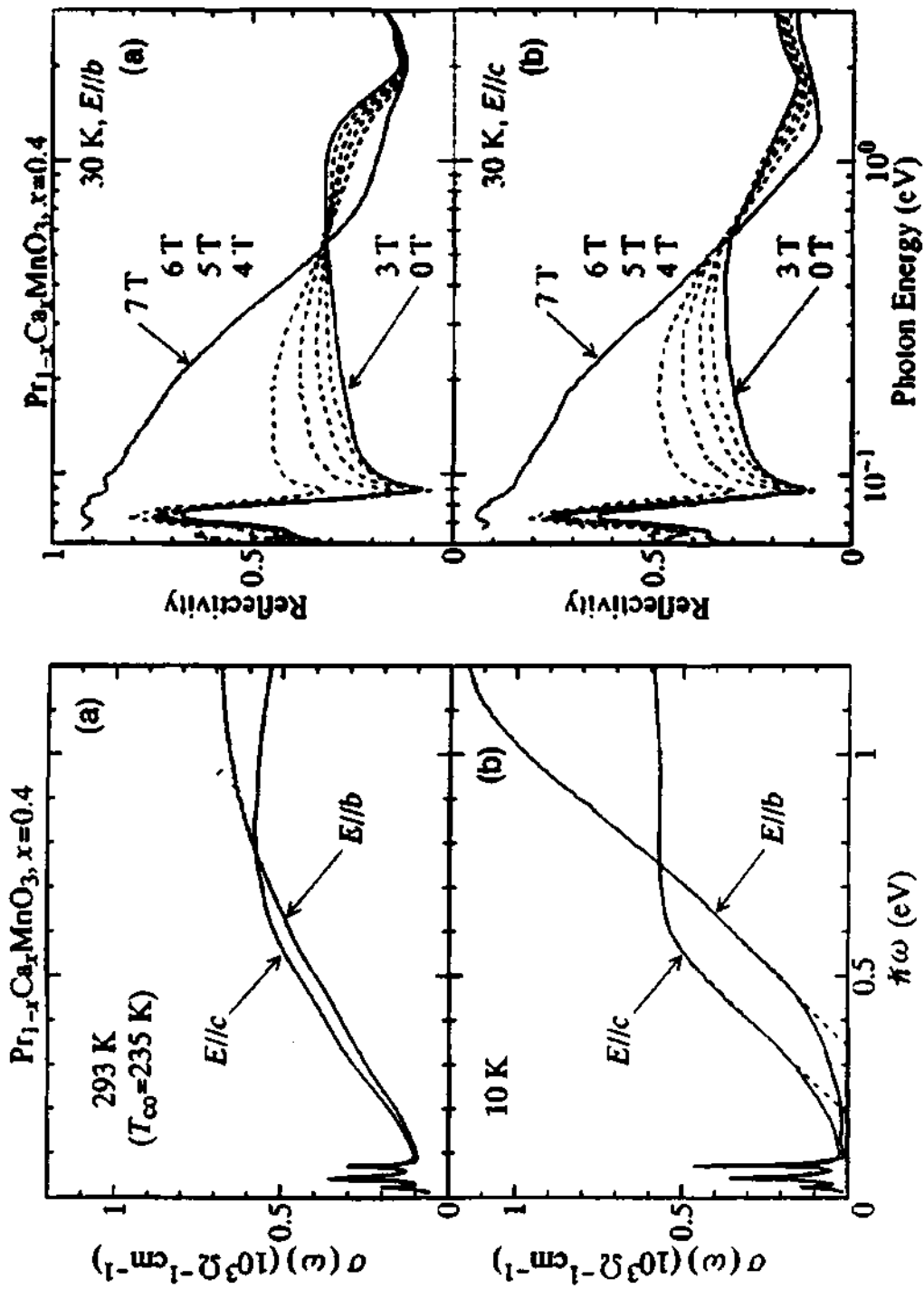


Fig 1.21 & 1.22. The optical and reflectivity data of single crystal of $\text{Pr}_{0.6}\text{Ca}_{0.4}\text{MnO}_3$. The conductivity data shows the opening of the charge ordering gap whereas the reflectivity data shows the process of the I-M transition as a function of applied magnetic field [52].

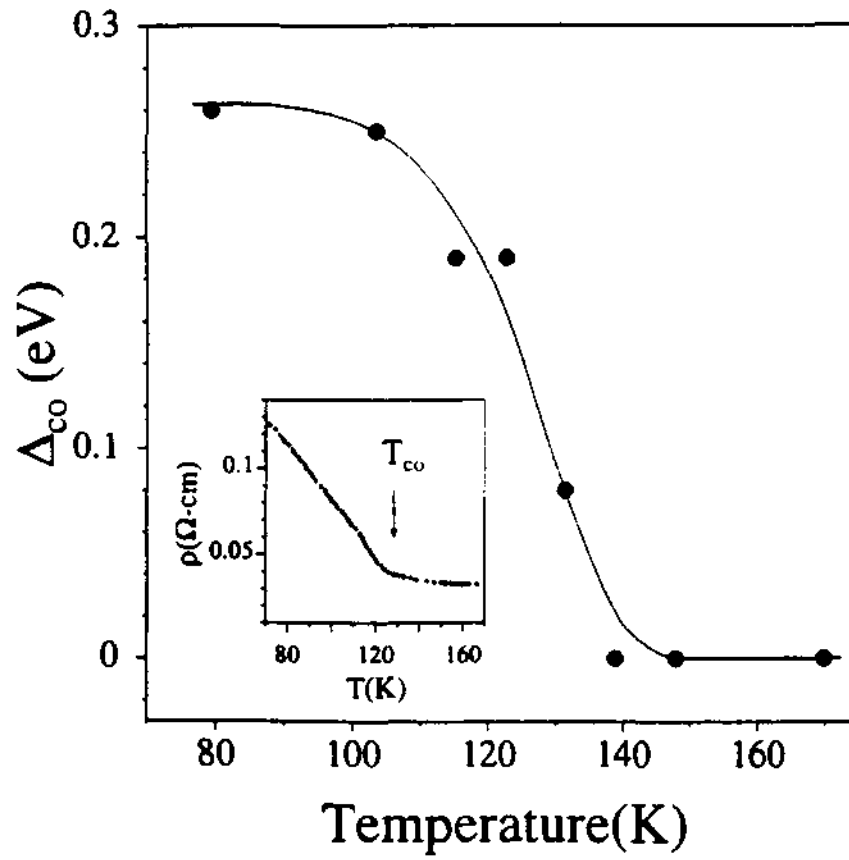


Fig. 1. 23. Charge ordering gap in $\text{Nd}_{0.5}\text{Sr}_{0.5}\text{MnO}_3$ as measured as a function of temperature by tunneling experiments [54].

therein leads to the changes in the one-electron e_g bandwidth. Thus, there is a competition between itinerancy and charge localization. However there are numerous exceptions. In particular it seems that the distribution of the cations in the A-site, the size mismatch and the deviation from the ideal perovskite structure all play an important role in deciding the properties of the material. All these aspects have been dealt with below.

In order to broadly summarize the variation of properties with respect to $\langle r_A \rangle$, Rao *et al* have classified the different compositions into four major classes [56] as shown in Fig. 1. 24. In Table 1, the ionic radii of some of the commonly employed rare earths are also listed. Phase diagrams have also been constructed for families such as $\text{Ln}_{0.5}\text{Ca}_{0.5}\text{MnO}_3$ and $\text{Ln}_{0.5}\text{Sr}_{0.5}\text{MnO}_3$ [48] to study the effect of average radii as are shown in Fig. 1. 25. These help in observing trends and patterns in their behavior. In the different compositions that make up the phase diagram, the radii is varied by changing the rare earth ion only. In terms of the crystal structure adopted, in the case of $\text{Ln}_{0.5}\text{Ca}_{0.5}\text{MnO}_3$ families, the compositions are seen to prefer the orthorhombic $Pnma$ space group, whereas in $\text{Ln}_{0.5}\text{Sr}_{0.5}\text{MnO}_3$ families there is a progression from $Pnma$ to $I4/mcm$ through $Imma$. This structural change is also reflected in the electronic properties as seen in Fig. 1. 10. The properties of $\text{Ln}_{0.5}\text{Sr}_{0.5}\text{MnO}_3$ are also consequently seen to vary more drastically than in $\text{Ln}_{0.5}\text{Ca}_{0.5}\text{MnO}_3$ family.

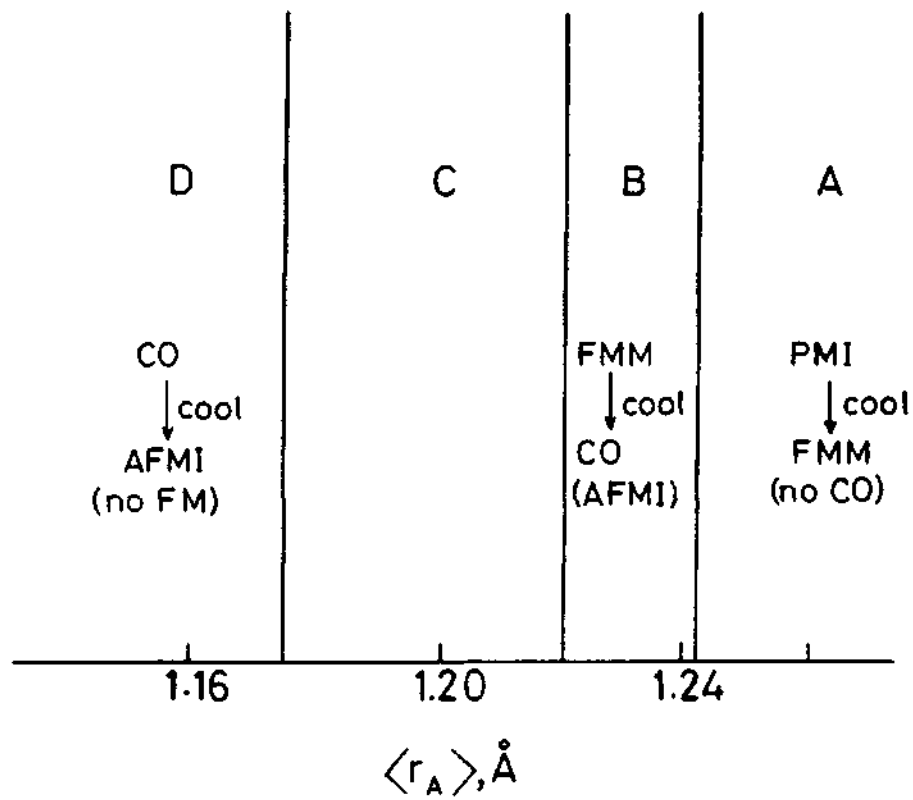


Fig. 1. 24. Rare earth manganates classified into 4 sections as a function of average $\langle r_A \rangle$ [56].

Table 1. 1 Radii of a few rare earths and alkaline earths.

Element	Radii (Å)
La	1.216
Pr	1.179
Nd	1.163
Gd	1.107
Y	1.073
Sr	1.31
Ca	1.18

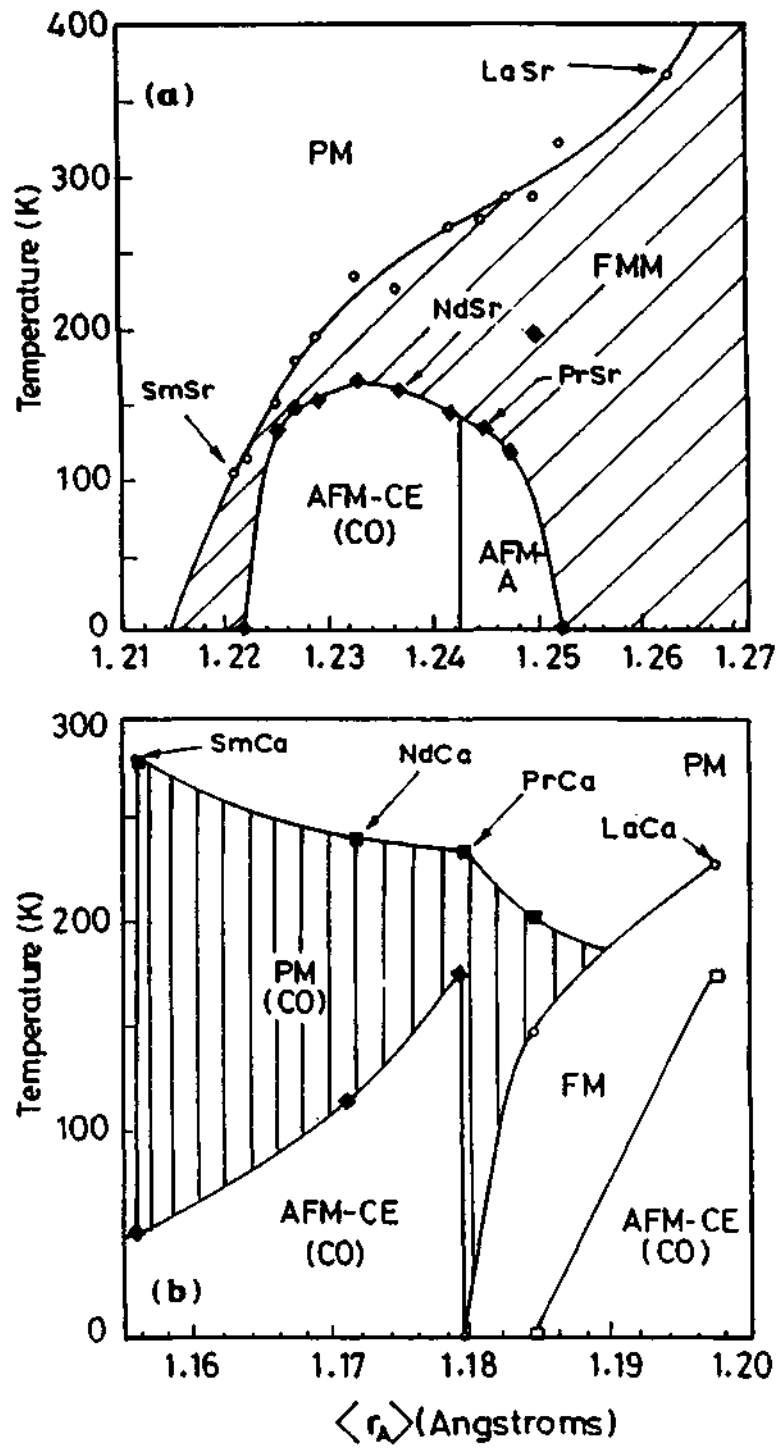


Fig. 1. 25. Phase diagram for $\text{Ln}_{0.5}\text{Ca}_{0.5}\text{MnO}_3$ and $\text{Ln}_{0.5}\text{Ca}_{0.5}\text{MnO}_3$ as a function of average radii $\langle r_A \rangle$ [54].

The effect of $\langle r_A \rangle$ on the T_C and T_{CO} for the general composition $Ln_{0.5}A_{0.5}MnO_3$ [57] is shown in Fig. 1. 26. As mentioned earlier, the DE mechanism does not account for all the observed properties. On plotting the one-electron bandwidth W as a function of $\langle r_A \rangle$ [57] as shown in Fig. 1. 27, it is seen readily that the variation is too small. For example for $\Delta(\langle r_A \rangle) \cong 1.26-1.24 \text{ \AA}$ the variation in T_C is given by $\Delta T_C = 100 \text{ K}$. If one employs the equation for W based on the DE mechanism, then,

$$W \propto \frac{\cos(\omega)}{(d_{Mn-O})^{3.5}}$$

where $\omega = \frac{1}{2} [\pi - \langle Mn-O-Mn \rangle]$ and this does not account for the steep change [58]. In fact W scales as $[1 - \cos(\omega/2)]$ whereas for T_C it has been found to scale as $[(1 - \cos(\omega/2))^2]$ [57]. In order to explain this it has been suggested covalent overlap between the A-site and the anion must be taken into account [1].

The effect of magnetic field on the melting of the charge ordered state has also been found to be dependent on the effective radii $\langle r_A \rangle$. For example, with $\langle r_A \rangle = 1.13 \text{ \AA}$ as in $Y_{0.5}Ca_{0.5}MnO_3$, the charge ordered state is highly stabilized and even in high magnetic fields ($> 25T$), the CO state does not melt, whereas in $Nd_{0.5}Sr_{0.5}MnO_3$ with a $\langle r_A \rangle = 1.24 \text{ \AA}$ ($T_{CO} = T_N = 135 \text{ K}$), the CO can be melted on applying a smaller field (6T). This variation allows the compositions to be drafted into three categories [1,2]: (a) compositions that are ferromagnetic and become

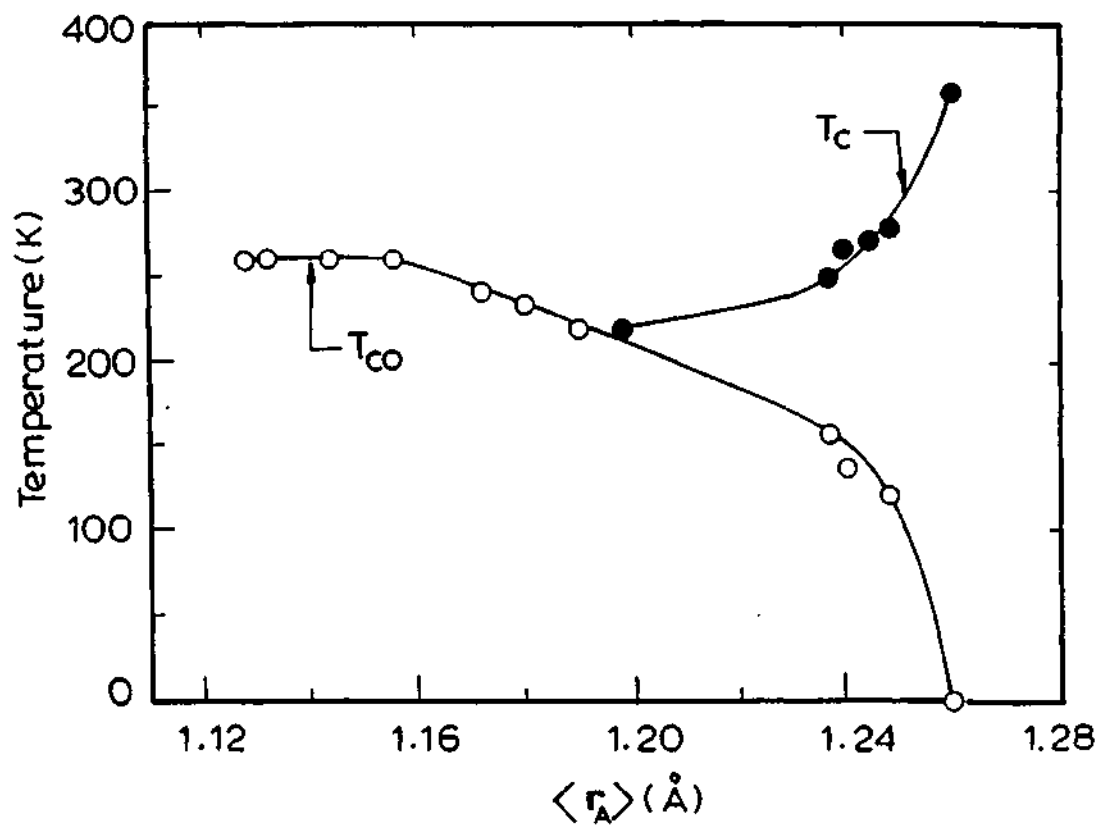


Fig. 1. 26. The variation of curie temperature, T_C and the charge ordering temperature T_{CO} as a function of $\langle r_A \rangle$ [57].

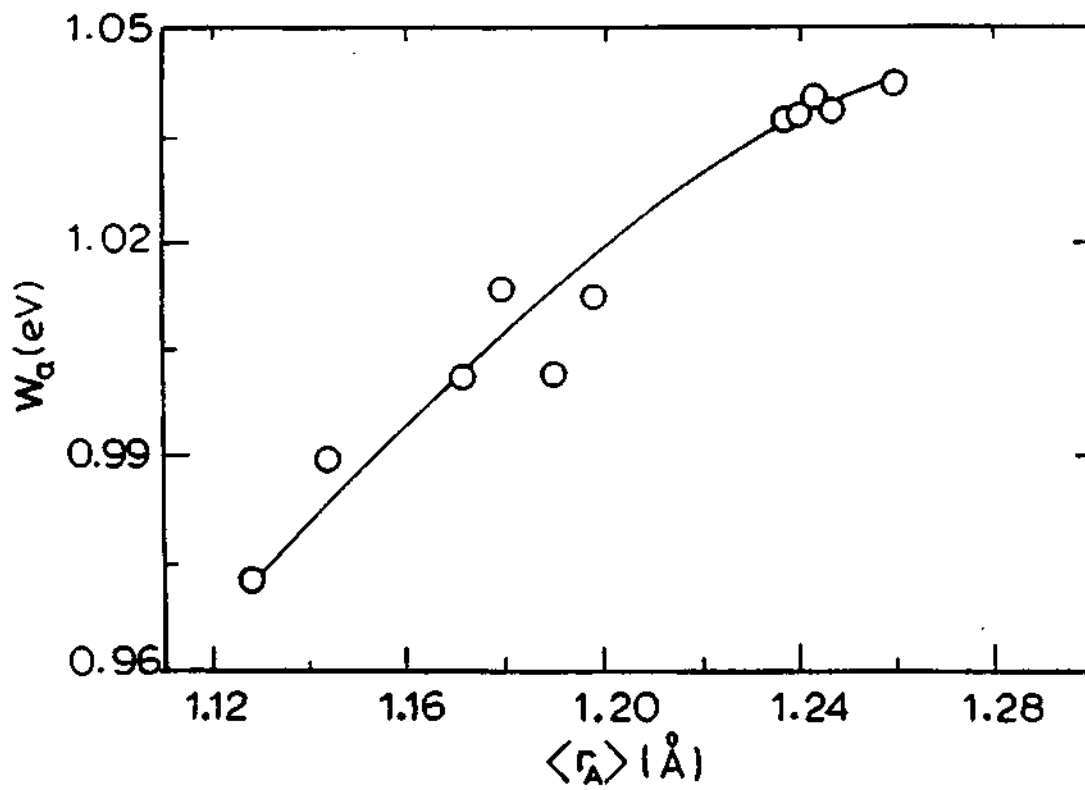


Fig. 1. 27. The variation of the one electron band width, W , as a function of average radii $\langle r_A \rangle$ [57].

charge ordered at low temperatures (as in $\text{Nd}_{0.5}\text{Sr}_{0.5}\text{MnO}_3$ where $T_{\text{CO}} = T_{\text{N}}$). Here small magnetic fields are enough to melt the CO state and transform them into the FMM state, (b) compositions that are charge ordered in the paramagnetic state ($T_{\text{N}} < T_{\text{CO}}$). These require moderate magnetic fields to transform into FMM state as in $\text{Pr}_{0.7}\text{Ca}_{0.3}\text{MnO}_3$ (shown in Fig. 1. 12) and (c) compositions that are charge ordered in paramagnetic state but do not transform into FMM state even under high magnetic field as in $\text{Y}_{0.5}\text{Ca}_{0.5}\text{MnO}_3$.

As mentioned earlier, the effect of variation of radii is not well characterized by the parameter $\langle r_{\text{A}} \rangle$ alone. Not only is the size mismatch not represented but the pseudo-random distribution of the A-site cations in the perovskite structure has no place in the expression for $\langle r_{\text{A}} \rangle$. To account for this, the variance σ^2 (also called the second moment) is employed [59-61]. It is given by;

$$\sigma^2 = \sum_i x_i r_i^2 - \left(\sum_i x_i r_i \right)^2 ; \sum_i x_i = 1$$

The variation of σ^2 with respect to T_{C} and T_{CO} [62] is shown in Fig. 1. 28a for $\langle r_{\text{A}} \rangle = 1.24 \text{ \AA}$ (as in $\text{Nd}_{0.5}\text{Sr}_{0.5}\text{MnO}_3$). It is seen that T_{C} is more sensitive to σ^2 than T_{CO} unlike in the $\langle r_{\text{A}} \rangle$ studies. However the insulator-metal temperature, T_{MI} , shows extreme sensitivity to σ^2 . In Fig. 1. 28b, a typical plot of the variance against T_{MI} for $\langle r_{\text{A}} \rangle = 1.23 \text{ \AA}$ corresponding to the $\text{Ln}_{0.7}\text{Ca}_{0.3}\text{MnO}_3$ series is shown [61]. It is seen to have a linear relationship with negative slope, wherein,

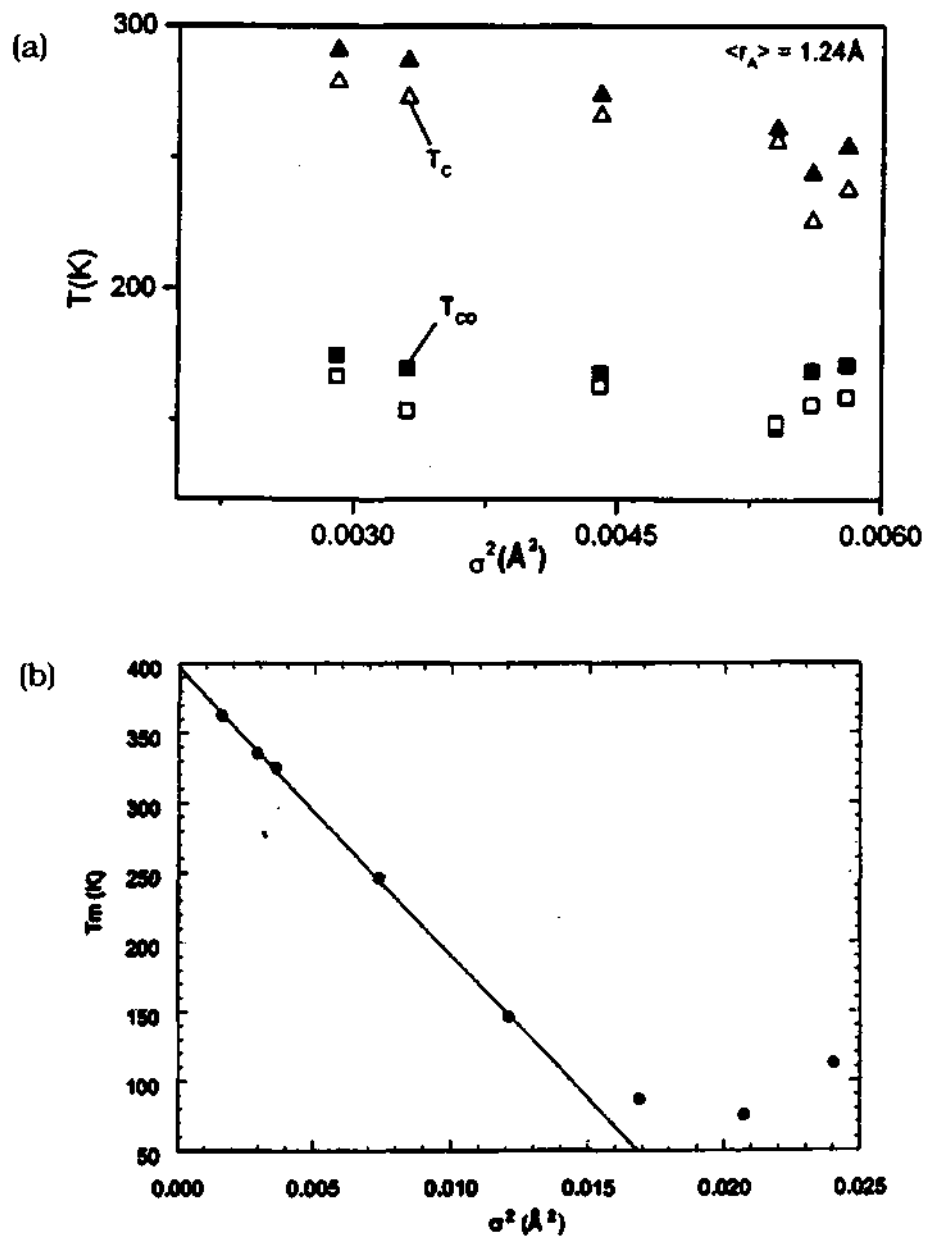


Fig. 1. 28. (a) Variation of T_c and T_{co} against variance σ^2 (open symbol represents data from magnetization and the closed symbols from resistivity measurements); (b) Variation of I-M transition temperature against σ^2 [61,62].

extrapolation to $\sigma^2 = 0$, gives the maximum T_{MI} that the system can possibly exhibit.

An interesting aspect in the variation of $\langle r_A \rangle$ is the region 'C' in Fig. 1. 24 where compositions follow no trend. As an example, consider $\text{La}_{0.5}\text{Ca}_{0.5}\text{MnO}_3$ ($\langle r_A \rangle = 1.20 \text{ \AA}$) and $\text{Nd}_{0.25}\text{La}_{0.25}\text{Ca}_{0.5}\text{MnO}_3$ ($\langle r_A \rangle = 1.19 \text{ \AA}$), which lie between compositions with $\langle r_A \rangle = 1.17 \text{ \AA}$ ($\text{Pr}_{0.6}\text{Ca}_{0.4}\text{MnO}_3$) and $\langle r_A \rangle = 1.24 \text{ \AA}$ ($\text{Nd}_{0.5}\text{Sr}_{0.5}\text{MnO}_3$). In the case of $\text{La}_{0.5}\text{Ca}_{0.5}\text{MnO}_3$ [63] the composition has $T_C = 225 \text{ K}$ followed by T_{CO} and T_N at 135 K simultaneously. Thus like in $\text{Nd}_{0.5}\text{Sr}_{0.5}\text{MnO}_3$ spin-ordering drives charge ordering. However, in the case of $\text{Nd}_{0.25}\text{La}_{0.25}\text{Ca}_{0.5}\text{MnO}_3$ [64]; it charge orders at $T_{CO} = 220 \text{ K}$ and then a gap opens at the Fermi-level local density of states (LDOS). However, this CO state is not stable and it undergoes a reentrant transition into the ferromagnetic metallic state at 150 K . In between these two states, a large orthorhombic distortion is also seen and there is a two-phase coexistence. Thus there is a series of phase transitions which occurs by changing the average radii by 0.01 \AA . In Fig. 1. 29, the CO gap measured as from scanning tunneling spectroscopic (STS) measurements is shown for $\text{Nd}_{0.25}\text{La}_{0.25}\text{Ca}_{0.5}\text{MnO}_3$ along with that for $\text{Nd}_{0.5}\text{Sr}_{0.5}\text{MnO}_3$ for comparison [64].

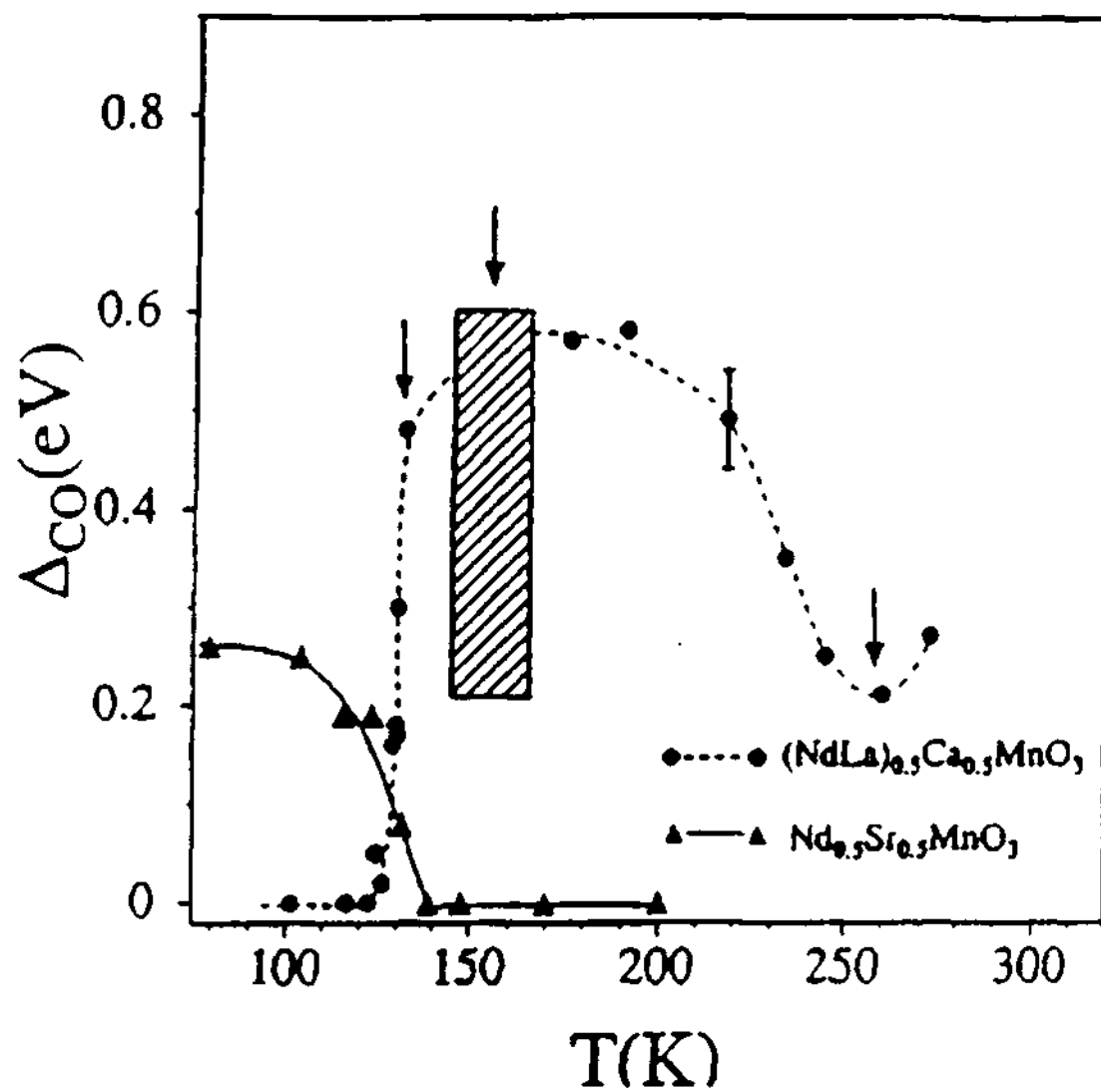


Fig. 1. 29. Variation of the charge ordering temperature as measured from tunneling measurements [64].

Effects of impurity doping

Partial substitution of the B-site cation i.e., of the Mn-site with impurity dopants (M) has been found to produce drastic changes in the observed properties of rare-earth manganates. A few examples of the impurity dopants include Cr^{3+} , Co^{3+} [65-68], Ni^{2+} , Fe^{3+} , Mg^{2+} , Al^{3+} , Sn^{4+} [66-70], Cu^{2+} [71] and Ru^{4+} [72]. Often the substitution is as low as 1-3% although some studies have employed as much as 10%. The doping of the Mn-site is expected to be far more effective in controlling the properties of the material rather than $\langle r_A \rangle$ simply because it focuses directly on the Mn—O—Mn angle. As an example, consider the progressive substitution of Ru^{4+} in $\text{Nd}_{0.5}\text{Sr}_{0.5}\text{MnO}_3$. In Fig. 1. 30, in both the magnetization and the resistivity measurements, it is seen that just 1% doping melts the charge ordered state and induces a I-M transition. This has been observed in other systems such as $\text{Pr}_{0.5}\text{Ca}_{0.5}\text{MnO}_3$ as well, where both Cr^{3+} and Ru^{4+} have been employed. In one of the broad ranging studies, the general family $\text{Ln}_{0.5}\text{Ca}_{0.5}\text{Mn}_{1-x}\text{M}_x\text{O}_3$ has been investigated with many rare earths (La, Pr, Nd, Sm, Eu, Gd and Tb) and dopants (Cr, Co, Ni, Fe, Mg, Al and Sn) [66]. It has been observed that charge ordering is destroyed in all cases and an I-M transition is observed, barring the case of Gd where the application of a magnetic field is required. Chromium and ruthenium substitution has also been found to be the most effective in terms of the maximum magnetic moment observed. The study marks that for I-M transition to be observed in Cr-doped samples, the lowest

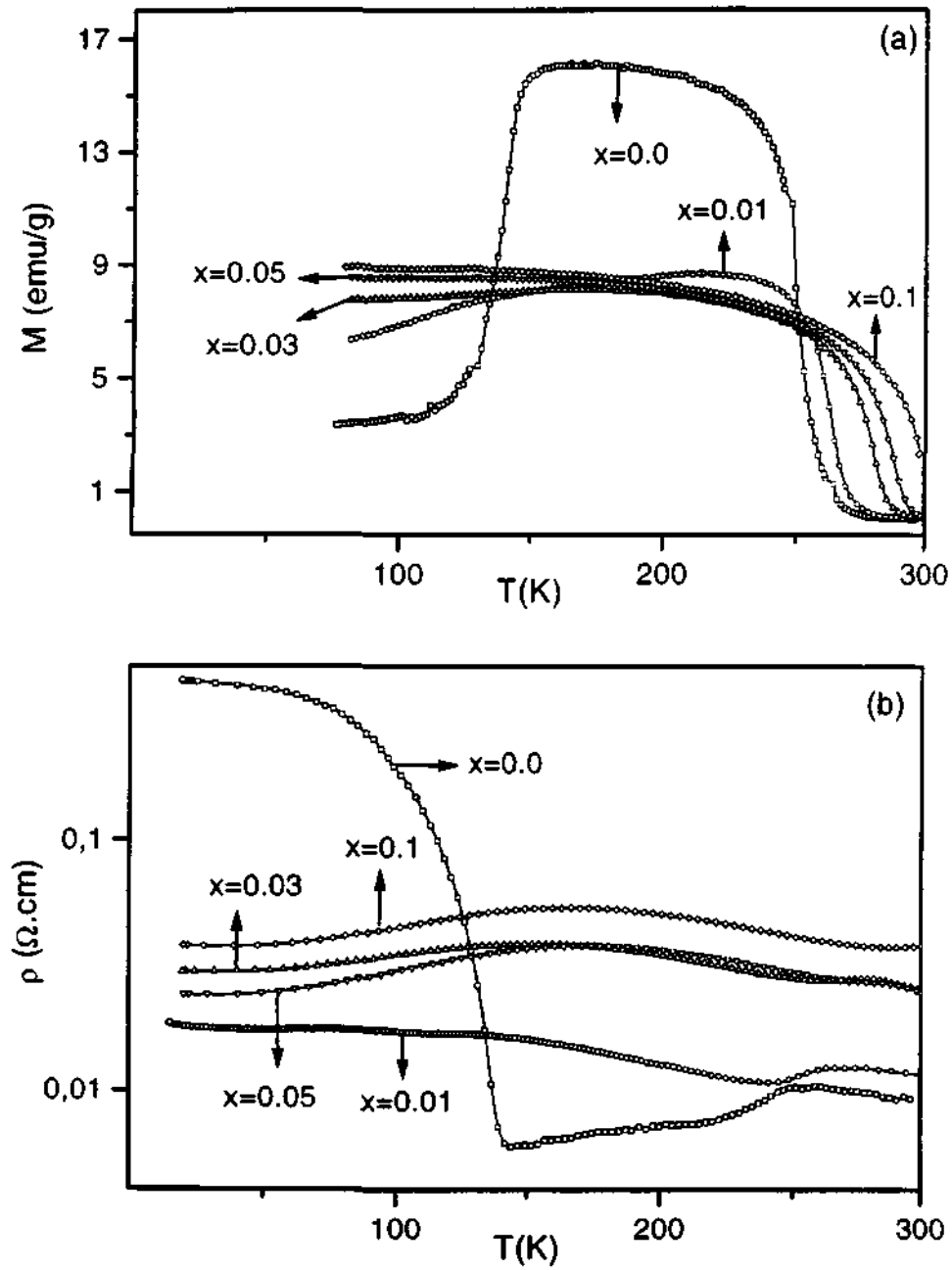


Fig. 1. 30. The effect of the concentration of the impurity dopant ruthenium (Ru⁴⁺) on the composition Nd_{0.5}Sr_{0.5}MnO₃ as seen by magnetization and resistivity [72].

value that $\langle r_A \rangle$ can have is 1.14 Å. It should be noted that in undoped samples for $\langle r_A \rangle = 1.14$ Å as seen from Fig. 1. 25, the composition exhibits only charge ordering and no ferromagnetism.

One of the striking features found in rare-earth manganates is the so-called electron-hole asymmetry. In the electron doped regime ($x > 0.5$ in $\text{Ln}_{1-x}\text{A}_x\text{MnO}_3$), the CO state is dominant as observed from the phase diagrams in Fig. 1. 10. However unlike hole-doped regions ($x \leq 0.5$), it not possible to induce the FMM state under any conditions either by varying $\langle r_A \rangle$, by applying magnetic fields or both simultaneously. In light of this observation several attempts have been made to induce the FMM state and observe appreciable MR in electron-doped manganates. Examples include the doping of Nb^{5+} , Ta^{5+} , W^{6+} and Mo^{6+} in CaMnO_3 [44]. However even on the application of 7T field on the impurity doped compositions, the ratio of the resistivities ρ_0/ρ_{7T} is a mere 2-5 times, even at the low temperature of 25 K. Thus the effect is too small to be comparable to the CMR effect mentioned earlier in the hole doped compositions. In the case of $\text{Pr}_{0.4}\text{Ca}_{0.6}\text{MnO}_3$ addition of 10% Cr results in a ratio drop of 10^6 at 30 K. Lower doping content ($\sim 3\%$) yields GMR ratio of less than 10. Out of the many dopant employed in the literature, Ru^{4+} ($t_{2g}^4 e_g^0$) has been found to be most effective. Doping of 4% Ru^{4+} in $\text{Pr}_{0.4}\text{Ca}_{0.6}\text{MnO}_3$ has been reported to induce both ferromagnetism and metallicity [73]. The value CMR ratio is around $\sim 10^5$ at 50 K. However, it should be cautioned that doping in excess of 3% there is the risk of

clustering of the Ru ions. In addition phase separation problems can also arise [73]. Other compositions such as $\text{Ca}_{0.85}\text{Sm}_{0.15}\text{MnO}_3$ have also been reported to exhibit the CMR effect on doping. However, this is not comparable to similar CMR effect observed in corresponding hole compounds.

Isotopic substitution and phase separation

Isotopic substitutions, involving the replacement of ^{16}O by ^{18}O (around 90%) have also been investigated to examine the role of oxygen in charge ordering and related process. As an example, consider the case of $\text{La}_{0.125}\text{Pr}_{0.525}\text{Ca}_{0.3}\text{MnO}_3$ where the isotopic substitution is seen to destroy the natural I-M transition [74] and renders the material insulating till 4 K. In $\text{Pr}_{0.67}\text{Ca}_{0.33}\text{MnO}_3$, substitution causes the I-M transition to take place under much higher fields [75]. Overall, it is seen that the CO state seems to be favored under isotopic substitution. The charge ordering temperature T_{CO} has been found to increase with ^{18}O substitution in $\text{La}_{0.5}\text{Ca}_{0.5}\text{MnO}_3$ and $\text{Nd}_{0.5}\text{Sr}_{0.5}\text{MnO}_3$ by around 10 K [76]. By magnetization measurements, it is seen that T_{CO} scales as a function of the applied field, wherein at an applied field of 5.4T, the drop is ~40 K [76]. In thin films of $\text{La}_{0.75}\text{Ca}_{0.25}\text{MnO}_3$ (LCMO) and $\text{Nd}_{0.7}\text{Ca}_{0.3}\text{MnO}_3$ (NDMO) on 95% ^{18}O substitution, the T_{c} falls by 14 K for LCMO and ~18 K for NDMO [77].

Phase separation has recently has also been recently investigated in rare earth manganates. Electron microscopy has been employed to observe the phase

separated regions. Thus, in $\text{La}_{1-x-y}\text{Pr}_y\text{Ca}_x\text{MnO}_3$ ($x = 0.375$), submicrometer scale phase separation of CO regions and FMM domains have been observed [78]. In Fig. 1. 31 the schematic representation of phase separated regions of FM domain and CO regions are shown at the composition $x = 0.5$. In $\text{La}_{0.5}\text{Ca}_{0.5}\text{MnO}_3$ and $\text{Nd}_{0.25}\text{La}_{0.25}\text{Ca}_{0.5}\text{MnO}_3$ similar segregation have been reported [63,64]. It is found that the compositions at the end of phase diagrams tend to phase separate exhibit and spin glass like behavior. Examples include compositions such as $\text{Ca}_{0.9}\text{Sm}_{0.1}\text{MnO}_3$ and $\text{Sr}_{0.9}\text{Pr}_{0.1}\text{MnO}_3$ [79]. In the former case, ferromagnetic clusters are seen to grow from microscopic to domain dimensions depending on the temperature, whereas the space group remains constant ($Pnma$). In the latter case, the crystal symmetry has been found to change from $Pm3m$ at room temperature to $I4/mcm$ at 200 K. Also the antiferromagnetism in this composition is seen to arise from both G- and C-type, which coexist with little distortion of the lattice.

The case of phase separation is particularly interesting in the composition $\text{Nd}_{0.5}\text{Sr}_{0.5}\text{MnO}_3$. It exhibits a high temperature FMM phase (> 225 K) with $Imma$ symmetry, an intermediate-temperature phase of A-type ferromagnetic with $Imma$ symmetry that begins at 220 K and last till 150 K, upon which the material goes into the CE-type antiferromagnetic charge ordered state with $P2_1/m$ symmetry [80]. The unique aspect is the presence of the FMM state at 150 K. The fractional compositions of each of these phases are shown in Fig. 1. 32 as a

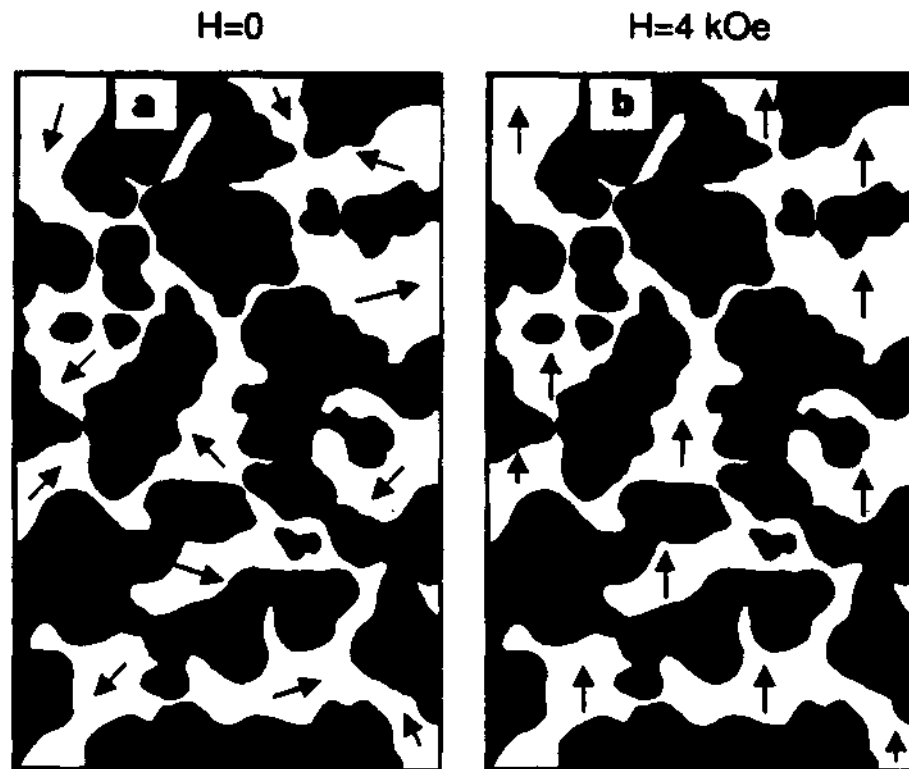


Fig. 1. 31. Schematic representation of phase separation in $\text{La}_{1-x-y}\text{Pr}_x\text{Ca}_y\text{MnO}_3$.

The dark regions represent charge-ordered insulating areas whereas the bright areas represent ferromagnetic metallic areas. In (a) the ferromagnetic domains ($0.5 \mu\text{m}$) are random oriented whereas in (b) they are aligned in a magnetic field of 4 kOe.

function of temperature. These phases have domain dimensions, as they are seen in x-ray and neutron diffraction studies. In Fig. 1. 33, the phase compositions under zero and 6T field are also shown. The phase corresponding to the charge ordered state is completely melted, but the antiferromagnetic regions corresponding to A-type continues to exist in the ferromagnetic background.

Recent studies have focussed on the combined study of oxygen isotope substitution leading to phase separation. Examples include compositions such as $(\text{La}_{0.25}\text{Pr}_{0.75})_{0.7}\text{Ca}_{0.3}\text{MnO}_3$ where ^{16}O sample is metallic below 100 K. Upon 75% substitution of ^{18}O , it becomes an antiferromagnetic insulator below 150 K. Careful investigation have shown that AFM starts in ^{16}O sample as well but is not favoured [74]. In fact the amount of isotope substitution seems to be critical to the phase separation process [81].

The process of impurity dopant melting the charge ordered state has also been investigated for possible phase separation. In $\text{Nd}_{0.5}\text{Ca}_{0.5}\text{MnO}_3$ the T_{CO} occurs at 250 K and is accompanied by orbital ordering. At 170 K the material exhibits Néel temperature. With 10% Cr doping the material shows I-M transition. At lower doping concentrations such as 2%, an applied magnetic field of 7T is required to do the same. It is seen that ferromagnetic clusters develop on the application of the magnetic field in the antiferromagnetic background [82].

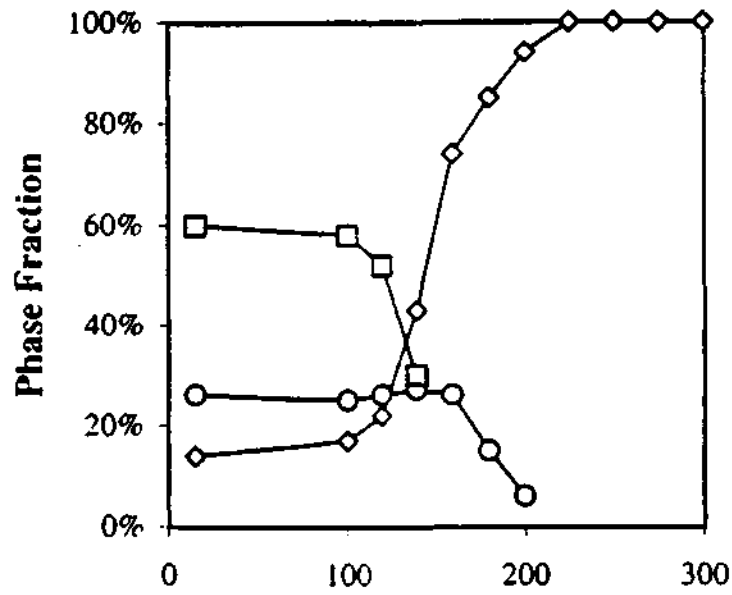


Fig. 1. 32. The variation in the percentage fractions of the phase separated components as a function of temperature in $\text{Nd}_{0.5}\text{Sr}_{0.5}\text{MnO}_3$ [80]. The FMM phase are represented by diamonds; A-type AFM phase by circles and CE-type CO phase by squares.

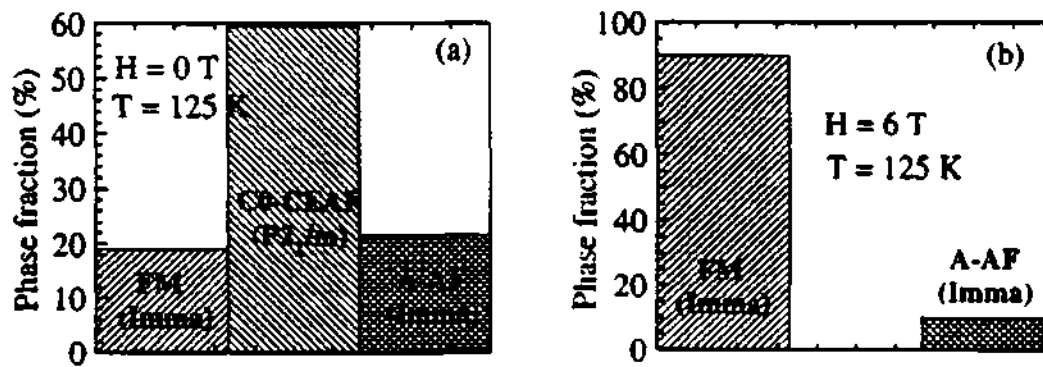


Fig. 1. 33. The different fractions that form due to phase separation in $\text{Nd}_{0.5}\text{Sr}_{0.5}\text{MnO}_3$ in a magnetic field of (a) 0T and (b) 6T [80].

This has also been referred to as a relaxor ferromagnetic akin to the relaxor ferroelectrics where a ferroelectric cluster is embedded in a paraelectric domain.

Thin films and layered manganates

The process of charge ordering confined to two dimensions as in thin films and layered manganates has also been recently investigated. Thin films of charge ordered compositions including $\text{Y}_{0.5}\text{Ca}_{0.5}\text{MnO}_3$ (YCM), $\text{Nd}_{0.5}\text{Ca}_{0.5}\text{MnO}_3$ (NCM), $\text{Gd}_{0.5}\text{Ca}_{0.5}\text{MnO}_3$ (GCM) and $\text{Pr}_{0.7}\text{Ca}_{0.3}\text{MnO}_3$ (PCM) have been seen to undergo I-M transitions upon application of moderate electric currents [83,84]. This is an interesting feature because as mentioned earlier in systems such as $\text{Y}_{0.5}\text{Ca}_{0.5}\text{MnO}_3$ the application of magnetic fields till 25T does not melt the charge ordered state. In Fig. 1. 34 typical plots of electric field effects are shown for NCM and YCM on Si(100) substrate. Heating effects due to high currents are not believed to be the cause as the threshold for this is around 50 mA. Films of these materials are also seen to exhibit memory effects as well as non-ohmic behavior. In Fig. 1. 35 the memory effect is exhibited for NCM films grown on LaAlO_3 (100) substrate. It is seen that in both the cooling and the heating cycle, the resistance values are the same near the charge ordered region.

In the case of films of $\text{Nd}_{0.5}\text{Sr}_{0.5}\text{MnO}_3$, the onset of metallicity is around 300 K itself. The characteristic jump seen at ~ 140 K for T_{CO} in single crystalline material is not so sharp. However, it exhibits memory effects and non-ohmic

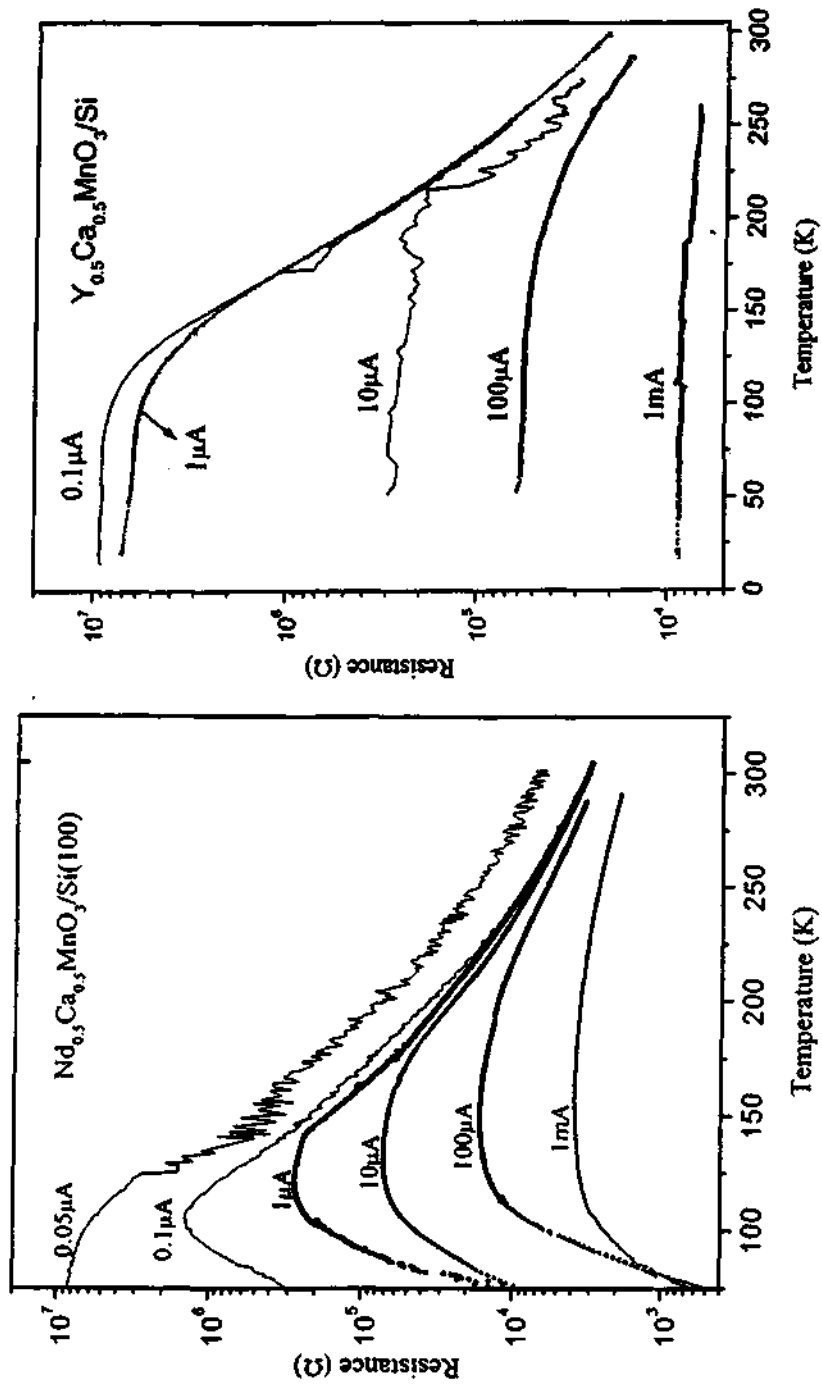


Fig. 1. 34. Electric field effects due to different currents on thin films of $\text{Nd}_{0.5}\text{Ca}_{0.5}\text{MnO}_3$ and $\text{Y}_{0.5}\text{Ca}_{0.5}\text{MnO}_3$ grown on Si (100) [83,84].

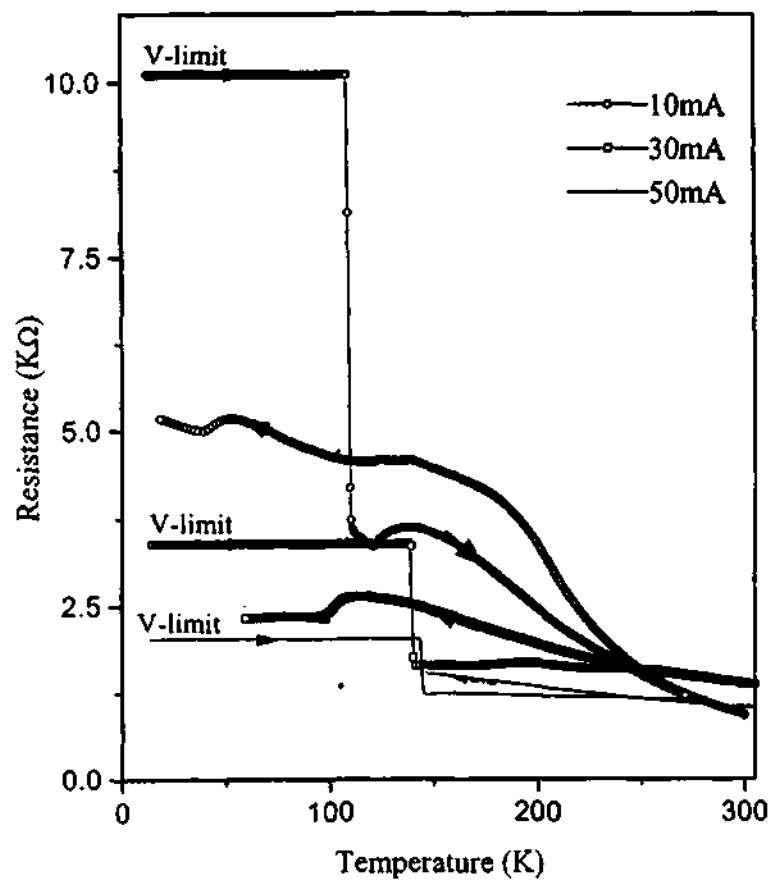


Fig. 1. 35. Heating and cooling cycles on thin film of $\text{Nd}_{0.5}\text{Ca}_{0.5}\text{MnO}_3$ deposited on Si (100) displaying memory effect [84].

behavior. Another interesting feature of thin films is the effect on charge ordering by impurity dopants. In GCM, 3% Cr melts the CO state inducing an I-M transition whereas a similar feature is not seen in the bulk.

Structurally, thin films of material having different structure than in the bulk have also been grown as in the case of $\text{Pr}_{0.5}\text{Ca}_{0.5}\text{MnO}_3$ on LaAlO_3 (101) wherein monoclinic structure has been observed [85]. These films have lot of strain built in and are seen to exhibit anomalous features [86].

Layered manganates have been the focus of attention since they exhibit unique behavior due to quasi-two-dimensional electronic structure [87]. They are represented by $(\text{Ln},\text{A})_{n+1}\text{Mn}_n\text{O}_{3n+1}$ where 'n' represents the dimensionality (shown in Fig. 1. 36). The basic structure of the homologous series is the alternate stacking of rock-salt-type block layers $(\text{Ln},\text{A})_2\text{O}_2$ and $n\text{-MnO}_2$ sheets along the z-axis. In the composition $\text{La}_{2-2x}\text{Sr}_{1+2x}\text{Mn}_2\text{O}_7$ CMR effect has been observed for $x \geq 0.17$ and is shown in Fig. 1. 37 [88-91]. With $n = 1$ as in the $\text{Ln}_{1-x}\text{Sr}_{1+x}\text{MnO}_4$ (K_2NiF_4) structure, metallicity is observed for $x > 0.7$. Charge ordering is observed in $\text{La}_{0.5}\text{Sr}_{1.5}\text{MnO}_4$ at 220 K along with orbital ordering. In the $n = 2$ series, charge ordering has been observed in $\text{LaSr}_2\text{Mn}_2\text{O}_7$ [91]. The interplay of charge, orbital and spin ordering in these compounds leads to its unusual properties and hence its investigation.

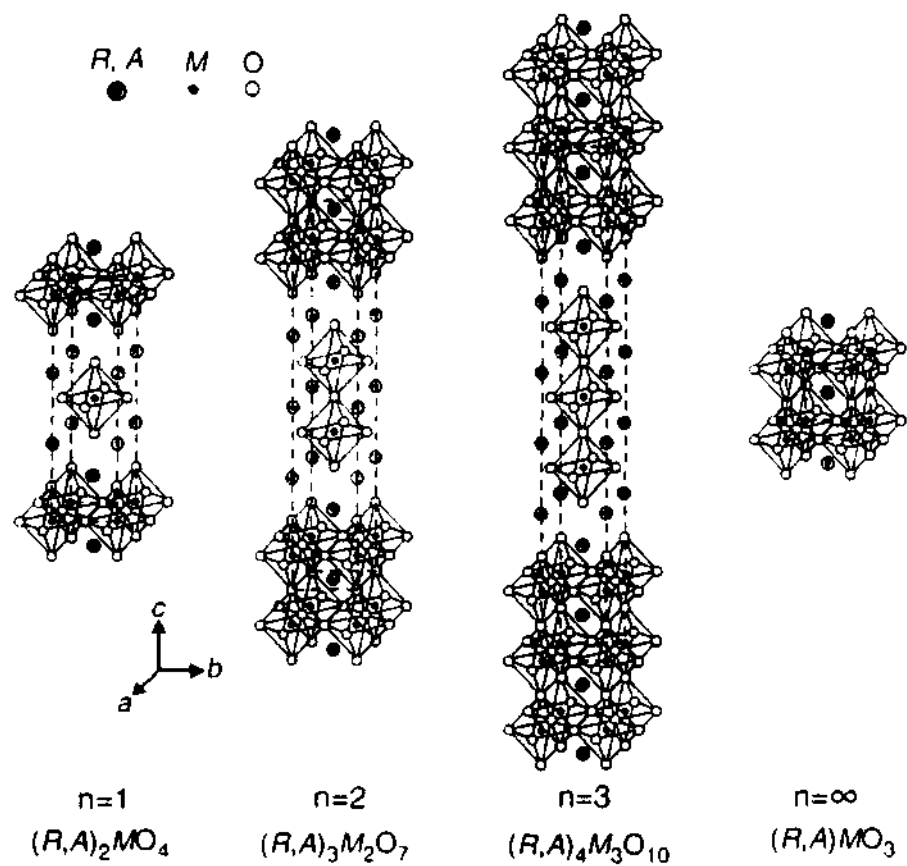


Fig. 1. 36. Layered manganates represented by the general formula $(Ln,A)_{n+1}Mn_nO_{3n+1}$ showing the quasi-two dimensional nature of these materials [87].

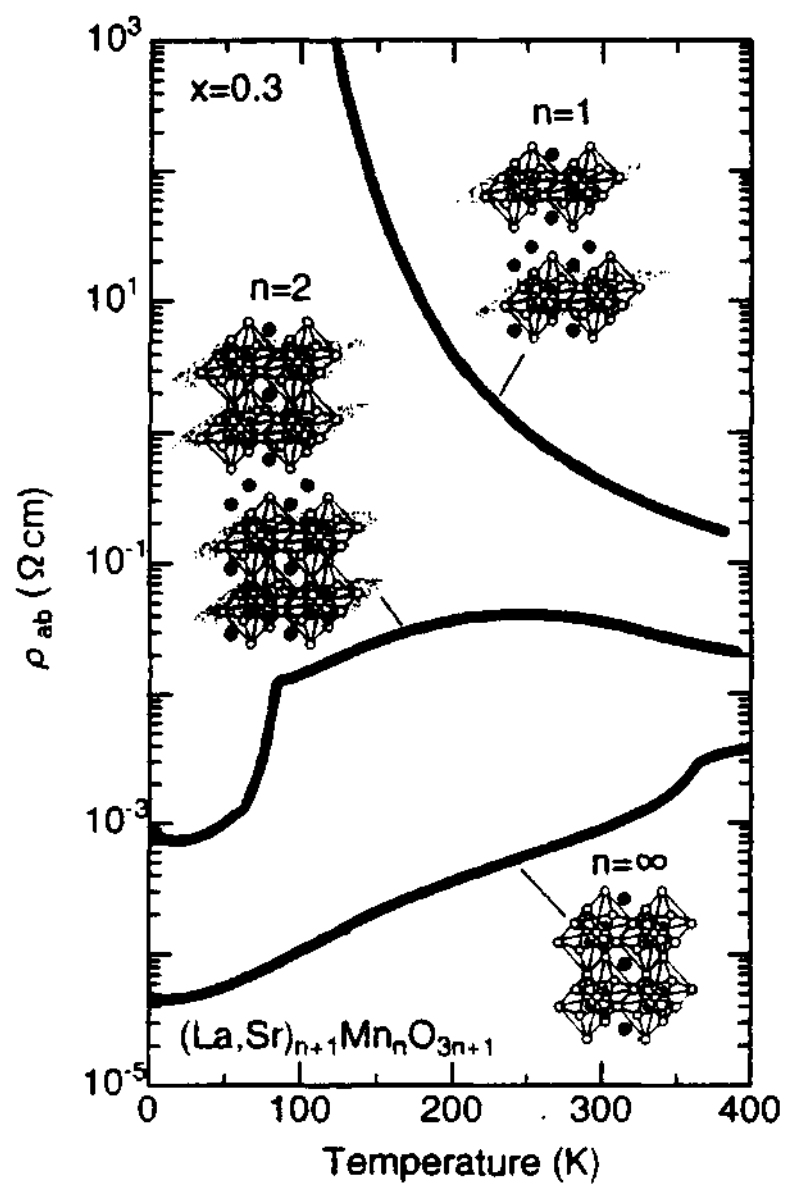


Fig. 1. 37. The effect of dimensionality in the Ruddlesden-Popper series as measured by resistivity [87].

1.2 SCOPE OF THE PRESENT INVESTIGATIONS

1.2.1 A Comparative Study of the Hole- and the Electron-Doped Rare Earth Manganates

Rare earth manganates of the formula, $\text{Ln}_{1-x}\text{A}_x\text{MnO}_3$ (Ln = rare earth, A = alkaline earth) exhibit extraordinary properties such as colossal magnetoresistance (CMR) and charge ordering [1-2]. The manganates with $x < 0.5$, where the trivalent Ln ions are substituted by divalent A ions, have come to be designated as hole-doped. Accordingly, the manganates with $x > 0.5$ where the Ln ion substitutes a divalent A ion are being referred to as electron-doped [92-94]. The manganates exhibiting CMR, largely, have compositions in the range $0.1 < x < 0.5$, wherein the average radius of the A-site cations, $\langle r_A \rangle$, is fairly large. These manganates become ferromagnetic due to the double-exchange mechanism of electron hopping between Mn^{3+} ($t_{2g}^3 e_g^1$) and Mn^{4+} ($t_{2g}^3 e_g^0$) via the oxygen, and undergo an insulator-metal transition around the ferromagnetic T_C . CMR is generally highest around T_C and the T_C is sensitive to $\langle r_A \rangle$. When $\langle r_A \rangle$ is sufficiently small, the materials do not ordinarily exhibit ferromagnetism, but instead become charge-ordered insulators. Thus, charge ordering and double-exchange are competing interactions in the manganates. As x in $\text{Ln}_{1-x}\text{A}_x\text{MnO}_3$ increases, crossing over from the hole-doped to the electron-doped regime ($x > 0.5$), charge ordering becomes the dominant interaction and ferromagnetism does not appear to occur in any of the compositions. In this regime, CMR occurs over a narrow range of compositions, $0.80 < x < 1.0$, but there is no long-range

ferromagnetism or metallicity associated with the materials [92-94]. The various features of the manganates are nicely borne out by the approximate phase diagrams shown in Figure 1. 10, prepared based on available data. What is noteworthy is the marked absence of symmetry in these phase diagrams. While the presence of electron-hole asymmetry in the manganates is not surprising, considering that the introduction of e_g electrons increases the lattice distortion and their removal would have the opposite effect, the asymmetry has some unusual features.

Electron-hole asymmetry is encountered in cuprate superconductors [95]. In the cuprates, superconductivity occurs in the electron-doped regime, although not as prominently as in the hole-doped regime. The electron-hole asymmetry in the rare earth manganates, involving the total absence of ferromagnetic metallic (FMM) state in the electron-doped regime, is therefore worthy of investigation. We have studied this interesting problem by comparing the structures and properties of the hole- and the electron-doped manganates of similar compositions in the $\text{Pr}_{1-x}\text{Ca}_x\text{MnO}_3$ system ($x = 0.36$ and 0.64). Although there have been several studies on hole-doped compositions of this system [1,2], a careful comparison of hole- and electron-doped materials seemed to be necessary. In particular, we have examined whether ferromagnetism can be induced in the electron-doped material by appropriate cation substitution in the Mn-site or/and application of magnetic fields. In addition, we have investigated

the effect of the radius of the A-site cation as well as the site-disorder as defined by σ^2 (known as the variance) which as mentioned in the introduction (Sec 1.1.5) is a measure of the A-site cation disorder.

In order to melt the charge ordered state in rare earth manganates, substitution of the Mn-site has been found to very effective. This idea stems from the fact that, in order to effect a transition from the antiferromagnetic charge ordered insulating state (AFMI) to the ferromagnetic metallic state (FMM), direct control of the manganese-oxygen framework should have a more pronounced effect on the observed properties. Examples include the doping of the Mn-site in $\text{Pr}_{0.6}\text{Ca}_{0.4}\text{MnO}_3$ with trivalent ions such as Fe^{3+} , Al^{3+} etc. [70]. Cr^{3+} ($t_{2g}^3 e_g^0$) and Ru^{4+} ($t_{2g}^4 e_g^0$) have been found effective in destroying charge-ordering in materials such as $\text{Nd}_{0.5}\text{Ca}_{0.5}\text{MnO}_3$ and $\text{Sm}_{0.5}\text{Ca}_{0.5}\text{MnO}_3$ [65,72,96] as well as $\text{Pr}_{0.5}\text{A}_{0.5}\text{MnO}_3$ (A = Ca or Sr). We sought it fit to consider the effect of doping of Ru^{4+} in the Mn-site in $\text{Pr}_{0.5}\text{Ca}_{0.5}\text{MnO}_3$. In order to compare the results obtained, we have also employed Cr^{3+} as a dopant. By employing the alkaline earth ion Sr in place of Ca, the properties of $\text{Pr}_{0.5}\text{A}_{0.5}\text{MnO}_3$ change drastically. The material exhibits properties similar to $\text{Nd}_{0.5}\text{Sr}_{0.5}\text{MnO}_3$ except that the charge ordered state is not seen. We have investigated the effect of doping on this material wherein Cr^{3+} and Ru^{4+} are the employed dopants. In both $\text{Pr}_{0.5}\text{Ca}_{0.5}\text{MnO}_3$ and $\text{Pr}_{0.5}\text{Sr}_{0.5}\text{MnO}_3$, doping $\text{Cr}^{3+}/\text{Ru}^{4+}$ produces marked effects, stabilizing the FMM state. We have then compared the effect of $\text{Cr}^{3+}/\text{Ru}^{4+}$ substitution in

$\text{Pr}_{0.6}\text{Ca}_{0.4}\text{MnO}_3$ and $\text{Pr}_{0.4}\text{Ca}_{0.6}\text{MnO}_3$. Since all these systems showed marked differences in the properties of these two manganates, in that the hole-doped composition was sensitive to magnetic fields and Mn-site doping (unlike in the electron-doped composition), we have examined the EPR structure of these two manganates as well.

In order to ensure that the Mn-O-Mn angle is not the limiting factor, we have prepared a manganate of the composition $\text{La}_{0.33}\text{Ca}_{0.33}\text{Sr}_{0.34}\text{MnO}_3$ with significantly large Mn-O-Mn angles, and studied the effects of B-site substitution and magnetic fields on the properties of this material.

In addition to bulk samples, we have carried out detailed studies on thin films of hole-doped $\text{Pr}_{0.6}\text{Ca}_{0.4}\text{MnO}_3$ and electron-doped $\text{Pr}_{0.4}\text{Ca}_{0.6}\text{MnO}_3$. The study includes the effect of both magnetic and electric fields on the properties of the films. Small electric fields have been shown to produce marked effects on the properties of certain manganates and bring about an insulator-metal (I-M) transition with the concomitant melting of the charge ordered state [83]. We have also examined the effect of doping in thin films of $\text{Pr}_{0.6}\text{Ca}_{0.4}\text{MnO}_3$ and $\text{Pr}_{0.4}\text{Ca}_{0.6}\text{MnO}_3$ with 3% Cr^{3+} and Ru^{4+} . These impurities are known to significantly affect the properties of charge-ordered manganates rendering them ferromagnetic and metallic in certain instances [43,65,96].

First principle calculations employing Linearized Muffin Tin Orbitals (LMTO) method have been carried out on two compositions namely that of hole-doped $\text{La}_3\text{CaMn}_4\text{O}_{12}$ and electron-doped $\text{LaCa}_3\text{Mn}_4\text{O}_{12}$ with a view of understanding the electron-hole asymmetry. The calculations reveal that the electronic structure is indeed asymmetric in the hole and the electron-doped composition. In the latter case due to the low concentration of e_g electrons and with the bandwidth near the Fermi-level being narrow, a gap of the Mott-Hubbard type is expected to occur.

1.2.2. Hopping conduction in charge-ordered rare-earth manganates,

$\text{Ln}_{1-x}\text{Ca}_x\text{MnO}_3$ (Ln=rare earth)

The mechanism of electron conduction in these compounds is of considerable interest, but most of the studies reported are concerned with $\text{La}_{0.7}\text{Ca}_{0.3}\text{MnO}_3$ [97-102] and similar compositions [103,104], which exhibit ferromagnetism and undergo insulator metal (I-M) transitions around the Curie temperature, T_C . $\text{La}_{0.7}\text{Ca}_{0.3}\text{MnO}_3$ becomes insulating only above 252 K (T_C) and several workers have examined the high resistivity data to understand the nature of the hopping conduction mechanism. The resistivity data have been fitted to models such as variable range hopping (VRH) [97-102,105], adiabatic and non-adiabatic small polaron hopping [98,105] and bipolaronic hopping [103]. Models

such as the VRH model is, however, are applicable in the low temperature regime.

We considered it instructive to investigate the conduction mechanism in charge-ordered materials that remain insulating from room temperature down to low temperatures. We have therefore investigated a series of charge-ordered rare-earth manganates in single crystal as well as polycrystalline forms. The solids examined include single and polycrystalline samples of $\text{Gd}_{0.5}\text{Ca}_{0.5}\text{MnO}_3$ and $\text{Nd}_{0.5}\text{Ca}_{0.5}\text{MnO}_3$ with the charge-ordering transition temperatures (T_{CO}) at 260 and 240 K respectively [92]. We have then compared the conduction behavior of single crystals of hole-doped $\text{Pr}_{0.6}\text{Ca}_{0.4}\text{MnO}_3$ and electron-doped $\text{Pr}_{0.4}\text{Ca}_{0.6}\text{MnO}_3$ with charge ordering transition temperatures around 230 K respectively. While both these compositions remain charge-ordered down to low temperatures, there is a basic difference between the two manganates. The former can be transformed into the ferromagnetic metallic state by applying a magnetic field or by substitution of impurities such as Cr^{3+} or Ru^{4+} in the Mn-site while the insulating state of the electron-doped composition is not affected by any such perturbation. A.c conductivity measurements have also been carried out on these manganates to throw light on the nature of conduction.

1.2.3 A- versus CE-type antiferromagnetism in $\text{Pr}_{0.5-x}\text{Nd}_x\text{Sr}_{0.5}\text{MnO}_3$

All the charge ordered rare earth manganates show antiferromagnetism of the CE-type. Accordingly, $\text{Nd}_{0.5}\text{Ca}_{0.5}\text{MnO}_3$ as well as $\text{Nd}_{0.5}\text{Sr}_{0.5}\text{MnO}_3$ shows CE-type antiferromagnetism at low temperatures. However, neighbouring compositions $\text{Nd}_{0.45}\text{Sr}_{0.55}\text{MnO}_3$ shows A-type antiferromagnetism. It has been recently found that in some samples of $\text{Nd}_{0.5}\text{Sr}_{0.5}\text{MnO}_3$ there is a transformation from a ferromagnetic state to an intermediate A-type (without charge ordering) and then to a CE-type antiferromagnet (with charge ordering). Amazingly, at very low temperatures, the ferromagnetic metallic state co-exists with A- and CE-type phases of $\text{Nd}_{0.5}\text{Sr}_{0.5}\text{MnO}_3$. It is also noteworthy that $\text{Pr}_{0.5}\text{Sr}_{0.5}\text{MnO}_3$ which is ferromagnetic at 250 K on cooling, goes to a A-type antiferromagnet unlike $\text{Nd}_{0.5}\text{Sr}_{0.5}\text{MnO}_3$ which shows charge ordering ($T_{\text{CO}} = 160$ K). We considered it interesting to investigate A-type versus CE-type antiferromagnetism in $(\text{Pr}_{1-x}\text{Nd}_x)_{0.5}\text{Sr}_{0.5}\text{MnO}_3$. The problem was to find out whether A-type AFM goes to CE-type AFM with increasing x .

1.2.4 Layered manganates

Layered manganates forming the members of the Ruddlesden-Popper phases can be represented by the general formula $(\text{Ln}_{1-x}\text{A}_x)_{n+1}\text{Mn}_n\text{O}_{3n+1}$ where Ln = rare earth, A = alkaline earth and 'n' is the number of corner shared $\text{MnO}_{6/2}$ octahedral sheets forming the layer. The reduction in dimensionality from 3D to

pseudo 2D reduces the one electron bandwidth 'W' and brings the system in manganates. For example, $\text{La}_{0.5}\text{Sr}_{0.5}\text{MnO}_3$ (3D, $n = \infty$) do not show any charge ordering, however $\text{La}_{0.5}\text{Sr}_{1.5}\text{MnO}_4$ (2D, $n = 1$) and $\text{LaSr}_2\text{Mn}_2\text{O}_7$ (2D, $n = 2$) systems show charge-ordering transitions at 217 K [106] and 210 K [107] respectively. Moritomo et al [108] studied the effect of internal pressure on the charge-ordering behaviour of the layered manganates of the type $\text{La}_{0.5}\text{Sr}_{1.5}\text{MnO}_4$ ($\text{Ln} = \text{La, Pr, Nd and Sm}$) and found that the charge-ordering is suppressed as the average radius (r_{Ln}) of the rare earth ion (Ln^{3+}) is increased and that no charge-ordering is seen for $\text{Ln} = \text{Nd}$. In $\text{La}_{0.5}\text{Sr}_{1.5}\text{MnO}_4$, each two dimensional corner-shared $\text{MnO}_{6/2}$ octahedral sheet forming the layer are separated by a rigid layer of SrO, possessing the rock salt structure, which do not allow the co-operative tilting of the octahedra for small r_{Ln} . This is in contrast to the 3D-perovskite manganates where a small $\langle r_{\text{A}} \rangle$ results in co-operative tilting and rotation of the $\text{MnO}_{6/2}$ octahedra.

It would be interesting to investigate whether charge ordering in layered manganates having small rare earth and alkaline earth as in $\text{Nd}_{0.5}\text{Ca}_{1.5}\text{MnO}_4$, since $\text{Nd}_{0.5}\text{Sr}_{1.5}\text{MnO}_4$ does not appear to show charge ordering.

1.3 EXPERIMENTAL

1.3.1 Synthesis

Polycrystalline materials

All the samples were prepared by employing the ceramic route [109]. The rare earth oxides were preheated at 1173 K for 8 h before taking them out into near moisture free environment. For the composition $\text{Pr}_{1-x}\text{Ca}_x\text{MnO}_3$ where $x = 0.64$ and 0.36 , the starting materials employed were Pr_6O_{11} (Rare-earths India Ltd), CaCO_3 and MnO_2 (Aldrich). Stoichiometric amounts of the starting materials were mixed and fired at an initial temperature of 1173 K (900°C) for 12 hours in ceramic crucibles. They were then remixed and fired for an additional 12 hours at 1473 K (1200°C) in an alumina crucible. The so obtained powder was finely ground, pelletized into circular discs (dia = 1 cm, thickness = 0.1 mm) and fired at a final temperature of 1673 K for 24 hours in a platinum boat, with an intermediate grinding.

For the series involving the variation of σ^2 , the materials involving La i.e., $\text{La}_{0.1}\text{Y}_{0.26}\text{Ca}_{0.46}\text{Sr}_{0.18}\text{MnO}_3$ and $\text{La}_{0.16}\text{Y}_{0.2}\text{Ca}_{0.526}\text{Sr}_{0.114}\text{MnO}_3$, two heatings were done at 1473 K before one final firing at 1673 K for 12 h. The other compositions $\text{Nd}_{0.18}\text{Sm}_{0.18}\text{Ca}_{0.553}\text{Sr}_{0.087}\text{MnO}_3$ and $\text{Nd}_{0.18}\text{Gd}_{0.18}\text{Ca}_{0.518}\text{Sr}_{0.122}\text{MnO}_3$ were prepared employing the same procedure as for $\text{Pr}_{0.64}\text{Ca}_{0.36}\text{MnO}_3$ except that the final heating was for only 12 h. The starting rare- and alkaline earth compounds employed in these preparations were Nd_2O_3 , Sm_2O_3 , Gd_2O_3 and SrCO_3 .

In the case of the impurity doping involving Cr^{3+} and Ru^{4+} , the starting material for these were Cr_2O_3 and $\text{RuO}_2 \cdot x\text{H}_2\text{O}$ (Fluka). The chromium salt was heated to 400°C for 6 hours before being employed. The amount of ruthenium in salt necessary was calculated based on the weight fraction listed. Stoichiometric amounts of the necessary impurity dopant were weighed and mixed with other salts before the initial grinding. The sample preparation was carried out as in the case of $\text{Pr}_{0.64}\text{Ca}_{0.36}\text{MnO}_3$.

Strontium containing compounds of the range $\text{Pr}_{0.5-x}\text{Nd}_x\text{Sr}_{0.5}\text{MnO}_3$ ($x = 0.0, 0.05, 0.1, 0.2, 0.3, 0.4, \text{ and } 0.5$) were prepared employing the starting material SrCO_3 (Aldrich) and the respective rare earth oxides. Stoichiometric amounts were ground and the materials were synthesized as in the case of $\text{Pr}_{0.64}\text{Ca}_{0.36}\text{MnO}_3$.

Single crystalline materials

Single crystals of the material $\text{Pr}_{0.36}\text{Ca}_{0.64}\text{MnO}_3$ were prepared employing the floating zone method [110]. Initially, stoichiometric amounts of Pr_6O_{11} , CaCO_3 and MnO_2 were weighed and thoroughly ground. The mixture was fired for 12 h at 1173 K, reground and fired again at 1473 K for 24 h. The mixture so obtained was again thoroughly reground and fired for another 12-24 h. The so obtained powder showed the formation of the phase as determined by x-ray diffraction, magnetization and resistivity. The amount of

the material prepared was around 30 gms. The finely ground powder was then pressed into thin cylindrical rods (0.8 cm dia, 6 cm length) using latex tubes under a hydrostatic pressure of 5 tons. The rods were then carefully transferred into platinum boats and fired at 1673 K for 12 h for sintering.

Two rods of the material (seed and feed) were employed to grow the single crystal employing the floating zone furnace (NEC, Japan). The growth rate was 15-20 mm/hr wherein the two rods were rotated in opposite directions in a pure N₂ atmosphere (99.999%). The crystal was cooled at 3 mm/h to room temperature before being cut into slices of 1 mm thickness. These were then annealed in O₂ atmosphere for 36-48 h at 850°C (determined by TGA analysis).

Single crystals of Gd_{0.5}Ca_{0.5}MnO₃ and Nd_{0.5}Ca_{0.5}MnO₃ were prepared in a similar way. However, the growth rate was ~ 8 mm/h and growth was carried out in air with a flow rate of 4 litres/min. The cut pieces (8 mm x 1 mm) were also annealed in O₂ atmosphere.

In the case of layered manganate, Nd_{0.5}Ca_{1.5}MnO₄ (n = 1), stoichiometric amounts of the material were weighed and thoroughly mixed. It was then fired at 1173 K, followed by remixing and firing for 24 h at 1423 K (1150°C). The powder was then thoroughly reground and fired for another additional 12 hours at the same temperature. A final temperature of 1523 K

(1250°C) was attained in a platinum crucible of another 12 hours. The so obtained powder was carefully kept in an evacuated chamber. The material should be preferably quenched to room temperature to avoid growth of three-dimensional perovskite phase that begins to form at lower temperatures. It was also noticed that on slight exposure to atmospheric moisture results in phase separation (white specks are seen homogeneously through out the material). Single crystal of the material was grown employing the same procedure as in $\text{Gd}_{0.5}\text{Ca}_{0.5}\text{MnO}_3$. The crystal obtained was hygroscopic and therefore sealed in airtight container.

Thin Films

Thin films of $\text{Pr}_{0.6}\text{Ca}_{0.4}\text{MnO}_3$ and $\text{Pr}_{0.4}\text{Ca}_{0.6}\text{MnO}_3$ as well as films containing 3% of the dopant Cr^{3+} and Ru^{4+} were deposited by using nebulized spray pyrolysis [111]. The substrates employed were single crystals of LaAlO_3 (LAO) and silicon (Si), cut along (100) face. The starting materials employed were organometallics of the respective element. They include $\text{Pr}(\text{acac})_3$ (tris-acetylacetonato praseodymium), $\text{Ca}(\text{acac})_2$ (bis-acetylacetonato calcium), $\text{Mn}(\text{acac})_3$ (tris-acetylacetonato manganese), $\text{Cr}(\text{acac})_3$ (tris-acetylacetonato chromium) and $\text{Ru}(\text{acac})_4$ (quad-tris-acetylacetonato ruthenium). Stoichiometric amounts of the material were made into 1mM solutions using methanol. Air was used as the carrier gas with a flow rate of 1.5 litres/min. The desired compositions were deposited wherein the substrates were

maintained at 450 K. The films so obtained were annealed at 973 K (700°C) for 12 hours in oxygen atmosphere.

1.3.2 Characterization and Measurements

X-ray diffraction patterns were recorded employing a SEIFERT XRD 3000TT instrument in the θ - θ flat bed geometry. The patterns were recorded between $\theta=5^\circ$ - 40° with a step width of 0.05° and a dwell time of one-second. The polycrystalline samples were thoroughly ground before recording and all the compositions showed single phase. As an example, in Fig 1.38, we show the diffraction pattern for hole-doped $\text{Pr}_{0.64}\text{Ca}_{0.36}\text{MnO}_3$. In addition, we also show the effect of 3% Cr^{3+} and Ru^{4+} in the Mn-site of $\text{Pr}_{0.64}\text{Ca}_{0.36}\text{MnO}_3$. We observe no additional features, indicating that the material is single phase. In Fig 1.39, we show similar effects in electron-doped $\text{Pr}_{0.36}\text{Ca}_{0.64}\text{MnO}_3$. In the case of thin films of $\text{Pr}_{1-x}\text{Ca}_x\text{MnO}_3$, the x-ray diffraction patterns contained the substrate peak as well.

All the diffraction patterns were indexed employing PROSZKI program. For Rietveld analysis, the scan range was between $\theta = 5^\circ$ - 50° wherein the dwell time was 8 secs. The total scan time was 8 h, each step being 0.02° . The XRD pattern was analyzed using the structure refinement program GSAS [112]. For thin films, the patterns were collected by grazing angle diffraction method wherein the scans are done in the θ - Ω geometry. All the scans were collected between $\theta = 5^\circ$ - 30° . The elemental composition was

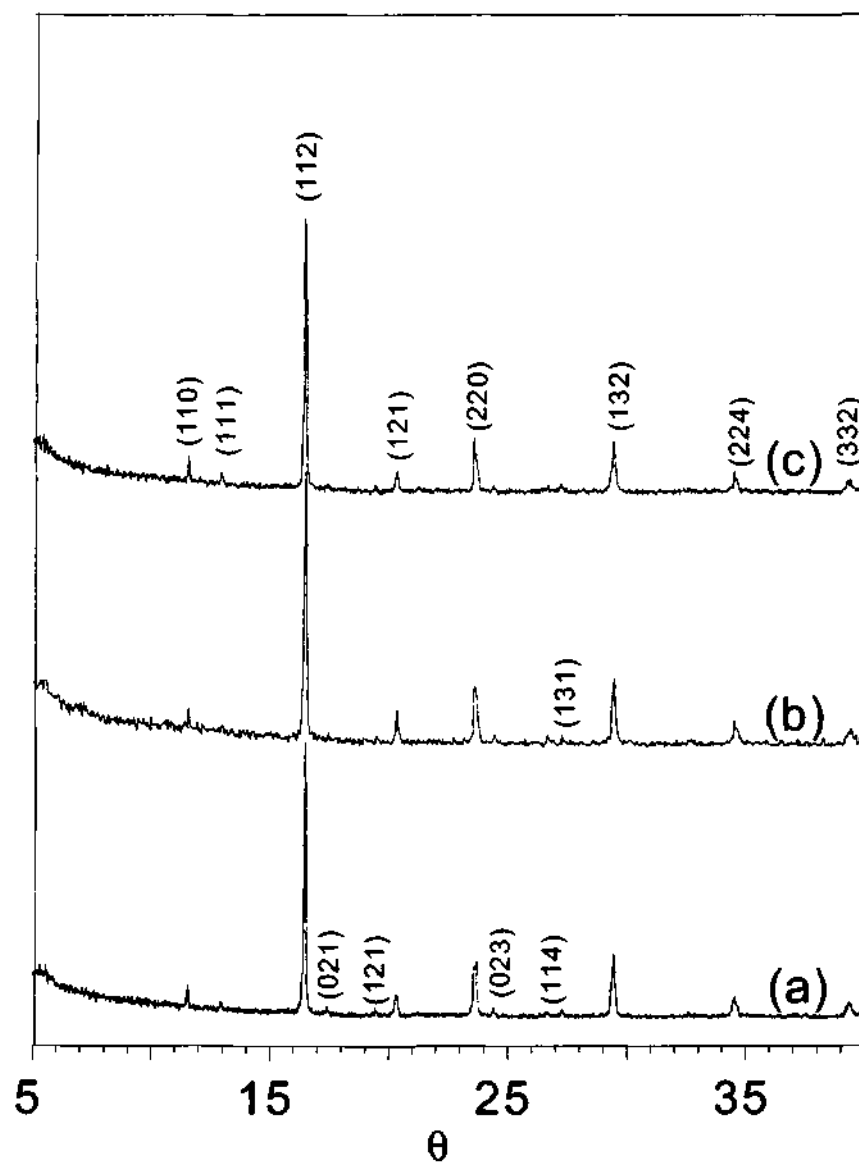


Fig. 1. 38. Powder x-ray diffraction data for (a) $\text{Pr}_{0.64}\text{Ca}_{0.36}\text{MnO}_3$ (b) $\text{Pr}_{0.64}\text{Ca}_{0.36}\text{Mn}_{0.97}\text{Cr}_{0.03}\text{O}_3$ and (c) $\text{Pr}_{0.64}\text{Ca}_{0.36}\text{Mn}_{0.97}\text{Ru}_{0.03}\text{O}_3$.

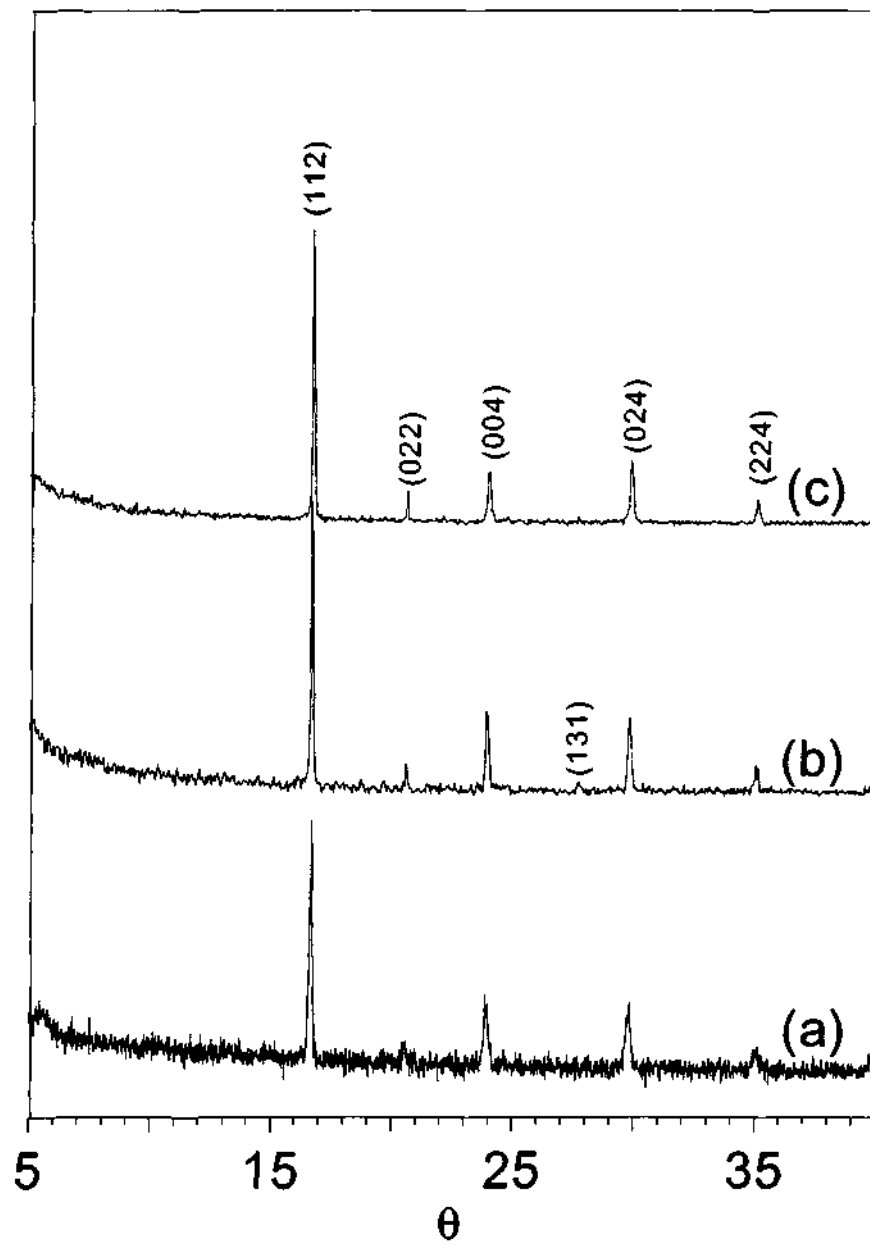


Fig. 1. 39. Powder x-ray diffraction data for (a) $\text{Pr}_{0.36}\text{Ca}_{0.64}\text{MnO}_3$ (b) $\text{Pr}_{0.36}\text{Ca}_{0.64}\text{Mn}_{0.97}\text{Cr}_{0.03}\text{O}_3$ and (c) $\text{Pr}_{0.36}\text{Ca}_{0.64}\text{Mn}_{0.97}\text{Ru}_{0.03}\text{O}_3$.

ascertained by employing energy dispersive x-ray analysis (EDAX) technique with a LEICA S440i machine equipped with ISIS software.

Electrical resistivity measurements were carried out on both polycrystalline and single crystalline samples by employing the four-probe method. The apparatus is connected to a helium cryostat and the data was collected between 300-20 K. A Keithley current source meter and voltmeter was used. The samples were circular and had dimensions of 1 cm diameter and < 1 mm thickness. D.c magnetic measurements were carried out using a vibrating sample magnetometer (VSM-7300, Lakeshore Inc.) between 300-50 K wherein the maximum field attainable is 1T. Samples approximately weighing 0.1 gm were employed for the measurements. Magnetoresistivity measurements were carried out using a cryocooled closed cycle superconducting magnet designed by us along with Cryo Industries of America, Manchester, MA. The field employed in the measurement could be varied from 0-15T.

A.c. impedance measurements were carried out from 77 K-220 K employing a Hewlett-Packard 4192A-impedance analyzer between 100 Hz to 13 MHz employing the two-probe technique. The cooling apparatus was a homemade device housed in glass tubing filled with helium and kept in a liquid nitrogen bath. The temperature variation was carried out by adjusting

the length of the glass tube with respect to the level of the liquid within an accuracy of $\pm 1^\circ\text{C}$.

Electron paramagnetic resonance (EPR) was carried out employing a VARIAN E-109X band spectrometer. The maximum attainable field was 1T and the sample could be cooled all the way to 20 K employing a closed cycle helium cryostat.

1.4 RESULTS AND DISCUSSION

1.4.1 A Study of Electron-Hole Asymmetry in Rare Earth Manganates

The phase diagrams of two rare-earth manganates, $\text{Ln}_{1-x}\text{Ca}_x\text{MnO}_3$ ($\text{Ln} = \text{La}$ and Pr) in Fig. 1. 10 clearly demonstrate the electron-hole asymmetry present in these materials, and also the preponderance of the charge-ordered (CO) state in the electron-doped regime ($x > 0.5$). The ferromagnetic metallic (FMM) state, generally found in the hole-doped regime ($x \leq 0.5$), is favored by the large size of the A-site cations [113,114]. Thus, the FMM state occurs till $x = 0.5$ in $\text{La}_{1-x}\text{Ca}_x\text{MnO}_3$ (Fig. 1. 10). In $\text{Pr}_{1-x}\text{Ca}_x\text{MnO}_3$, the FMM state is not found at any composition and there is only a ferromagnetic insulating (FMI) state when $0.1 \leq x \leq 0.3$. The charge-ordering regime in $\text{La}_{1-x}\text{Ca}_x\text{MnO}_3$ is $0.5 \leq x \leq 0.85$, but is considerably wider ($0.3 \leq x \leq 0.85$) in $\text{Pr}_{1-x}\text{Ca}_x\text{MnO}_3$. Accordingly, charge-ordering occurs in both hole- and the electron-doped compositions of the latter system. Charge ordering in these systems is ascertained by the appearance of superlattice reflections in the diffraction patterns and by the occurrence of anomalies (observation of maxima) in the temperature variation of magnetic susceptibility and the activation energy for conduction [92].

Effects of cation size and size-disorder

In Fig. 1. 40, we plot the known charge-ordering transition temperatures, T_{CO} , in $\text{Ln}_{0.5}\text{Ca}_{0.5}\text{MnO}_3$ and $\text{Ln}_{0.36}\text{Ca}_{0.64}\text{MnO}_3$ against the average radius of the A-

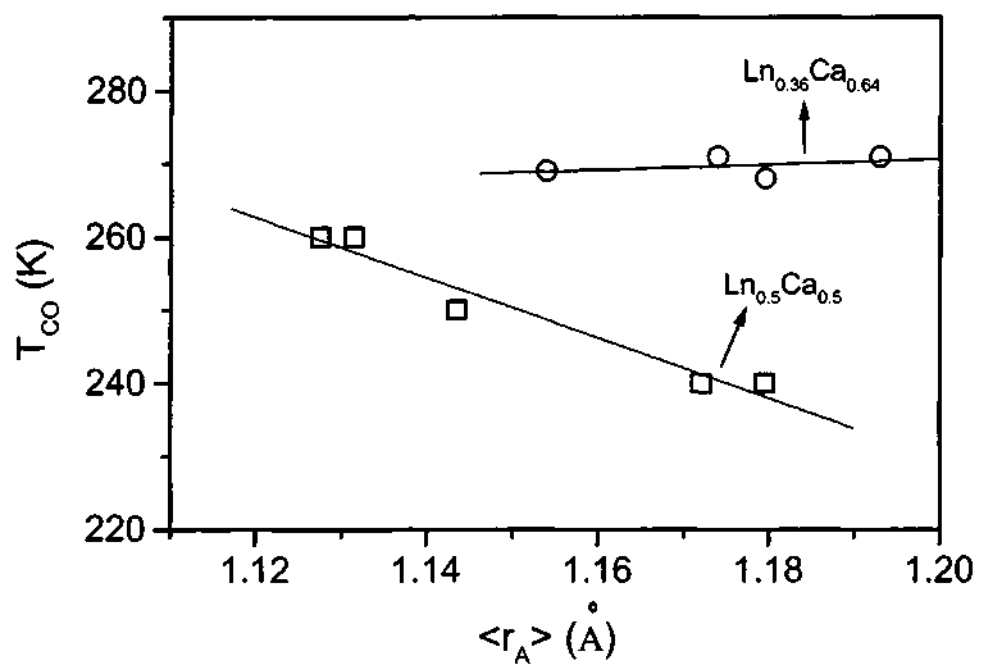


Fig. 1. 40. Variation of the charge-ordering transition temperature, T_{CO} , with the average size of A-site cation.

site cations $\langle r_A \rangle$. Here, $\langle r_A \rangle$ is varied by changing the Ln ion. While T_{CO} increases with the decrease in $\langle r_A \rangle$ in the case of $\text{Ln}_{0.5}\text{Ca}_{0.5}\text{MnO}_3$, it is not very sensitive to $\langle r_A \rangle$ in electron-doped $\text{Ln}_{0.36}\text{Ca}_{0.64}\text{MnO}_3$. In Table 1.2, we compare the T_{CO} values and other properties of $\text{Ln}_{0.64}\text{Ca}_{0.36}\text{MnO}_3$ and $\text{Ln}_{0.36}\text{Ca}_{0.64}\text{MnO}_3$. The T_{CO} value is generally higher in the latter system compared to the hole-doped materials, but there is little variation with $\langle r_A \rangle$ in both the series of compounds. In the series of manganates listed in Table 1.2, the cation size disorder [59], as measured by the variance, σ^2 , is quite small. It may be noted that in the electron-doped manganates, T_{CO} increases with electron concentration, x , but the ferromagnetic component [59] (in the cluster regime $0.0 < x < 0.2$ in $\text{Ca}_{1-x}\text{Ln}_x\text{MnO}_3$) is only slightly affected by $\langle r_A \rangle$ for a fixed value of x .

The effect of cation size disorder on the charge-ordering transition in $\text{Ln}_{0.5}\text{Ca}_{0.5}\text{MnO}_3$ has been investigated by keeping the average radius of the A-site cation fixed, and varying the σ^2 . The value of σ^2 is varied by making different combinations of the Ln and alkaline earth ions [62]. The slope of the linear $T_{CO} - \sigma^2$ plot for $\text{Ln}_{0.5}\text{Ca}_{0.5}\text{MnO}_3$ is 10975 \AA and the intercept of the plot, T_{CO}^0 , is 236 K. The value of T_{CO}^0 corresponds to that of the disorder free manganate. We have not been able to obtain sufficient reliable data on the variation of T_{CO} with σ^2 (at fixed $\langle r_A \rangle$) in hole-doped compositions of the type $\text{Ln}_{0.64}\text{Ca}_{0.36}\text{MnO}_3$, but the limited data available show only small changes. In the case of electron-doped $\text{Ln}_{0.36}\text{Ca}_{0.64}\text{MnO}_3$, however, we have obtained reliable data for two series of

Table 1. 2 Effect of $\langle r_A \rangle$ on charge-ordering in $\text{Ln}_{1-x}\text{Ca}_x\text{MnO}_3$ ($x=0.36, 0.64$)

Ln	$\text{Ln}_{0.64}\text{Ca}_{0.36}\text{MnO}_3$					$\text{Ln}_{0.36}\text{Ca}_{0.64}\text{MnO}_3$						
	$\langle r_A \rangle$ (Å)	σ^2 (Å ²)	Lattice parameter (Å)			T_{CO}^a (K)	$\langle r_A \rangle$ (Å)	σ^2 (Å ²)	Lattice parameter (Å)			T_{CO}^a (K)
			<u>A</u>	<u>B</u>	<u>c</u>			<u>a</u>	<u>b</u>	<u>c</u>		
La	1.203	0.0003	5.454	5.468	7.704	- ^b	1.193	0.0013	5.390	5.391	7.588	271
Pr	1.179	0.0000	5.413	5.442	7.676	210	1.179	0.0000	5.374	5.369	7.576	268
Nd	1.169	0.0001	5.407	5.458	7.646	212	1.174	0.0001	5.388	5.361	7.570	271

^a From magnetization measurements ($H = 100$ gauss).

^b This compound exhibits ferromagnetism and an insulator-metal transition around the T_c (~ 250 K).

manganates with fixed $\langle r_A \rangle$ values of 1.180 and 1.174 Å respectively, corresponding to $\text{Pr}_{0.36}\text{Ca}_{0.64}\text{MnO}_3$ and $\text{Nd}_{0.36}\text{Ca}_{0.64}\text{MnO}_3$. These compounds, along with their structural data and T_{CO} values, are listed in Table 1.3. We show the plots of T_{CO} against σ^2 for the two series of manganates in Fig. 1. 41. The plots are linear giving slopes 6408 and 5813 $\text{K}\text{Å}^{-2}$ respectively for fixed $\langle r_A \rangle$ of 1.180 and 1.174 Å respectively. The intercept, T_{CO}^0 , is around 266 K in both the cases, a value considerably higher than in $\text{Ln}_{0.5}\text{A}_{0.5}\text{MnO}_3$ [62]. An examination of the phase diagram in Fig. 1. 10 shows that in $\text{La}_{1-x}\text{Ca}_x\text{MnO}_3$, the T_{CO} reaches a maximum value around $x = 0.65$. We see a similar maximum in the phase diagram of $\text{Pr}_{1-x}\text{Ca}_x\text{MnO}_3$ as well. In the latter system, however, T_{CO} increases with the hole concentration, x , in the hole-doped regime ($0.3 < x \leq 0.5$), and with the electron concentration, $1-x$, in the electron-doped regime ($0.6 < x \leq 0.85$). In spite of some of these apparent similarities, the hole-doped and the electron-doped compositions exhibit significant differences in their electronic and magnetic properties, as detailed in the following sections.

Comparison of hole- and electron-doped $\text{Pr}_{1-x}\text{Ca}_x\text{MnO}_3$ ($x = 0.36$ and 0.64)

In order to understand the nature of electron-hole asymmetry in the rare earth manganates, it is useful to compare the electronic and magnetic properties of comparable compositions of the hole- and electron-doped materials. Thus, the hole-doped $\text{La}_{0.7}\text{Ca}_{0.3}\text{MnO}_3$ becomes ferromagnetic around 252 K, at which temperature it exhibits an insulator-metal transition. The electron-doped

Table 1. 3 Structure and properties of $\text{Ln}_{0.36-x}\text{Ln}'_x\text{Ca}_{0.64-y}\text{Sr}_y\text{MnO}_3$ with fixed $\langle r_A \rangle$ values

Composition	σ^2 (\AA^2)	Lattice parameter (\AA)			% D (300 K)	T_{CO}^a (K)
		\underline{a}	\underline{b}	\underline{c}		
$\langle r_A \rangle = 1.174 \text{ \AA}$						
$\text{Nd}_{0.36}\text{Ca}_{0.64}\text{MnO}_3$	0.0001	5.388	5.361	7.570	0.33	271 (261)
$\text{Pr}_{0.28}\text{Gd}_{0.08}\text{Ca}_{0.64}\text{MnO}_3$	0.0003	5.353	5.366	7.548	0.18	279 (270)
$\text{La}_{0.185}\text{Gd}_{0.175}\text{Ca}_{0.64}\text{MnO}_3$	0.0011	5.354	5.369	7.537	0.27	257 (253)
$\text{La}_{0.225}\text{Y}_{0.135}\text{Ca}_{0.64}\text{MnO}_3$	0.0017	5.353	5.370	7.563	0.15	249 (248)
$\text{Sm}_{0.36}\text{Ca}_{0.554}\text{Sr}_{0.086}\text{MnO}_3$	0.0022	5.355	5.372	7.569	0.15	263 (258)
$\text{Nd}_{0.1}\text{Gd}_{0.26}\text{Ca}_{0.528}\text{Sr}_{0.112}\text{MnO}_3$	0.0033	5.355	5.364	7.580	0.06	245 (243)
$\text{Gd}_{0.15}\text{Y}_{0.21}\text{Ca}_{0.433}\text{Sr}_{0.207}\text{MnO}_3$	0.0066	5.346	5.374	7.567	0.21	~229 (223)
$\langle r_A \rangle = 1.18 \text{ \AA}$						
$\text{Pr}_{0.36}\text{Ca}_{0.64}\text{MnO}_3$	0.0000	5.374	5.369	7.576	0.11	267 (267)
$\text{Nd}_{0.18}\text{Sm}_{0.18}\text{Ca}_{0.553}\text{Sr}_{0.087}\text{MnO}_3$	0.0019	5.369	5.370	7.580	0.07	~256 (251)
$\text{Nd}_{0.18}\text{Gd}_{0.18}\text{Ca}_{0.518}\text{Sr}_{0.122}\text{MnO}_3$	0.0031	5.363	5.376	7.573	0.14	250 (245)
$\text{La}_{0.16}\text{Y}_{0.2}\text{Ca}_{0.526}\text{Sr}_{0.114}\text{MnO}_3$	0.0043	5.364	5.370	7.578	0.07	~241 (~238)
$\text{La}_{0.1}\text{Y}_{0.26}\text{Ca}_{0.46}\text{Sr}_{0.18}\text{MnO}_3$	0.0060	5.386	5.369	7.550	0.32	234 (222)

^a The values in parentheses are obtained from resistivity data; %D is the orthorhombic distortion

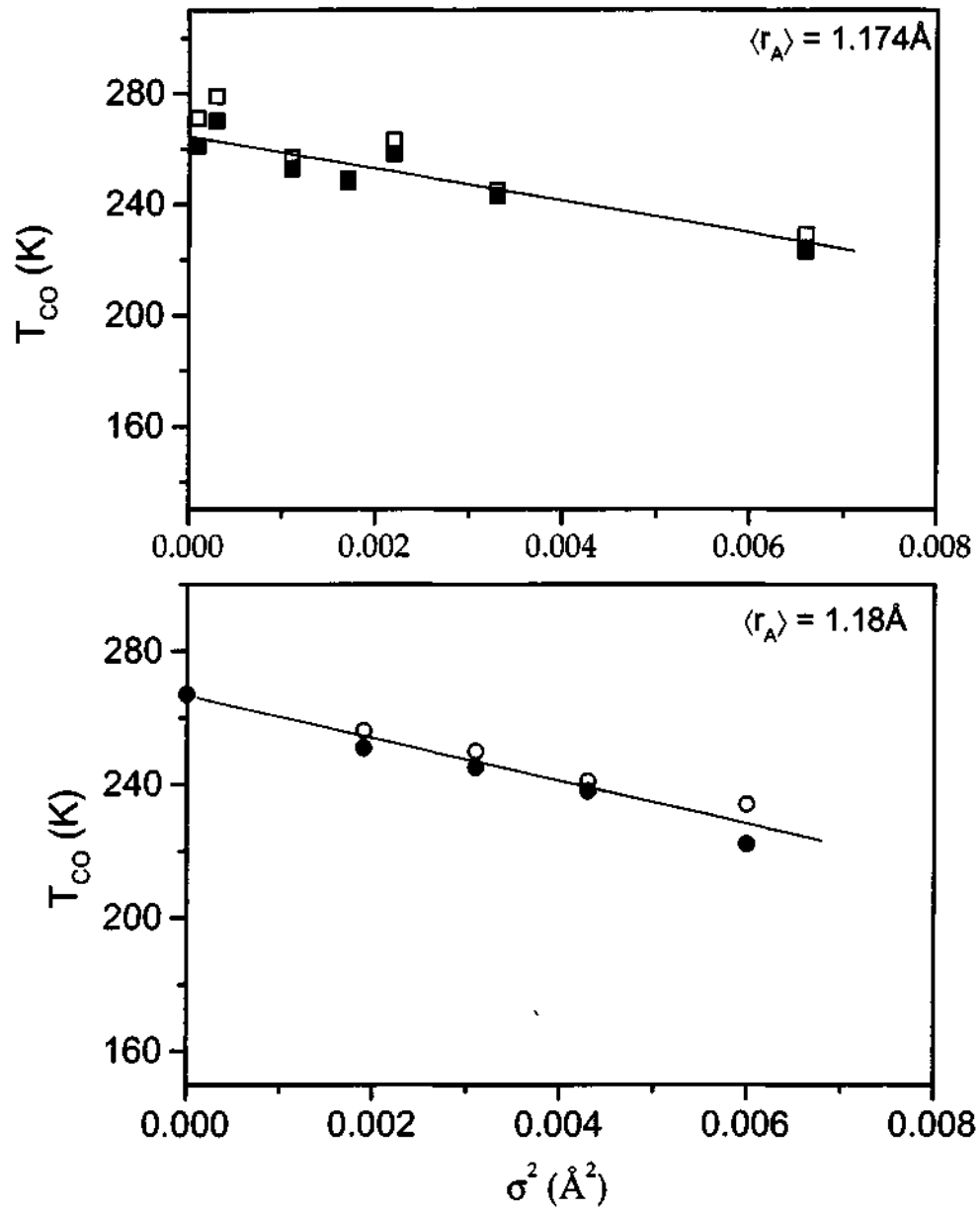


Fig. 1. 41. Variation of the charge-ordering temperature in $\text{Ln}_{0.36}\text{Ca}_{0.64}\text{MnO}_3$ with σ^2 for fixed $\langle r_A \rangle$ values. Open symbols represent data obtained from magnetic measurements and the corresponding closed symbols are from resistivity measurements.

$\text{La}_{0.3}\text{Ca}_{0.7}\text{MnO}_3$, on the other hand, gets charge-ordered at 271 K and does not exhibit the FMM state at any temperature. A better appreciation of the differences in the properties of the hole- and electron-doped manganates is obtained by comparing the properties of $\text{Pr}_{1-x}\text{Ca}_x\text{MnO}_3$ at the same carrier concentration (equal values of $1-x$ and x). We have carried out detailed studies on $\text{Pr}_{0.64}\text{Ca}_{0.36}\text{MnO}_3$ and $\text{Pr}_{0.36}\text{Ca}_{0.64}\text{MnO}_3$, both of which are charge-ordered.

$\text{Pr}_{0.64}\text{Ca}_{0.36}\text{MnO}_3$ and $\text{Pr}_{0.36}\text{Ca}_{0.64}\text{MnO}_3$, are both orthorhombic (*Pbnm*), but the unit cell is larger in the former as expected based on the relative sizes of Mn^{3+} and Mn^{4+} . In Fig. 1. 42 and Fig. 1. 43, we show the observed, calculated and difference plots based on the Rietveld analysis of the powder data of $\text{Pr}_{0.64}\text{Ca}_{0.36}\text{MnO}_3$ and $\text{Pr}_{0.36}\text{Ca}_{0.64}\text{MnO}_3$ respectively. In Table 1.4 and Table 1.5, we list the atomic coordinates and the lattice parameters of the two manganates obtained from the Rietveld analysis. The Mn-O distances in $\text{Pr}_{0.64}\text{Ca}_{0.36}\text{MnO}_3$ are longer than in $\text{Pr}_{0.36}\text{Ca}_{0.64}\text{MnO}_3$, but the Mn-O-Mn angles in the two are comparable.

Both $\text{Pr}_{0.64}\text{Ca}_{0.36}\text{MnO}_3$ and $\text{Pr}_{0.36}\text{Ca}_{0.64}\text{MnO}_3$ get charge-ordered in the paramagnetic state, with transition temperatures (T_{CO}) of 210 and 268 K respectively. They show maxima in the magnetization curves at the charge-ordering transition temperatures (Fig. 1. 44). $\text{Pr}_{0.64}\text{Ca}_{0.36}\text{MnO}_3$ also shows an antiferromagnetic transition around 140 K. The nature of the transitions has been

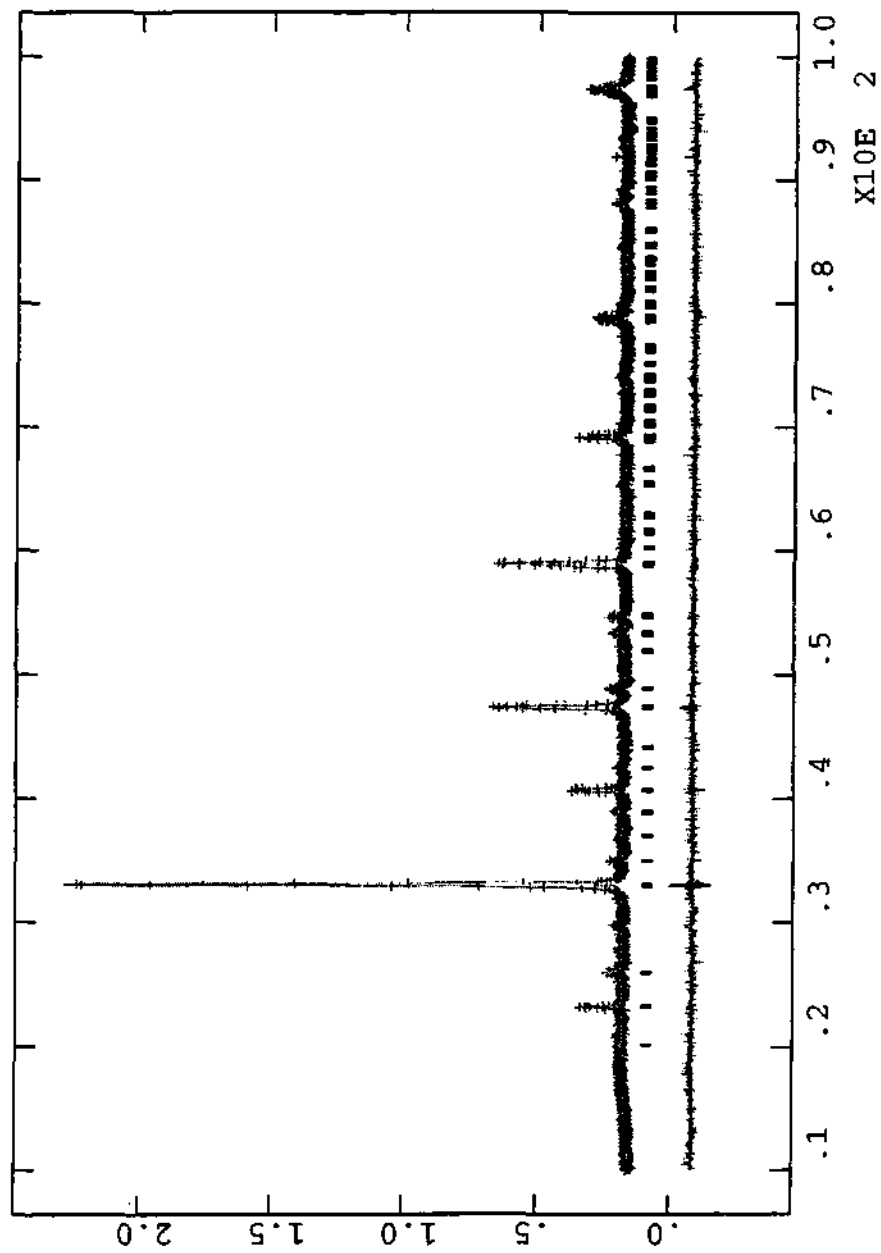


Fig. 1. 42. Observed, calculated and difference plots of $\text{Pr}_{0.64}\text{Ca}_{0.36}\text{MnO}_3$ obtained from x-ray powder diffraction data.

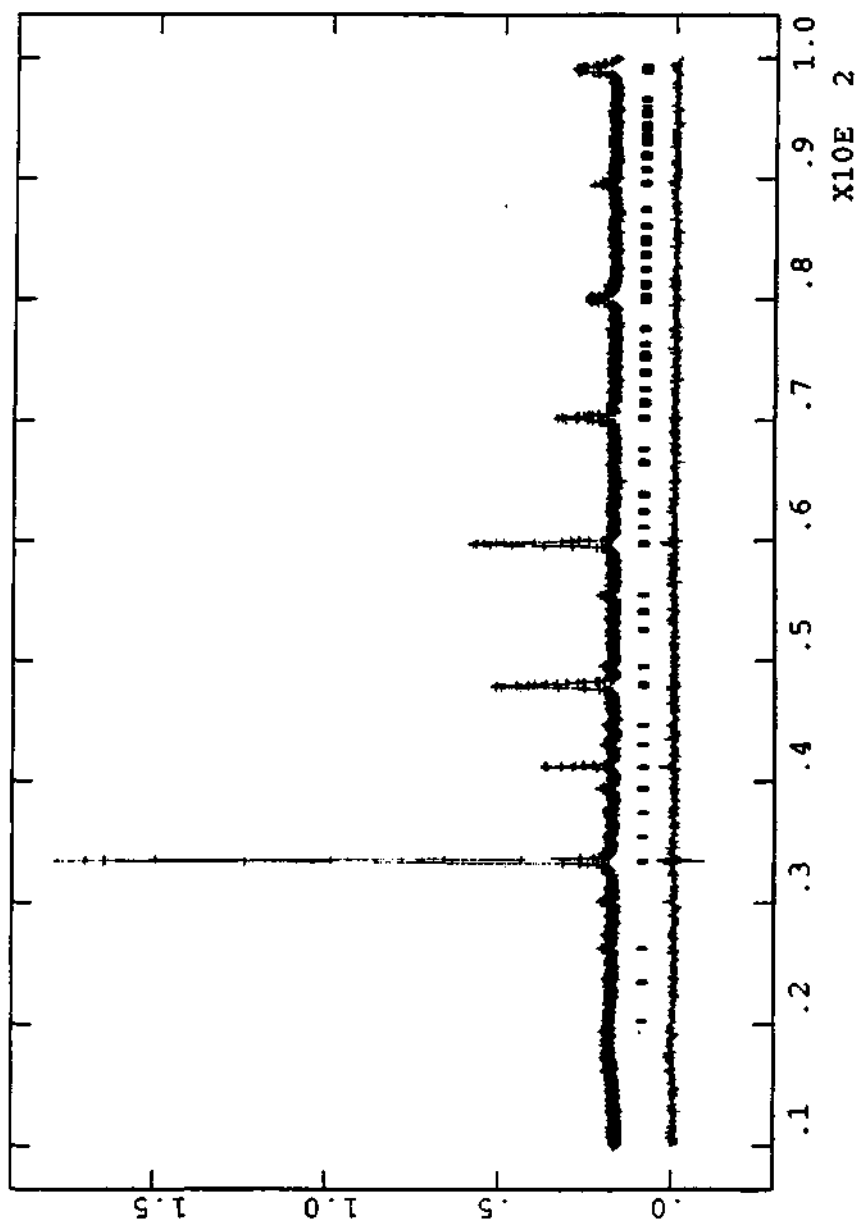


Fig. 1. 43. Observed, calculated and difference plots of $\text{Pr}_{0.36}\text{Ca}_{0.64}\text{MnO}_3$ obtained from x-ray powder diffraction data.

Table 1. 4 Atomic coordinates and structural parameters of $\text{Pr}_{0.64}\text{Ca}_{0.36}\text{MnO}_3$

Atom	Site	x	Y	z	Frac	U_{iso}
Pr	4c	-0.0083	0.0315	0.2500	0.6400	0.0049
Ca	4c	-0.0083	0.0315	0.2500	0.3600	0.0049
Mn	4b	0.5000	0.0000	0.0000	1.0000	0.0040
O	8d	0.0529	0.4939	0.2500	1.0000	0.0405
O	4c	-0.7115	0.2809	0.0354	1.0000	0.0122

bond	distance (Å)
Mn – O	2 x 1.935
	2 x 1.941
	2 x 1.989

bond	angle (deg)
Mn – O – Mn	4 x 157.6
	2 x 162.9

$a = 5.4310 \text{ \AA}$, $b = 5.4573 \text{ \AA}$, $c = 7.6761 \text{ \AA}$; Sp. gp : Pbnm , $R_{\text{wp}} = 3.45 \%$

Table 1. 5 Atomic coordinates and structural parameters of $\text{Pr}_{0.36}\text{Ca}_{0.64}\text{MnO}_3$

Atom	Site	x	Y	z	Frac	U_{iso}
Pr	4c	-0.5207	0.4746	0.2500	0.3600	-0.0033
Ca	4c	-0.5207	0.4746	0.2500	0.6400	-0.0033
Mn	4b	0.5000	0.0000	0.0000	1.0000	0.0063
O	8d	0.0544	0.5213	0.2500	1.0000	0.0901
O	4c	-0.2854	0.2717	-0.0460	1.0000	-0.0367

bond	distance (Å)
Mn – O	2 x 1.892
	2 x 1.993
	2 x 1.916

bond	angle (deg)
Mn – O – Mn	4 x 155.6
	2 x 161.2

$a = 5.3664 \text{ \AA}$, $b = 5.3746 \text{ \AA}$, $c = 7.5603 \text{ \AA}$; Sp. gp : $Pbmm$, $R_{\text{wp}} = 3.28 \%$

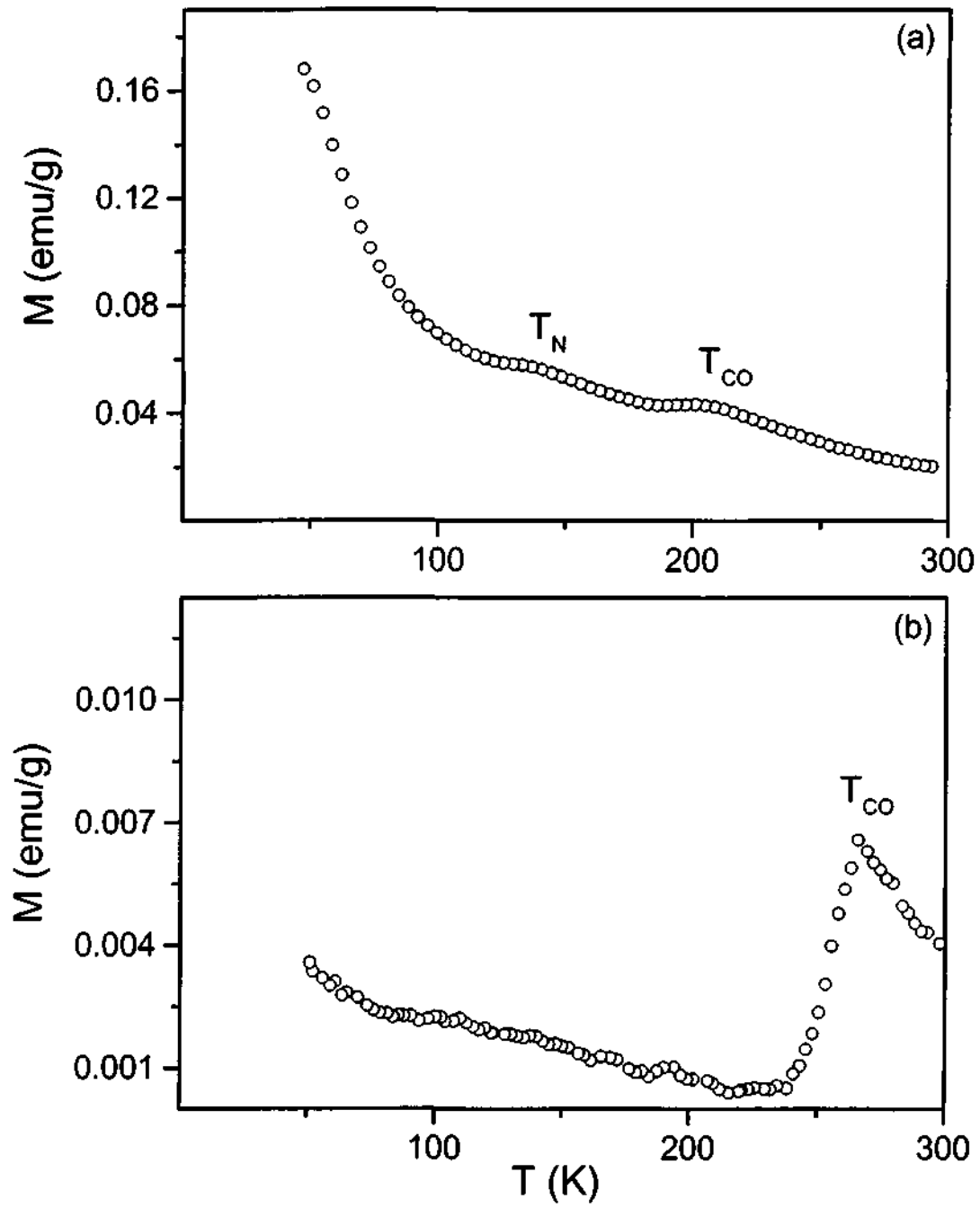


Fig. 1. 44. Temperature variation of the magnetization data of (a) $\text{Pr}_{0.64}\text{Ca}_{0.36}\text{MnO}_3$ and (b) $\text{Pr}_{0.36}\text{Ca}_{0.64}\text{MnO}_3$.

ascertained independently by diffraction studies as well as EPR and other measurements [1,2,115]. Both $\text{Pr}_{0.64}\text{Ca}_{0.36}\text{MnO}_3$ and $\text{Pr}_{0.36}\text{Ca}_{0.64}\text{MnO}_3$ are insulators down to low temperatures as expected of charge-ordered compositions, but the electron-doped composition shows a more marked change in resistivity at T_{CO} (Fig. 1. 45). The difference between the two lies in the effect of magnetic fields. Application of a magnetic field of 12T melts the CO state to a metallic state in the case of $\text{Pr}_{0.64}\text{Ca}_{0.36}\text{MnO}_3$ (Fig. 1. 45a). A 12T magnetic field has no effect whatsoever on the resistivity of $\text{Pr}_{0.36}\text{Ca}_{0.64}\text{MnO}_3$ (Fig. 1. 45b).

Effect of Cr^{3+} and Ru^{4+} substitution in the Mn-site

Substitution of Cr^{3+} or Ru^{4+} in the Mn-site of certain charge-ordered manganates is known to destroy the CO state, rendering them ferromagnetic and metallic [43,65,116,117]. We have carried out some studies on the effect of $\text{Cr}^{3+}/\text{Ru}^{4+}$ doping in $\text{Pr}_{0.5}\text{Ca}_{0.5}\text{MnO}_3$ and $\text{Pr}_{0.5}\text{Sr}_{0.5}\text{MnO}_3$ to illustrate the nature of changes brought about by such doping.

In Fig. 1. 46a and 1. 46b, we show the magnetization and resistivity curves for $\text{Pr}_{0.5}\text{Ca}_{0.5}\text{MnO}_3$. The magnetization data exhibits two features at ~ 230 K and ~ 150 K corresponding to the charge ordering temperature (T_{CO}) and the Néel temperature (T_{N}) respectively. The resistivity data reveals the material to be insulating. The effect of 3% Cr^{3+} doping on the magnetization behavior is shown in Fig. 1. 47a. The charge ordering feature at ~ 230 K found in the parent

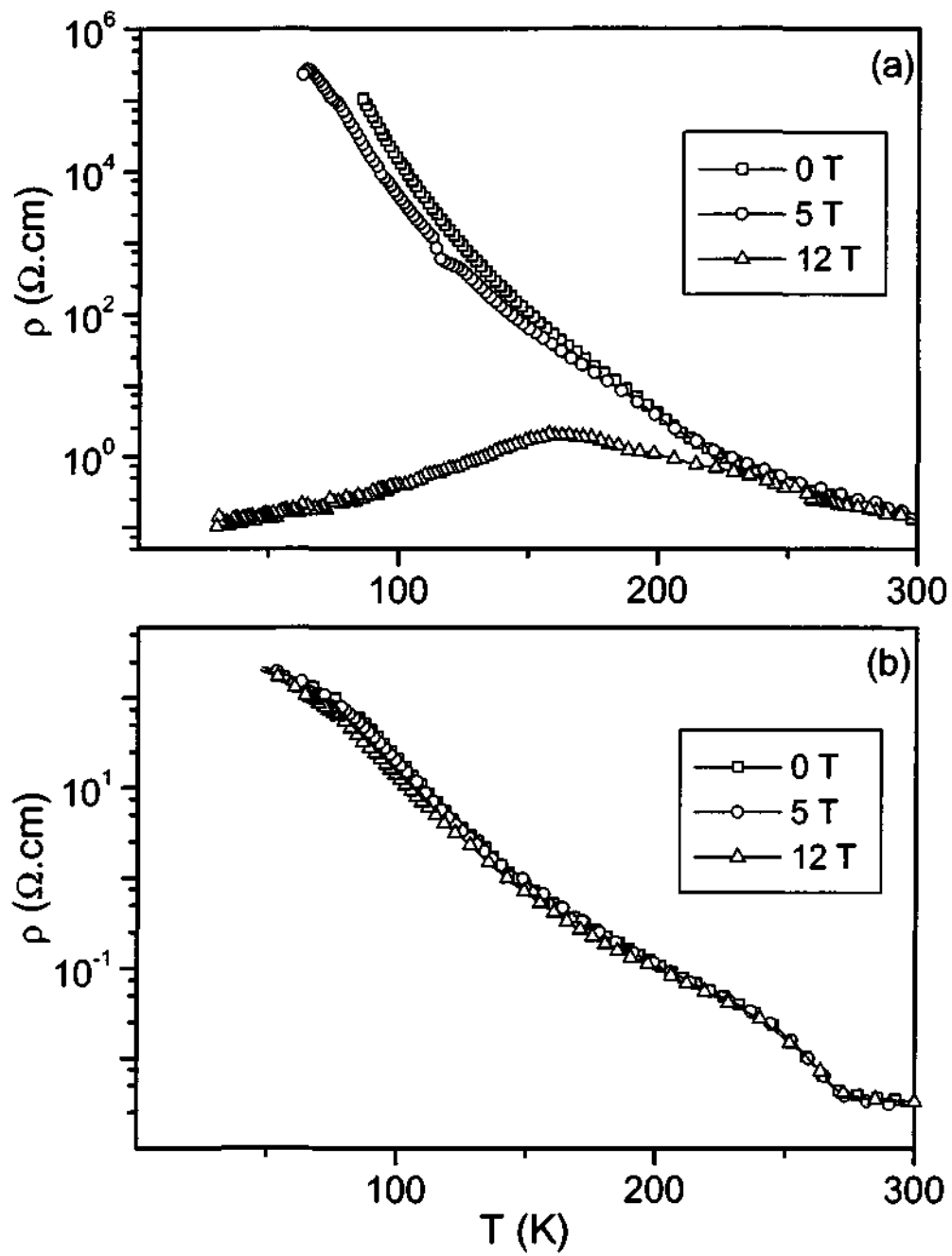


Fig. 1.45. Temperature variation of the electrical resistivity of (a) $\text{Pr}_{0.64}\text{Ca}_{0.36}\text{MnO}_3$ and (b) $\text{Pr}_{0.36}\text{Ca}_{0.64}\text{MnO}_3$. Effect of magnetic fields is shown.

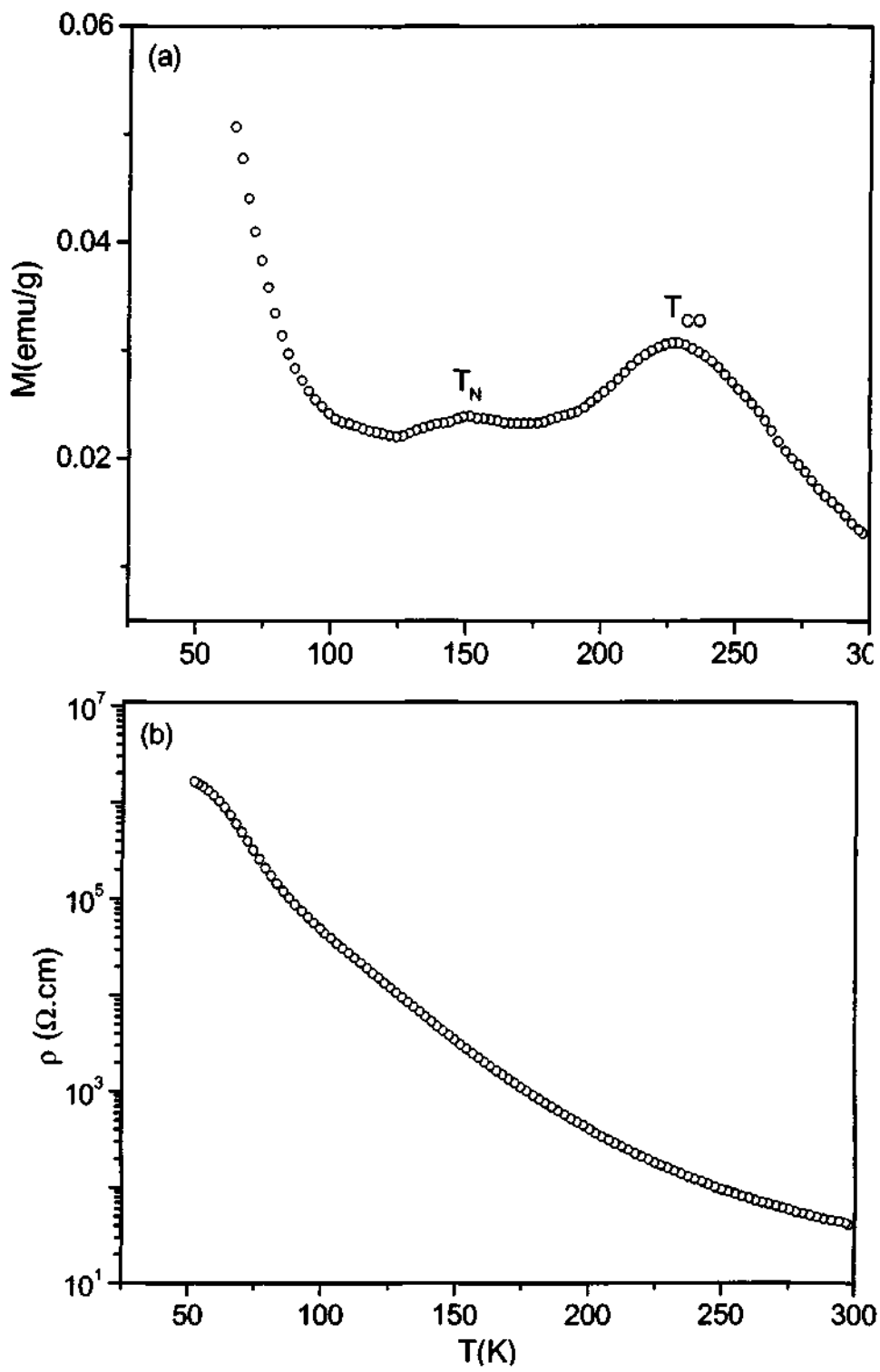


Fig. 1. 46. (a) Magnetization data and (b) resistivity data of $\text{Pr}_{0.5}\text{Ca}_{0.5}\text{MnO}_3$.

compound is completely suppressed. The antiferromagnetic behavior is also absent, giving in place to a ferromagnetic behavior with a Curie temperature $T_C \sim 130$ K. In Fig. 1. 47b, we show the corresponding resistivity data. The material undergoes an I-M transition at $T_{IM} = 130$ K. In earlier studies of this compound similar results have been obtained where they report T_{IM} at 140 K [68]. In view of this result, we have sought to investigate the effect of ruthenium doping in the Mn-site of $\text{Pr}_{0.5}\text{Ca}_{0.5}\text{MnO}_3$. In Fig. 1. 48a and 1. 48b we show the magnetization and the resistivity data obtained with 1% and 3% Ru doping respectively. When 1% Ru^{4+} is employed, it is seen that a ferromagnetic transition is induced with a T_C at ~ 150 K. This temperature is similar to that obtained with 3% Cr^{3+} doping. However on closer inspection, we see that the charge ordering is not completely destroyed as shown in the inset of Fig. 1. 48a. On increasing the Ru content to 3%, there is a shift in the ferromagnetic Curie temperature, with the T_C occurring at ~ 215 K. Interestingly, the resistivity behavior shows little shift in the T_{IM} . The I-M transition is much broader in the case of Ru^{4+} doping in comparison to the much sharper transition observed in the case of chromium doping. Also seen in Fig. 1. 48b, is that the resistivity value reduces and the transition occurs over a broad range of temperature with increase in ruthenium content. The effect of Ru^{4+} found here is similar to that observed in $\text{Nd}_{0.5}\text{Ca}_{0.5}\text{MnO}_3$, as the radius of Nd^{3+} is close to that of Pr^{3+} and consequently the material exhibits charge ordering at $T_{CO} = 240$ K and has no inherent I-M transition. Doping with 1% ruthenium has been found to destroy the charge ordered state giving rise to a

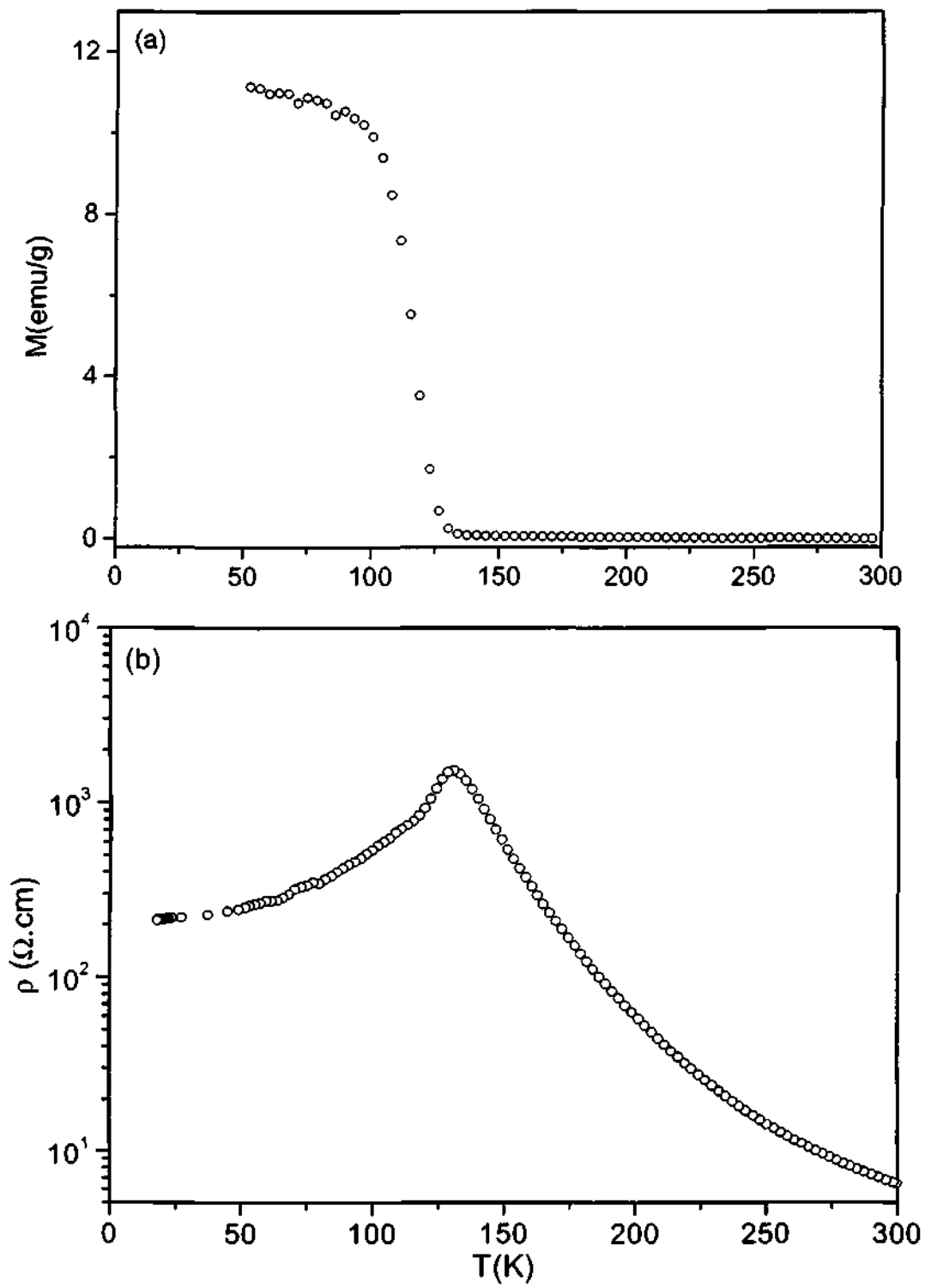


Fig. 1. 47. (a) Magnetization data and (b) resistivity data of $\text{Pr}_{0.5}\text{Ca}_{0.5}\text{Mn}_{0.97}\text{Cr}_{0.03}\text{O}_3$.

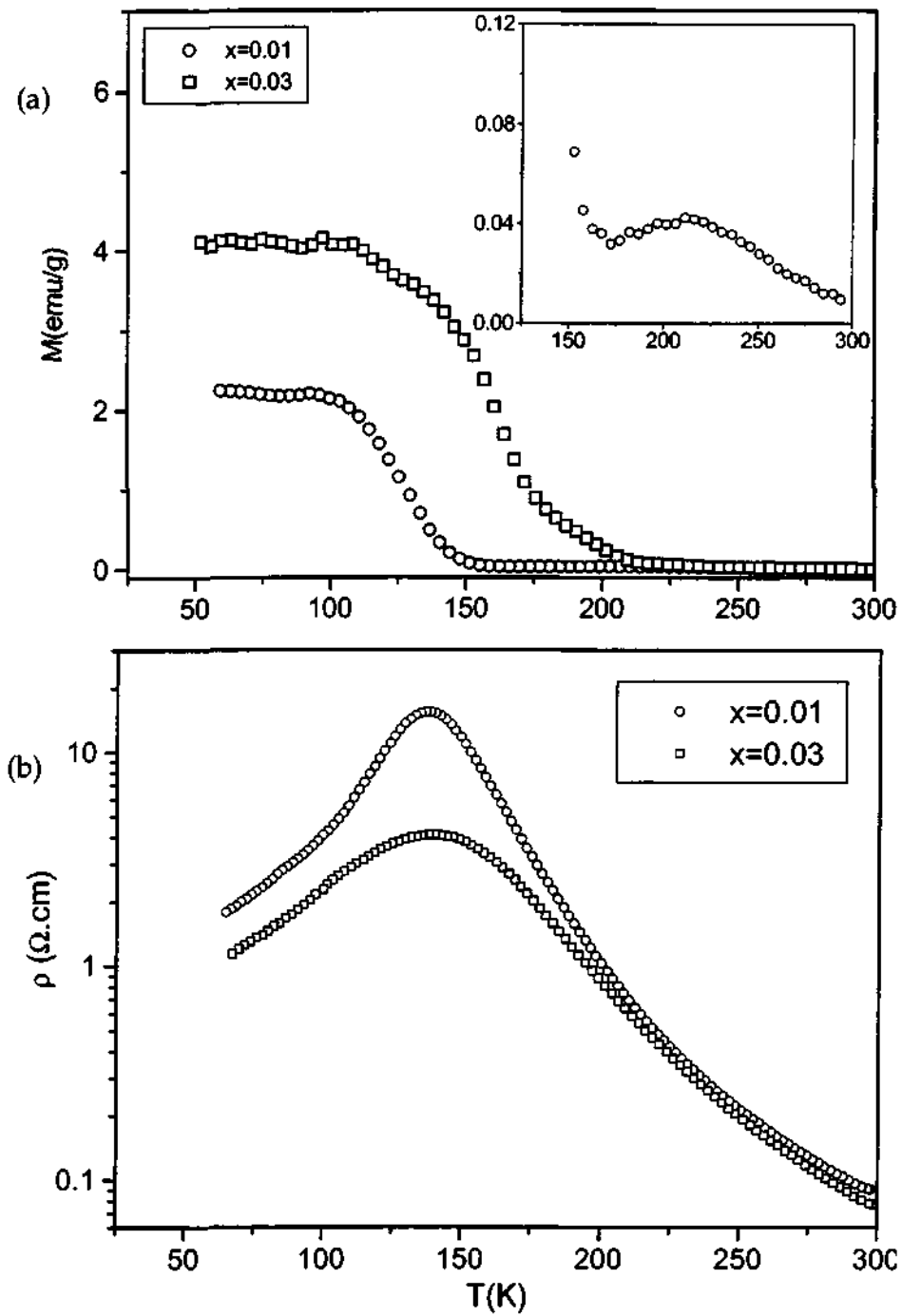


Fig. 1. 48. (a) Magnetization data and (b) resistivity data of $\text{Pr}_{0.5}\text{Ca}_{0.5}\text{Mn}_{1-x}\text{Ru}_x\text{O}_3$ ($x=0.01, 0.03$). Inset shows the magnetization data of $\text{Pr}_{0.5}\text{Ca}_{0.5}\text{Mn}_{0.99}\text{Ru}_{0.01}\text{O}_3$ on an enlarged scale exhibiting charge ordering.

ferromagnetic state with a $T_C = 135$ K. An I-M transition has been observed occurring at 139 K [72]. When the doping concentration is increased to 3%, the T_C has been found to shift to 157 K. Additionally, the I-M transition temperature has also been found to increase ($T_{IM} = 149$ K). Thus, the trends observed in $\text{Pr}_{0.5}\text{Ca}_{0.5}\text{MnO}_3$ are in tandem with $\text{Nd}_{0.5}\text{Ca}_{0.5}\text{MnO}_3$. In Table 1.6, we list the various properties seen as a result of Cr and Ru doping.

The effect of chromium and ruthenium substitution has also been investigated in the material $\text{Pr}_{0.5}\text{Sr}_{0.5}\text{MnO}_3$. The change of the alkaline A-site cation from Ca to Sr results in drastic changes as observed from the magnetization and resistivity behavior as shown in Fig. 1. 49a and 1. 49b. The magnetization data shows that the material develops ferromagnetism with a Curie temperature $T_C = 250$ K and then goes into an antiferromagnetic state with Néel temperature $T_N \sim 120$ K (A-type). The small feature at 250 K in the resistivity behavior corresponds to an I-M transition and at ~ 140 K it becomes an insulator again. In Fig. 1. 50a and 1. 50b we show the effect of 3% Cr and 3% Ru doping in the Mn-site of $\text{Pr}_{0.5}\text{Sr}_{0.5}\text{MnO}_3$ respectively. The antiferromagnetic state is completely destroyed in both the cases. In the case of Ru doping, the T_C shifts to a higher temperature i.e., occurring at ~ 275 K. The resistivity data shows that whereas the high temperature I-M transition is retained for both Cr and Ru doping, at lower temperatures, the material undergoes a transition into the metallic state. Interestingly, in the case of Ru-doped sample the high temperature

Table 1. 6 Various properties exhibited by $\text{Pr}_{0.5}\text{Ca}_{0.5}\text{Mn}_{1-x}\text{M}_x\text{O}_3$.

Compositions		T_{CO} (K)	T_{N} (K)	T_{C} (K)	T_{IM} (K)
	$x = 0.0$	230	150	-	-
$\text{M} = \text{Cr}^{3+}$	$x = 0.03$	-	-	130	130
$\text{M} = \text{Ru}^{4+}$	$x = 0.01$	215	-	150	140
	$x = 0.03$	-	-	215	145

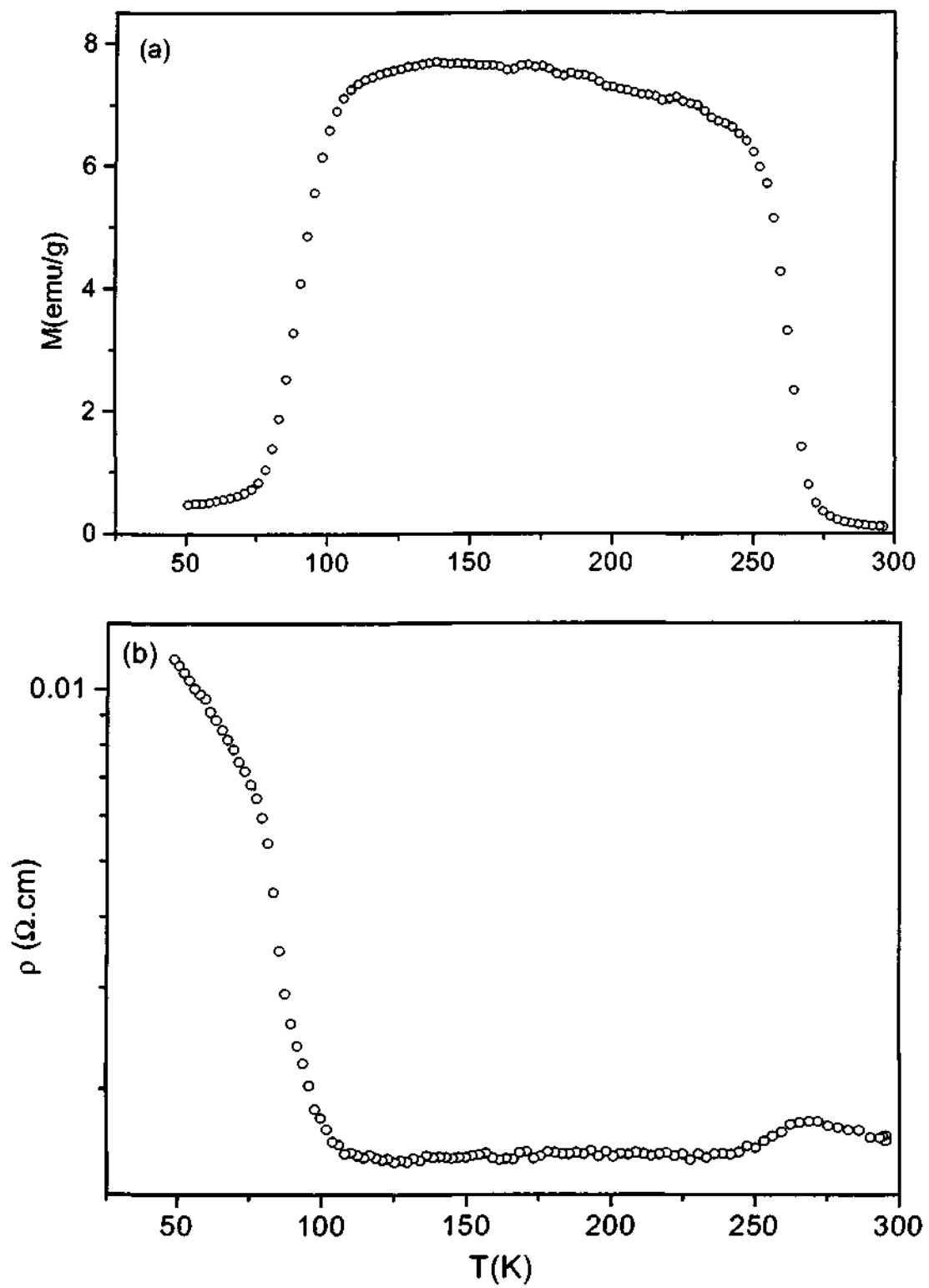


Fig. 1. 49. (a) Magnetization data and (b) resistivity data of $\text{Pr}_{0.5}\text{Sr}_{0.5}\text{MnO}_3$.

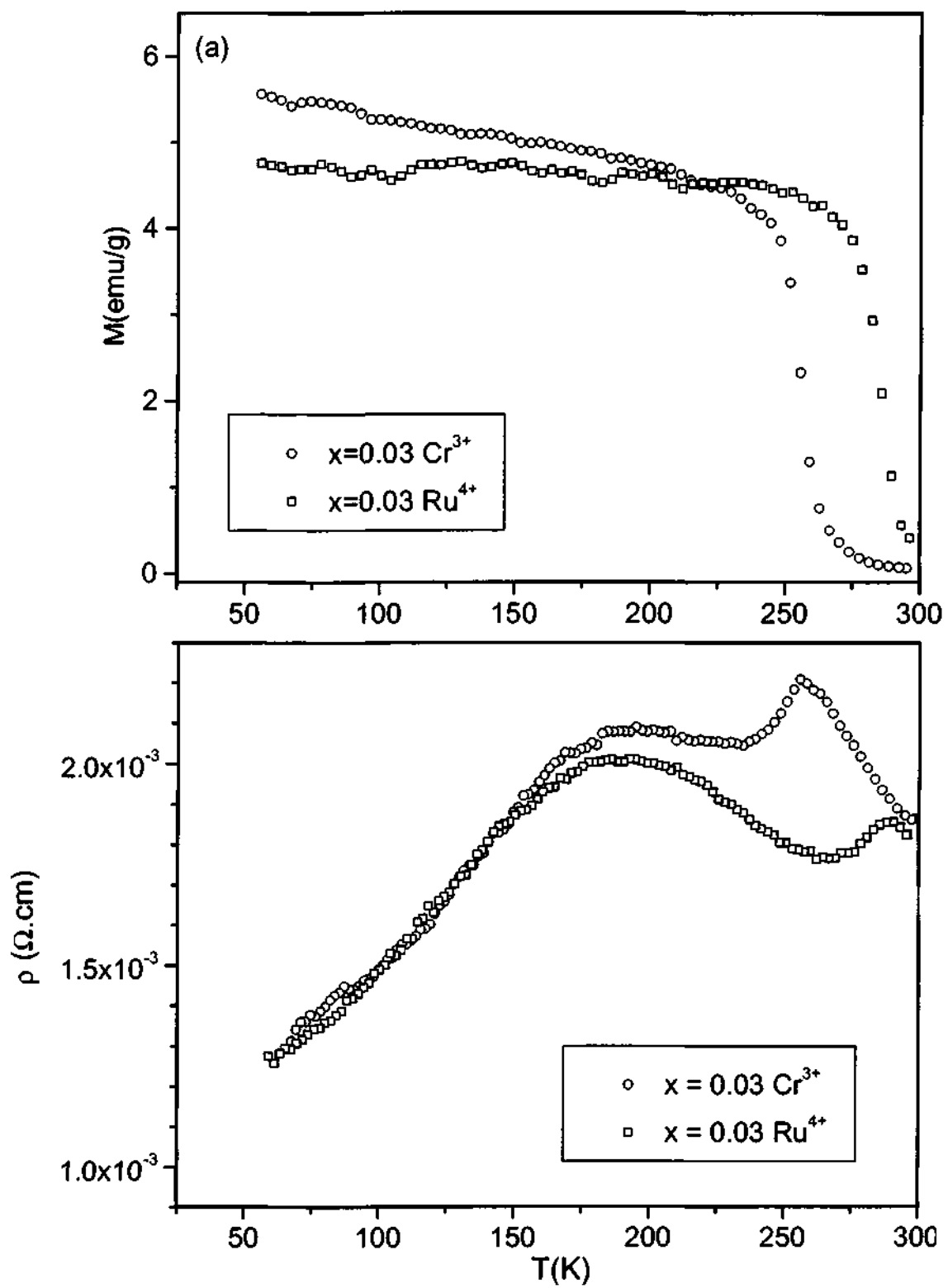


Fig. 1.50. (a) Magnetization data and (b) resistivity data of $\text{Pr}_{0.5}\text{Sr}_{0.5}\text{Mn}_{0.97}\text{M}_{0.03}\text{O}_3$

($M = \text{Cr}^{3+}, \text{Ru}^{4+}$).

I-M transition shifts, a behavior that needs to be further explored. We also find that before the onset of metallicity at ~ 100 K, the material exhibits a weak insulating state. Earlier studies on this material with chromium doping have been carried out where the concentration levels are too high ($> 10\%$) [67]. This leads to the strong possibility of clustering effects leading to percolation effects as seen in recent studies. The above results obtained can be compared with $\text{Nd}_{0.5}\text{Sr}_{0.5}\text{MnO}_3$. Studies of ruthenium doping on this material with CE-type spin ordering reveals that not only is the charge ordering ($T_{\text{CO}} = 147$ K) destroyed for 1% Ru^{4+} doping, but I-M transition is induced with $T_{\text{C}} = 274$ K as well. The shift in T_{C} observed in $\text{Pr}_{0.5}\text{Sr}_{0.5}\text{MnO}_3$ on increasing the Ru content is also paralleled where with doping concentration of 3%Ru, the T_{C} shifts to 283 K. It is surprising that irrespective of the nature of ordering present (A-or CE-type), the effect of doping is exactly the same. The results are summarized in Table 1.7.

The ability of the dopant ($\text{Cr}^{3+}/\text{Ru}^{4+}$) to drastically alter the electronic properties of the material under low concentrations can be understood in terms of its ability to perturb the ordering process. It has argued that the long range ordering of the orbitals are broken by the dopant ions. However, an aspect that needs to be addressed in this context is the possibility of phase-segregation. In the case of single crystals of $\text{Nd}_{0.5}\text{Ca}_{0.5}\text{MnO}_3$ doped with 3% Cr^{3+} , recent studies employing variable temperature neutron diffraction have revealed the presence

Table 1. 7 Various properties exhibited by $\text{Pr}_{0.5}\text{Sr}_{0.5}\text{Mm}_{1-x}\text{M}_x\text{O}_3$.

Compositions		T_N (K)	T_C (K)	T_{IM} (K)
x = 0.0		120	270	270
M = Cr^{3+}	x = 0.03	-	275	275
M = Ru^{4+}	x = 0.03		285	285

of ferromagnetic clusters that lie in an antiferromagnetic background, also referred to as relaxor-ferromagnets [82].

The effect of Cr^{3+} doping on $\text{Pr}_{1-x}\text{Ca}_x\text{MnO}_3$ has been investigated in the composition region $0.6 \leq x \leq 0.7$, the Cr^{3+} content going till 12% [43]. These workers find a marked effect when Cr^{3+} is around 10%, at which composition one would expect clustering of the dopant ions leading to superexchange-induced ferromagnetism. We have substituted Mn by Cr^{3+} or Ru^{4+} keeping the dopant concentration at 3% to avoid clustering. On doping with 3% Cr^{3+} , $\text{Pr}_{0.64}\text{Ca}_{0.36}\text{MnO}_3$ becomes ferromagnetic with a T_C of 130 K, but $\text{Pr}_{0.36}\text{Ca}_{0.64}\text{MnO}_3$ remains paramagnetic and charge-ordered, albeit with a slightly lower T_{CO} (215 K) as shown in Fig. 1. 51. 3% Ru doping shows similar differences between the two manganates (Fig. 1. 52).

In Fig. 1. 53, we show the effect of 3% Cr^{3+} doping on the resistivity of $\text{Pr}_{0.64}\text{Ca}_{0.36}\text{MnO}_3$ and $\text{Pr}_{0.36}\text{Ca}_{0.64}\text{MnO}_3$. The former exhibits an insulator-metal (I-M) type transition around 80 K, but the latter remains an insulator. The I-M transition in the hole-doped system is shifted to higher temperatures on applying magnetic fields. Application of magnetic fields does not render the Cr^{3+} doped $\text{Pr}_{0.36}\text{Ca}_{0.64}\text{MnO}_3$ metallic (Fig. 1. 53) at any temperature, indicating that it may not be possible to induce the FMM state in this electron-doped material even under favorable conditions. Results with 3% Ru^{4+} doping in the two manganates

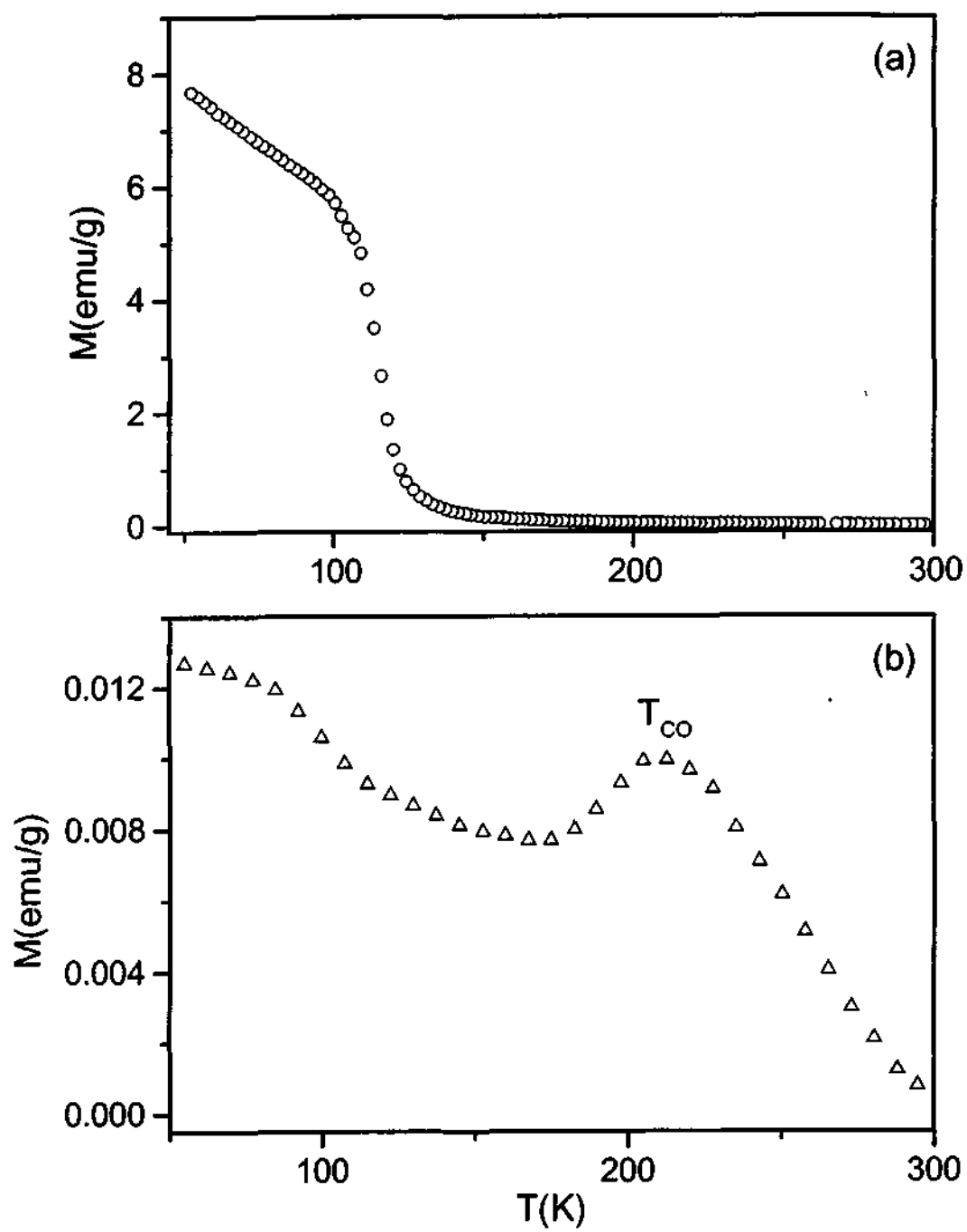


Fig. 1. 51. Effect of 3% Cr^{3+} on the magnetization of (a) $\text{Pr}_{0.64}\text{Ca}_{0.36}\text{MnO}_3$ and (b)

$\text{Pr}_{0.36}\text{Ca}_{0.64}\text{MnO}_3$.

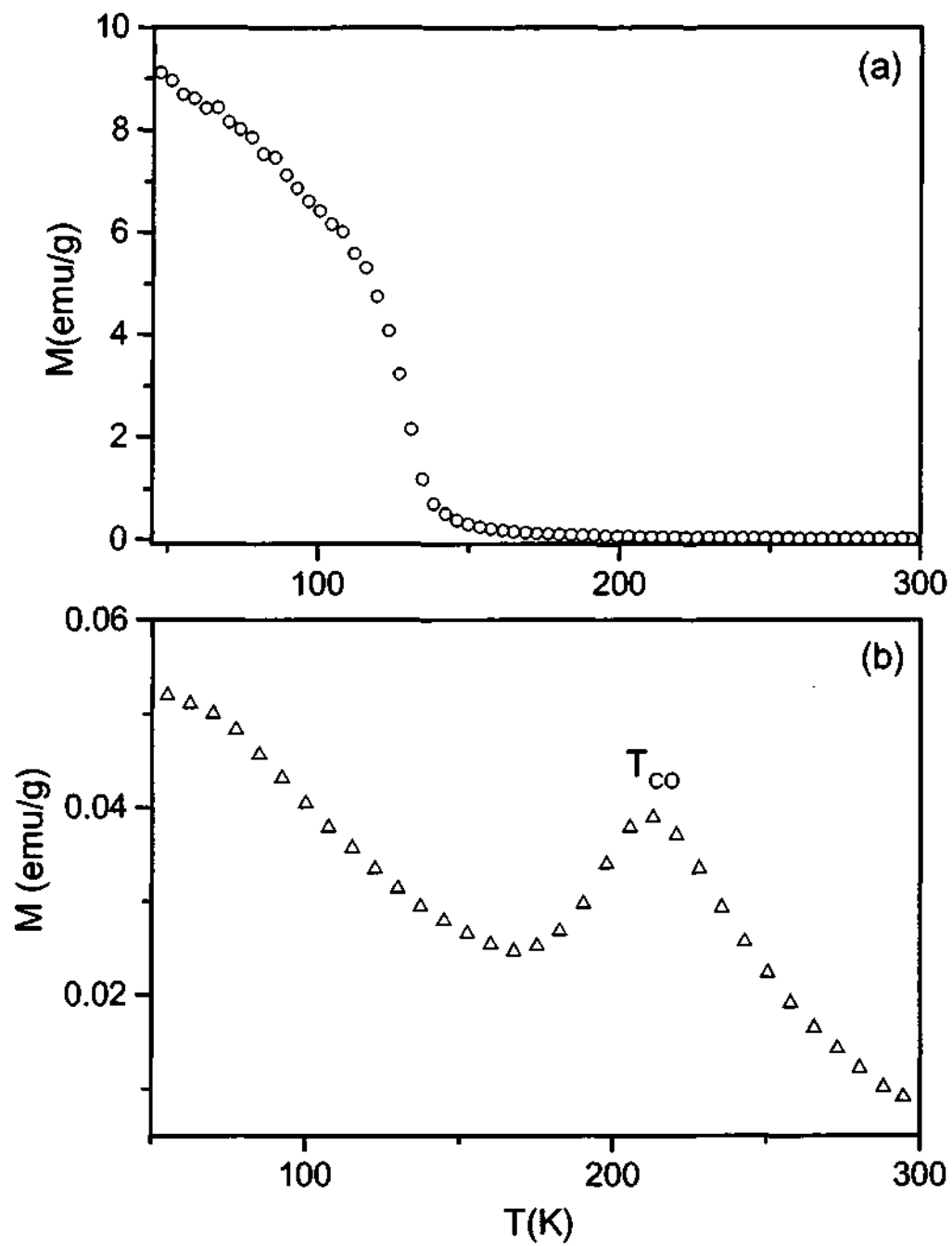


Fig. 1. 52. Effect of 3% Ru^{4+} on the magnetization of (a) $\text{Pr}_{0.64}\text{Ca}_{0.36}\text{MnO}_3$ and (b) $\text{Pr}_{0.36}\text{Ca}_{0.64}\text{MnO}_3$.

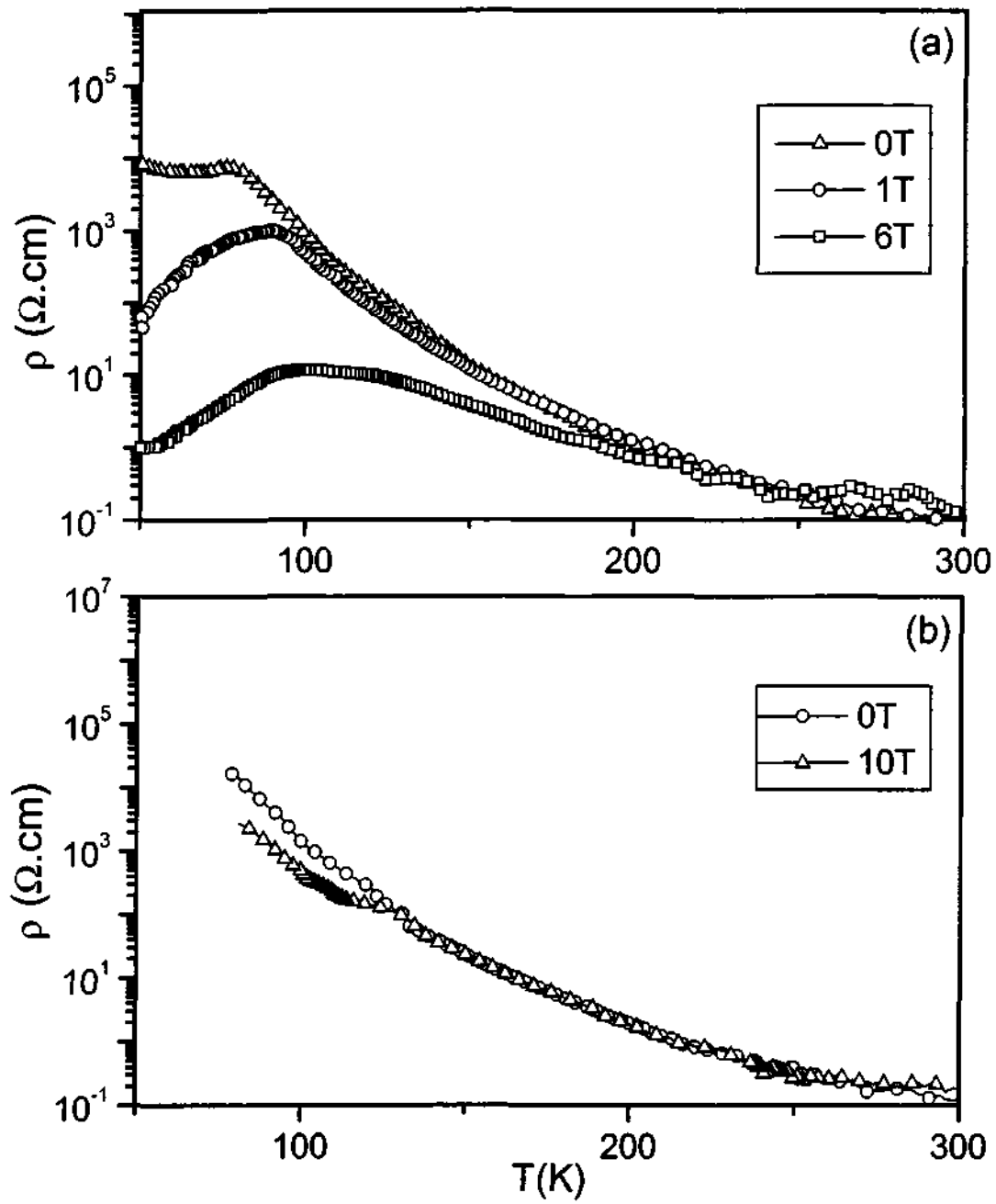


Fig. 1. 53. Effect of 3% Cr^{3+} doping on the electrical resistivity of (a) $\text{Pr}_{0.64}\text{Ca}_{0.36}\text{MnO}_3$ and (b) $\text{Pr}_{0.36}\text{Ca}_{0.64}\text{MnO}_3$ under different magnetic fields.

are similar, in that the hole-doped material becomes FMM while the CO state in the electron-doped material is essentially unaffected. In Fig. 1. 54, we show the results obtained with 3% Ru⁴⁺ doped Pr_{0.64}Ca_{0.36}MnO₃ and Pr_{0.36}Ca_{0.64}MnO₃. The effect of Cr³⁺ and Ru⁴⁺ on hole-doped Pr_{0.64}Ca_{0.36}MnO₃ is similar. However, the failure to destroy the CO state of Pr_{0.36}Ca_{0.64}MnO₃ with Cr/Ru doping as well as with a magnetic field of 12T is noteworthy. Raveau *et al* [73] have recently observed that Ru substitution in Ln_{0.4}Ca_{0.6}MnO₃ gives rise to FMM clusters, but the effect is prominent at high Ru concentrations (> 3%). The observed effect is probably due to clusters or domains containing Ru ions, as suspected by these authors. Furthermore, the observed magnetization in these samples is low. This raises the question as to whether long-range ferromagnetism can ever occur in the electron-doped manganates. We note here that Maignan *et al* [118] find a cluster glass state (but no long-range ferromagnetism) in Ca_{1-x}Sm_xMnO₃ (0 ≤ x ≤ 0.12). Neumeier and Cohn [119] observe only local ferromagnetic regions within an antiferromagnetic host in Ca_{1-x}La_xMnO₃ (0 ≤ x ≤ 0.2), as indeed observed earlier by Mahendiran *et al* [120].

Absence of long-range ferromagnetism in electron-doped manganates

In order to answer the above question, it is important to ensure that the Mn-O-Mn angle is not a limiting factor. This is because the Mn-O-Mn angles in Pr_{1-x}Ca_xMnO₃ is generally in the 156-162° range (Table 1.4 and Table 1.5), which may be considered to be somewhat small. For ferromagnetism to be favored in

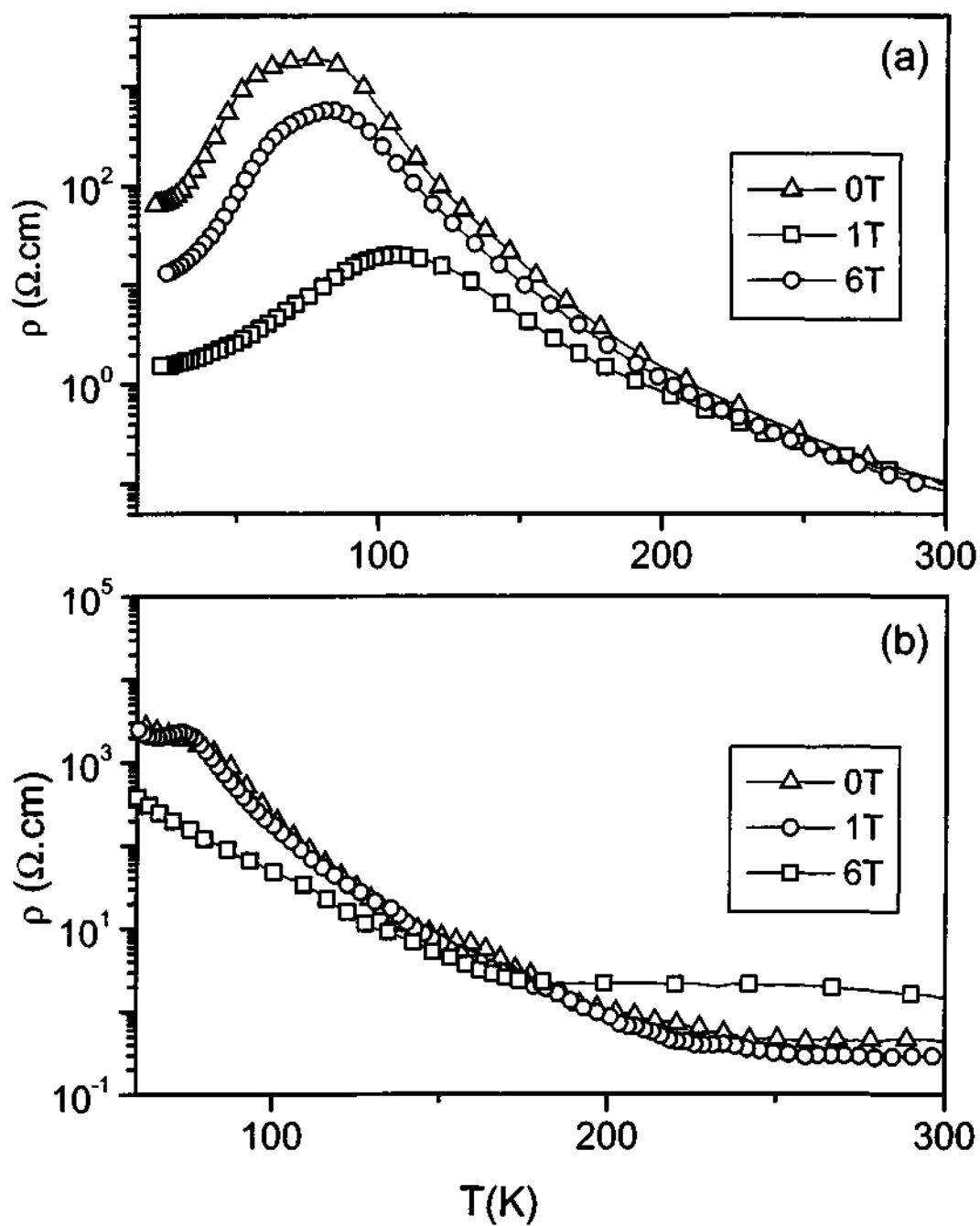


Fig. 1. 54. Effect of 3% Ru^{4+} doping on the electrical resistivity of (a) $\text{Pr}_{0.64}\text{Ca}_{0.36}\text{MnO}_3$ and (b) $\text{Pr}_{0.36}\text{Ca}_{0.64}\text{MnO}_3$ under different magnetic fields.

the electron-doped manganates, it is important to have a material with a much larger Mn-O-Mn angle. To decide on the composition of such a material, the following considerations are relevant. The Mn-O-Mn angle in CaMnO_3 and $\text{La}_{0.5}\text{Ca}_{0.5}\text{MnO}_3$ are around 158° and 160° respectively [121-123]. Therefore, substitution of Ca by any of the rare earths would not increase the Mn-O-Mn angle beyond 160° . It is however, possible to increase the angle by Sr substitution, as in $\text{Ca}_{1-x}\text{Sr}_x\text{MnO}_3$ and $\text{La}_{0.5}\text{Ca}_{0.5-x}\text{Sr}_x\text{MnO}_3$ [124,125]. We therefore prepared a manganate of the composition $\text{La}_{0.33}\text{Ca}_{0.33}\text{Sr}_{0.34}\text{MnO}_3$. The structure of the manganate is tetragonal ($I4/mcm$). In Fig. 1. 55, we show the observed, calculated and difference plots based on the Rietveld analysis of the powder data of $\text{La}_{0.33}\text{Ca}_{0.33}\text{Sr}_{0.34}\text{MnO}_3$. The atomic co-ordinates and structural parameters are listed in Table 1.8. The two Mn-O-Mn distances are around 1.91 and 1.95 Å, while the angles are 166.4° and 180° . These values of the angles are comparable to those found in some of the ferromagnetic and metallic compositions of the hole-doped manganates. Based on the above atomic coordinates, we have depicted the crystal structure in Fig. 1. 56.

In Fig. 1. 57, we show the magnetization and electrical resistivity data of $\text{La}_{0.33}\text{Ca}_{0.33}\text{Sr}_{0.34}\text{MnO}_3$. The material is a paramagnetic insulator down to 25 K, with a charge-ordering transition around 220 K. Application of magnetic fields till 12T has no effect on the electrical resistivity (Fig. 1. 57b). Clearly, the large Mn-O-Mn angles do not help to make this manganate ferromagnetic.

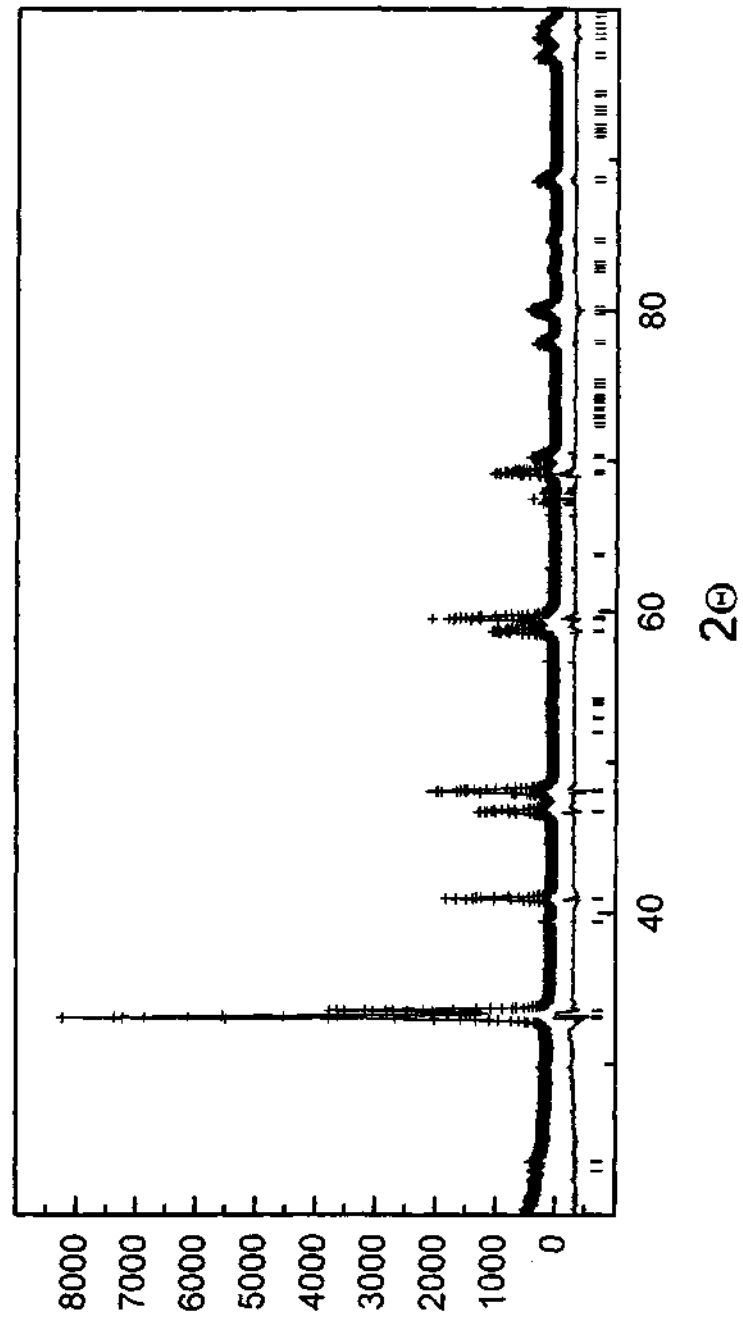


Fig. 1. 55. Observed, calculated and difference plots of the x-ray powder diffraction data of $\text{La}_{0.33}\text{Ca}_{0.33}\text{Sr}_{0.34}\text{MnO}_3$.

Table 1. 8 Atomic coordinates and structural parameters of $\text{La}_{0.33}\text{Ca}_{0.34}\text{Sr}_{0.34}\text{MnO}_3$

Atom	Site	x	Y	z	Frac	U_{iso}
La	4b	0.0000	0.5000	0.2500	0.3300	-0.0134
Ca	4b	0.0000	0.5000	0.2500	0.3300	0.0245
Sr	4b	0.0000	0.5000	0.2500	0.3400	0.0212
Mn	4c	0.0000	0.0000	0.0000	1.0000	0.0007
O	4a	0.0000	0.0000	0.2500	1.0000	0.0051
O	8h	0.2799	0.7799	0.0000	1.0000	0.0051

bond	distance (Å)
Mn – O	2 x 1.909
	2 x 1.949

bond	angle (deg)
Mn – O – Mn	4 x 166.4
	2 x 180.0

$a = 5.3608 \text{ \AA}$, $b_c = 7.7857 \text{ \AA}$; Sp. gp : $I4/mcm$, $R_{\text{wp}} = 11.82\%$.

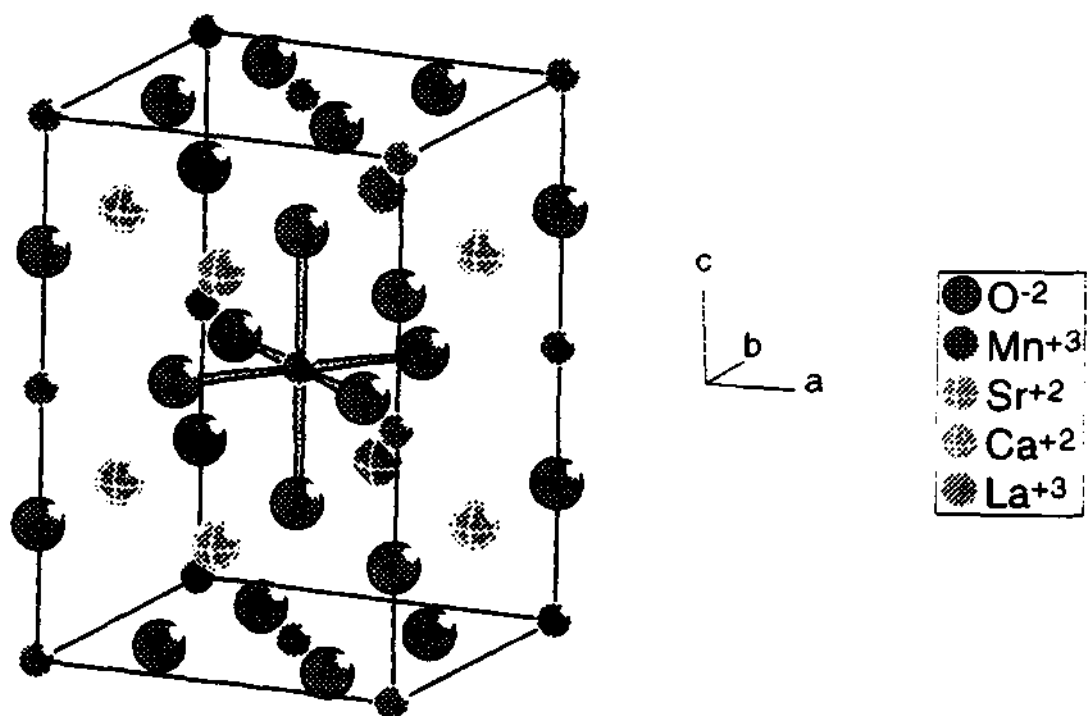
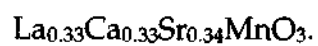


Fig. 1. 56. Schematic showing the tetragonal space group $I4/mcm$ as adopted by



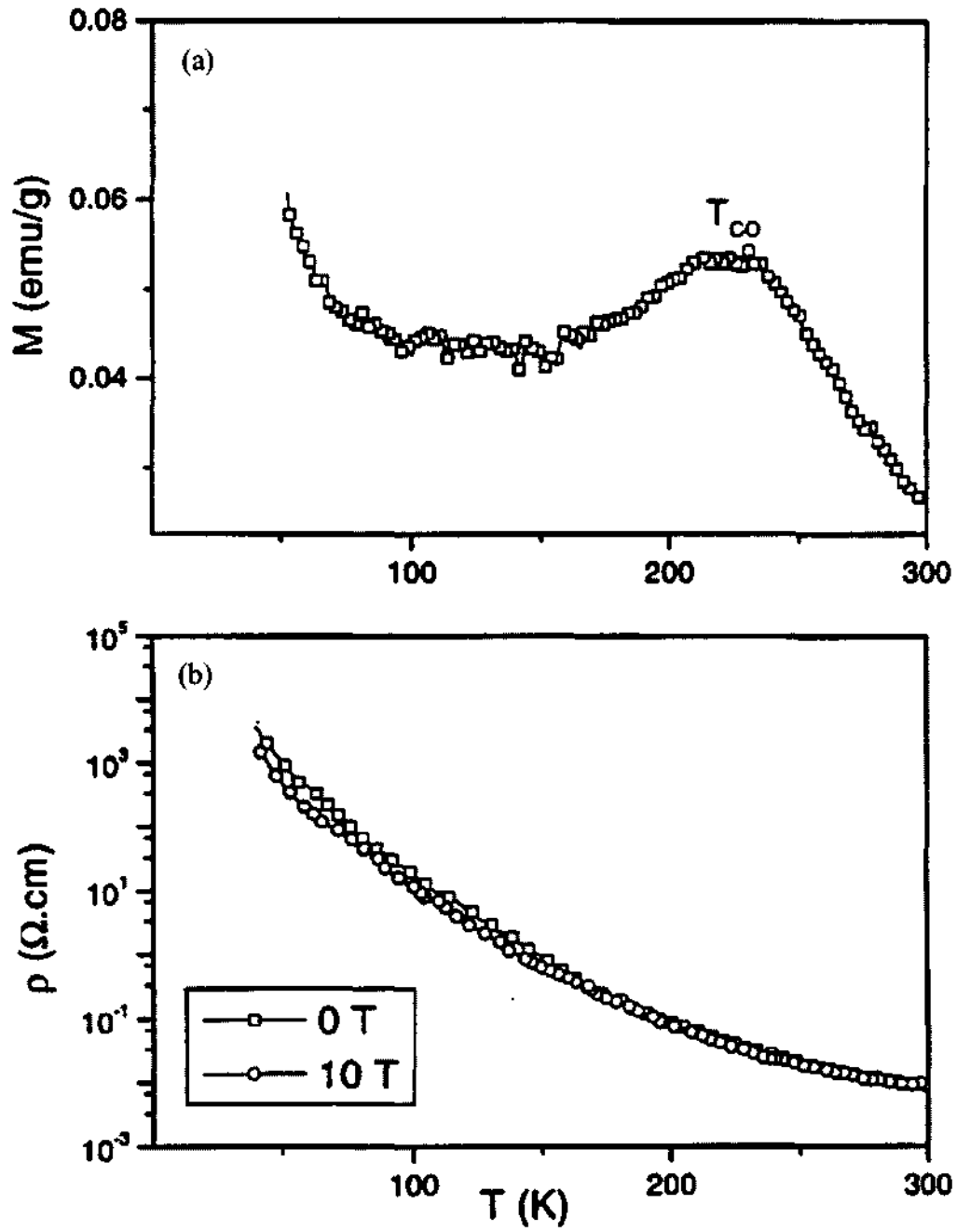


Fig. 1. 57. (a) Magnetization and (b) resistivity data of $\text{La}_{0.33}\text{Ca}_{0.33}\text{Sr}_{0.34}\text{MnO}_3$.

Effect of magnetic fields on the resistivity is also shown.

Furthermore, 3% Cr³⁺ doping of La_{0.33}Ca_{0.33}Sr_{0.34}MnO₃ does not transform it to a ferromagnetic metal (Fig. 1. 58). What is surprising is that the application of magnetic fields till 10T does not induce an I-M transition in the Cr-doped material as shown in Fig. 1. 58. The same holds for the 3% Ru⁴⁺ doped material and is shown in Fig. 1. 59. It must be remembered that the analogous hole-doped composition La_{0.67}A_{0.33}MnO₃ (A = Ca/Sr) becomes a ferromagnetic metal at fairly high temperatures (230-300 K) [1,2]. These results suggest that it may not be possible to make the electron-doped rare earth manganates exhibit long-range ferromagnetism and metallicity. As observed earlier, other studies also show at best local ferromagnetic interactions or presence of FM clusters [73,118-120].

The absence of long-range ferromagnetism and metallicity in the electron-doped manganates is difficult to comprehend. One difference that is noteworthy is that the hole-doped manganates possess a higher proportion of e_g electrons relative to the degenerate e_g orbitals. There are also some intrinsic differences between the Mn³⁺ (d⁴) and the Mn⁴⁺ (d³) ions. Although the structure of the parent LnMnO₃ compounds is influenced by the Jahn-Teller distorted Mn³⁺, the stability of this state is not sufficient to inhibit the electron transfer process when Mn⁴⁺ ions are introduced. The facile electron transfer required for double-exchange, and hence ferromagnetism, can be sustained in such a hole-doped system. By contrast, the high ligand-field stabilization of the preponderant Mn⁴⁺ ions in the electron-doped materials can inhibit electron transfer. In order to

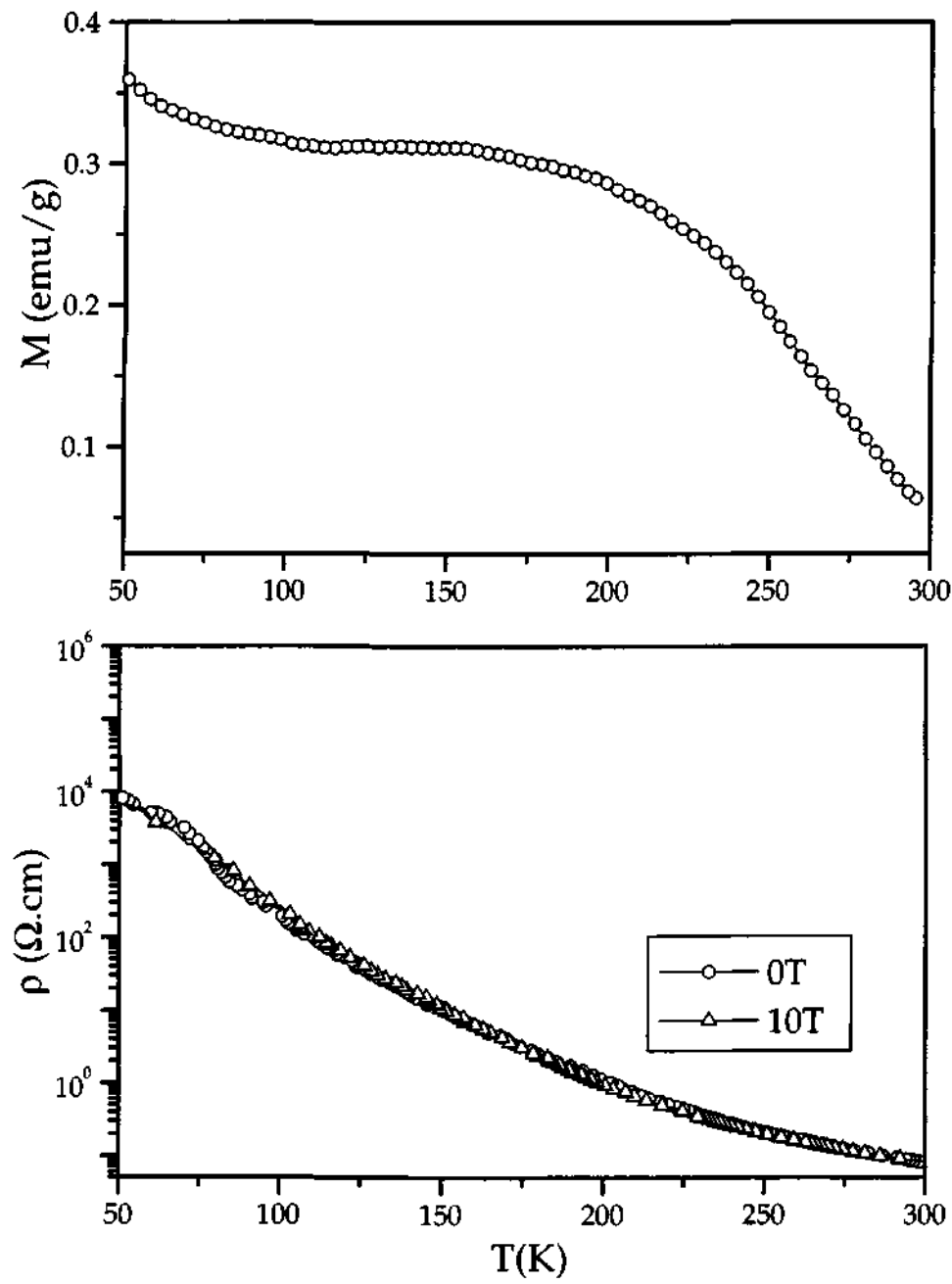


Fig. 1. 58. Effect of 3% Cr^{3+} doping on (a) the magnetization and (b) the resistivity of $\text{La}_{0.33}\text{Ca}_{0.33}\text{Sr}_{0.34}\text{MnO}_3$. Effect of magnetic fields on the resistivity is also shown.

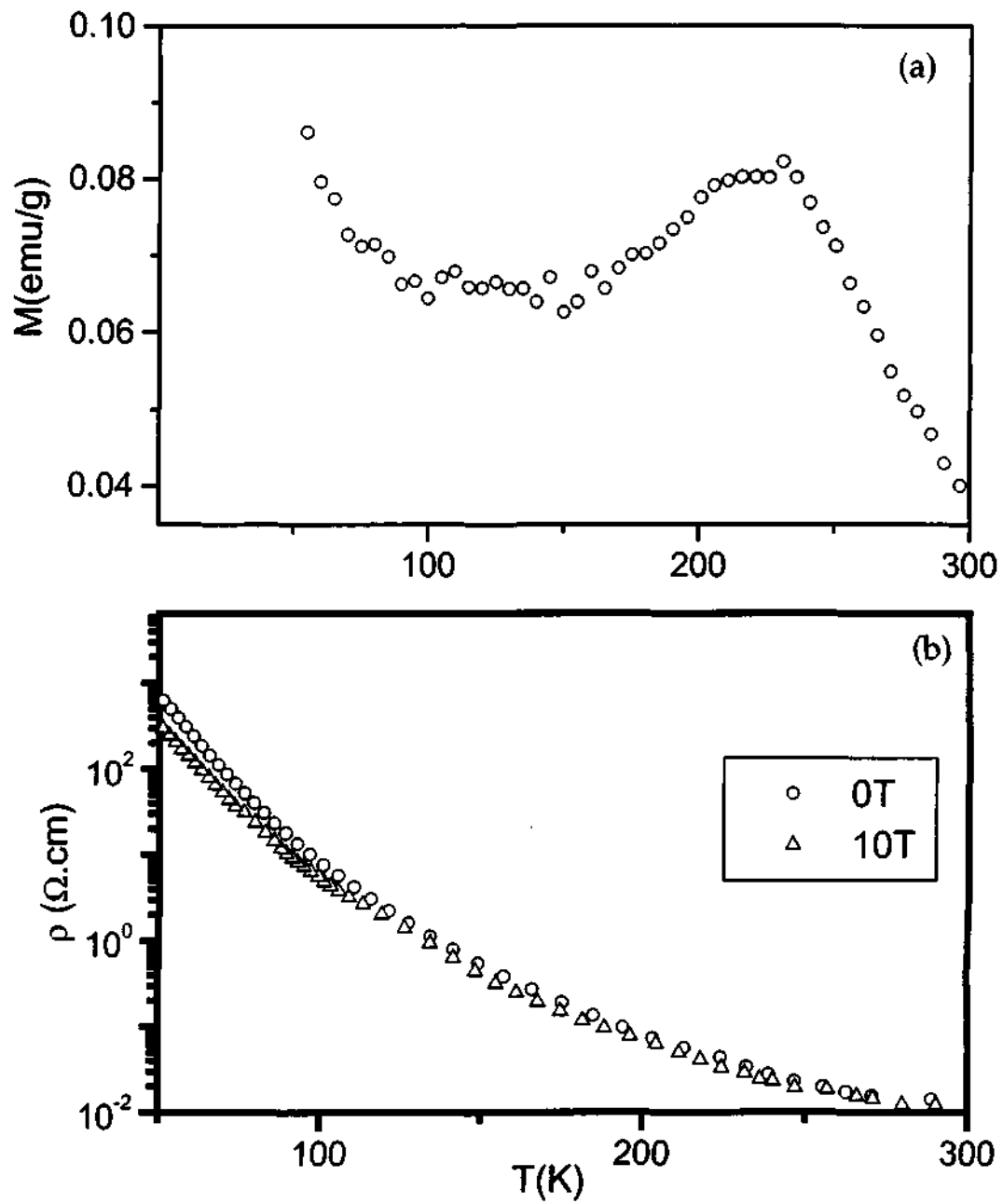


Fig. 1. 59. Effect of 3% Ru⁴⁺ doping on (a) the magnetization and (b) the resistivity of La_{0.33}Ca_{0.33}Sr_{0.34}MnO₃. Effect of magnetic fields on the resistivity is also shown

unravel the cause(s) for the absence of metallicity in the electron-doped manganates, we have carried out some electronic structure calculations, which will be discussed later.

Preliminary EPR investigations of $\text{Pr}_{0.6}\text{Ca}_{0.4}\text{MnO}_3$ and $\text{Pr}_{0.4}\text{Ca}_{0.6}\text{MnO}_3$

Electron paramagnetic resonance studies of single crystals of $\text{Pr}_{0.6}\text{Ca}_{0.4}\text{MnO}_3$ and $\text{Pr}_{0.4}\text{Ca}_{0.6}\text{MnO}_3$ have been carried out. In Fig. 1. 60a and 1.60b, we show the derivative spectra for the two crystals of $\text{Pr}_{0.6}\text{Ca}_{0.4}\text{MnO}_3$ and $\text{Pr}_{0.4}\text{Ca}_{0.6}\text{MnO}_3$ respectively as a function of temperature. The g -value obtained in the hole doped composition was found to be greater than the free electron value and increases till T_{CO} where it dips and then rises steadily [115]. However in electron-doped composition, the g -value is similar to that of free electron. A detailed study of the spectra is now in progress.

1.4.2 Thin films of $\text{Pr}_{0.6}\text{Ca}_{0.4}\text{MnO}_3$ and $\text{Pr}_{0.4}\text{Ca}_{0.6}\text{MnO}_3$

The films of $\text{Pr}_{0.6}\text{Ca}_{0.4}\text{MnO}_3$ and $\text{Pr}_{0.4}\text{Ca}_{0.6}\text{MnO}_3$ deposited on Si(100) were polycrystalline in nature while those deposited on LAO(100) were oriented along the (100) direction as determined by x-ray diffraction. The compositions obtained from the EDAX spectra were generally close to the expected calculated compositions.

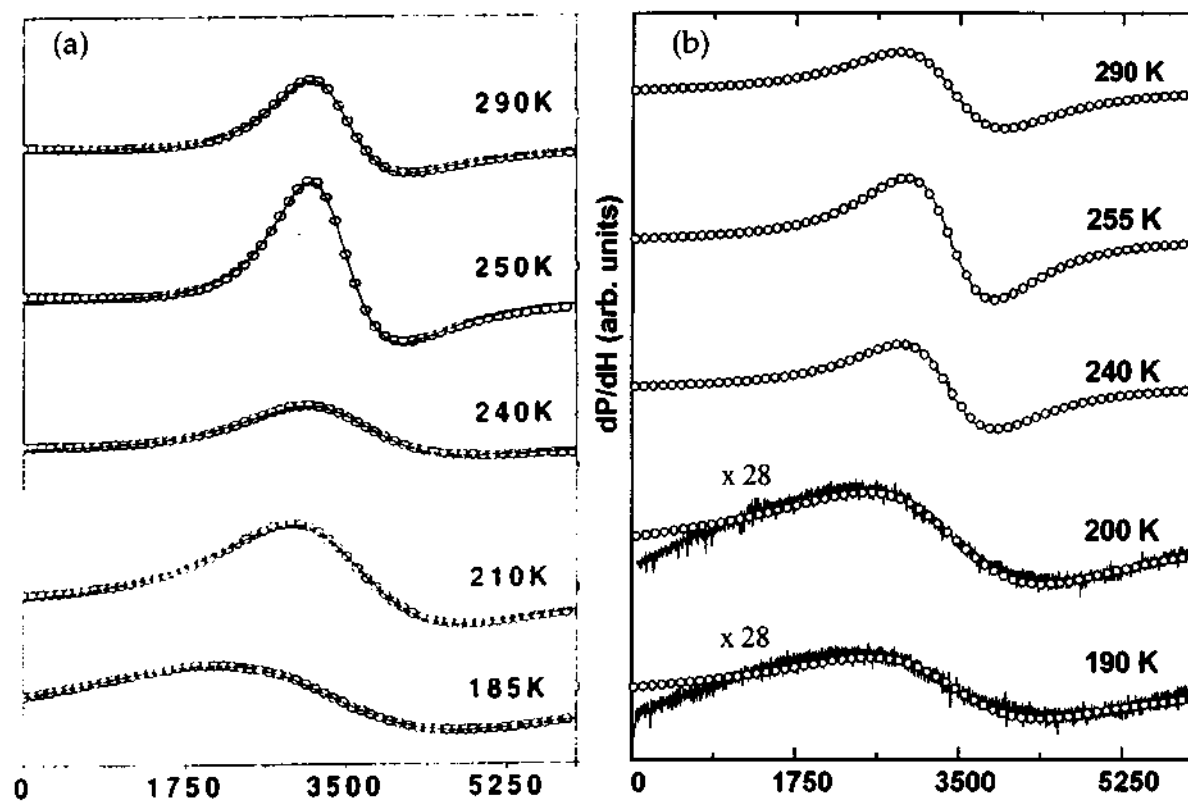


Fig. 1. 60. Derivative spectra of the EPR signal of (a) $\text{Pr}_{0.6}\text{Ca}_{0.4}\text{MnO}_3$ and (b) $\text{Pr}_{0.4}\text{Ca}_{0.6}\text{MnO}_3$ as a function of temperature. The solid lines are the fits to the signal obtained.

In Fig. 1. 61a, we show the temperature-variation of electrical resistance of a $\text{Pr}_{0.6}\text{Ca}_{0.4}\text{MnO}_3$ film deposited on LAO at different magnetic fields. It is insulating down to the lowest temperature in the absence of a magnetic field, but on the application of a magnetic field of 5T, there is an insulator-metal (I-M) transition. The I-M transition temperature increases from 175 K at 5T to 235 K at 10T. Magnetoresistance (MR) is ~98 % and 46 % respectively at 150 K and 200 K at 5T. This behavior is similar to that reported in literature for a single crystal of this material [40,126]. In contrast to the films of $\text{Pr}_{0.6}\text{Ca}_{0.4}\text{MnO}_3$, those of the electron-doped $\text{Pr}_{0.4}\text{Ca}_{0.6}\text{MnO}_3$ deposited on LAO show insulating behavior down to the lowest temperature, even on the application of magnetic fields, as can be seen from Fig. 1. 61b. The magnitude of MR is also low and reaches only 19% at 5T at 150 K.

In Fig. 1. 62a and 1. 62b, we show the effect of electric currents on the resistance of polycrystalline films of $\text{Pr}_{0.6}\text{Ca}_{0.4}\text{MnO}_3$ and $\text{Pr}_{0.4}\text{Ca}_{0.6}\text{MnO}_3$ respectively, deposited on Si(100) substrates. In the case of $\text{Pr}_{0.6}\text{Ca}_{0.4}\text{MnO}_3$, we clearly observe melting to a metallic state even with a modest current of 10 μA . The temperature of the I-M transition increases with the increasing current. The effect of electric fields on these films of the electron-doped manganate, $\text{Pr}_{0.4}\text{Ca}_{0.6}\text{MnO}_3$, is comparable to that found with those of hole-doped $\text{Pr}_{0.6}\text{Ca}_{0.4}\text{MnO}_3$. However, the resistance of the films of the electron-doped composition is slightly higher than that of the hole-doped composition.

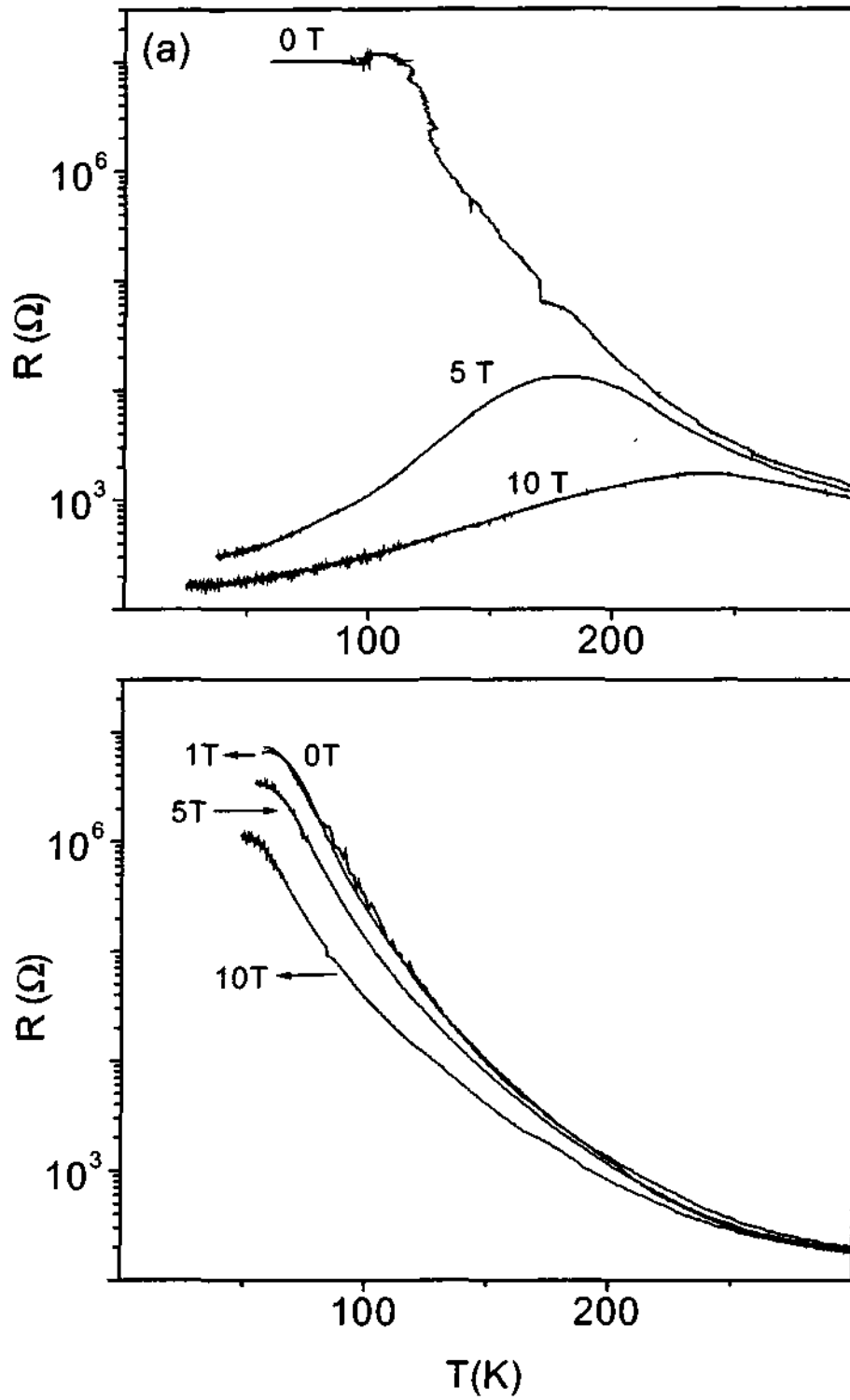


Fig. 1. 61. Temperature-variation of the electrical resistance of the thin films of (a) $\text{Pr}_{0.6}\text{Ca}_{0.4}\text{MnO}_3$ and (b) $\text{Pr}_{0.4}\text{Ca}_{0.6}\text{MnO}_3$ deposited on LAO(100) substrates at different magnetic fields.

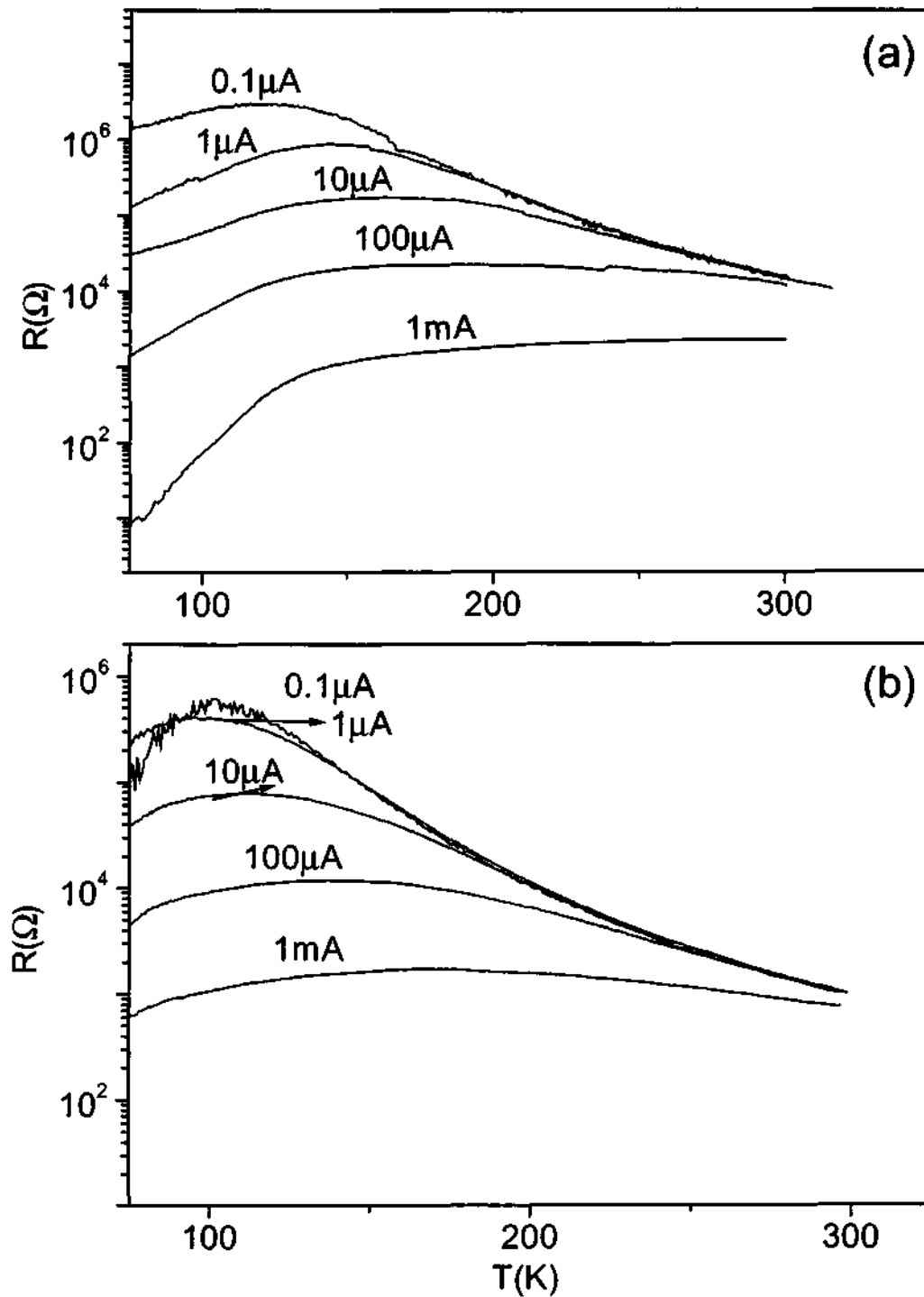


Fig. 1. 62. Temperature-variation of the electrical resistance of the thin films of (a) $\text{Pr}_{0.6}\text{Ca}_{0.4}\text{MnO}_3$ and (b) $\text{Pr}_{0.4}\text{Ca}_{0.6}\text{MnO}_3$ deposited on Si(100) for different values of the current.

Furthermore, the I-M transition is not as distinctive in the electron-doped sample as in the case of the hole-doped sample. In Fig. 1. 63a and 1. 63b, we show the temperature-variation of resistance of the films of $\text{Pr}_{0.6}\text{Ca}_{0.4}\text{MnO}_3$ and $\text{Pr}_{0.4}\text{Ca}_{0.6}\text{MnO}_3$ respectively, deposited on LAO(100) substrates. Although these films do not exhibit a distinct I-M transition with increasing current, they show a marked decrease in the resistance with increase in current. The electric-field induced I-M transitions and the marked decrease in the resistance with increasing current in these films can be understood in terms of the depinning of the charge-ordered state brought about by electric-fields [83].

When a charge-ordered manganate such as $\text{Nd}_{0.5}\text{Ca}_{0.5}\text{MnO}_3$ is doped with 3% Ru^{4+} , it becomes ferromagnetic and undergoes an I-M transition [72]. In Fig. 1. 64a and 1. 64b, we show the temperature-variation of the electrical resistance of the films of 3% Cr^{3+} doped $\text{Pr}_{0.6}\text{Ca}_{0.4}\text{MnO}_3$ and $\text{Pr}_{0.4}\text{Ca}_{0.6}\text{MnO}_3$ respectively, in comparison with the data for the undoped parent compositions. Although 3% Cr^{3+} doping does not render either of the materials metallic, there is a marked decrease in resistance in the case of the hole-doped sample. This observation is also verified in the case of 3% Ru^{4+} doped $\text{Pr}_{0.6}\text{Ca}_{0.4}\text{MnO}_3$ and $\text{Pr}_{0.4}\text{Ca}_{0.6}\text{MnO}_3$ films, as can be seen from the insets in Fig. 1. 64a and 1. 64b.

In Fig. 1. 65a and 1. 65b, we show the temperature-variation of electrical resistance in the absence and presence of a magnetic field of 5T for the thin films

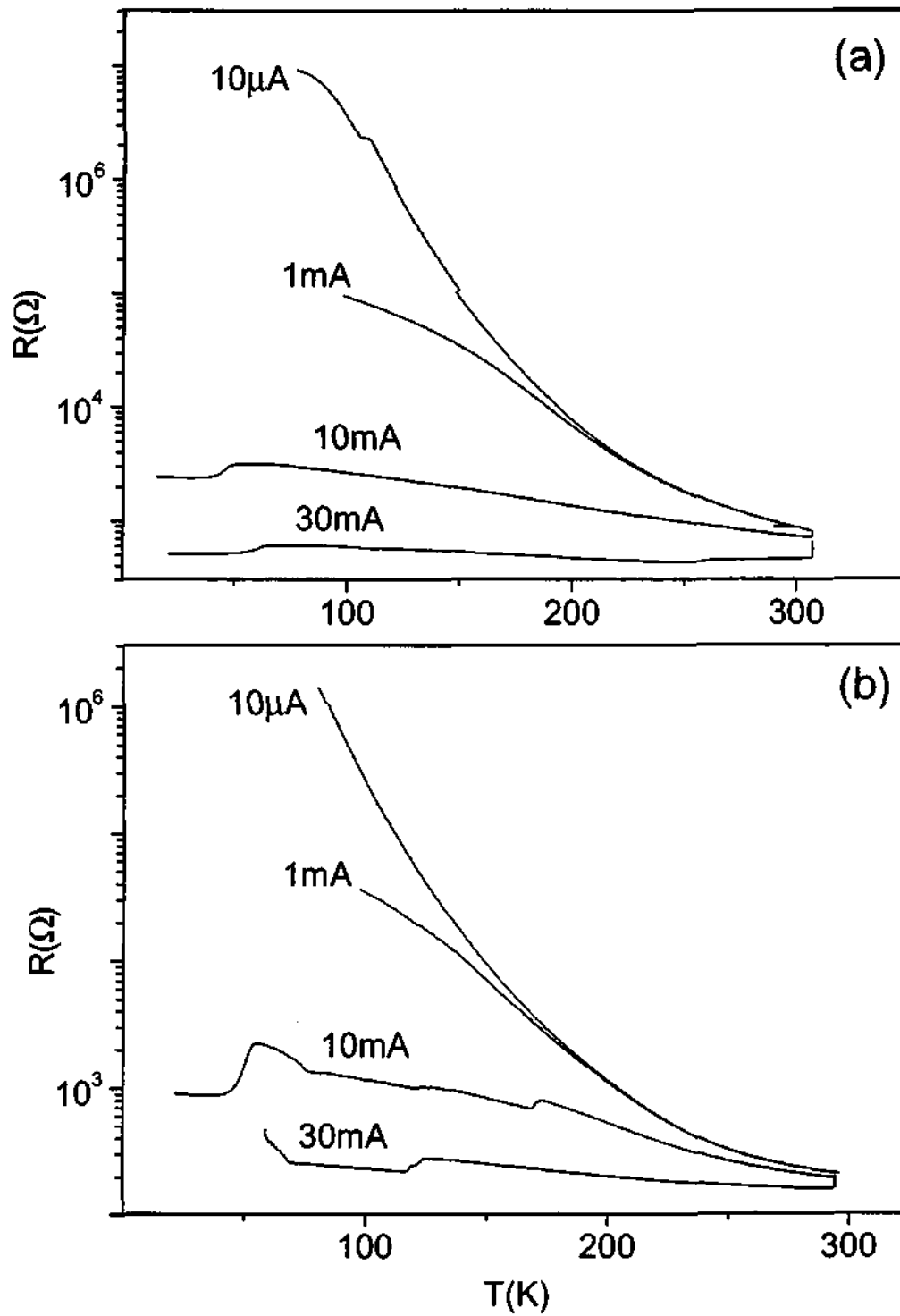


Fig. 1. 63. Temperature-variation of the electrical resistance of the thin films of (a) $Pr_{0.6}Ca_{0.4}MnO_3$ and (b) $Pr_{0.4}Ca_{0.6}MnO_3$ deposited on LAO(100) for different values of the current.

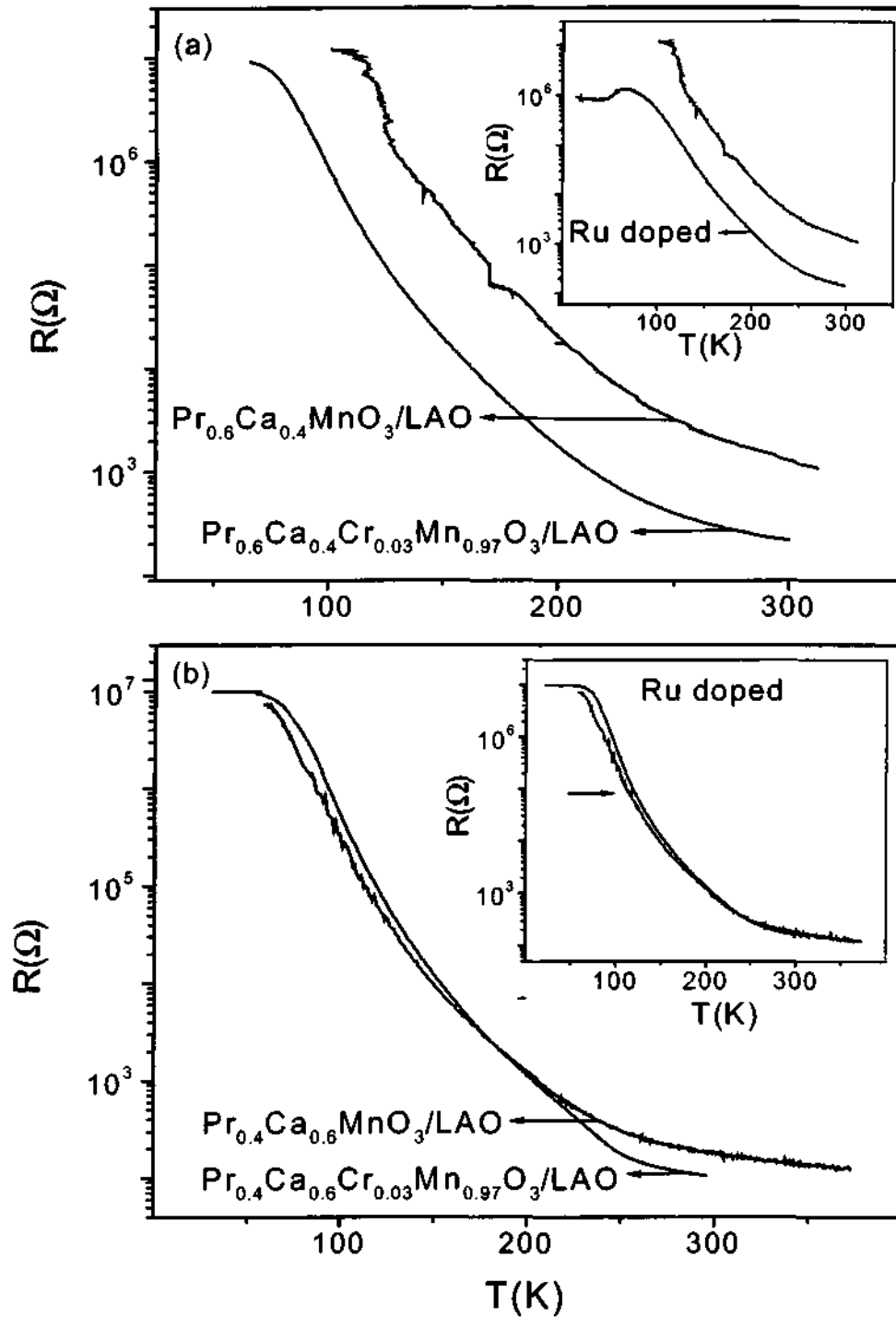


Fig. 1. 64. Temperature-variation of the electrical resistance of the thin films of (a) $\text{Pr}_{0.6}\text{Ca}_{0.4}\text{MnO}_3$ and $\text{Pr}_{0.6}\text{Ca}_{0.4}\text{Cr}_{0.03}\text{Mn}_{0.97}\text{O}_3$, and (b) $\text{Pr}_{0.4}\text{Ca}_{0.6}\text{MnO}_3$ and $\text{Pr}_{0.4}\text{Ca}_{0.6}\text{Cr}_{0.03}\text{Mn}_{0.97}\text{O}_3$ deposited on LAO(100) substrates. Insets show similar effects for the pure and 3% Ru^{4+} samples.

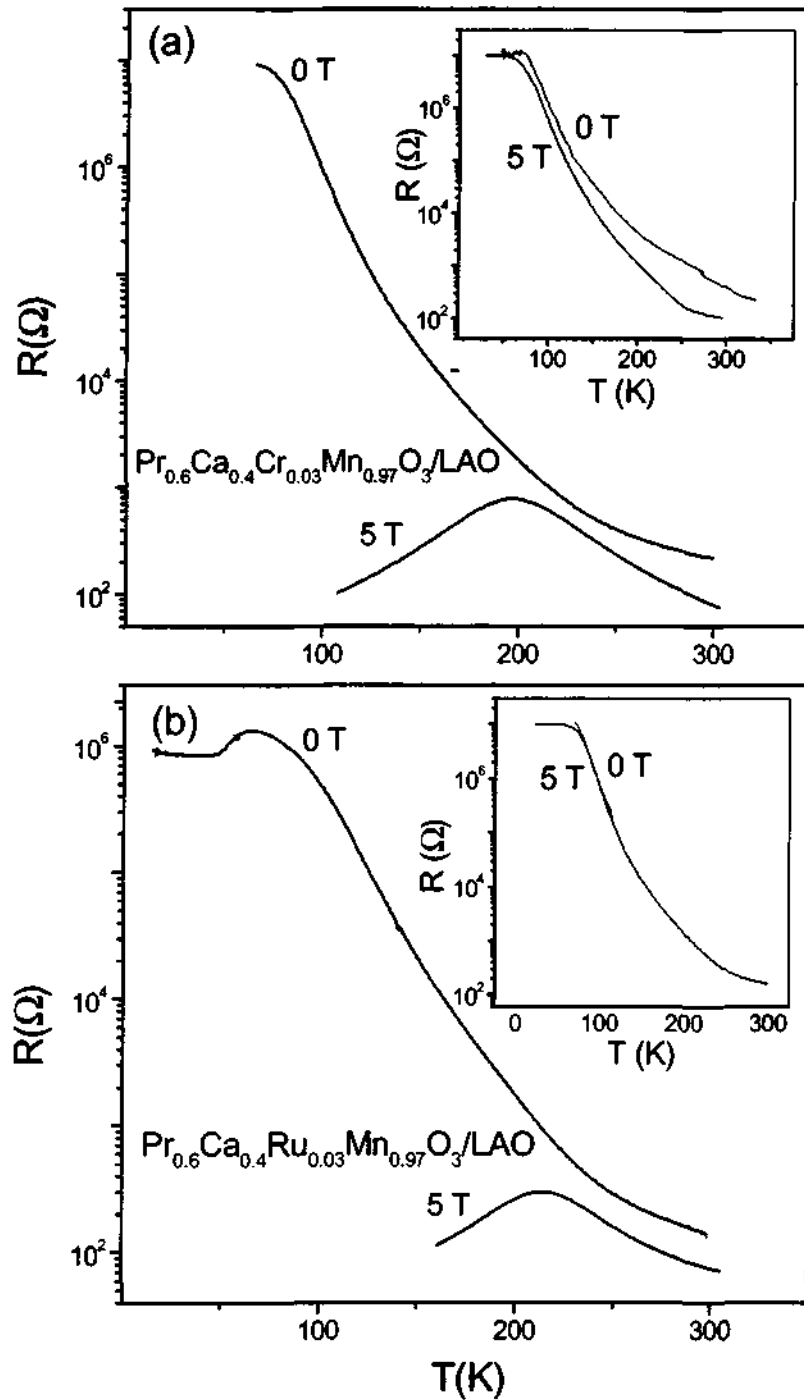


Fig. 1. 65. Temperature-variation of the electrical resistance of the thin films of $\text{Pr}_{0.6}\text{Ca}_{0.4}\text{Cr}_{0.03}\text{Mn}_{0.97}\text{O}_3$ and (b) $\text{Pr}_{0.6}\text{Ca}_{0.4}\text{Ru}_{0.03}\text{Mn}_{0.97}\text{O}_3$ at 0 and 5 tesla. Insets show similar magnetic-field effects for the electron-doped samples, $\text{Pr}_{0.4}\text{Ca}_{0.6}\text{Cr}_{0.03}\text{Mn}_{0.97}\text{O}_3$ and $\text{Pr}_{0.4}\text{Ca}_{0.6}\text{Ru}_{0.03}\text{Mn}_{0.97}\text{O}_3$.

of $\text{Pr}_{0.6}\text{Ca}_{0.4}\text{Cr}_{0.03}\text{Mn}_{0.97}\text{O}_3$ and $\text{Pr}_{0.6}\text{Ca}_{0.4}\text{Ru}_{0.03}\text{Mn}_{0.97}\text{O}_3$ deposited on LAO(100) substrates. On application of the magnetic field, an I-M transition manifests itself in both the cases. The I-M transition temperatures are 198 K and 216 K respectively in the Cr^{3+} and Ru^{4+} doped samples. Similar measurements on the electron-doped $\text{Pr}_{0.4}\text{Ca}_{0.6}\text{Cr}_{0.03}\text{Mn}_{0.97}\text{O}_3$ and $\text{Pr}_{0.4}\text{Ca}_{0.6}\text{Ru}_{0.03}\text{Mn}_{0.97}\text{O}_3$ compositions are shown in the insets of Fig. 1. 65a and 1. 65b respectively. Unlike the hole-doped compositions, a 5T magnetic field has no effect on the resistance of the electron-doped samples. This is in accordance with the behavior of the films of the parent $\text{Pr}_{0.6}\text{Ca}_{0.4}\text{MnO}_3$ and $\text{Pr}_{0.4}\text{Ca}_{0.6}\text{MnO}_3$. Thus, the combined effect of doping and magnetic field fails to render the electron-doped $\text{Pr}_{0.4}\text{Ca}_{0.6}\text{MnO}_3$ metallic even at low temperatures. The effect of electric fields is, however, comparable in the films of Cr^{3+} and Ru^{4+} doped $\text{Pr}_{0.6}\text{Ca}_{0.4}\text{MnO}_3$ and $\text{Pr}_{0.4}\text{Ca}_{0.6}\text{MnO}_3$ films, although the resistance of the electron-doped samples is somewhat higher than that of the hole doped samples. This is clearly seen from Fig. 1. 66a and 1. 66b for the 3% Cr^{3+} doped $\text{Pr}_{0.6}\text{Ca}_{0.4}\text{MnO}_3$ and $\text{Pr}_{0.4}\text{Ca}_{0.6}\text{MnO}_3$. The insets in these figures show similar electric-field effects on the 3% Ru^{4+} doped samples.

1.4.3 Electronic structure calculations

We have used first principles electronic structure calculations as manifest in the (spin) density functional Linearized Muffin-Tin Orbital method to examine whether the asymmetry in properties is reflected in a corresponding asymmetry

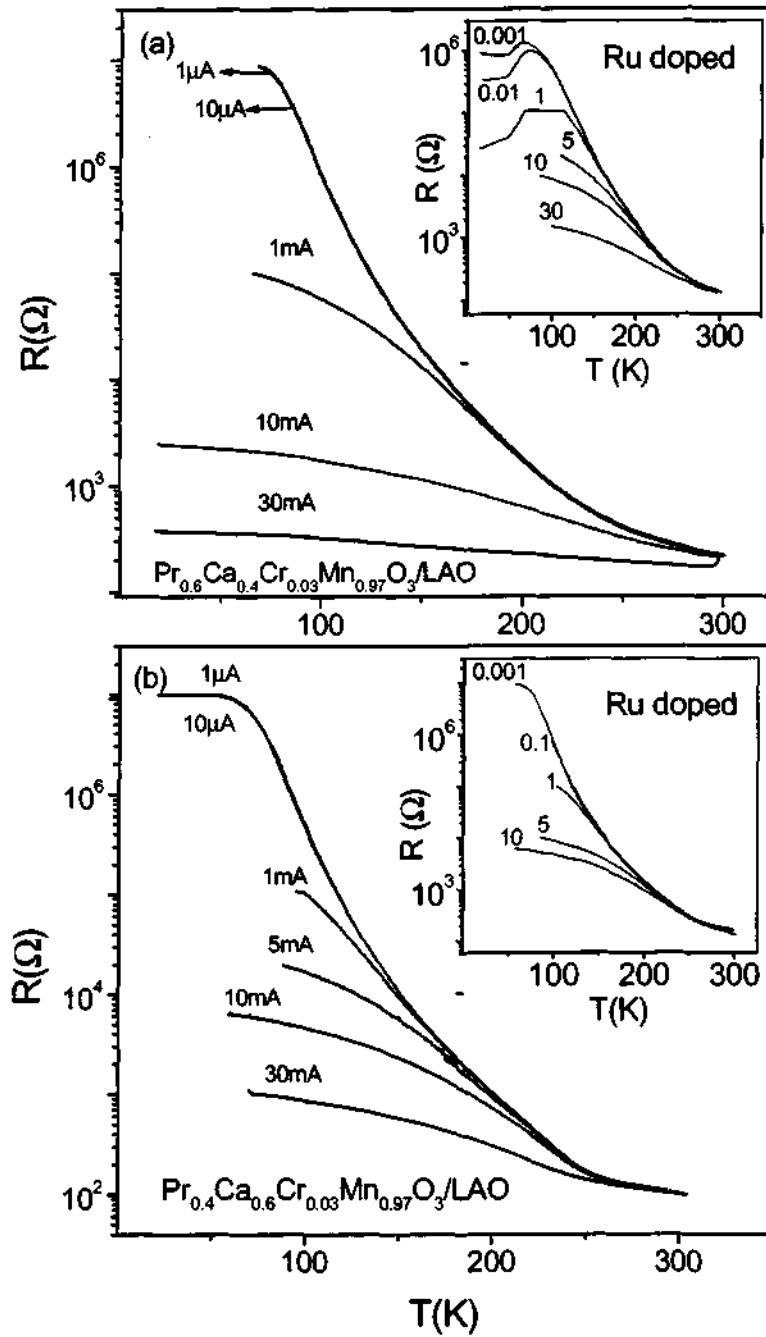


Fig. 1.66. Temperature-variation of the electrical resistance of the thin films of (a) $\text{Pr}_{0.6}\text{Ca}_{0.4}\text{Cr}_{0.03}\text{Mn}_{0.97}\text{O}_3$ and (b) $\text{Pr}_{0.4}\text{Ca}_{0.6}\text{Cr}_{0.03}\text{Mn}_{0.97}\text{O}_3$ deposited on LAO(100) for different values of the current. Insets show similar electric-field effects for 3% Ru^{4+} samples (numbers are in mA).

in the one-electron band structure. While in a more complete analysis, explicit electron correlation of the Hubbard U type would be intrinsic to the calculation [127] we have taken the view that one-electron bandwidths point to the possible role that correlation might play and that correlation could be a consequence of the one-electron band structure rather than as an integral part of the electronic structure. We have chosen the $\text{La}_{1-x}\text{Ca}_x\text{MnO}_3$ system for our calculations to avoid complications due to $4f$ electrons in the corresponding Pr system.

For our calculations on $\text{La}_3\text{CaMn}_4\text{O}_{12}$ ($\text{La}_{0.75}\text{Ca}_{0.25}\text{MnO}_3$), we have used the structure reported by Radaelli et al [122,123] refined from powder neutron diffraction data on 20 K. Ordering the La and Ca in a supercell yields a structure with the same lattice parameters but in the space group Pm with 14 atoms (rather than 4) in the asymmetric unit. This structure is displayed in Fig. 1. 67. La and Ca have closely similar radii and ordering them over crystallographically distinct sites is unphysical. However the bond lengths and angles in the structures used in our calculations closely follow the experiments. For the electron-doped $\text{La}_{0.25}\text{Ca}_{0.75}\text{MnO}_3$ ($\text{LaCa}_3\text{Mn}_4\text{O}_{12}$), we have used the cell and positional parameters of the refined 300 K neutron powder diffraction structure of $\text{La}_{0.33}\text{Ca}_{0.67}\text{MnO}_3$ from Radaelli et al [122,123]. Again, the supercell is in the space group Pm rather than in the orthorhombic $Pnma$ space group. Calculations were performed using the Stuttgart TB-LMTO-ASA program [127,128] The basis sets consisted of $6s$, $5d$ and $4f$ orbitals for La, $4s$ and $3d$ orbitals for Ca, $4s$, $4p$ and $3d$ orbitals for Mn, and

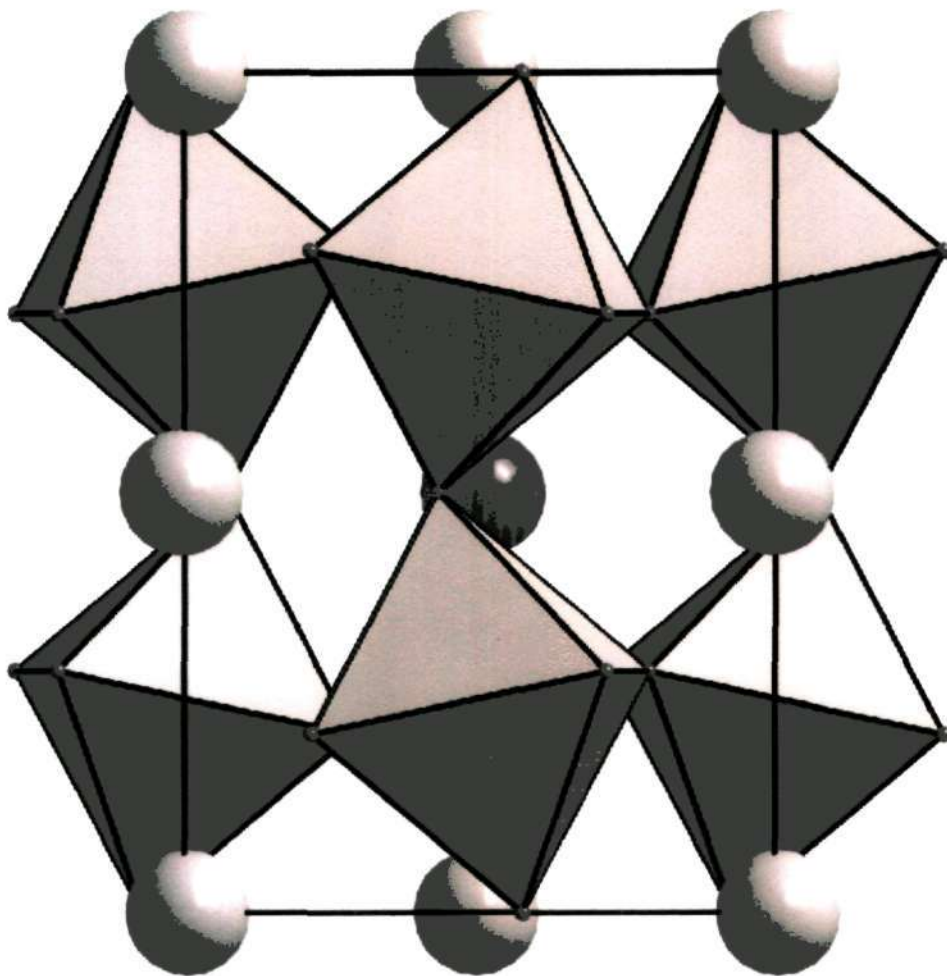


Fig. 1. 67. Monoclinic (space group Pm) structure of $\text{La}_3\text{CaMn}_4\text{O}_{12}$. The dark spheres are La and the light sphere is Ca. The view is looking down the short $a = a_P\sqrt{2}$ axis.

2p orbitals for O. The Atomic Sphere Approximation (ASA) relies on the partitioning of space into atom-centered spheres as well as empty spheres, the latter being critical in structures that are not closely packed. The basis for the empty spheres are 1s orbitals with the 2p component treated using down folding. The spheres are so chosen that the atom-centered spheres do not have a volume overlap of more than 16%. The calculations used 108 k points in the primitive Brillouin zone for achieving convergence. Due to the Pm supercell employed, the nature of the magnetism becomes a little more complex and perhaps artificial for both the systems studied. Indeed, there are now two types of somewhat indistinct Mn atoms in the unit cell. We have found a tendency for a ferrimagnetic ground state in both the manganates, the two Mn having opposite spins. For simplifying the comparison of the two electronic structures, the Mn were provided similar polarization at the start of the calculations; self-consistency yielded a ferromagnet in both the cases.

The calculations yielded a ferromagnetic ground state with a magnetic moment of $3.2 \mu_B$ per Mn for $\text{La}_3\text{CaMn}_4\text{O}_{12}$ (spin-only value $3.75 \mu_B$). Such a reduction in the magnetic moment from the expected value can arise due to an infelicitous choice of sphere radii and does not merit interpretation. The refined neutron moment on Mn is $3.5 \mu_B$ [122,123]. For ferromagnetic $\text{LaCa}_3\text{Mn}_4\text{O}_{12}$, the calculated magnetic moment was $3 \mu_B$ (spin only value 3.25). Fig. 1. 68 compares the spin-polarized densities of state (DOS) in the two spin directions for Mn and

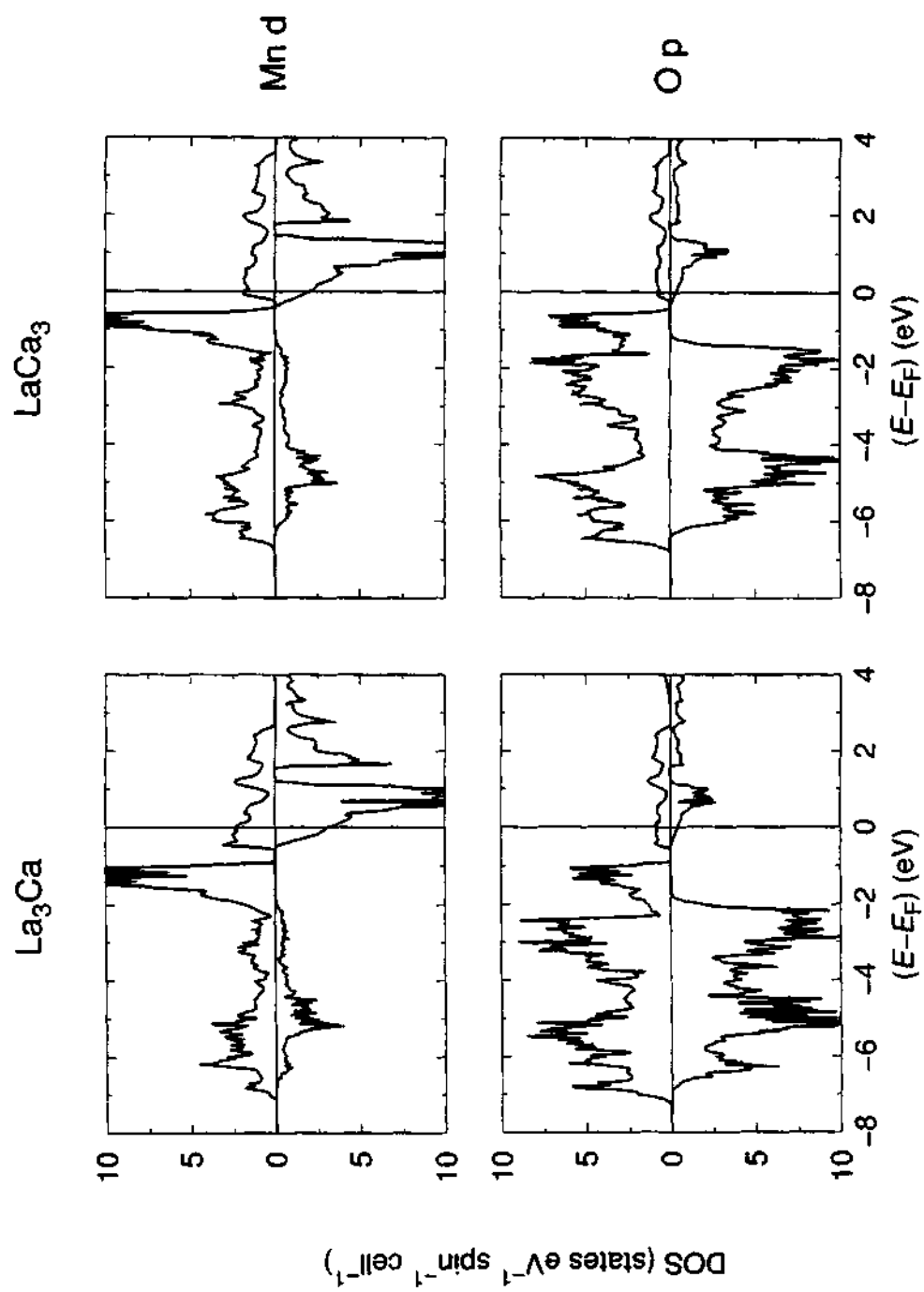


Fig. 1. 68. LMTO densities of state for Mn and O in $\text{La}_3\text{CaMn}_4\text{O}_{12}$ and $\text{LaCa}_3\text{Mn}_4\text{O}_{12}$ near the Fermi energy. The upper halves of each panel display up spin states and the lower halves, down spin.

O in the two compositions. In each panel, the majority up-spin states are depicted in the upper half and the minority down-spin states in the lower half.

In both the manganates, we find filled localized $t_{2g}^3 (\uparrow)$ states with a small bandwidth, of the order 1.5 eV, polarizing a broader conduction band that is essentially $e_g (\uparrow)$ derived, although some $t_{2g} (\downarrow)$ states also occur at the Fermi energy. In $\text{La}_3\text{CaMn}_4\text{O}_{12}$, the Fermi energy E_F lies in a relatively broad conduction band. Both Mn and O states are present at E_F indicating some covalency. Of note is the spin-differentiation at the Fermi energy - there being significantly more spin-down Mn states at the E_F than spin-up states. In the case of $\text{LaCa}_3\text{Mn}_4\text{O}_{12}$, the E_F again lies in an $e_g (\uparrow)$ derived conduction band, but because of the smaller number of e_g electrons, the E_F is at the band edge. Through the examination of the so-called "fat-bands"-energy bands that have been decorated with the character of the corresponding orthonormal orbitals, we know that the e_g states in the perovskite systems [129] are derived from the combination of the narrow d_{z^2} bands and the broader bands formed by the strong covalent overlap between O p_x and p_y and metal $d_{x^2-y^2}$ orbitals. A scheme depicting the nature of the overlap is displayed in Fig. 1. 69. In $\text{LaCa}_3\text{Mn}_4\text{O}_{12}$, where there is a much smaller filling of the e_g , it is the relatively narrow d_{z^2} derived band that is mostly occupied. The finding that the E_F lies on a band edge suggests that this oxide would be susceptible to the opening of a gap in the density of states at the E_F , through correlations of the Hubbard type. At the same

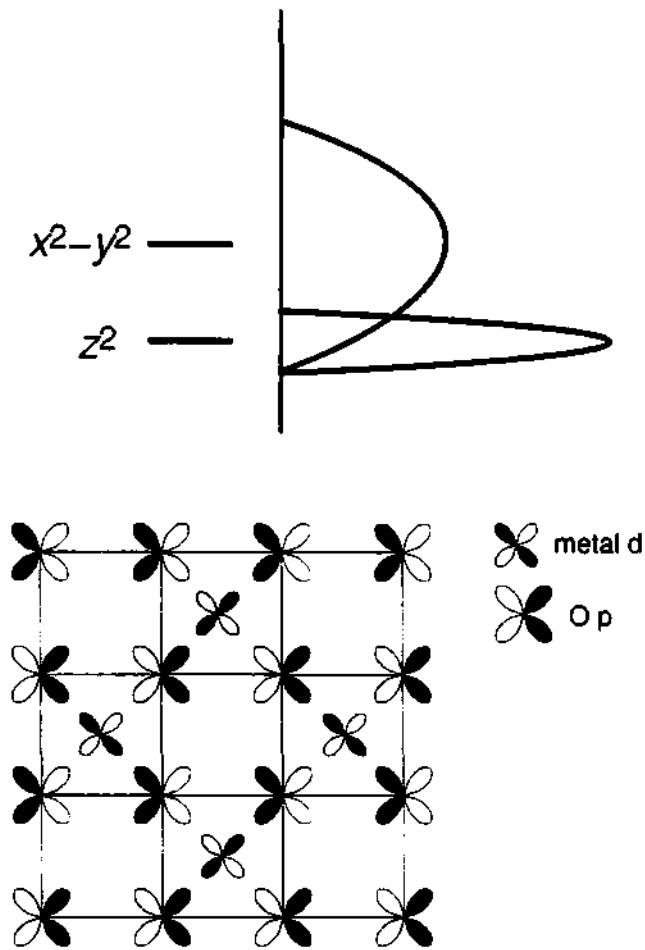


Fig. 1. 69. Scheme displaying the Jahn-Teller distorted e_g states becoming bands in solids such as perovskite manganese oxides. Due to overlap between metal $d_{x^2-y^2}$ and O p_x and p_y , the $d_{x^2-y^2}$ derived and are significant broader. A scheme for such overlap is displayed along the ab -plane.

time, the propensity for the localized and the delocalized states to be separated through a mobility edge (the formation of an Anderson insulator) is also increased by the E_F lying on a band edge. In systems such as the present ones, disorder due to disparate ions occupying the A-site of the perovskite structure cannot be avoided. A point of interest is that in $\text{LaCa}_3\text{Mn}_4\text{O}_{12}$, the DOS at the E_F shows a smaller spin-differentiation than in $\text{La}_3\text{CaMn}_4\text{O}_{12}$. Spin differentiation is believed to be the key to the unusual magnetic field dependence of the electrical transport properties such as colossal magnetoresistance [130]. This suggests that the electron-doped manganates may be less interesting with respect to the CMR properties.

1.4.4 Hopping conduction in the charge ordered manganates

Investigations of the conduction mechanism in rare-earth manganates have shown that the consideration of the electron-phonon coupling is crucial to its understanding [131]. The lattice-electron (or simply the polaron) in these systems are localized in narrow bands (Sec. 1.4.3) near the Fermi-level. Two mechanisms have been postulated for the polaron propagation. One is by thermal activation at high temperatures and the other by quantum tunneling at extremely low temperatures. Holstein formulated [132] a mechanism which accounts for the origin and dynamics of the polarons. In this model, the important parameter which determines the conduction mechanism is the Debye

temperature (θ_D). This temperature which is the characteristic parameter for lattice vibrations modulates the polaronic bandwidth. The resulting conduction mechanism falls into three temperatures categories in this model. They are:

- (a) $T \ll \theta_D$: In this regime, the polaron propagation is by tunneling.
- (b) $T < \theta_D/2$: The polaron propagates by both tunneling and thermal activation.
- (c) $T > \theta_D$: The motion of the polaron is primarily through thermal activation.

In the high temperature region i.e., when the polaron entirely depends on the thermal activation the resistivity is found to be given by $\rho = BT\exp(W/k_B T)$. However when $T < \theta_D/2$, the resistivity is found to be dependent on temperature as $\rho = C\exp(T^{-1/4})$. In the literature, the debye temperature for charge ordered $\text{Pr}_{0.67}\text{Ca}_{0.33}\text{MnO}_3$ [133] has been estimated to be ~ 500 K (obtained by extrapolating the high temperature region). We have investigated the conduction mechanism in our samples by not only this model but those with other temperature dependencies as well.

In Fig. 1. 70a and 1. 70b, we present the resistivity data of a single crystal of $\text{Gd}_{0.5}\text{Ca}_{0.5}\text{MnO}_3$. The manganate is insulating over the entire temperature range studied. In order to find the conduction mechanism in this material, we have used the resistivity behavior of these two manganates below the charge ordering transition temperature to avoid the resistivity anomaly occurring at

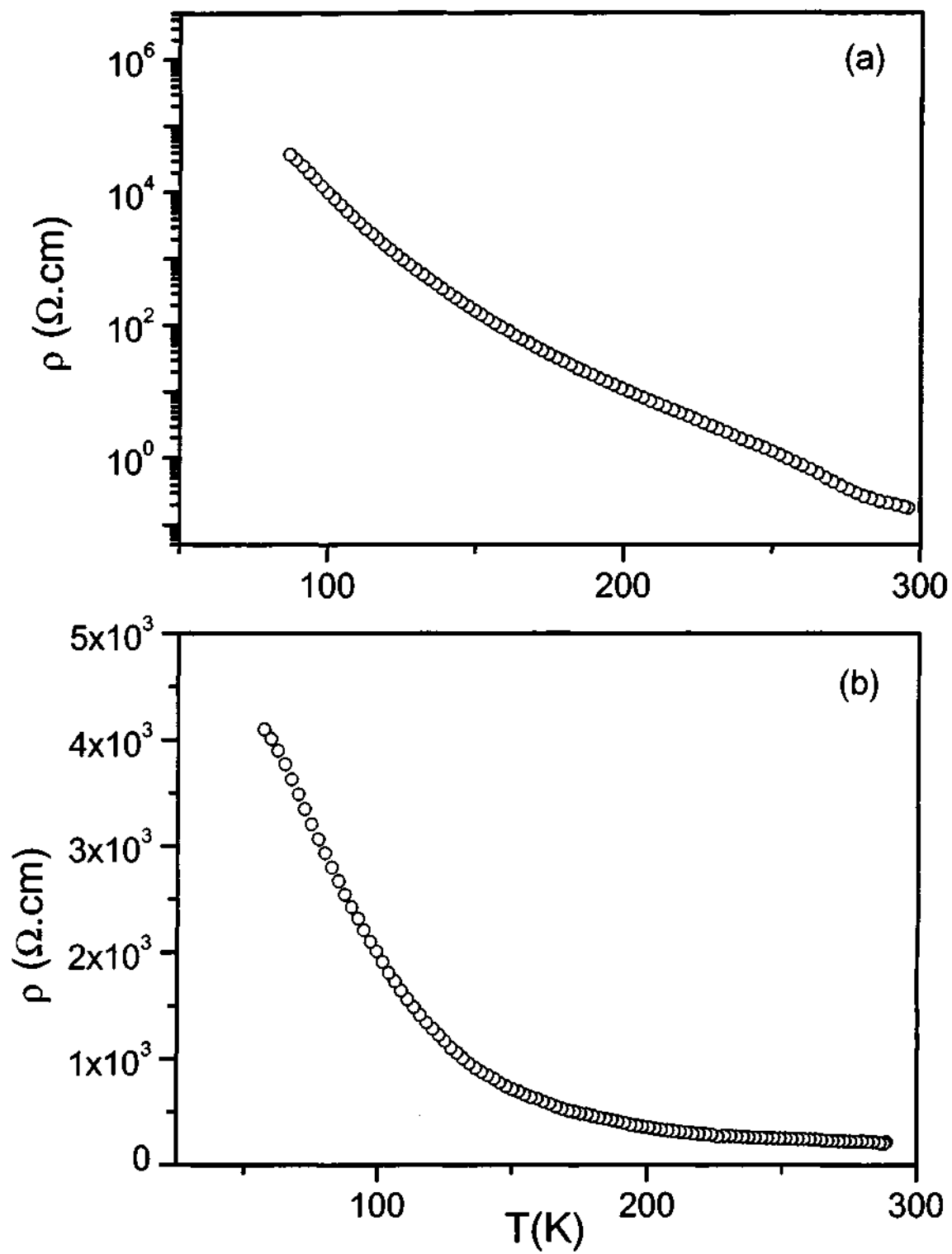


Fig. 1.70. Resistivity data of single crystal of (a) $\text{Gd}_{0.5}\text{Ca}_{0.5}\text{MnO}_3$ and (b) $\text{Nd}_{0.5}\text{Ca}_{0.5}\text{MnO}_3$.

T_{CO} . We have fitted the resistivity data to the generalized form of activated-hopping model wherein the resistivity is given by,

$$\rho \propto \exp\left(\frac{T_0}{T}\right)^{1/n} \quad (1)$$

Here, $n = 1$ and 4 correspond respectively to Arrhenius and Mott's variable-range hopping (VRH) mechanisms, while $n = 2$ corresponds to hopping dominated by Coulomb interaction [134, 135]. We have also fitted the data to the polaron-hopping conduction model as described by,

$$\frac{\rho}{T^s} \propto \exp\left(\frac{W}{k_B T}\right) \quad (2)$$

where $s = 1$ and $s = 3/2$ correspond to adiabatic and non-adiabatic polaron conduction mechanisms respectively. The quantity W is the overall activation energy, which accounts for the polaron binding energy as well. Lastly, we have examined the bipolaron conduction mechanism wherein the pairs of bound polarons move and are responsible for the conduction. In this model the resistivity is given by,

$$\rho\sqrt{T} \propto \exp\left(\frac{W}{k_B T}\right) \quad (3)$$

We have quantified the fits of the resistivity data to the various models in terms of the values of standard deviation (sd) and the regression (r). The results are presented in Table 1.9 for $Gd_{0.5}Ca_{0.5}MnO_3$ and $Nd_{0.5}Ca_{0.5}MnO_3$. The best fits for

Table 1. 9 Resistivity behavior of $\text{Ln}_{0.5}\text{Ca}_{0.5}\text{MnO}_3$ ($\text{Ln} = \text{Gd or Nd}$)

Model	$\text{Gd}_{0.5}\text{Ca}_{0.5}\text{MnO}_3^{(a)}$		$\text{Nd}_{0.5}\text{Ca}_{0.5}\text{MnO}_3^{(b)}$		$\text{Nd}_{0.5}\text{Ca}_{0.5}\text{MnO}_3^{(c)}$	
	R	Sd	r	Sd	R	Sd
n=1, Eqn 1	0.996	0.207	0.995	0.056	0.996	0.196
n=2, Eqn 1	0.999	0.078	0.998	0.027	0.999	0.095
n=4, Eqn 1	0.999	0.018	0.999	0.015	0.999	0.046
s=1, Eqn 2	0.995	0.238	0.995	0.069	0.996	0.210
s=3/2, Eqn 2	0.995	0.252	0.995	0.093	0.995	0.226
Eqn 3	0.996	0.198	0.995	0.045	0.995	0.194

^(a) Single crystal data over the temperature range 90-211 K;

^(b) Single crystal data over the temperature range 98-220 K;

^(c) Polycrystalline data over the temperature range 93-190 K

the resistivity data of the single crystal samples are found with the VRH model with $n = 4$ in Eqn. 1. Accordingly, the lowest sd values are formed for $T^{-1/4}$ fits. In Fig. 1. 71, a typical fit for the resistivity data is shown for the case of $Gd_{0.5}Ca_{0.5}MnO_3$. The correlation is poor for both adiabatic and non-adiabatic polaronic mechanisms. It is noteworthy that unlike in these two charge-ordered manganates, the high-temperature resistivity data of $La_{0.7}Ca_{0.3}MnO_3$ above the metal-insulator transition temperature is best described by the small polaron model (Eqn. 2). In Fig. 1. 72a, the resistivity data of $La_{0.7}Ca_{0.3}MnO_3$ is shown. We have fitted the high temperature insulating region and the best fit was obtained for the adiabatic small polaron model as shown in Fig. 1. 72b. Thus in the case of $La_{0.7}Ca_{0.3}MnO_3$, our results corroborate with those in the literature.

Having found that the $T^{-1/4}$ law (Eqn. 1, $n=4$) best describes the resistivity data of single crystalline $Gd_{0.5}Ca_{0.5}MnO_3$ and $Nd_{0.5}Ca_{0.5}MnO_3$, we examined whether this law is obeyed in a polycrystalline sample of $Nd_{0.5}Ca_{0.5}MnO_3$. The polycrystalline material also obeys this law as justified by the results listed in Table 1. 9. The regression and sd values are satisfactory, although the sd's tend to be slightly higher than those for the single crystalline samples.

We have examined the temperature variation of the activation energy, E_a , as defined by,

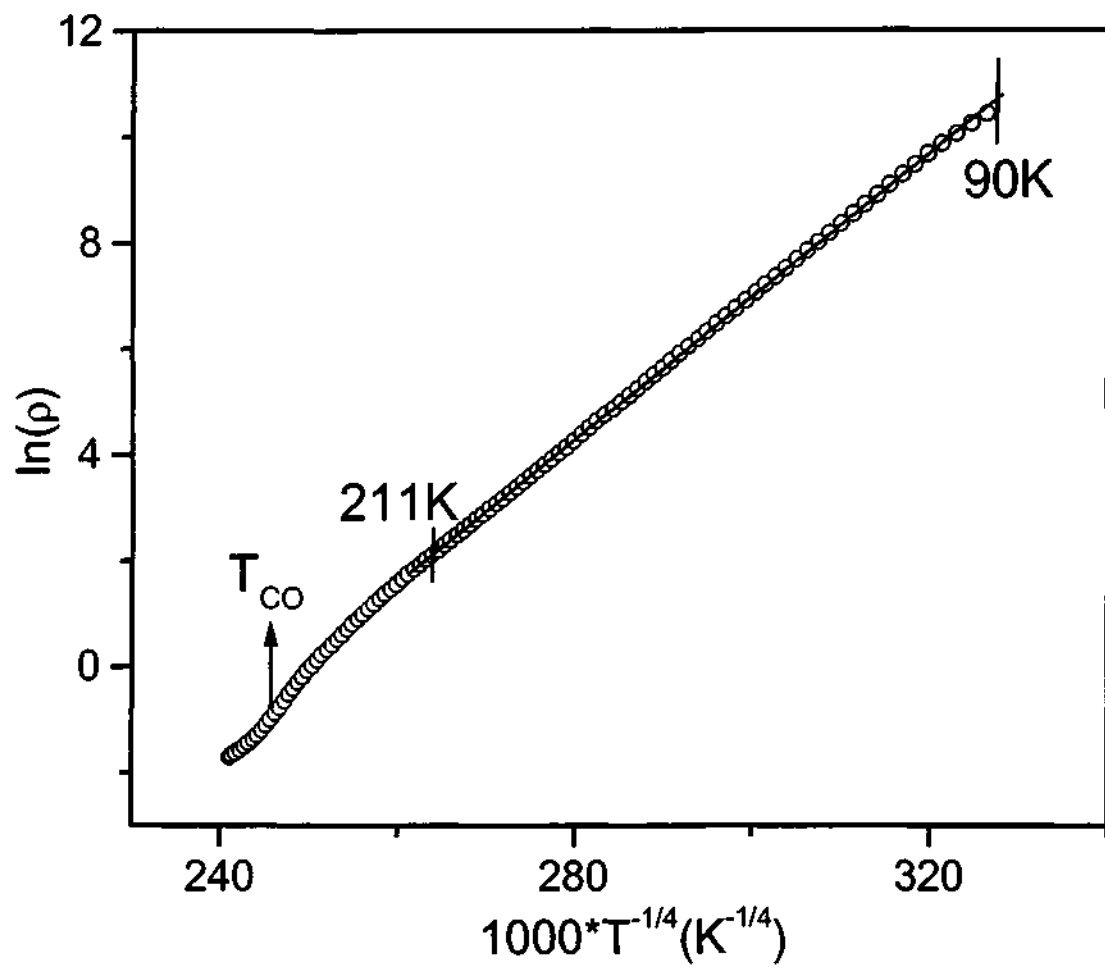


Fig. 1. 71. Fit of resistivity data of single crystal $\text{Gd}_{0.5}\text{Ca}_{0.5}\text{MnO}_3$ with $n=4$ in Eqn. 1 below the charge ordering temperature.

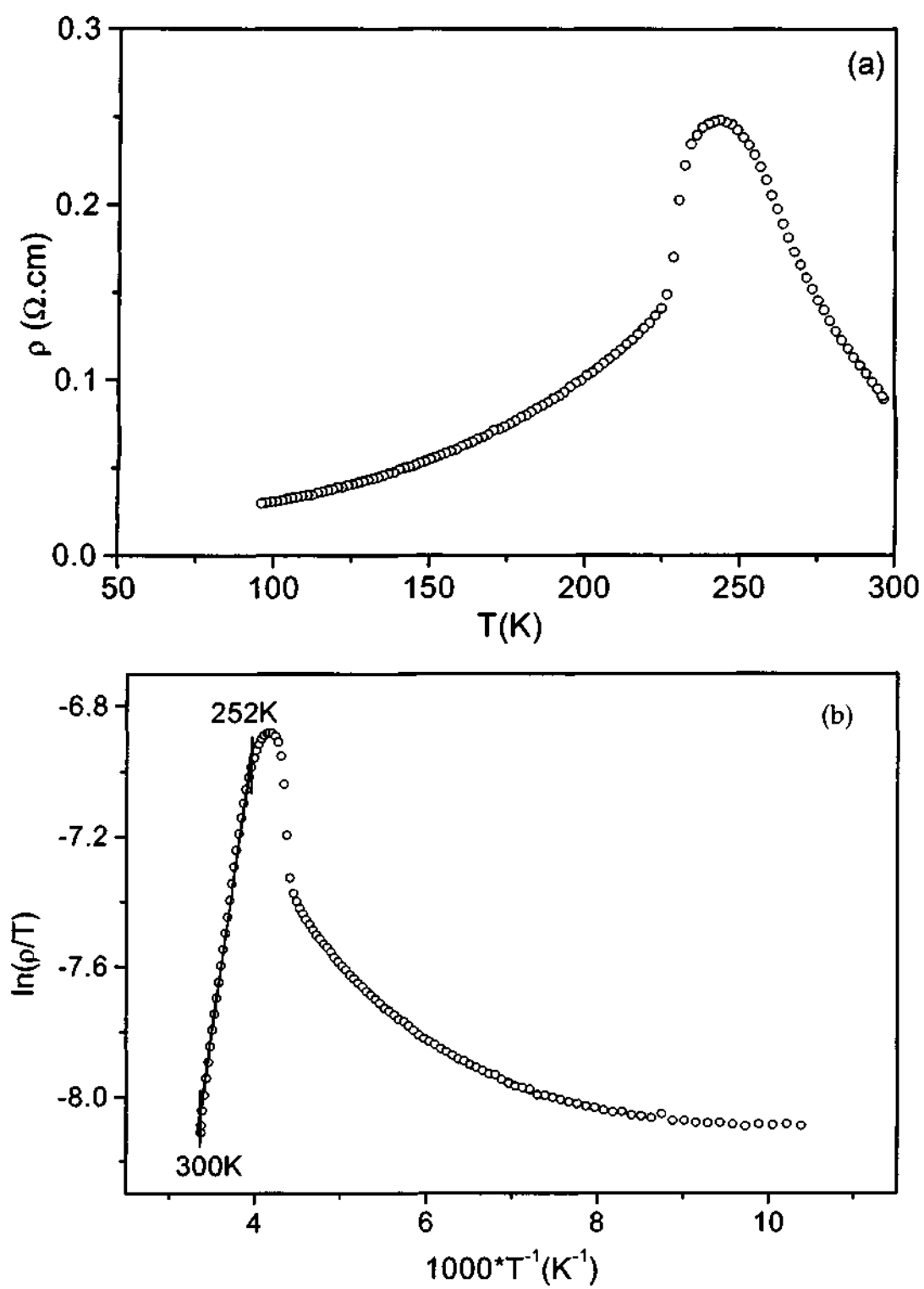


Fig. 1.72. (a) Resistivity data and (b) Fit to the resistivity data with $s = 1$ in Eqn. 2 of $\text{La}_{0.7}\text{Ca}_{0.3}\text{MnO}_3$.

$$E_a = \frac{d(\ln\rho)}{d\left(\frac{1}{k_B T}\right)} \quad (4)$$

In Fig. 1. 73, we show the plots of E_a against temperature for single crystal of $Gd_{0.5}Ca_{0.5}MnO_3$. We clearly see the charge-ordering transition around 270 K as an anomaly in E_a . The signature of variable range hopping mechanism is seen here in terms of the non-zero slopes of the plots below the charge-ordering temperature, which indicates that the energy barrier to hopping changes as a function of temperature. In Fig. 1. 73b, we show the variation of E_a for the case of $La_{0.7}Ca_{0.3}MnO_3$. The low temperature region corresponding to the metallic state has zero hopping activation energy. This clearly indicates that there is a significant barrier for electron transport in the charge-ordered regime. In the literature [136], a quantity l , defined as,

$$l = \frac{\ln\left(\frac{E_a}{k_B T}\right)}{\ln(T)} \quad (5)$$

has been employed to describe hopping conduction. Here l is related to n in eqn. 1 by $l = (-1/n)$. A plot of $\ln(E_a/k_B T)$ against $\ln T$ shows a linear regime below T_{CO} and gives a value of $-1/4$ for l in the case of $Gd_{0.5}Ca_{0.5}MnO_3$ shown in the inset of Fig. 1. 73.

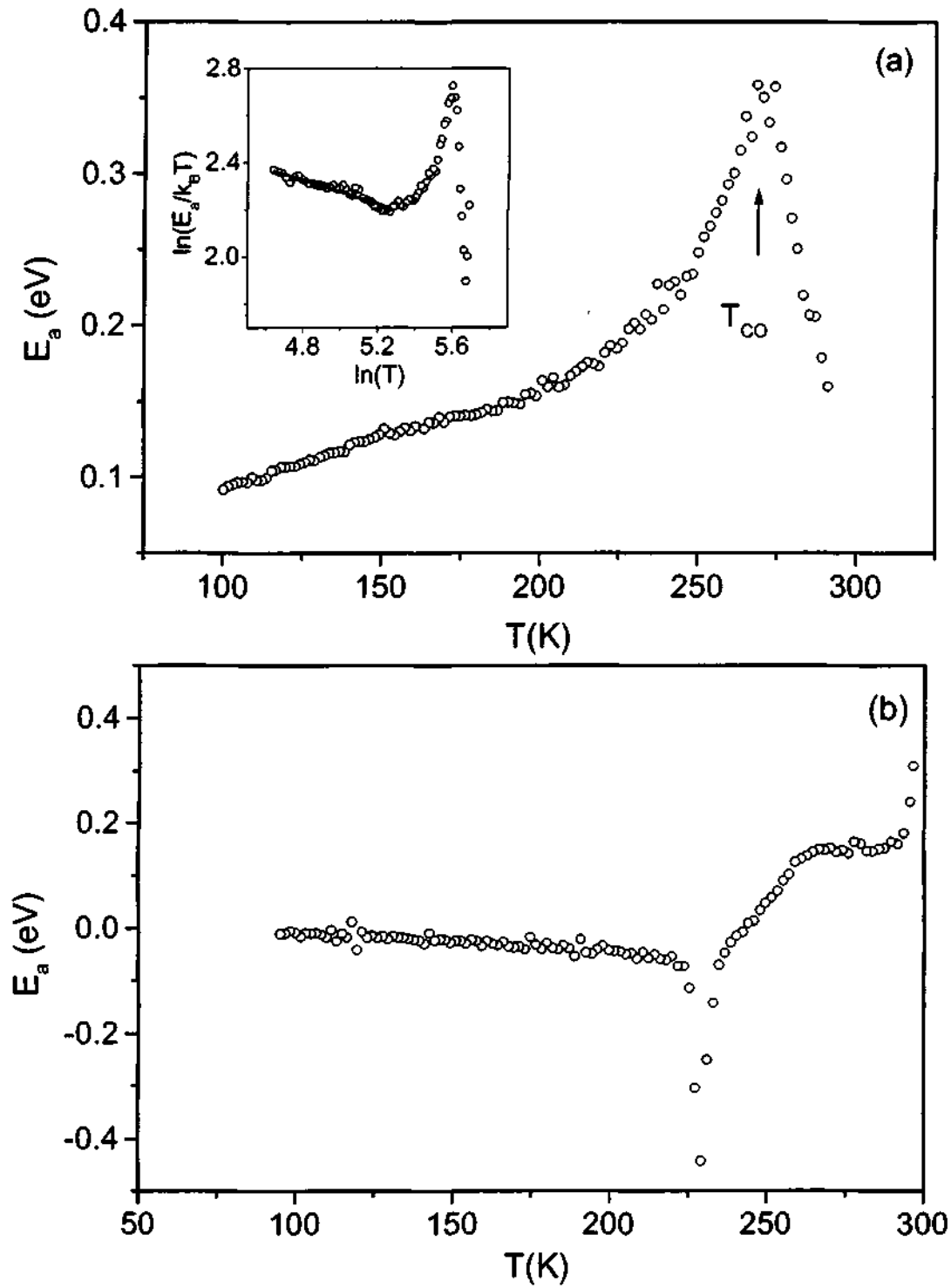


Fig. 1.73. Variation in the localization energy E_a for (a) $\text{Gd}_{0.5}\text{Ca}_{0.5}\text{MnO}_3$ and (b) $\text{La}_{0.7}\text{Ca}_{0.3}\text{MnO}_3$. The inset show the variation of $\ln(E_a/kT)$ vs $\ln T$ giving a value of $n=4$.

We have compared the resistivity behavior of single crystals of the analogous hole- and electron-doped compositions, $\text{Pr}_{0.6}\text{Ca}_{0.4}\text{MnO}_3$ and $\text{Pr}_{0.4}\text{Ca}_{0.6}\text{MnO}_3$. In Table 1. 10 we show the s and the r values obtained for different values of n in Eqn. 1. In the case of $\text{Pr}_{0.6}\text{Ca}_{0.4}\text{MnO}_3$, the best fit was obtained for $n = 4$ as shown in Fig. 1. 74a. While $n = 4$ gives a reasonable fit for $\text{Pr}_{0.4}\text{Ca}_{0.6}\text{MnO}_3$ (Fig. 1. 74b), $n = 2$ is almost as good (Table 1. 10). Furthermore, the r values are low compared to those found in $\text{Pr}_{0.6}\text{Ca}_{0.4}\text{MnO}_3$ and in $\text{Ln}_{0.5}\text{Ca}_{0.5}\text{MnO}_3$. Thus, the resistivity behavior of the electron-doped $\text{Pr}_{0.4}\text{Ca}_{0.6}\text{MnO}_3$ appears to be unusual, with none of the 'n' values being completely satisfactory. From the fits of the resistivity data to Eqn. 1, we obtain the slope and the T_0 values. From the T_0 value, we can calculate the density of states $N(E_F)$ by using the relation,

$$T_0 = \frac{16\alpha^3}{k_B N(E_F)} \quad (6)$$

Assuming a value of α to be 2.5 nm^{-1} , we estimate the density of states to be generally between 10^{18} and $10^{20} \text{ eV}^{-1}\text{cm}^{-3}$.

We have measured the a.c. conductivity response of these samples. The dependence of the real part of the a.c. conductivity on the frequency is given by the relation [137],

$$\sigma(\omega) = \sigma(0) + A\omega^s \quad (7)$$

Table 1. 10 Resistivity behavior of single crystal of hole- and electron-doped manganates

Model	Pr _{0.6} Ca _{0.4} MnO ₃ (a)		Pr _{0.4} Ca _{0.6} MnO ₃ (b)	
	r	Sd	R	sd
n=1, Eqn 1	0.997	0.127	0.989	0.088
n=2, Eqn 1	0.999	0.042	0.994	0.062
n=4, Eqn 1	0.999	0.010	0.996	0.052

Data over the temperature range 80-165 K; (b) Data over the temperature range 97-182K.

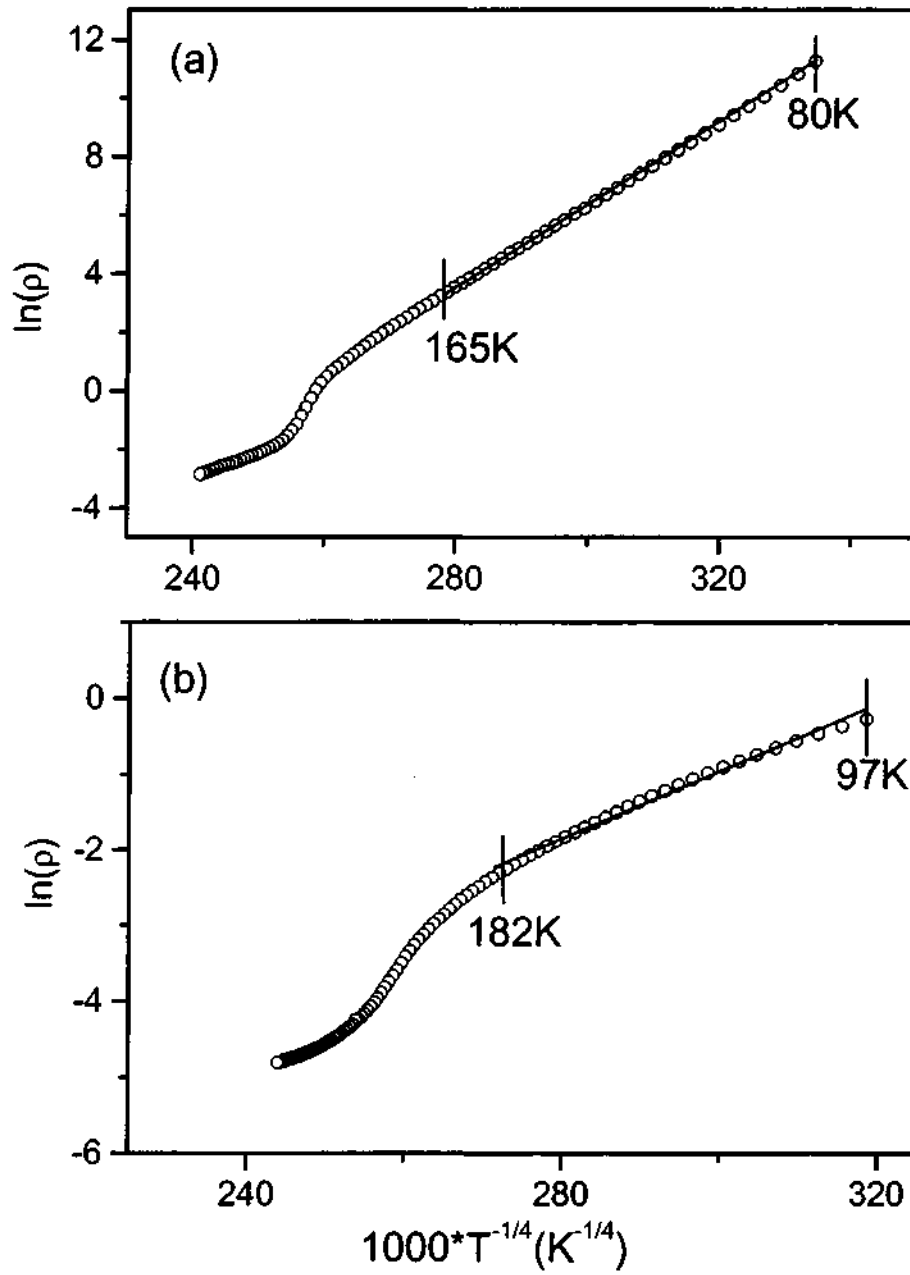


Fig. 1. 74. Fit of resistivity data of single crystalline sample below the charge ordering temperature of (a) $\text{Pr}_{0.6}\text{Ca}_{0.4}\text{MnO}_3$ with $n=4$ in eqn. 1 and (b) $\text{Pr}_{0.4}\text{Ca}_{0.6}\text{MnO}_3$ with $n=4$ in Eqn. 1.

The exponent s generally has values in the range $0 < s \leq 1$. In the variable range hopping mechanism, the electrons encounter varying energy barriers depending on the range of hopping which in turn depends on the temperature. In Fig. 1. 75, we show typical data obtained for single crystalline data of $\text{Gd}_{0.5}\text{Ca}_{0.5}\text{MnO}_3$ and $\text{Nd}_{0.5}\text{Ca}_{0.5}\text{MnO}_3$ over a range of temperatures. Similar data were obtained for polycrystalline samples also. The value of s from the slopes of the curves ($\log(\omega) > 5$) is around 0.6 in the region of 100 K for single crystals of $\text{Gd}_{0.5}\text{Ca}_{0.5}\text{MnO}_3$ and $\text{Nd}_{0.5}\text{Ca}_{0.5}\text{MnO}_3$. The value of s goes through a minimum and rises again as required by the equation [138],

$$s = b\sqrt{T} \exp\left(\frac{W - E_0}{2k_B T}\right) \quad (8)$$

Here $b^2 = (\tau_0 \sigma_0 k_B) / (Ce^2 l_0^2)$, τ_0 being related to the relaxation time τ given by the equation $\tau = \tau_0 \exp(W/k_B T)$. The value of s has a minimum corresponding to $W - E_0 = k_B T_{\min}$ and this is seen around 140 K in $\text{Gd}_{0.5}\text{Ca}_{0.5}\text{MnO}_3$ as shown in Fig. 1. 76. We have calculated the relaxation time in these materials. At 100 K, in both hole and electron doped compositions, τ lies between 10^{-6} - 10^{-8} s.

We have extended the study to hole-doped $\text{Pr}_{0.64}\text{Ca}_{0.36}\text{MnO}_3$ which shows a behavior similar to $\text{Gd}_{0.5}\text{Ca}_{0.5}\text{MnO}_3$ as seen in Fig. 1. 77a. An exception to this behavior occurs in the electron-doped $\text{Pr}_{0.36}\text{Ca}_{0.64}\text{MnO}_3$ (Fig. 1. 77b) where the frequency dependence is quite different. The value of 's' obtained at 140 K is around ~ 2.3 . This is an unusually high value and moreover the value of s goes

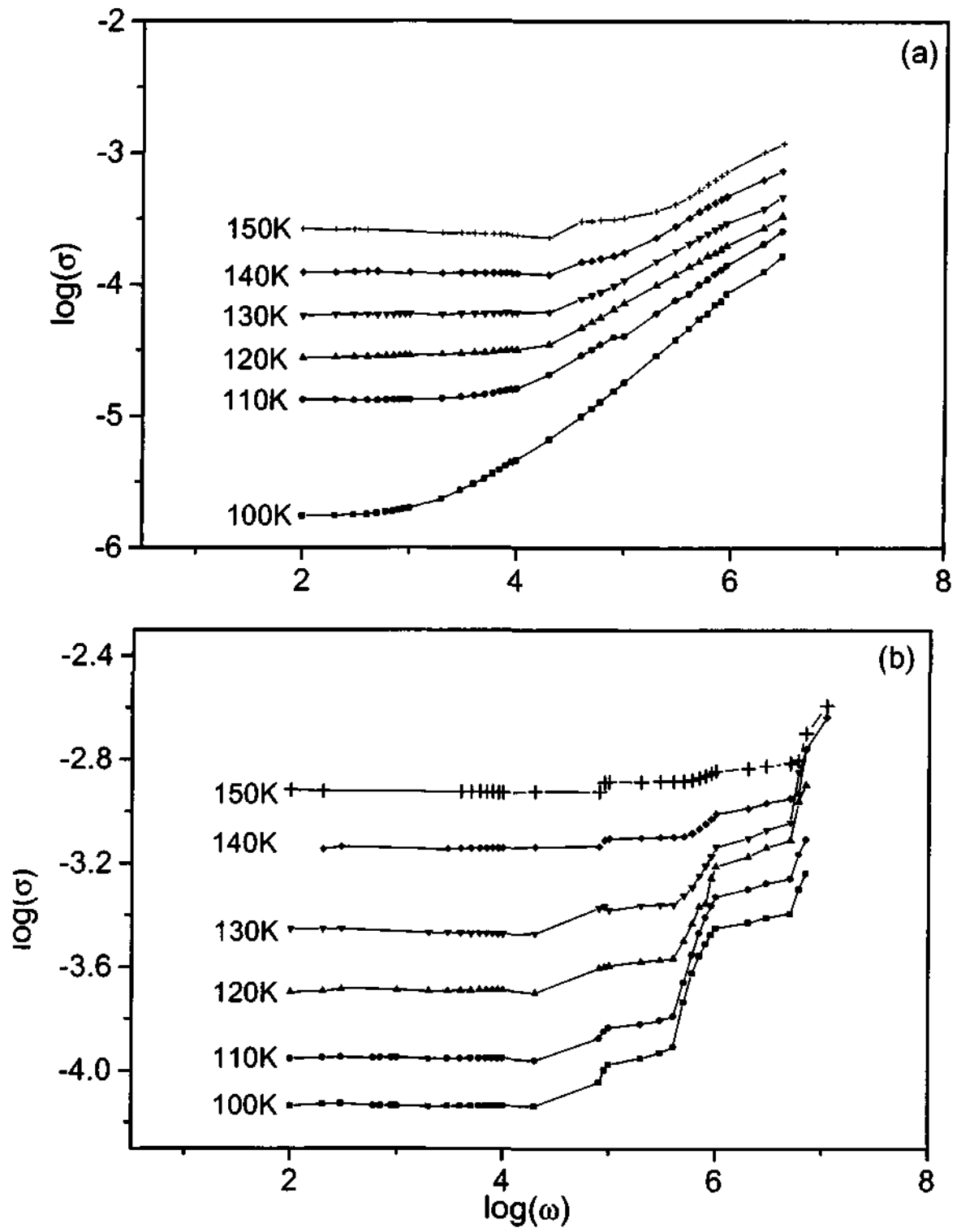


Fig 1. 75. A.c conductivity data of single crystal of (a) $\text{Gd}_{0.5}\text{Ca}_{0.5}\text{MnO}_3$ and (b) $\text{Nd}_{0.5}\text{Ca}_{0.5}\text{MnO}_3$ for a range of temperatures below the charge ordering transition.

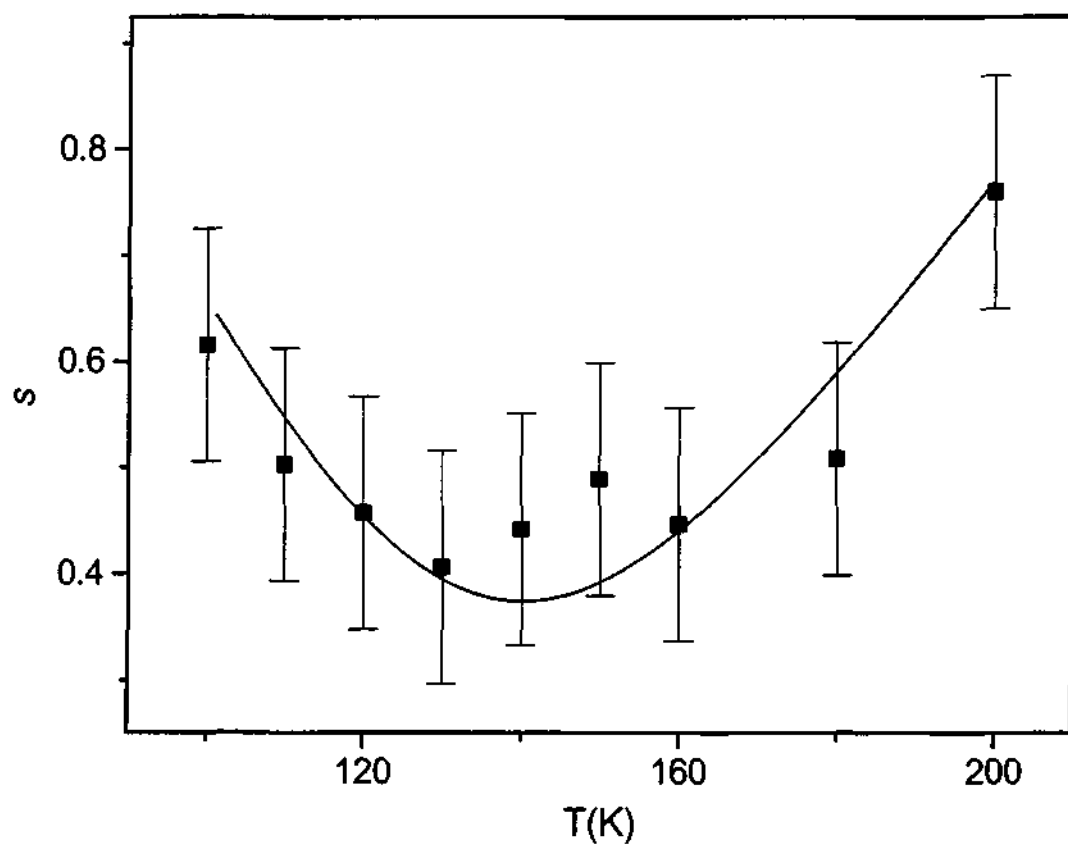


Fig. 1. 76. The variation of slope s for different temperatures in single crystal of $\text{Gd}_{0.5}\text{Ca}_{0.5}\text{MnO}_3$.

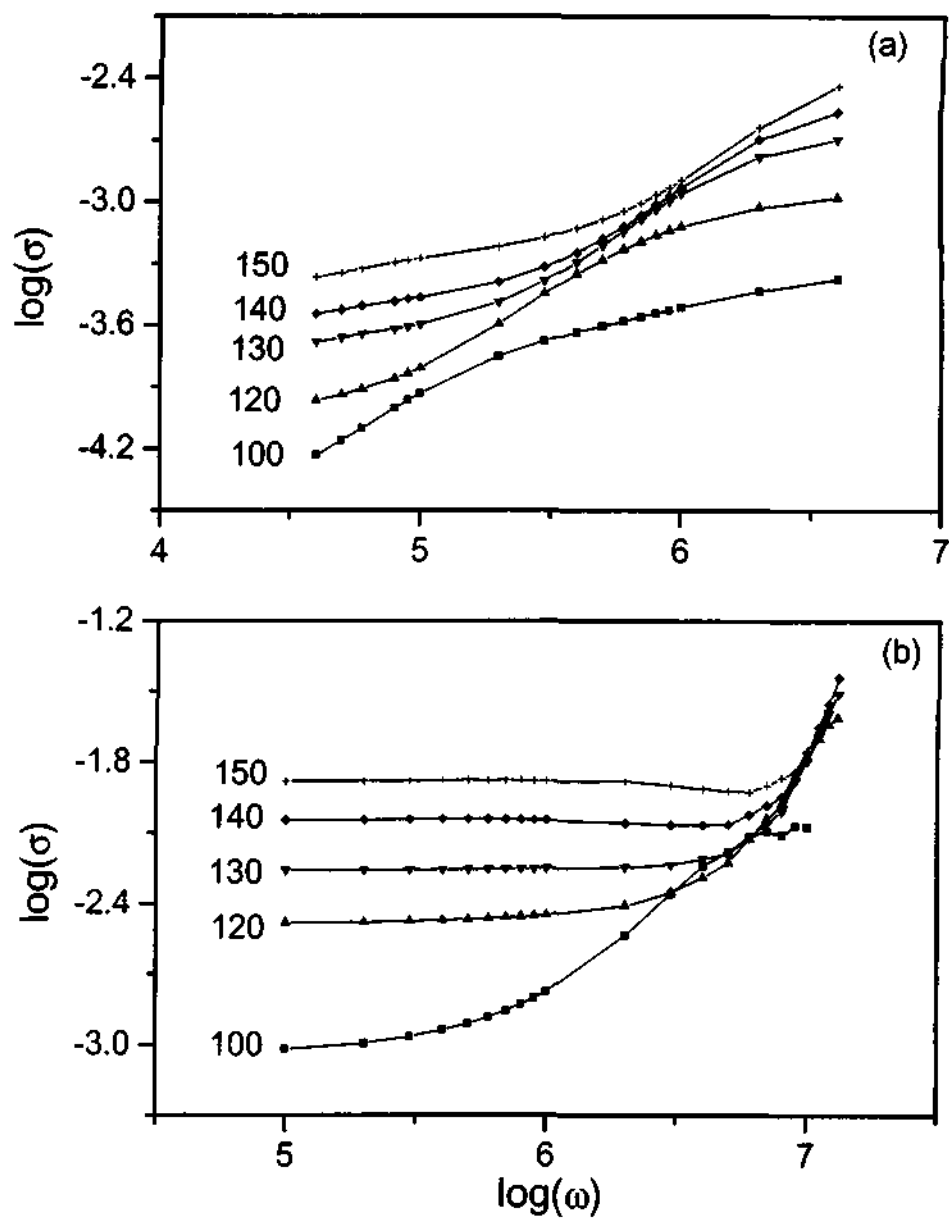


Fig. 1. 77. A.c. conductivity data of (a) $\text{Pr}_{0.64}\text{Ca}_{0.36}\text{MnO}_3$ and (b) $\text{Pr}_{0.36}\text{Ca}_{0.64}\text{MnO}_3$ as a function of frequency.

through a maximum. In Fig. 1. 78, we show this quantity as a function of temperature. This indicates to the fundamental differences in the electronic structure and conduction mechanism in the analogous hole-doped and electron-doped composition. It must be noted that the hole-doped material must accommodate the CE type charge-ordered structure by Mn^{3+} ions in the occupied d_{z^2} orbitals. The electron-doped material, on the other hand, need not interrupt this network, forming possibly either a Wigner crystal or a bistrife structure.

1.4.5 A- versus CE-type antiferromagnetism in $Pr_{0.5-x}Nd_xSr_{0.5}MnO_3$

In Fig. 1. 79, we show the powder diffraction profiles for $x=0.0, 0.1, 0.2$ and 0.5 . In Table 1.11, we list the cell parameters of these compositions. In $Pr_{0.5}Sr_{0.5}MnO_3$ ($x = 0.0$), the material adopts the tetragonal space group $I4/mcm$, whereas in $Nd_{0.5}Sr_{0.5}MnO_3$ ($x = 0.5$), orthorhombic $Imma$ symmetry is adopted. Comparing the x-ray diffraction profiles for $Pr_{0.5}Sr_{0.5}MnO_3$ and $Nd_{0.5}Sr_{0.5}MnO_3$, we see that near $\theta = 16.6^\circ$, the intensity of the split peaks are reversed in this region. The same observation is made near $\theta = 23.5^\circ$. Normally, peak positions specific to a space group are monitored. However, in the comparison of $I4/mcm$ and $Imma$ space groups of these materials, we find that in powder diffraction patterns, the lines are too closely spaced to warrant the exclusion of one particular symmetry. In Fig. 1. 79, we clearly see that as we go from $x = 0.1$ to 0.2 , i.e, from $Pr_{0.4}Nd_{0.1}Sr_{0.5}MnO_3$ to $Pr_{0.3}Nd_{0.2}Sr_{0.5}MnO_3$, the space group changes from tetragonal to orthorhombic symmetry. In the case of $Pr_{0.3}Nd_{0.2}Sr_{0.5}MnO_3$

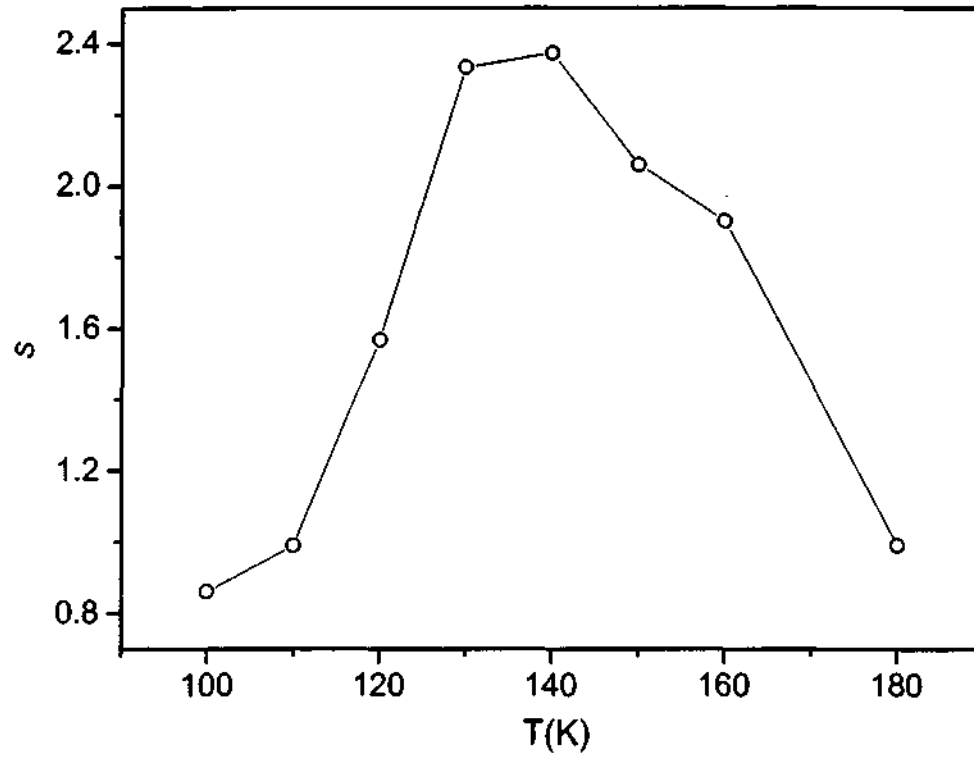


Fig. 1. 78. Variation of exponent 's' obtained from the a.c. conductivity data of $\text{Pr}_{0.36}\text{Ca}_{0.64}\text{MnO}_3$.

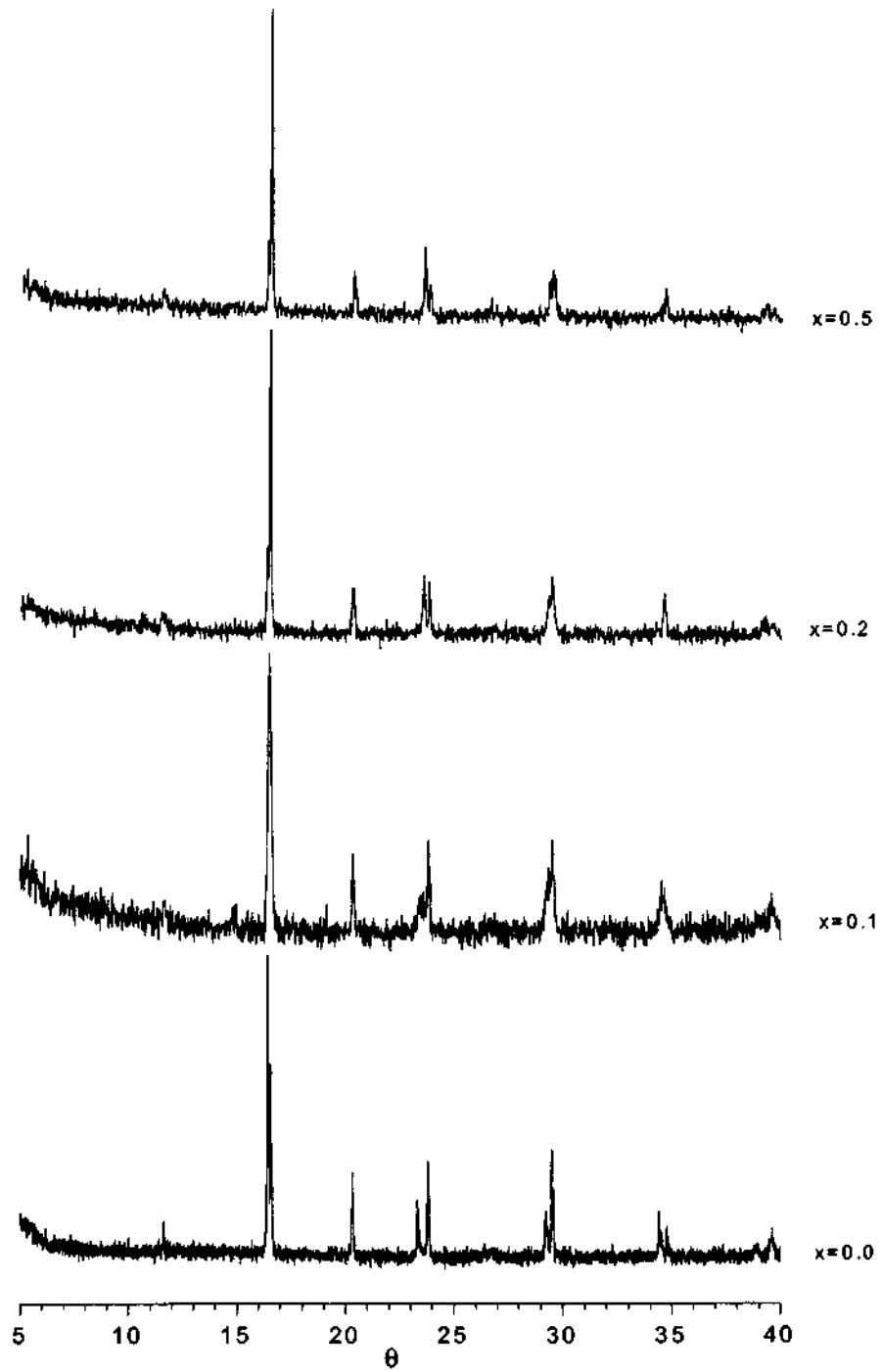


Fig. 1. 79. X-ray powder diffraction data of $\text{Pr}_{0.5-x}\text{Nd}_x\text{Sr}_{0.5}\text{MnO}_3$ showing phase transition from $I4/mcm$ to $Imma$ at $x = 0.2$.

Table 1. 11 Space group and unit cell parameters for $\text{Pr}_{0.5-x}\text{Nd}_x\text{Sr}_{0.5}\text{MnO}_3$ as a function of composition.

Composition (x)	Sp. Group	a (Å)	b (Å)	c (Å)	Volume (Å ³)
0.0	<i>I4/mcm</i>	5.4049	5.4049	7.7842	227.39
0.05	<i>I4/mcm</i>	5.4032	5.4032	7.7772	227.05
0.1	<i>I4/mcm</i>	5.3902	5.3902	7.7392	226.42
0.2	<i>Imma</i>	5.4765	5.4323	7.6352	227.15
0.3	<i>Imma</i>	5.4776	5.4183	7.6330	226.54
0.4	<i>Imma</i>	5.4276	5.4688	7.6303	226.49
0.5	<i>Imma</i>	5.4280	5.4653	7.6341	226.14

(*Imma* space group), we must point out that a small fraction of the composition can possibly coexist in *I4/mcm* space group (as in phase mixtures), given the fact that the lines are near superimposable in position. However this possibility needs to be explored employing a detailed Rietveld analysis. We also observed that the unit cell volume decreases till at $x = 0.1$, then shows a discontinuous jump at $x = 0.2$, decreasing again with increasing Nd content (Table 1.11).

In Fig. 1. 80a, we show the magnetization data of $\text{Pr}_{0.5-x}\text{Nd}_x\text{Sr}_{0.5}\text{MnO}_3$ for $x = 0.0, 0.1, 0.3$ and 0.5 . It is clearly seen that $\text{Pr}_{0.5}\text{Sr}_{0.5}\text{MnO}_3$ exhibits ferromagnetism transition ($T_C = 270$ K) and has onset of antiferromagnetism (A-type) at 110 K. In the case of $\text{Nd}_{0.5}\text{Sr}_{0.5}\text{MnO}_3$, the ferromagnetic transition is at ~ 250 K and the antiferromagnetic transition to a CE-type occurs at ~ 140 K. In Fig. 1. 80b, we show the resistivity data for $\text{Pr}_{0.5-x}\text{Nd}_x\text{Sr}_{0.5}\text{MnO}_3$, we show the resistivity data for $\text{Pr}_{0.5-x}\text{Nd}_x\text{Sr}_{0.5}\text{MnO}_3$ with $x = 0.0$ corresponding to $\text{Pr}_{0.5}\text{Sr}_{0.5}\text{MnO}_3$ and with $x = 0.5$ corresponding to $\text{Nd}_{0.5}\text{Sr}_{0.5}\text{MnO}_3$. Also shown are the effects of two intermediate compositions at $x = 0.1$ and $x = 0.3$. In the case of $\text{Pr}_{0.5}\text{Sr}_{0.5}\text{MnO}_3$, the material exhibits a high temperature insulator-metal transition around T_C (~ 265 K) followed by an insulating phase at ~ 110 K. $\text{Nd}_{0.5}\text{Sr}_{0.5}\text{MnO}_3$ on the other hand exhibits an I-M transition at 250 K followed by insulating state at 150 K. Unlike in $\text{Pr}_{0.5}\text{Sr}_{0.5}\text{MnO}_3$, the onset of the insulating state in $\text{Nd}_{0.5}\text{Sr}_{0.5}\text{MnO}_3$ is also concomitant with charge ordering setting in.

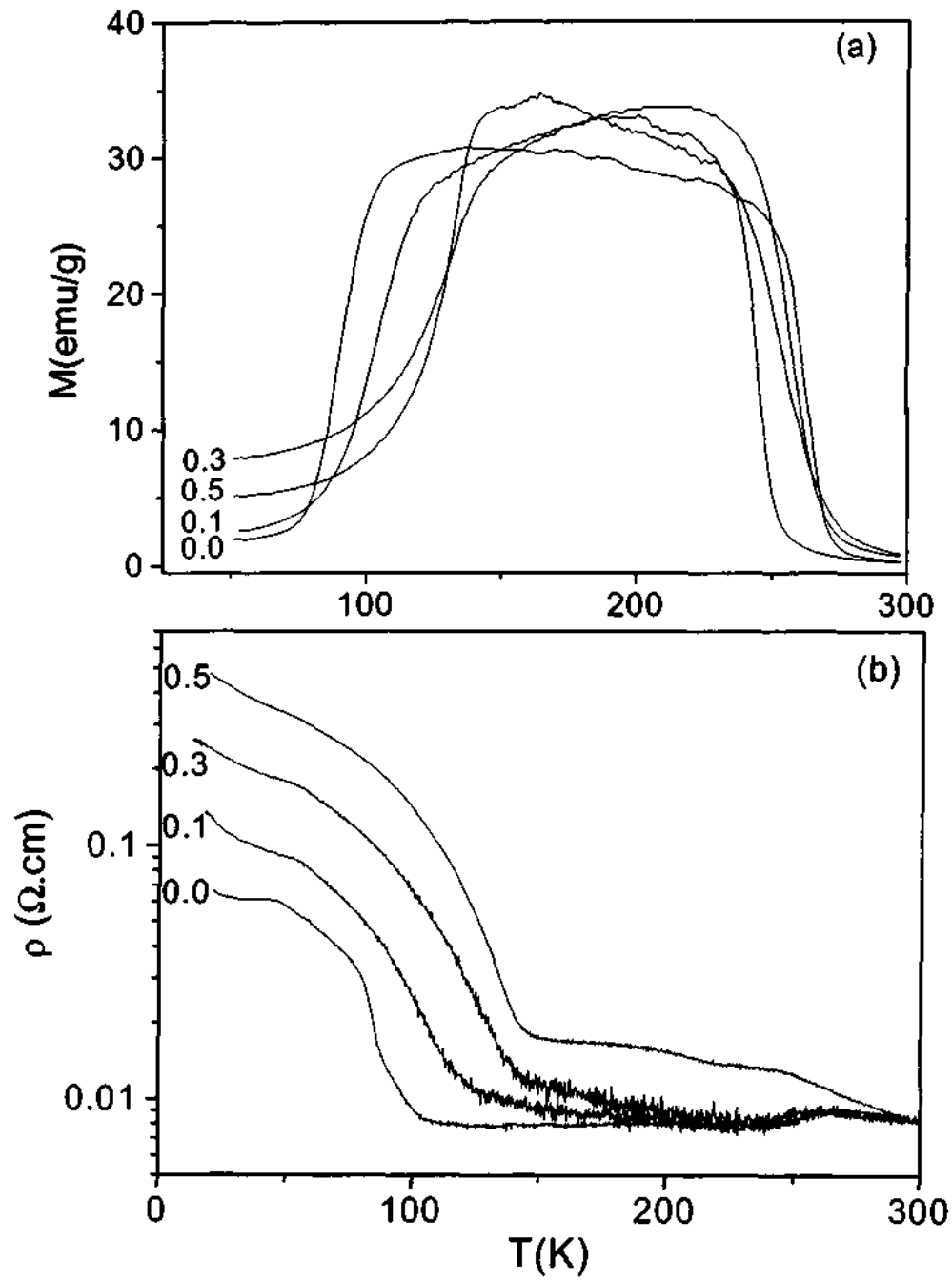


Fig. 1. 80. (a) Magnetization data and (b) resistivity data of $\text{Pr}_{0.5-x}\text{Nd}_x\text{Sr}_{0.5}\text{MnO}_3$.

As seen in Fig. 1. 80b, on increasing the Nd content to $x = 0.1$ corresponding to $\text{Pr}_{0.4}\text{Nd}_{0.1}\text{Sr}_{0.5}\text{MnO}_3$, the onset of the low temperature insulating state shifts to a marginally higher value of 120 K. In the magnetization data, we see that the Néel temperature also shifts to a higher temperature corresponding to 125 K. The Curie temperature T_C however exhibits a smaller shift in comparison. On increasing the Nd content to $x = 0.3$ i.e., in $\text{Pr}_{0.2}\text{Nd}_{0.3}\text{Sr}_{0.5}\text{MnO}_3$, we see that in resistivity and magnetization data, the onset of the antiferromagnetic insulating state shifts to a higher temperature. In Fig 1.81a, we have plotted the variation in T_C and T_N obtained from the magnetization data as a function of increasing Nd content. We find that the slope is higher in the case of T_N than in T_C . This reflects that the antiferromagnetic/charge-ordering temperature is very sensitive to radii effect or in other words it depends on the internal pressure. In Fig. 1. 81b, we show the difference plot of T_C and T_N . We gather from the difference plot that the transition from A-type to CE-type antiferromagnet is a gradual process with increasing x . In order to validate this, we have carefully examined the powder x-ray diffraction data.

1.4.6 Layered manganates

In Fig. 1. 82, we show the x-ray diffraction pattern of $\text{Nd}_{0.5}\text{Ca}_{1.5}\text{MnO}_4$. The low angle peak corresponding to (002) peak is indicative of the layered structure. The material adopts the tetragonal space group $I4/mcm$ symmetry. The lattice

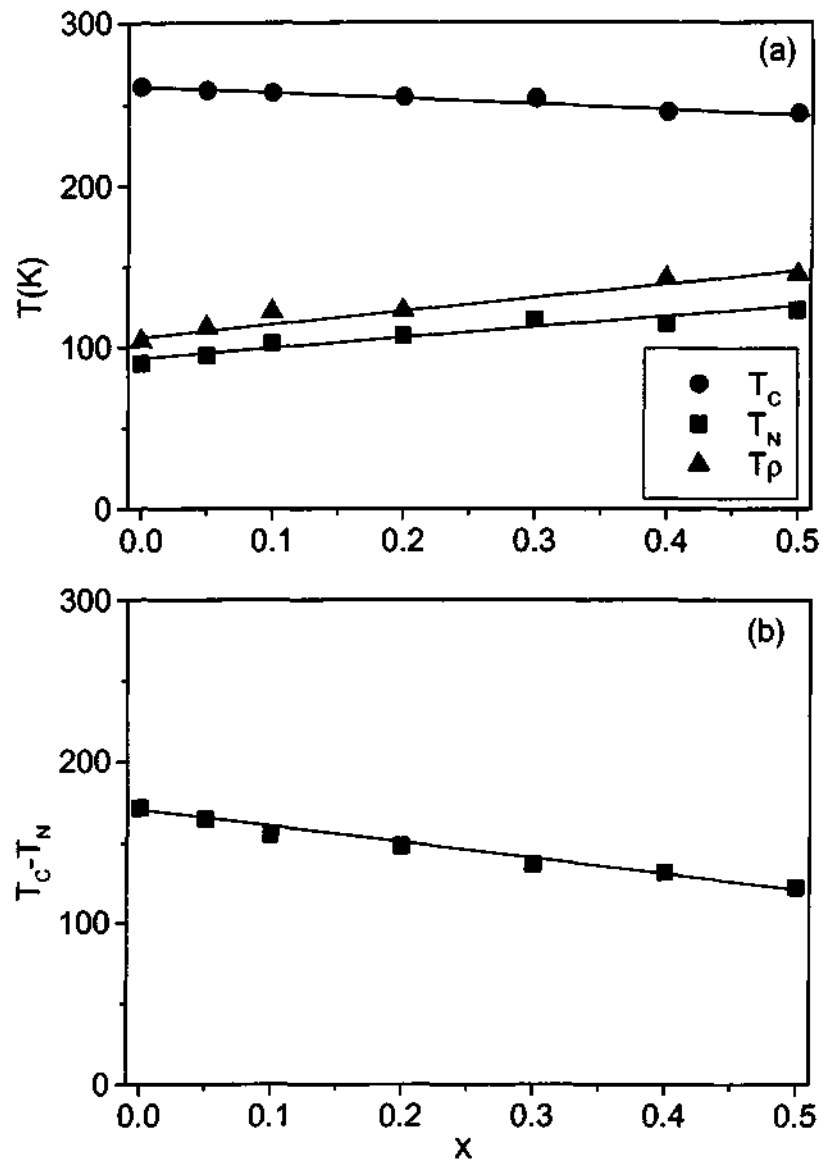


Fig. 1. 81. (a) The Curie temperature (T_C) and the Néel temperature (T_N) obtained from magnetization data plotted as a function of x in $\text{Pr}_{0.5-x}\text{Nd}_x\text{Sr}_{0.5}\text{Sr}_{0.5}\text{MnO}_3$. Also show is the corresponding insulating phase onset temperature (T_ρ) obtained from the resistivity data. In (b) the difference of Curie and Néel temperature is shown as a function of composition change.

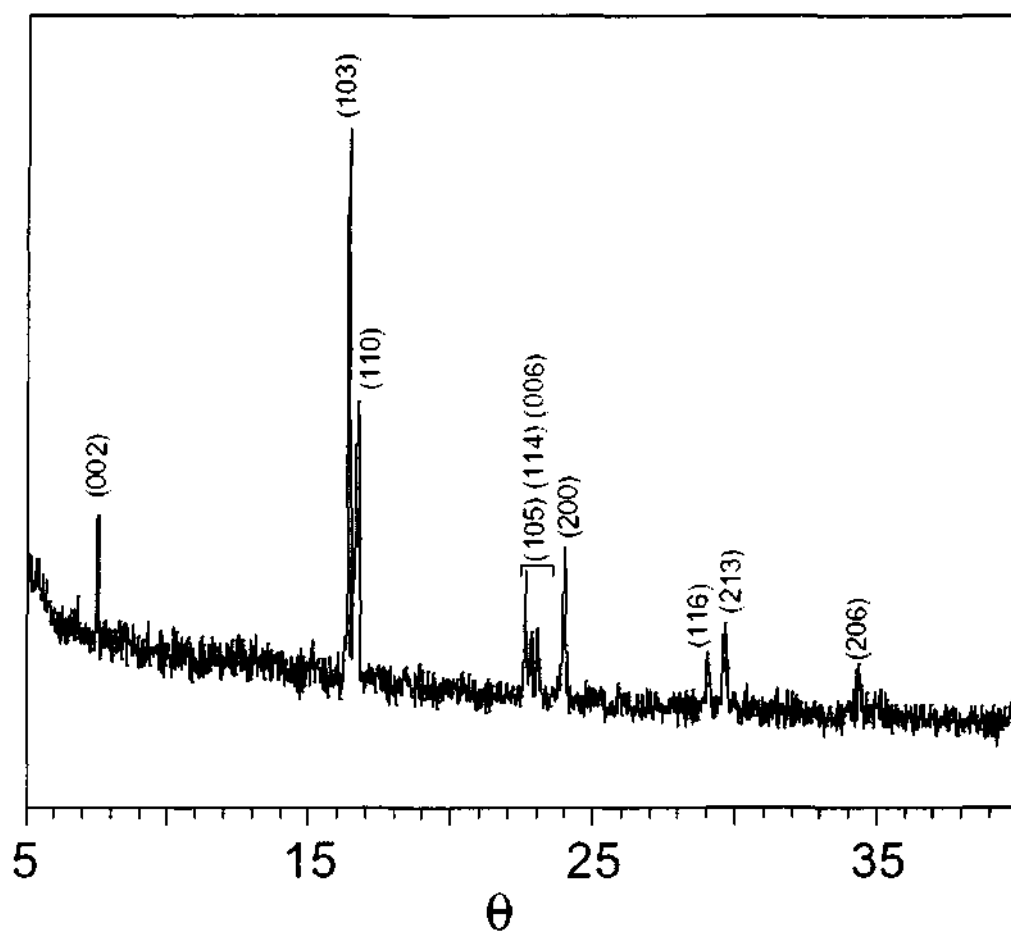


Fig. 1. 82. X-ray powder diffraction pattern of layered manganate $\text{Nd}_{0.5}\text{Ca}_{1.5}\text{MnO}_4$
($n = 1$ Ruddlesden-Popper series).

constants obtained were: $a = b = 3.7901 \text{ \AA}$ and $c = 11.8053 \text{ \AA}$. In Fig. 1. 83a and 1.83b, we show the magnetization and resistivity behavior of single crystal of this material. The resistivity data reveals $\text{Nd}_{0.5}\text{Ca}_{1.5}\text{MnO}_4$ to be insulating over the entire temperature range. Moreover, the data fits well with an activated energy hopping behaviour with a constant activation energy. No evidence of charge ordering has been seen. The magnetization data shows the material to be paramagnetic. This preliminary finding is important, because in the case of $\text{Nd}_{0.5}\text{Sr}_{1.5}\text{MnO}_4$, Moritomo et al [108], found no trace of charge ordering. Thus in this $n = 1$ layered material, even on lowering the average radii (by replacing Sr by Ca), we find no evidence of charge ordering. Further studies are necessary to fully understand the charge ordering process in these layered manganates.

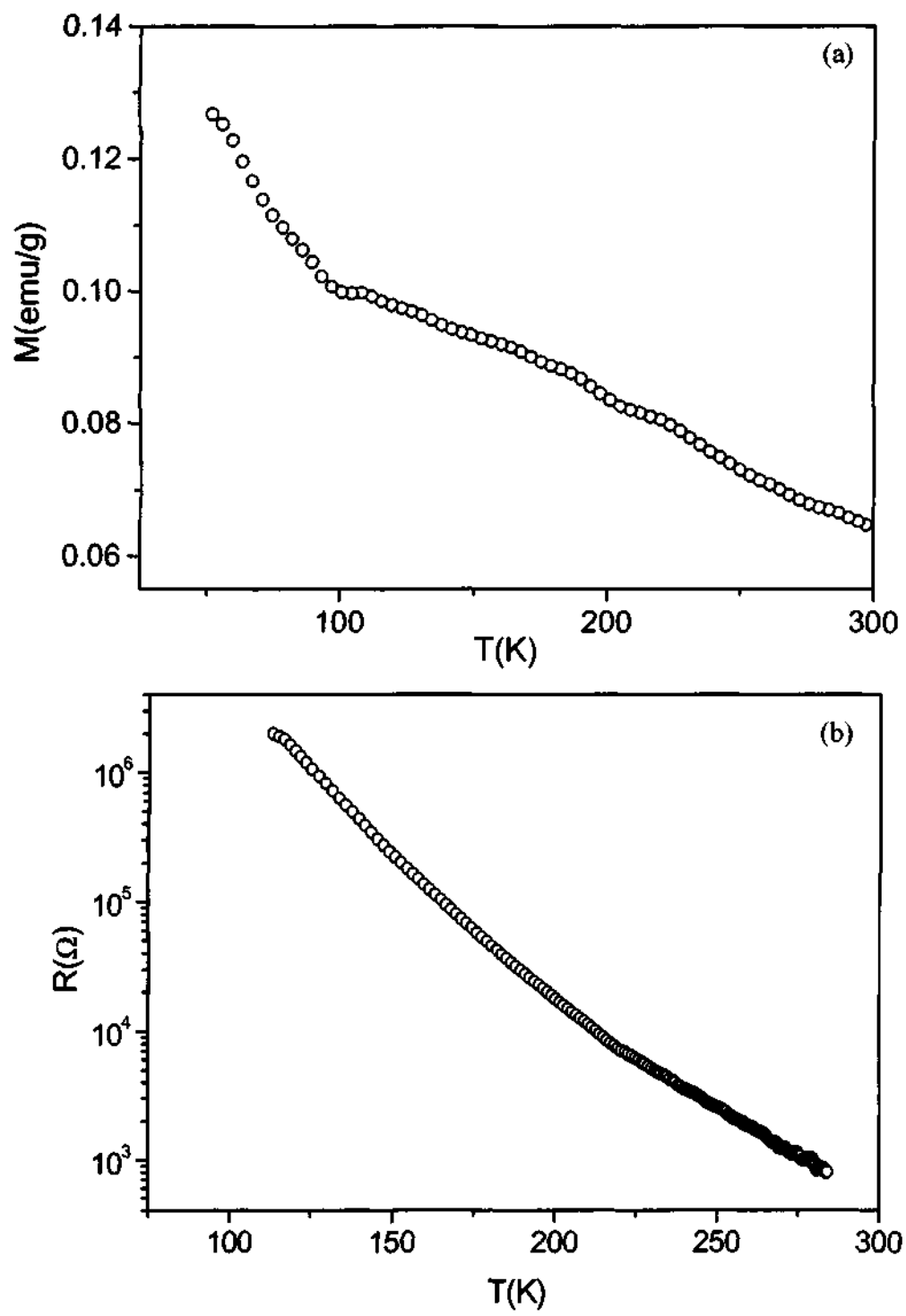


Fig. 1. 83. (a) Magnetization data and (b) resistivity data of $\text{Nd}_{0.5}\text{Ca}_{1.5}\text{MnO}_4$ as a function of temperature.

REFERENCES

- [1] C. N. R. Rao and B. Raveau (Eds), *Colossal Magnetoresistance, Charge ordering and Related Properties of Manganese oxides*, World Scientific (1998) Singapore.
- [2] C. N. R. Rao, *J. Phys. Chem. B*, **104** (2000) 5877.
- [3] A. P. Ramirez, *J. Phys.; Condens. Matter*, **9** (1997) 8171.
- [4] A. M. Imada; A. Fujimori and Y. Tokura, *Rev. Mod. Phys.*, **70** (1998) 1039.
- [5] E. J. W. Verwey, *Nature (London)*, **144** (1939) 327.
- [6] P. A. Miles; W. B. Westphal and A. von Hippel, *Rev. Mod. Phys.*, **29** (1957) 279.
- [7] J. M. Honig, *The Metallic and the Nonmetallic States of Matter* (Eds: P. P. Edwards and C. N. R. Rao), Taylor and Francis (1985) London.
- [8] J. M. Honig, *Proc. Indian. Acad. Sci., Chem. Sci.*, **96** (1986) 391.
- [9] N. Tsuda; K. Nasu; A. Yanase and K. Siratori, *Electronic Conduction in Oxides*, Springer (1991) Berlin.
- [10] M. L. Rudee; J. D. Smith and D. T. Margulies, *Phys. Rev.* **B59** (1999) R11633.
- [11] M. L. Rudee; J. D. Smith and D. T. Margulies, *Microsc. Microanal.*, **6** (2000) 400.
- [12] M. Takano and Y. Takeda, *Bull. Inst. Chem. Res.*, **61** (1983) 406.
- [13] P. D. Battle; T. C. Gibb and P. Lightfoot, *J. Solid State Chem.*, **84** (1990) 271.
- [14] J. M. Tranquada; J. E. Lorenzo; D. J. Buttrey and V. Sachan, *Phys. Rev.*, **B52** (1995) 3581.
- [15] C. H. Chen; S. -W. Cheong and A. S. Cooper, *Phys. Rev. Lett.*, **71** (1993) 2461.

- [16] T. T. Katsufuji; T. Tanabe; T. Ishikawa; Y. Fukuda; T. Arima and Y. Tokura, *Phys. Rev.*, **B54** (1996) R14230.
- [17] J. R. Carvajal; G. Rouse; C. Masquelier and M. Hervieu, *Phys. Rev. Lett.*, **81** (1998) 4660.
- [18] A. S. Willis; N. P. Raju and J. E. Greedan, *Chem. Mater.*, **11** (1999) 1510.
- [19] Y. Tokura (Ed), *Colossal Magnetoresistive Oxides*, Gordon & Breach Science Publishers, 1999.
- [20] M. R. Oliver; J. O Dimmock; A. L. McWhorter and T. B. Reed, *Phys. Rev.* **B5** (1972) 1078.
- [21] J. B. Goodenough, *Localized to Itinerant Electronic Transition in Perovskite Oxides*, Springer (2001) Berlin.
- [22] P. W. Anderson and H. Hasegawa, *Phys. Rev.*, **100** (1955) 675.
- [23] C. Zener, *Phys. Rev.*, **82** (1951) 403.
- [24] P. -G. de Gennes, *Phys. Rev.*, **118** (1960) 141.
- [25] P. W. Anderson, *Phys. Rev.*, **86** (1952) 694.
- [26] R. Kubo; *Phys. Rev.*, **87** (1952) 568.
- [27] E. O. Wollan and W. C. Koehler, *Phys. Rev.*, **100** (1955) 545.
- [28] J. B. Goodenough, *Phys. Rev.*, **100** (1955) 564.
- [29] J. B. Goodenough; A. Wold; R. J. Arnolt and N. Menyuk, *Phys. Rev.*, **124** (1961) 373.
- [30] P. M. Levy, *Solid State Phy.* **47** (1994) 367.
- [31] P. M. Levy and S. Zhang, *J. Magn Magn. Matter.*, **151** (1995) 315.

- [32] R. von Helmolt; B. Holzapel; I. Schultz and K. Samwer, *Phys. Rev. Lett.*, **71** (1993) 2331.
- [33] K. Chahara; T. Ohno; M. Kasai and Y. Kozono, *Appl. Phys. Lett.*, **63** (1993) 1990.
- [34] M. McCormack; S. Jin; T. Tiefel; R. M. Fleming; J. M. Phillips and R. Ramesh, *Appl. Phys. Lett.*, **64** (1994) 3045.
- [36] R. Mahesh; R. Mahendiran; A. K. Raychaudhuri and C. N. R. Rao, *J. Solid State Chem.*, **114** (1995) 297.
- [37] A. Urshibara; Y. Moritomo; T. Arima; A. Asamitsu; G. Kido and Y. Tokura, *Phys. Rev.*, **B51** (1995) 297.
- [38] M. F. Hundley; J. H. Nickel; R. Ramesh and Y. Tokura (Eds), *Science and Technology of Magnetic Oxides, Mater. Res. Soc. Sym. Proc.*, Pittsburgh (1998) 494.
- [39] H. Yoshizawa; H. Kawano; Y. Tomioka and Y. Tokura, *Phys. Rev.*, **B52** (1995) R13145.
- [40] Y. Tomioka; A. Asamitsu; Y. Moritomo and Y. Tokura, *J. Phys. Soc. Jpn.* **64** (1995) 3626.
- [41] R. Mahendiran; S. K. Tiwary; A. K. Raychaudari; T. V. Ramakrishnan; R. Mahesh; N. Rangavittal and C. N. R. Rao, *Phys. Rev.*, **B53** (1996) 3348.
- [42] A. Arulraj; P. N. Santhosh; R. S. Gopalan; A. Guha; A. K. Raychaudari; N. Kumar and C. N. R. Rao, *J. Phys: Condens. Matter*, **10** (1998) 3652.

- [43] C. Martin; A. Maignan; F. Damay; M. Hervieu and B. Raveau, *J. Solid State Chem.*, **134** (1997) 198.
- [44] B. Raveau; Y. M. Zhao; C. Martin; M. Harvieu and A. Maignan, *J. Solid State Chem.*, **149** (2000) 203.
- [45] E. Pollert; S. Krupicka; and E. Kuzmicova, *J. Phys. Chem. Solids*, **43** (1982) 1137.
- [46] M. Roy; J. F. Mitchell; A. P. Ramirez and P. Schiffer, *J. Phys.: Condens. Matter* **11** (1999) 4843.
- [47] H. Kuwahara; Y. Tomioka; A. Asamitsu; Y. Moritomo; and Y. Tokura; *Science*, **270** (1995) 961.
- [48] P. M. Woodward; T. Vogt; D. E. Cox; A. Arulraj; C. N. R. Rao; P. Karen and A. K. Cheetham, *Chem. Mater*, **10** (1998) 3652.
- [49] H. Yoshizawa; H. Kawano; Y. Tomioka and Y. Tokura, *Phys. Rev.*, **B52** (1995) 13145.
- [50] Y. Tomioka; A. Asamitsu; H. Kuwahara; Y. Moritomo and Y. Tokura, *Phys. Rev.*, **B53** (1996) R1689.
- [51] Y. Tokura and N. Nagaosa; *Science*, **288** (2000) 462.
- [52] Y. Okimoto; Y. Tomioka; Y. Onose; Y. Otsuka and Y. Tokura, *Phys. Rev.*, **B57** (1998) R9377.
- [53] S. Ishihara and N. Nagaosa, *J. Phys. Soc. Jpn.* **66** (1997) 3678.
- [54] A. Biswas; A. K. Raychaudhuri; R. Mahendiran; A. Guha; R. Mahesh and C. N. R. Rao, *J. Phys: Condens. Matter*, **9** (1997) L355.

- [55] A. Sekiyama; S. Suga; Fujikawa; S. Imada; T. Iwasaki; T. Matsuda; T. Matsushita; K. V. Kaznachejev; A. Fujimoro, H. Kuwahara and Y. Tokura, *Phys. Rev.* **B59**, (1999) 15528.
- [56] N. Kumar and C. N. R. Rao, *J. Solid State Chem.*, **129**, (1997) 363.
- [57] A. Arulraj, *Colossal Magnetoresistance, Charge-Ordering and Properties of Rare Earth Manganates and Related Properties (Thesis)*, (1999).
- [58] M. Medaede, J. Mesot, P. Lacorre, S. Rosenkranz, P. Fischer and K. Gobrecht, *Phys. Rev.*, **B52** (1995) 9248.
- [59] L. M. R-. Martinez and J. P. Attfield, *Phys. Rev.*, **54** (1996) R15622.
- [60]] L. M. R-. Martinez and J. P. Attfield, *Phys. Rev.*, **58** (1998) 2426.
- [61] J. P. Attfield, *Chem. Mater.*, **10** (1998) 3239.
- [62] P. V. Vanitha; P. N. Santhosh; R. S. Singh; C. N. R. Rao and J. P. Attfield, *Phys. Rev.*, **59** (1999) 13539.
- [63] P. G. Radaelli; D. E. Cox; M. Marezio and S.W-. Cheong, *Phys. Rev.*, **B55** (1997) 3015.
- [64] A. Arulraj; A. Biswas; A. K. Raychaudhuri; C. N. R. Rao; P. M. Woodward; T. Vogt; D. E. Cox and A. K. Cheetham, *Phys. Rev.*, **B57** (1998) R8115.
- [65] A. Barnabé; A. Maignan; M. Hervieu and B. Raveau, *Eur. Phys. J.*, **B1** (1998) 145.
- [66] A. Barnabé; A. Maignan; M. Hervieu; ; F. Damay; C. Martin and B. Raveau, *Appl. Phys. Lett.*, **71** (1997) 3907.

- [67] C. Martin; A. Maignan; F. Damay; M. Hervieu; B. Raveau; Z. Jirak; G. André and F. Bourée, *J. Magn. Magn. Matter*, **202** (1999) 11.
- [68] B. Raveau; A. Maignan and C. Martin, *J. Solid State. Chem.*, **130** (1997) 162.
- [69] A. Maignan; ; F. Damay; C. Martin and B. Raveau, *Mater. Res. Bull.*, **32** (1997) 965.
- [70] F. Damay; A. Maignan; C. Martin and B. Raveau, *J. Appl. Phys.*, **82** (1997) 1485.
- [71] K. Y. Wang; W. H. Song; J. M. Dai, S. L. Ye; S. G. Wang; Y. P. Sun and J. J. Du, *Phys. Stat. Sol(a)*, **184** (2001) 515.
- [72] P. V. Vanitha; A. Arulraj; A. R. Raju and C. N. R. Rao; *C. R. Acad. Sci. Paris, II* (1999) 595.
- [73] B. Raveau; A. Maignan; C. Martin; R. Mahendiran and M. Hervieu, *J. Solid State Chem.*, **151** (2000) 330.
- [74] A. M. Balagurov; V. Yu. Pomjakushin; D. V. Sheptyakov; V. L. Aksenov; N. A. Babushkina; L. M. Belova; A. N. Taldenkov; A. V. Inyushkin; P. Fischer; M. Gutmann; L. Keller; O. Yu. Gorbenko and A. R. Kaul, *Phys. Rev.*, **60** (1999) 383.
- [75] B. G. Landa; M. R. Ibarra; J. M. De Teresa; G. Zhao; K. Conder; H. Keller, *Solid State Commun.*, **105** (1995) 567.
- [76] G. Zhao; K. Ghosh; H. Keller; R. L. Greene, *Phys. Rev.* **B59**, (1999) 81.
- [77] Guo-meng Zhao; D. J. Kang; W. Prellier; M. Rajeswari; H. Keller; T. Venkatesan and R. L. Greene, *Phys. Rev.*, **B63** (2000) 060402(R).

- [78] N. A. Babushkina; L. M. Belova; O. Yu. Gorbenko; A. R. Kaul; A. A. Bosak; V. I. Ozhogin and K. I. Kugel, *Nature*, **391** (1998) 159.
- [79] C. Martin; A. Maignan; M. Hervieu; B. Raveau; Z. Jirak; M. M. Savosta; A. Kurbakov; V. Trounov, G. André and F. Bourée, *Phys. Rev.*, **B62** (2000) 6442.
- [80] P. M. Woodward; D. E. Cox; T. Vogt; C. N. R. Rao and A. K. Cheetham, *Chem. Mater.*, **11** (1999) 3528.
- [81] N. A. Babushkina; A. N. Taldenkov; L. M. Belova; E. A. Chistotina; O. Yu. Gorbenko; A. R. Kaul; K. I. Kugel and D. I. Khomskii, *Phys. Rev.*, **B62** (2000) R6081.
- [82] T. Kimura; Y. Tomioka; R. Kumai; Y. Okimoto and Y. Tokura, *Phys. Rev. Lett.*, **83** (1999) 3940.
- [83] C. N. R. Rao; A. R. Raju; V. Ponnambalam; S. Parashar and N. Kumar, *Phys. Rev.*, **B61** (2000) 591.
- [84] A. Guha; A. Ghosh; A. K. Raychaudhuri; S. Parashar; A. R. Raju and C. N. R. Rao, *Appl. Phys. Lett.*, **75** (1999) 3381.
- [85] A. M. H. Gosnet; M. Hervieu; Ch. Simo; B. Mercey; B. Raveau, *J. Appl. Phys.*, **88** (2000) 3545.
- [86] L. V. Saraf; S. B. Ogale; Z. Chen; R. P. Godfrey; T. Venkatesan; R. Ramesh, *Phys. Rev.*, **B62** (2000) R11961.
- [87] T. Kimura and Y. Tokura, *Ann. Rev. Mater. Sci.*, **30** (2000) 445.
- [88] Y. Moritomo, A. Asamitsu, H. Kuwahara and Y. Tokura, *Nature*, **380** (1996) 141.

- [89] T. Ishikawa; K. Ookura and Y. Tokura; *Phys. Rev.*, **B59** (1999) 8367.
- [90] M. Tokunaga; N. Miura; Y. Moritomo and Y. Tokura, *Phys. Rev.*, **B59** (1999) 11151.
- [91] J. Q. Li; Y. Matsui; T. Kimura and Y. Tokura, *Phys. Rev.*, **B57** (1998) 3205.
- [92] C. N. R. Rao; A. Arulraj; A. K. Cheetham and B. Raveau, *J. Phys.: Condens. Matter*, 2000, **12**, R83.
- [93] A. Maignan; C. Martin; F. Damay and B. Raveau, *Chem. Mater.*, 10 (1998) 950.
- [94] P. N. Santhosh; A. Arulraj; P. V. Vanitha; R. S. Singh; K. Sooryanarayana and C. N. R. Rao, *J. Phys.: Condens. Matter*, 11 (1999) L27.
- [95] T. V. Ramakrishnan and C. N. R. Rao, *Superconductivity Today* (Second Edition) University Press (1999) India.
- [96] A. Barnabé; M. Hervieu; C. Martin; A. Maignan and B. Raveau, *J. Mater. Chem.*, 8 (1998) 1405.
- [97] M. Jaime, V. Salamon, V. Pettit, V. Rubinstein, R. E. Treece, J. S. Horowitz, D. B. Chrisey, *Appl. Phys. Lett.*, 68 (1996) 1576;
- [98] M. Jaime, V. Salamon, V. Rubinstein, R. E. Treece, J. S. Horowitz, D. B. Chrisey, *Phys. Rev.*, **B54** (1996) 11914.
- [99] M. Viret, L. Ranno, J. M. D. Coey, *Phys. Rev.*, **B55** (1997) 8067.
- [100] V. H. Crespi, L. Li, Y. X. Jia, K. Khazeni, A. Zetll, M. L. Cohen, *Phys. Rev.*, **B53** (1996) 14303.
- [101] Y. X. Jia, K. Khazeni, D. Yen, C. S. Lee, A. Zetll, *Solid State Commun.*, 94 (1995) 917.

- [102] J. M. D. Coey, M. Viret, L. Ranno, K. Ounadjela, *Phys. Rev. Lett.*, **75** (1995) 3910.
- [103] G. -M. Zhao, Y. S. Wang, D. J. Kang, W. Prellier, M. Rajeshwari, H. Keller, T. Venkatesan, C. W. Chu, R. L. Greene, *Phys. Rev.*, **B62** (2000) 11949.
- [104] G. Ji, X. J. Fan, J. H. Zhang, C. S. Xiong, G. Li, *J. Phys. D: Applied Phys.*, **31** (1998) 3036.
- [105] P. S. A. Kumar, P. A. Joy, S. K. Date, *J. Phys.: Condens. Matter*, **10** (1998) L269.
- [106] B. J. Sternlib, J. P. Hill, U. C. Wildgruber, G. M. Luke, B. Nachumi, Y. Moritomo and Y. Tokura, *Phys. Rev. Lett.*, **76** (1996) 2169.
- [107] J. Q. Li, Y. Matsui, T. Kimura and Y. Tokura, *Phys. Rev.*, **B57** (1998) 3205.
- [108] Y. Moritomo, A. Nakamura, S. Mori, N. Yamamoto, K. Ohoyama and M. Ohashi, *Phys. Rev.*, **B56** (1997) 14879.
- [109] C. N. R. Rao, *Chemical Approaches to the Synthesis of Inorganic Materials*, Wiley Eastern, 1994.
- [110] E. I. Givargizov and S. A. Grinberg (Eds), *Growth of Crystals*, NewYork, 1991.
- [111] A. R. Raju; H. N. Aiyer and C. N. R. Rao, *Chem. Mater.*, **7** (1995) 225.
- [112] A. L. Larson and R. B. Von Dreele, GSAS (*General Structure Analysis System*), Las Alamos National Laboratory (LANL), USA.
- [113] Hwang, H. Y.; Cheong, S. W.; Radaelli, P. G.; Marezio, M.; Batlogg, B. *Phys. Rev. Lett.* **1995**, **75**, 914.

- [114] Mahesh, R.; Mahendiran, R.; Raychaudhuri, A. K.; Rao, C. N. R. *J. Solid State Chem.* **1995**, *120*, 204.
- [115] Gupta, R.; Joshi, J. P.; Bhat, S. V.; Sood, A. K.; Rao, C. N. R. *J. Phys. Condens. Matter*, **2000**, *12*, 6919.
- [116] Raveau, B.; Maignan, A.; Martin, C.; Hervieu, M. *Chem Mater.* **1998**, *10*, 2641.
- [117] Vanitha, P. V.; Singh, R. S.; Natarajan, S.; Rao, C. N. R. *J. Solid State Chem.* **1998**, *137*, 365.
- [118] Maignan, A.; Martin C.; Damay, F.; Raveau, B.; Hejtmanek, J. *Phys. Rev.* **1998**, *B58*, 2758.
- [119] Neumeier, J. J.; Cohn, J. L. *Phys. Rev.* **2000**, *B61*, 14319.
- [120] Mahendiran, R.; Tiwary, S. K.; Raychaudhuri, A. K.; Ramakrishnan, T. V.; Mahesh, R.; Rangavittal, N.; Rao, C. N. R. *Phys. Rev.* **1996**, *B53*, 3348.
- [121] Poeppelmeier, K. R.; Leonowicz, M. E.; Scanlon, J. C.; Longo, J. M.; Yellon, W. B. *J. Solid State Chem.* **1982**, *45*, 71.
- [122] Radaelli, P. G.; Cox, D. E.; Marezio, M.; Cheong, S. W.; Schiffer, P. E.; Ramirez, A. P. *Phys. Rev. Lett.* **1995**, *75*, 4488.
- [123] Radaelli, P. G.; Cox, D. E.; Capogna, L.; Cheong, S. -W.; Marezio, M. *Phys. Rev.* **1999**, *B59*, 14440.
- [124] Taguchi, H.; Sonoda, M.; Nagao, M. *J. Solid State Chem.* **1998**, *137*, 82.
- [125] Sundaresan, A.; Paulose, P. L.; Mallik, R.; Sampathkumaran, E. V. *Phys. Rev.* **1998**, *B57*, 2690.

- [126] A. Guha, A.K. Raychaudhuri, A.R. Raju, C.N.R. Rao, *Phys. Rev.*, **B62** (2000) 5320.
- [127] Andersen, O.K.; Jepsen, O. et al *The Stuttgart TB-LMTO-ASA-47 Program*,
MPI für Feukörperforschung, Stuttgart, 1998
- [128] Skriver, H. L. *The LMTO Method*; Springer, Berlin, 1984.
- [129] Felser, C.; Seshadri, R.; Leist, A.; Tremel, W. *J. Mater. Chem.* **1998**, *8*, 787.
- [130] Pickett, W. E.; Singh, D. J. *Phys. Rev.* **1996**, *B53*, 1146.
- [131] A. J. Millis; P. B. Littlewood and B. I. Shraiman, *Phys. Rev. Lett.*, **76** (1995)
5144.
- [132] T. Holstein, *Annals of Physics*, **8** (1959) 343.
- [133] M. R. Ibarra and J. M. De Teresa in *Colossal Magnetoresistance, Charge ordering and Related Properties of Manganese oxides*, World Scientific (1998)
Singapore, 120.
- [134] N. F. Mott, *Metal-Insulator Transitions*, Taylor & Francis (1990) London.
- [135] B. I. Shklovskii and A. L. Efros, *Electronic-Properties of Doped Semiconductors*,
Springer-Verlag (1984) Berlin.
- [136] R. Laiho; K. G. Lisunov; E. Lahderanta; V. N. Stamov and V. S.
Zakhavlinskii, *J. Phys.: Condens. Matter*, **13** (2001) 1233.
- [137] A. K. Jonscher, *Science*, **267** (1977) 673.
- [138] S. R. Elliot, *J. Non-Cryst. Solids*, **170** (1994) 97.

PART 2

METAL NANOPARTICLES AND THEIR CRYSTALLINE ARRAYS

Summary

The present work deals with the preparation of metal nanoparticles, followed by capping by alkane thiols as well as polymers. It is well known that metal nanoparticles need capping agents in order to stabilize them and prevent them from coagulation. Alkanethiols serve as ideal capping agents, since they self-assemble on surfaces of various solid substrates.

By employing ethylene glycol to reduce metal salts, sub-micron and nanometric particles of Au, Ag, Pd, Pt and Ru have been prepared. Transmission and scanning electron microscopy have been employed to characterize the particles. The role of the alcohol in the synthesis has also been investigated employing FT-IR spectroscopy.

A new procedure has been developed for the thiol-derivatization of Au, Ag and Pt nanoparticles. These derivatized particles are extremely stable and show no coagulation. More interestingly, they self-assemble into 2D arrays. Various techniques have been employed to characterize the nanocrystalline

arrays. The techniques include transmission electron microscopy (TEM), scanning tunnelling microscopy (STM) and x-ray diffraction (XRD). X-ray photoelectron spectroscopy (XPS) has been employed to obtain information on the electronic properties as well as the surface composition. Ultraviolet-visible spectroscopy (UV-Vis) has also been used in the study. The 2D arrays formed by the nanoparticles show low angle x-ray diffraction peaks. The STM image reveals the ordering as seen in TEM. The procedure has been successful in retaining the particle geometry. In terms of particle size and geometry, it has been established that the shape distribution is not crucial unlike particle size deviation as observed in the citric acid reduced sols of Au.

We have been able to build superlattices of metal nanoparticles on a metal substrate, the layers being separated from each other by 1, 10-decanedithiol, which act as spacer molecules. Accordingly, we have deposited Pt nanoparticles of mean diameter of ~ 1 nm and ~ 5 nm on Au substrates as well as Au nanoparticles (~ 6 nm) on an Ag substrate. Several characterization techniques such as XRD, STM and XPS have been employed in investigating these systems. Ultraviolet photoelectron spectroscopic (UPS) measurements were also carried out to probe the band structure of thiol-derivatized metal nanoparticles. The XRD patterns show that the particles are assembled on each layer. XPS studies revealed that we could build upto 5 layers of metal nanoparticles. Each layer showed characteristic XRD patterns. The STM image on the layers showed that

the particles are arranged in hexagonal geometry in each layer. UPS measurements showed that the bare metal features near Fermi-level are completely suppressed by dithiol assembly and no features of the nanoparticles were observed.

The interaction of the sulfur-containing conducting polymer, poly-octylthiophene with Au nanoparticles has been investigated. They form novel self-contained circular structures, which exhibit interesting fluorescence properties. We also studied this system employing near-field optical microscopy (NSOM) technique. Other characterization techniques employed include optical microscopy, SEM, TEM and photoluminescence (PL). We observed that the circular structures contained Au-nanoparticles held together by the polymer which was self-coiled. The PL measurements revealed that centre of the structure has more polymer than at the edges of the circular structures.

Papers related to this work have appeared in *Chem. Commun.* (1997), *J. Phys. Chem. B* (1998), *J. Phys. Chem. B* (1999), *Bull. Mater. Sci.* (1999), *Curr. Sci.* (2001) and *Chem. Phys. Lett.* (2001)

METAL NANOPARTICLES AND THEIR CRYSTALLINE ARRAYS

2.1 AN OVERVIEW OF METAL NANOPARTICLES AND THEIR ARRAYS

Small clusters of atoms of metallic elements exhibit intriguing physical properties [1]. Some of these properties have diverse technical applications. The properties of these clusters (also known as quantum dots) differ from those of free atoms and also from that of the bulk solid. Hence, the central question concerning the metallic phase is the development of the metallic behaviour starting from the atomic state. In the bulk metal, free electrons are responsible for the physical properties. These electrons have energy levels that are basically quasi-continuous in nature and hence account for the observed phenomena, such as the conductivity associated with the bulk metallic phase. However when the size of the metal is reduced, typically to the nanometre scale (shown schematically in Fig 2.1) as in quantum dots (also referred to as zero dimensional-0D material), these 'free electrons' become confined, wherein, the de-Broglie wavelength becomes comparable with the particle size. The result of such confinement manifests itself in the reduction of conductivity. The conduction band observed in the bulk metal will be absent and instead, discrete states will be present. Therefore, any attempt to incorporate these materials in a

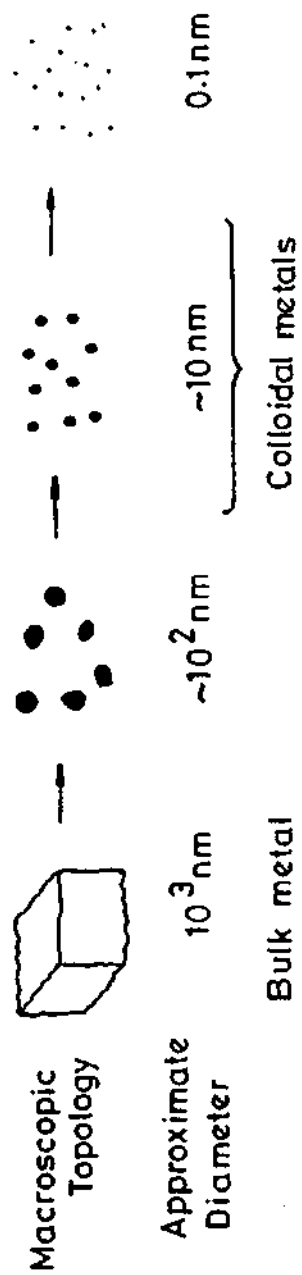


Fig. 2. 1 An artist's impression of the fragmentation or the division of a bulk metal giving rise to particles in the nanoscale regime.

future application such as a nanodevice, will prompt us first to synthesize and characterize these 0D materials or assemblies of these in 1D (quantum wires), 2D (quantum wells) arrays or 3D (superlattices) arrays [2,3].

This introduction focuses on recent as well as past works accomplished in the area of quantum well arrays of noble metal particles. A brief section is devoted to the synthesis of metal nanoparticles since new pathways have been developed to obtain 2D arrays using preformed clusters. It is concluded with some interesting applications in this field.

2.1.1 Synthesis of metal colloids

Metal colloids or sols as we know have existed since middle ages. Purple of cassins, a polymer coated gold colloid was a well know and used pigment in those days. Colloidal gold was first identified by Juncher in 1730 [4]. To the scientific community, the reason for the intense colour of these pigment materials was revealed by Sir Michael Faraday in 1857 when he prepared the first gold sol [5]. Since then the subject of colloidal chemistry has had a steady growth. However, over the last decade or so, there has been a sudden spurt in the activity to prepare metal sols in a narrow size distribution coupled with selective shape synthesis as well as the desire to have specific surfactant coatings. This is because

of their potential application in diverse fields like catalysis [6] and microelectronics [7].

Before undertaking a fascinating journey into the science of making clusters and colloids, it is necessary to differentiate between these two terms. Colloids are particles that have diameters that lie between 10-40 nm whereas clusters usually have diameters less than 10 nm. In terms of nomenclature, clusters are often referred by their 'magic number' whereas no such usage is employed for colloids. The distinction between the two terms becomes extremely important when physical properties are involved. Measurements of properties related to colloids (>20 nm) largely resemble those of the bulk whereas clusters exhibit quantum size effects [1]. Having noted these essential differences, we now proceed to see the synthesis aspects related to colloids and clusters.

Colloids have been synthesized in a variety of ways. However, all of them fall into two distinct categories (a) the dispersion method and (b) the reduction method. In the dispersion method, the bulk material is broken down into smaller particles resulting in the formation of colloids. An example is the arcing of metal electrodes to produce fine metal particles. The second method i.e., the reduction method relies on assembling metal atoms into colloids, by the suitable reduction of the corresponding metal salts. A suitable reducing agent would be such as a freshly prepared sodium borohydride (NaBH_4) solution.

Of all the metal colloids, gold is perhaps the best studied. Depending on their size, the colour of the sol can vary from light brown to red to rubyred through purple to blue. One of the well-known method involves the reduction of gold chloride (HAuCl_4) by using citric acid or trisodium citrate in an aqueous medium [8]. Various minute alterations to this methodology alongside experimental conditions have enabled preparation of gold sols with diameter ranging from tens of nanometer to a few microns [9]. In such methods as the above employed, the particle diameters obtained resemble a gaussian distribution. When truly monodisperse colloids are necessary, the germ-growth method is evoked [10]. This method involves the reduction of HAuCl_4 salt (usually with hydroxyammonium chloride) in an aqueous medium; the medium pre-seeded with a gold colloid of a smaller dimension. The smaller particles act as nucleation centres and help in the growth of colloids to desired size.

Other preparative methods are also employed in the preparation of gold colloids such as involving the use of alcohol as the reducing agent. A general method involving the synthesis of metal nanoparticles such as gold, silver, palladium and copper is the polyvinylpyrrolidone (PVP) method. In this procedure, ethanol is used as the reducing agent as well as the dispersion medium while PVP serves as the stabilizing agent [11]. Depending on the ratio of the metal salt to PVP (usually 1:5 or 1:10), either a colloidal or cluster sol can be

produced. Micron sized particles of metals such as Au, Ag, Cu, Co and Ni [12-15] have been synthesized by employing a similar strategy expect that the refluxing medium was ethylene glycol.

The above methods employed chemical reducing agents. In an altogether different technique, laser has been used to produce colloidal gold [16]. Here, dimethyl gold (III) hexafluoro-acetylacetonate (DMG-HF), a volatile substance is cast as a film on a substrate like a quartz slide and then laser of appropriate energy is shined to obtain colloidal gold. Thus, colloids can be prepared by the dispersion method in a solvent free environment.

A widely employed procedure reported in the synthesis of colloidal gold (30-400 nm range) is by the microemulsion method employing sodium (bis-2-ethylhexyl) sulfo succinate (AOT) [17]. In this procedure two preformed microemulsions are mixed; one microemulsion formed by HAuCl₄/AOT (n-heptane) and the other by N₂H₄. H₂SO₄/AOT (n-heptane) to obtain colloidal gold. Alteration of the emulsion ratio results in the variation of the diameter. Recently this method has been used in the preparation of shape selective copper nanoparticles [18]. In the procedure, Cu(AOT)₂ complex taken in iso-octane medium is directly reduced with hydrazine in an aqueous medium. The ratio of H₂O/AOT has been varied to obtain either cylindrical, spherical or a mixture of both shapes.

Although a majority of reported synthesis centres on gold colloids, palladium and platinum colloids have also been well documented in literature albeit to a lesser extent. These colloids can be prepared employing the citrate method (used in gold colloidal synthesis) starting from H_2PdCl_4 and H_2PtCl_6 salts as the starting material [19-21]. It has also been observed that palladium gives near monodisperse particles whereas platinum does not. Recently, shape controlled platinum nanoparticles have been prepared for the first time. By bubbling hydrogen gas through an aqueous solution of K_2PtCl_4 in the presence of sodium polyacrylate (serves as the protecting agent), cube shaped particles have been observed [22]. Various other metal sols have also been reported wherein the procedure employed is a variant of one of the above strategies. By employing the electrochemical technique, nickel nanoparticles have been recently synthesized wherein the particle diameter has been controlled from 20 to 600 nm [23].

Having seen the various preparative methods for obtaining colloidal metal particles, we shall now turn our attention to the synthesis of noble metal clusters. Clusters can be synthesized containing a fixed number of atoms and possessing unique geometry. These numbers are referred to as the magic numbers [24] and such clusters are associated with exceptional stability. The magic number series include the numbers 13, 55, 147, 309, 561, etc. Typically in a M_{13} cluster, 12 atoms surround the central atom. If an additional 42 atoms encapsulate a M_{13} cluster, it results in a M_{55} cluster. This process can be

generalized and it is observed that the total number of surface atoms follows the expression $10n^2 + 2$, n representing the encapsulating shell. An example of a metal cluster possessing magic number nuclearity is $\text{Au}_{55}(\text{PPh}_3)_{12}\text{Cl}_6$. Its structure is shown in Fig. 2. 2 although it must be mentioned that in light of a recent study, this picture of ccp packed gold atoms is questioned [25].

Among the various magic number clusters that have been synthesized, M_{55} type is the most extensively studied as they are easier to synthesize and reproduce. Gold [26], platinum, ruthenium and rhodium [27] are metals that have been synthesized in this class. The general method of preparation involves the reduction of specific metal precursor (or complex) by the use of B_2H_6 as the reducing agent, to obtain these high nuclearity clusters. Clusters of these type are under trial as important catalytic material, in particular $\text{Rh}_{55}[\text{P}(t\text{-Bu})_3]_{12}\text{Cl}_{20}$ and $\text{Rh}_{55}[\text{PPh}_3]_{12}\text{Cl}_{20}$ [28].

One of the largest magic number cluster compound that has been synthesized is $\text{Pd}_{561}(\text{phen})_{36}\text{O}_{200\pm 20}$ [29,30]. The synthesis involves the hydrogen gas reduction of $\text{Pd}(\text{CH}_3(\text{COO}))_2$ in the presence of phenanthroline (ligand) in aqueous solution, followed by the careful oxygenation (they react violently with oxygen) of this solution to obtain giant Pd_{561} clusters. This procedure if repeated with platinum acetate in place of palladium acetate one obtains $\text{Pt}_{309}\text{Phen}_{360}\text{O}_{30\pm 10}$ clusters [31].

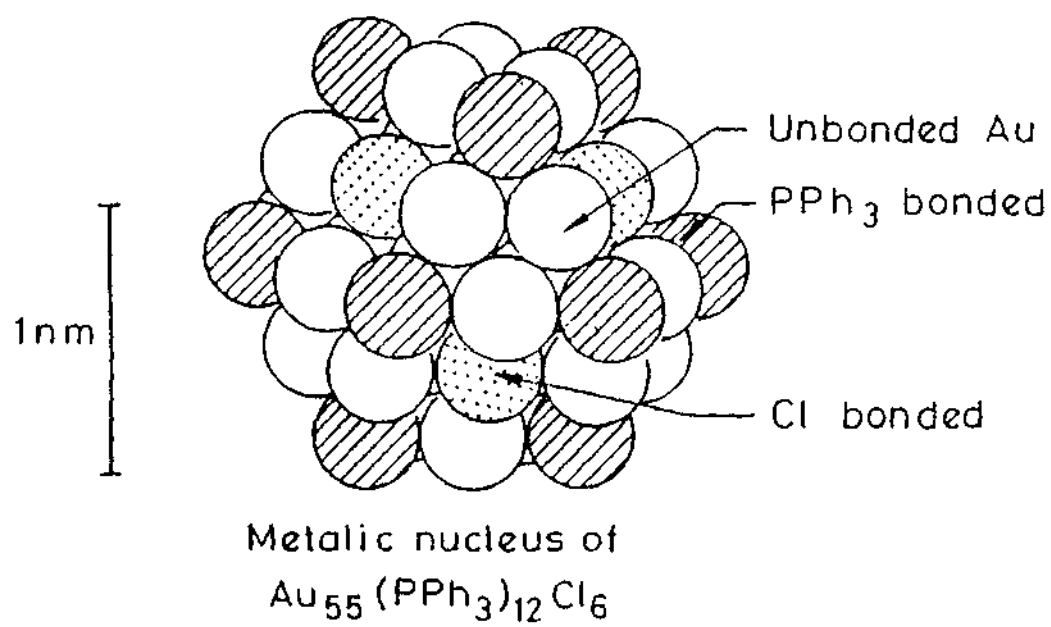


Fig. 2. 2. A model depicting the Au_{55} cluster packed in a FCC lattice type.

Apart from the clusters associated with magic numbers (and hence specific diameter and shape), particles with varying nuclearity and therefore different sizes can also be prepared. For example, clusters of Au with a mean dia of 1.5 nm have been prepared by the reduction of HAuCl_4 salt in an aqueous medium by the use of partially hydrolyzed THPC (Tetrakis(hydroxymethyl) phosphonium chloride) [32]. The average nuclearity of these clusters is 170. By varying the initial amount of HAuCl_4 , clusters till 6 nm can be prepared in a continuous manner.

A general method used in the preparation of transition metal clusters involves the reduction of the respective metal salts in aprotic solvents such as THF by the use of dissolved alkalides or electrides [33,34]. The alkalide $\text{K}^+(\text{18C6})_2\text{K}^-$ has been used in the preparation of gold nanoparticles of size ~ 5 nm. Excellent reviews in the synthesis and characterization of transition metal nanoparticles have been covered in the literature [8,35-43].

2.1.2 SAMs and nanoparticle arrays

The surface of gold is known for its chemical inertness to chemisorption, to even the most polar organic molecules. Yet when thiol containing organic molecules are evaporated onto gold substrate they adsorb [44]. These adsorbed molecules are seen to form densely packed, well ordered self-assembled monolayers (SAMs) which are characterized by high surface free energies that

distinguishes them from other molecular assemblies such as Langmuir-Blodgett films. These thiol containing organic molecules range from simple alkanethiols to biological macromolecules like DNA (Deoxyribose Nucleic Acid) [45] which contain disulphidic groups. Self-assembly has been observed with other transition metals also. Under appropriate conditions, SAMs on single crystalline as well as polycrystalline surfaces of silver, copper and platinum substrates have also been prepared [46, 47].

Traditionally organic monolayers have been made using Langmuir-Blodgett (LB) technique. However LB techniques suffer from numerous drawbacks that normal SAM preparation technique does not [48]. The main difference lies in the strong specific interaction between the adsorbate and the substrate which drives the spontaneous formation of the monolayer film which is not seen in LB films. Extensive studies have been carried out to understand the nature of this strong interaction. These include numerous physical techniques; such as electron energy loss spectroscopy (EELS) [49], low energy electron diffraction (LEED) [49,50], x-ray photoelectron spectroscopy (XPS) [48,50-53], ultraviolet photoelectron spectroscopy (UPS) [54,55], Auger spectroscopy [49], He diffraction [56,57], scanning probe microscopy (SPM) [58-60], electrochemistry [61-63] and several others. A few important results from these studies are discussed below so that they can be employed to understand a similar interaction involving the case of metal nanoparticle-thiol surfaces.

Self-assembled monolayers form on platinum, silver and copper surfaces in addition to gold surfaces where it is most stable and well formed. For an ordered SAM alkane chain length, n , must follow the rule, $n \geq 9$. The density packing of SAMs is different for different metals, the highest density being for copper. Whereas, thiols pack consummately on Au, it is not so in the case of silver and copper. The contact angle of the thiol molecule is $\sim 35^\circ$ on gold surface whereas on silver surface it is $\sim 10^\circ$. The conformation of the alkane molecules is largely trans, but on raising temperature above 300 K, the gauche density starts increasing [64]. The surface composition of these SAMs has revealed that sulfur exists as thiolate species, whereas on the contrary no oxidation state has been observed for the substrate metal. The interaction of the thiol molecules has been seen to reverse the oxidation process in metal surfaces such as in silver and copper by "peeling off" the oxide layer to form a SAM [46]. These SAMs once formed, are very stable systems and the underlying metal surface is therefore highly protected. Therefore these thiol molecules can be treated as ideal surfactants. They can then help in the stabilization of metal clusters and colloids. Furthermore, organic molecules can be modified by chemical reactions and can therefore be suitably modified to yield tailor made surfactants.

As mentioned before, gold nanoparticles are among the most studied of noble metal clusters. This is because of facile preparation, characterization and stability. Nanoparticles of Au with mean diameter 1-3 nm was perhaps the first thiol derivatized noble metal clusters [65,66]. Their preparation involves the

usage of a two phase liquid-liquid system. In this method, $[\text{AuCl}_4]^-$ ions in an aqueous medium are phase transferred by employing phase transfer reagents to a non-aqueous medium like toluene to be finally reduced in the presence of an alkanethiol (dodecanethiol in this case). It should be noted here that the nucleation, the growth as well as attachment of thiol molecules occurs almost simultaneously. The resulting sol can then be pumped free of the solvent to yield a solid, which is redispersable without any agglomeration leading to particle size increase. This is significant as unlike in the past, metal sols that are metastable systems can be treated as any other ordinary chemical on the shelf.

High Resolution Transmission Electron Microscopy (HRTEM) has revealed that a majority of the particles are either icosahedral or cuboctahedral in shape and a tiny few are twinned particles (which incidentally are predominant in many other preparations of Au sol [38]) and particles arrange themselves in the form of opal like structures [67].

A modification in the above synthesis has been to use dithiols in place of monothiols [68,69]. However two major differences exist in this kind of preparation. Firstly, the dithiol coated sol are not redispersable on removal of the solvent. Secondly and more important is that monothiol coated particles self-assemble in such a way that the thiol surfactants pack themselves allowing the

nanoparticles to come close to each other whereas in dithiol coated nanoparticles the particles are directly linked to each other.

To obtain a high quality two-dimensional array of gold nanocrystallites (associated with sharp diffraction peaks), the sols have been subjected to fractional crystallization cycles, wherein each step was monitored using mass-spectrometric analysis [70]. The purpose of these cycles has been to isolate single sized particles, wherein each fraction contains a fixed size of the Au nanocrystallite. Transmission electron microscopy (TEM) of each of these fractions show the presence of well ordered 2D array exhibiting diffraction spots. The x-ray diffraction (XRD) pattern shows lattice spacing at low angles (grazing angle) corresponding to a BCC type ordering of the array. In the case of silver nanoparticles, both 2-D and 3-D nanocrystalline arrays [71,72] have been prepared by in situ dosing of size selected Ag nanoclusters with alkylthiols and collecting these passivated clusters by passing them through a non-polar solvent like toluene. This method is however not a feasible route in the large scale synthesis of such systems in terms of the economics involved. The current aim of experimentalists is to obtain facile 3D ordering leading to the formation of crystals from a chemical route.

Other than the two-phase liquid-liquid system to thiol-derivatize nanoparticles, another procedure has been recently employed. Preformed Au

nanoparticles (~ 40 nm) in an aqueous medium (for example by the citrate method) are made to adsorb thiol molecules by using ethanol as the phase transfer solvent [73]. A number of functionalized surfactants have been studied in the self-assembly of Au nanoparticles prepared by this method.

In the 2D-self assembly of nanoparticles, it has been recently demonstrated that ordered lattice containing particles of two different sizes can be obtained. Specifically bimodal arrays of Au nanoparticles have been synthesized [74]. Bimodal arrays of Au and Ag have also been reported by this group [75].

Two-dimensional ordered lattices involving transition metal palladium nanoparticles have been synthesized by Rao *et al* [76]. In this study, particle size and thiol length variation have been studied to observe its effect on the ordering. It has been demonstrated that reasonable ordering is obtained when the particle diameter (d) and the thiol length (l) ratio (d/l) is between 1 and 4; the ordering optimized when ratio is maintained between 2 and 3. It must be noted that maintaining uniform diameter is better as it minimizes the entropy and leads to better packing. This is evident in the highly coherent 2D packing displayed in the case of cobalt nanoparticles encapsulated by oleic acid [77]. This 2D material is seen to exhibit properties observed in the bulk such as stacking faults and twin structures. Another possibility that is being explored is to employ thiolized

cluster compounds of fixed nuclearity as in magic number clusters. To this effect, 2D-lattices of thiolized Au₅₅ clusters, Pd₅₆₁ and Pd₁₄₁₅ clusters have been recently obtained [2,78].

A survey of literature will show that a number of novel variations have been employed in the selection of the surfactant. These include the use of functionalized alkanethiols [68,73] and aromatic systems containing mercapton groups [69,79]. In this context, the use of aryldithiol and arylisonitrile has been particularly novel. These materials act as molecular wires with their π -conjugated system offering a conduction "channel" between the clusters. It has been shown that the conductivity of these linked clusters vary from those of unlinked clusters [69].

Till recently, self-assembly of metal particles has been largely accomplished by the use of thiol oligomers. However, alkaneamines [80] have been used as substitutes for thiol molecules. The procedure adopted has been similar to the one described in the two-phase system with minor modifications. The formation of the clusters takes place in an aqueous medium following addition of the reducing agent NaBH₄ solution. By providing a high surface area of contact (stirring) between aqueous and non-polar solvent the Au nanocrystallites formed are transferred to alkaneamine containing phase. However, the stability of these particles are much lower. These leads to the

possible role of the phase transfer reagent as a passivating agent along with alkaneamine. To this effect, the sol has been prepared using the phase transfer reagent in the biphasic synthesis in the absence of alkylamine. It is seen that the Au nanoparticles coagulate and are not redispersable. This is in sharp contrast with earlier work reported, wherein similar preparations yielded sols that are infinitely stable. These leads to an important observation. The key to these agnostic points lies in the variation of the ratio of the Au ions to that of the reducing agent. Colloids are metastable by nature; the nucleation, growth and the stability very sensitive to the nature of the chemical surroundings. If concentrations of strong reducing agents like NaBH_4 vary even by tiny amounts, then let alone reproducibility, digressive results like the above are obtained. A final note in this aspect is that obtained from palladium clusters which are stabilized using only tetraalkyl ammonium salts. These are seen to form 2-D arrays when a it is supported on a substrate such as holey carbon grid [81]. Thus, it is seen that the self-assembly is not a feature restricted by the use of thiol surfactant alone.

In as much as oligomers have been used as surfactants in the self-assembly of metal nanoparticles, polymers have also been employed to obtain near perfect 2-D arrays. These polymers are so-called block co-polymers or the A-B diblock polymers and offer advantage to low molecular weight surfactants in respect to stability of self-organized structures. The kinetic stability of bulk co-

polymers is much larger and this helps in the size control of clusters by preventing agglomeration and Ostwald ripening. These block polymers form micelles in solutions and solid-films with regular micro domain structures. It is this aspect that helps in the formation of 2-D arrays. With the use of polystyrene-block-poly(2-vinylpyridine) [82], a microemulsion with one Au nanoparticle per micelle has been achieved, wherein TEM images (Fig. 2. 3) have shown remarkable ordering. Similar observations have been reported using poly(styrene)-b-poly(ethylene oxide) films [83]. Other novel structures are observed with polymers as well. An example is that of PS-*b*-PMMA (polystyrene-block-polymethyl-methacrylate) which is employed to prepare lamellar structures of Pd nanoparticles [84].

Finally, in a very interesting experiment Au colloids of 13 nm (mean dia) have been self-assembled into 2D structures by using DNA oligonucleotides [85]. These oligonucleotides have one end bearing a thiol group and this directs the long chain molecule in assisting the self-assembly process.

2.1.3 Properties of Self-Assembled 2D-Arrays

Self-assembled two-dimensional nanocrystalline arrays of noble metal particles in particular Au have been subjected to a number of studies; chemical, optical, electronic and thermal properties to name a few. Chemically, Au

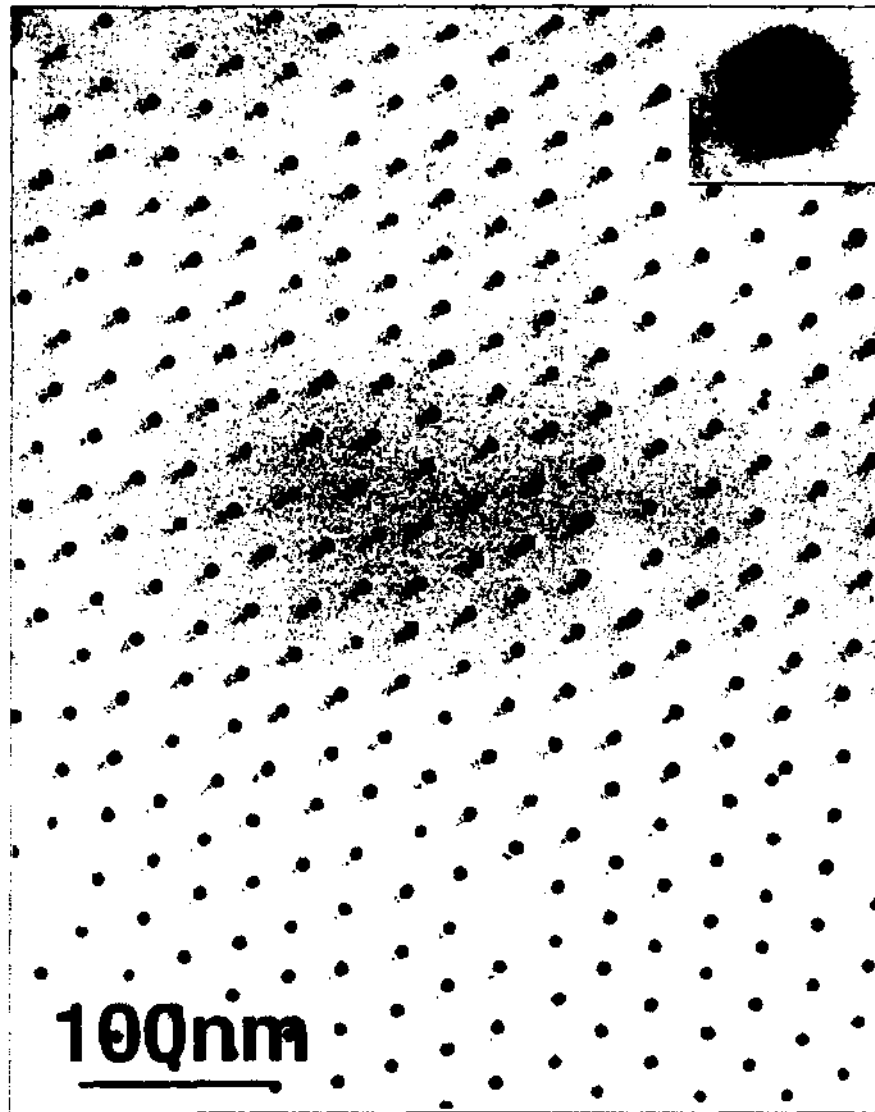


Fig. 2. 3. Block copolymer employed to assemble Au-nanoparticles [81].

nanocrystallites passivated by thiols are extremely resistant to acids and bases. They are in general soluble in non-polar solvents and totally insoluble in water or short chain alcohols. If thermally assisted, they undergo exchange reactions in solution with other organic moieties containing thiol group [86]. Flocculation studies of these thiol coated nanoparticles have been carried out [73]. The word flocculation essentially means aggregation and agglomeration. The distinction between the two is that aggregates once formed cannot be separated whereas it is not so in the latter. The flocculation rate of Au particles coated with different surfactants is monitored at a given pH by recording the integrated extinction-coefficient between 600-800 nm in a UV-Vis absorption study. The flocculation rate is then expressed as a function of time. This way the stability of a Au nanoparticles with different surfactant has been studied.

Optical properties include UV-Vis absorption studies which show characteristic plasmon absorption peaks of Au sols at 525 nm, wherein the intensity varies proportionately with the particle size [32]. X-ray diffraction studies of size selected Au nanoparticles [71] show two set of peaks, one at low angles and the other at high angles as shown in Fig 2.4. The high angle peaks are seen to be typical of FCC Au metal. The low angle peaks arise as a result of ordering seen in 2D array. These peaks are indexed as belonging to BCC lattice.

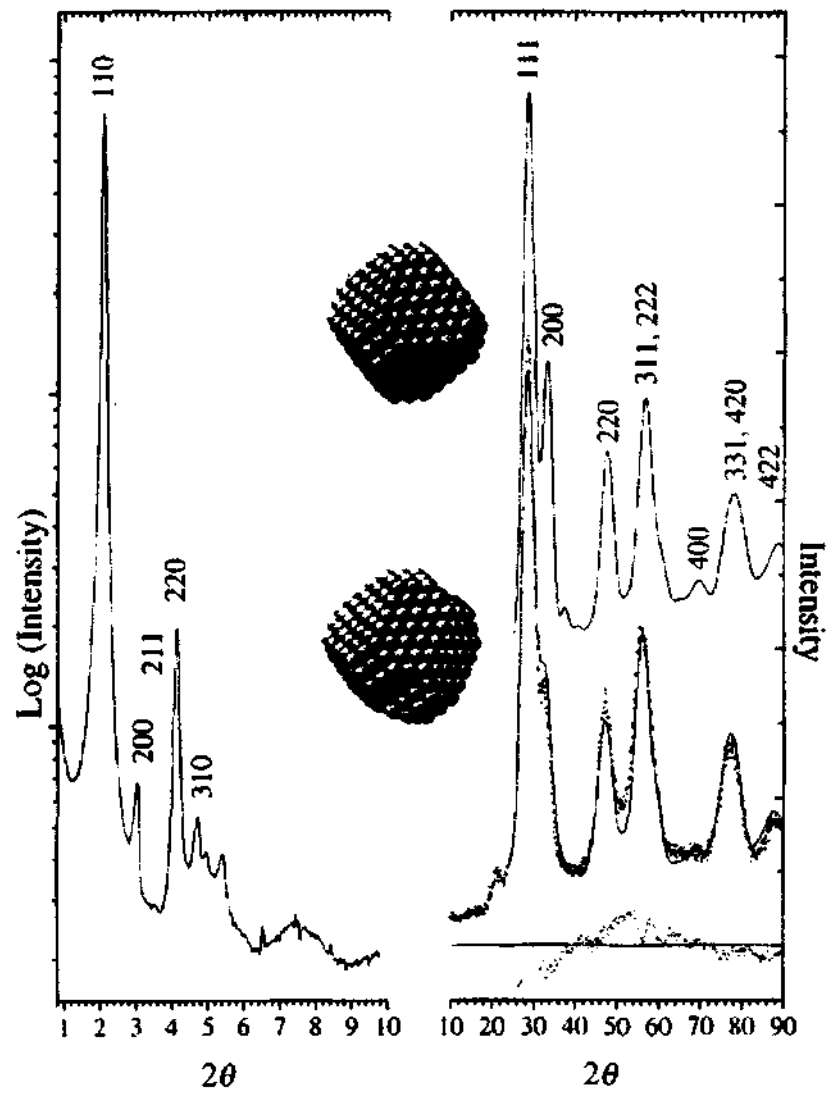


Fig. 2. 4. X-ray diffraction patterns of size selected Au nanoparticles in a 2D array. The low angle peaks correspond to the 2D-lattice whereas the higher angle peaks correspond to the bulk Au (FCC) lattice [71].

X-ray photoelectron spectroscopy of these materials show a peak at 83.8 eV characteristic of the Au(4f_{7/2}) core level in the bulk phase [68]. It is suggested that the Au-thiol bond does not have the character of Au-S linkage. This is important for two reasons. Firstly, several groups confirm the sulfur to be of thiolate species. Secondly, and more significant is the fact that small Au clusters show shifts in Au(4f_{7/2}) core level binding energy (~ 0.8 eV in extremely tiny particles) as a function of size [87]. Similar observations have been observed in alkaneamine coated Au nanoparticles [80]. Theoretical calculations based on these XPS results have shown that not more than 8% of the Au surface atoms are in the ionized state [80]. Ultraviolet photoelectron spectroscopy (UPS) studies on this can be expected to yield more information on the local density of states (LDOS) near E_F of Au metal thus giving more insight into the chemical state of the Au surface atoms. Such studies have been carried out only on dodecanethiol SAMs on Au(111) bulk surface. The UPS spectrum reveals that the LDOS at E_F is modified from that of the bare metal [54,55].

Proton NMR and ¹³C NMR have been carried out on alkaneamines [79] and alkanethiols [80,88,89] on gold clusters. The ¹H NMR studies have confirmed the presence of Au-N and Au-S bonds as seen in other studies. Variable temperature ¹³C NMR of dry powders of alkanethiols seem to show some sort of phase transition. Also the solid state ¹³C NMR has shown that at high temperatures that the gauche population of the alkane chain increases.

Thermal properties of these materials have been studied using TGA and DSC experiments [80]. The TGA of both derivatized and blank samples (i.e., that of pure alkaneamine\thiol) show nearly the same T_g , thus implying that essentially both the surfactants are essentially neutral in character. DSC measurements reveal that dodecanethiol capped Au nanoparticle undergo reversible endothermic cycles whereas dodecylamine undergo exothermic reversible cycles. More importantly, it has been observed that the temperatures of this desorptions are above 100°C, which correlates well with the observed stability.

Electronic properties of thiol derivatized Au clusters has been observations of intriguing results. In particular is the temperature dependence of conductivity [90]. A plot of σ vs T^{-1} and $T^{-1/2}$ yields straight line plots. Hence neither the Arrhenius nor the cermet model is successful in explaining the conductivity data. In the case of dithiol linked clusters similar results have reported.

2.1.4 Applications

In this concluding section, a few of the applications of nanoparticles as well as their assemblies will be dealt with. An important study is the conduction in single particles employing scanning tunneling spectroscopy. These particles

are expected to undergo charging effects like a capacitor and thereby exhibit coulomb staircase phenomena [91]. In Fig. 2. 5 STS data obtained from polyvinylpyrrolidone (PVP) coated Pd nanoparticles are shown. Clearly step features are seen and the step size is observed to decrease with increasing particle size. Such features are inherent to quantum structures. It has also been observed that the coulomb gap increases with decrease in particle size. In single clusters such as Au_{55} and Pt_{309} , the gaps indicate that they lie close to the metal-insulator boundary [92]. These studies pertaining to electronic conduction of nanoparticles are even more important in 2D and 3D assemblies. To this effect, Collier *et al* [94] have studied the conduction by varying the interparticle distance keeping the particle diameter constant. They find that at particular threshold distance, the coulomb gap vanishes. The potential importance of these materials as constituents of microelectronic devices is illustrated by the work of Schmid and co-workers who showed that in principle two Au_{55} clusters could be sufficient to construct a tunnel resonance resistor [95,96]. In the simplest device, two $\text{Au}_{55}(\text{PPh}_3)_{12}\text{Cl}_6$ clusters touch each other and on excitation an electron is transferred from the ground state to the first excited state in such a way that the wavefunctions of the excited electrons can overlap. In addition to increased conductivity seen by this excitation, other properties common to bulk metal such as low transparency has also been seen in observed in experiments with pellets of the above.

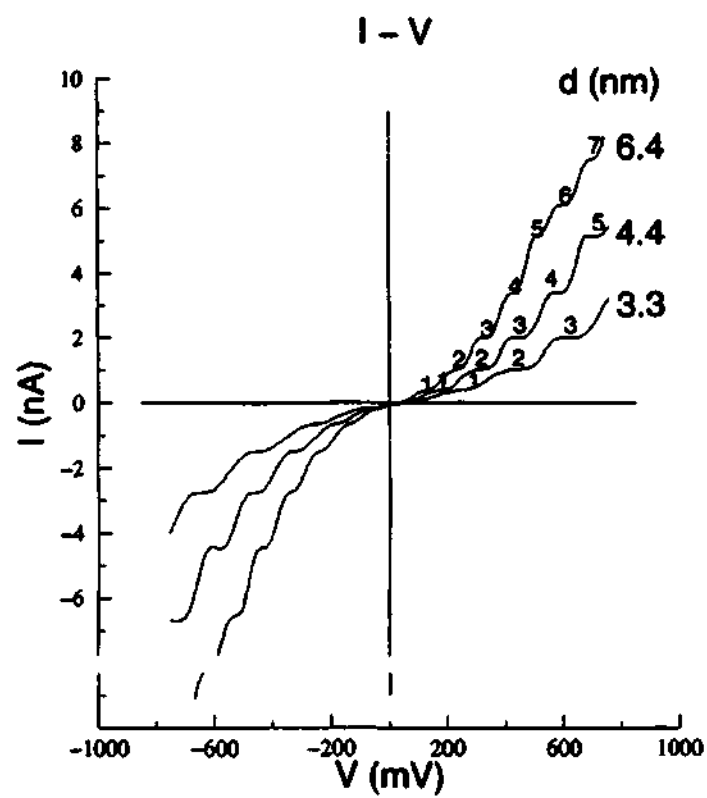


Fig 2. 5. STS measurement of PVP coated Pd nanoparticles of different sizes showing coulomb staircase phenomena [76].

Gold nanoparticles, in particular Au₁₁ clusters are being used in molecular labeling [97] in macromolecules such as proteins and nucleic acids. The strategy involved in these methods is that in a Au₁₁ cluster all the atoms barring one are bonded to non-labile ligands. When these clusters are mixed with DNA (say), the lone Au atom ligated to a labile ligand cleaves and the cluster attaches to the sulfur-containing moiety in the helical structure. When viewed in TEM, the sulfur species is identified and hence structure elucidation becomes easy. Currently, these molecular labeling compounds are available as on shelf products (Nanotech. Products, USA).

Probably, the most direct application of SAMs has been utilized in the microcontact printing process [98] used in design fabrication of sensors [99] and microelectrode arrays [100]. In this method, a stamp roller is used to deposit thiol molecules at specific intervals (micron distances) and facilitate the formation of regular arrays as shown in Fig. 2. 6. A width of 1.97 μm 1D arrays has been achieved by this process.

Metastable phases of many important compounds such as aragonite phase of CaCO₃ has been found to be stabilized [101] when grown on a thiol modified gold surface. By varying the thiol one can selectively grow vaterite and calcite modifications as well.

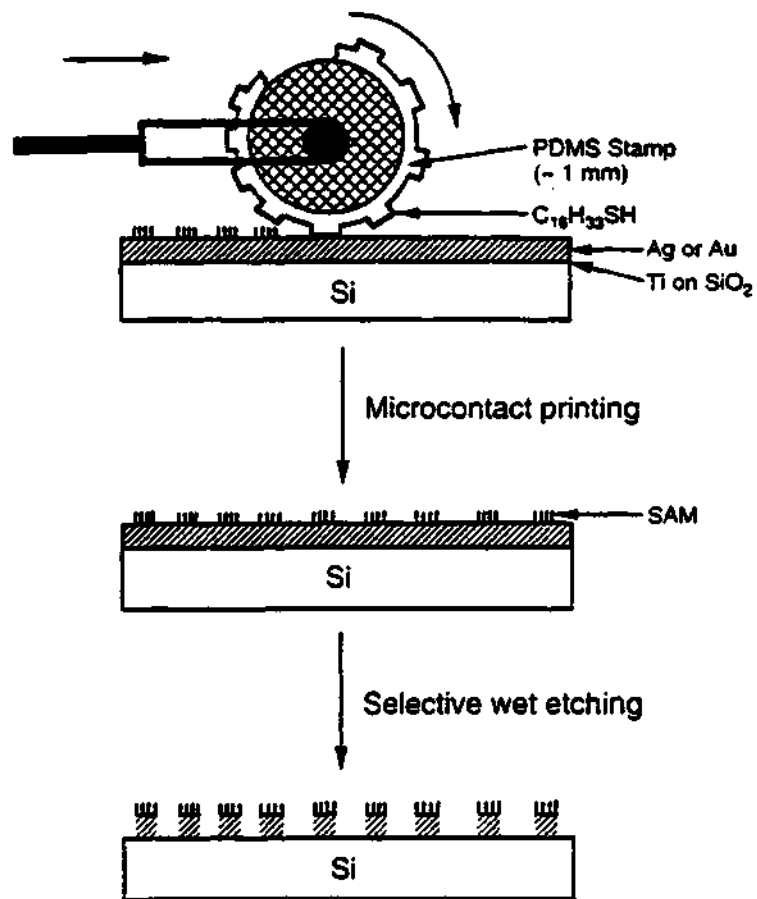


Fig. 2. 6. A PDMS roller used to selectively deposit SAM of width 1.97 μm (not to scale) [98].

By far one of the most important results obtained so far is the magnetic properties associated with the 2D-array of bimetallic FePt nanoparticles. Assemblies of these have shown a high degree of reversible magnetization and thereby promising them to be potential ultra-large storage device material [102].

2.2 SCOPE OF THE PRESENT INVESTIGATIONS

One of the current challenges in nanotechnology is to synthesize metal nanoparticles in various desired shapes and sizes and to organize them in a predetermined fashion. To this end, we considered it interesting to synthesize and characterize metal nanoparticles by various methods. We have assembled thiol-derivatized metal nanoparticles in two- and three-dimensions and also investigated the interaction of metal nanoparticles with sulfur containing conducting polymer-polyoctylthiophene.

2.2.1 Synthesis and characterization of metal colloids by the polyol process

Though numerous synthetic methodologies exist to prepare metal colloids as enumerated in Sec. 2.2.1, it is found that glycols or polyols are generally good reducing agents to prepare nanometric sized metal particles [11]. The conditions of reduction such as the salt concentration and the time of reaction are generally varied to obtain a range of sizes. In some instances, protecting agents such as poly(vinylpyrrolidone) (PVP) are used to control or stop the growth of metal colloids. One of the well-known methods for the preparation of metal colloids is that due to Figlarz and co-workers [12,13] employing ethylene glycol as the reducing agent. We have explored the synthesis of Au, Ag, Pt, Pd and Ru colloids of both submicron and nanometer dimensions employing this method

and attempted to understand the mechanism of the reduction process leading to the metal colloid.

2.2.2 Nanocrystalline arrays of metal nanoparticles

A two-dimensional array of nanoparticles comprises of these in a close packed structure separated by thiol molecules. Each particle in such an array which is a nanocrystallite need not bear any orientation relation between themselves. The length of the spacer thiol molecule and also the particle size can be varied to give rise to different 2D arrays. For example, beginning with particles of a specific desired shape, say hexagonal, it would be interesting to obtain an ordered 2D array of such particles.

Working along these lines, we have attempted to thiol-derivatize hydrosols of Au, Pt and Ag metal and to prepare 2D arrays of the thiolized nanoparticles. We have varied the mean diameter of the Au nanoparticles in the range of 1-5 nm and studied the effect on the ordering. We have also prepared thiol-derivatized Pt particles of near hexagonal shape and these were allowed to self-assemble into a 2D lattice. Our results on this new class of materials can be considered as the beginning, leading to future applications in nanotechnology.

2.2.3 Metal nanoparticle superlattices

A major motivation to engineer 3D structures involving nanoparticles is that they can be expected to exhibit novel properties that manifest from the size quantization. This can then be used to design nanoelectronic devices, sensors, and the like. Thus, Colvin *et al* [103] have made use of a self-assembly of semiconductor nanocrystals to construct an optoelectronic device. Murray *et al* [104] have demonstrated the self-organization of CdSe nanocrystallites into a three-dimensional superlattice. Multilayers of semiconductor CdS nanoparticles have been deposited on a gold substrate using the self-assembly of dithiol molecules [105, 106]. Although there are indications that multilayers of metal particles can be formed by use of dithiols [106] there is no definitive evidence, based on spectroscopic, microscopic, and diffraction studies, for such superstructures. It was our interest to prepare superlattices of well-characterized metal quantum dots by use of spacer molecules. In the first, nanoparticles were deposited onto a metal substrate layer by layer, each layer being separated by dithiol molecules to form a superlattice. Such a stacking gives rise to order in the vertical direction and therefore can be termed as vertical self-organization.

We have also tried several possibilities in forming superlattices of the nanoparticles employing the first method. The size of the metal nanoparticles and the metal itself, as well as the metal substrates has been varied. Accordingly, Pt nanoparticles of mean diameter ~1.5 and 5 nm have been deposited layer by

layer on Au substrates. Another system where Au nanoparticles of mean dia 6 nm were deposited on an Ag substrate, has also been obtained. The formation of each layer was monitored by a variety of techniques. In addition to this, we have grown multilayers of alternate semiconducting and metallic nanoparticles and verified the process of vertical self-organization.

2.2.4 Polymer blends of Au nanoparticles

Conjugated polymers such as derivatives of polyparaphenylenevinylene and polythiophene have appreciable photoluminescence, (PL) efficiency and provide a viable option as the active medium in light emitting diodes [107, 108]. The formation of optical quality polymer films processed from common solvents on different substrates is a significant advantage for these polymer-based devices. On the other hand, metal nanoparticles are known to possess interesting structural, electronic and optical [109] properties. This combination of metal nanoparticles and conducting polymers in the field of molecular electronics has been studied recently, to demonstrate concepts such as molecular bridges between metal clusters [110]. We have investigated complex film patterns obtained from solutions of Au nanoparticles and polyoctylthiophene (P3OT) in solvents where the nanoparticle stability and polymer solubility is assured. The possibility of Au nanoparticle interacting with thiophene in the polymer, leading to conformational/structural rearrangement of the polymer chains at the phase boundaries is probed as the electronic structure of the polymer is also expected

to be strongly perturbed in an environment consisting of these metal nanoparticles. Two phases in the films can be easily distinguished using optical microscopy because of the contrasting fluorescent properties, but, the observable length scales is however Rayleigh limited ($\sim\lambda/2$). The structure of the composites and the distribution of the nanoparticles as revealed by transmission electron microscopy (TEM) and scanning electron microscopy (SEM), are also reported. The source of the PL in the polymer region is known to arise from the radiative decay of the intrachain singlet exciton level [111]. We use fluorescence microscopy and near-field scanning optical microscopy (NSOM) to study the spatial variation in PL, along with TEM for morphological studies of the phase separated system. NSOM is used to acquire spectra from regions with a size less than that of the wavelength of the light source employed, and the results demonstrates the capability of this technique to differentiate the components in the submicron length scale of these multiphase systems. The shear-force feedback technique in NSOM provides a topographic image, in parallel with the optical image.

2.3 EXPERIMENTAL

2.3.1 Preparation of submicron- and nanoparticles of noble metals

The procedure employed for the preparation of metal colloids is as follows. A known quantity of the relevant compound of the metal was taken in ethylene glycol (EG) in presence of PVP and the mixture refluxed for a definite period. In order to obtain colloids of nanometric dimensions, we employed a smaller quantity of metal compound as well as the protecting agent (PVP). The quantity of the metal compound was typically ~ 50 mg and that of PVP ~ 7 gm. In order to obtain micron-size particles, we employed larger quantities of the metal compound, varying between 0.1-5 gm. The refluxing temperature was generally between 100-120°C in most cases. The metal compounds used in the preparation of Au, Ag, Pt, Pd and Ru colloids were HAuCl_4 , AgNO_3 , H_2PtCl_6 , $\text{Pd}(\text{NO}_3)_2$ and $\text{RuCl}_3 \cdot 6\text{H}_2\text{O}$ respectively. In Table 2.1 we summarise the reaction conditions for the preparation of the various metal colloids. The metal colloids once formed were examined by a variety of characterisation techniques.

2.3.2 Thiol-derivatization of metal hydrosols

Thiol-derivatization of metal nanoparticles has been carried out in two ways. In the first method, which was developed in our laboratory, a hydrosol containing desired metal nanoparticles is initially prepared using the known methods and thiol-derivatization of the nanoparticles is achieved by an acid

Table 2. 1 Reaction conditions for the synthesis of colloids of nanometer and submicron dimensions

Metal	Nanometer(nm)			Micron(μ m)		
	Metal salt (mg)	PVP (g)	Temp ($^{\circ}$ C)	Metal salt (g)	PVP (g)	Temp ($^{\circ}$ C)
Au	50	7	120	0.4	10	190
Ag	50	1.5	110	5	5	160
Pt	500	0.5	110	-	-	-
Pd	-	-	-	0.1	0.1	300
Ru	90	0.9	150	-	-	-

mediated transfer of the nanoparticles to a solution of thiol in toluene. In the second method originally due to Brust et al [65], an organosol is first prepared by the transfer of metal ions from an aqueous solution to toluene using n-tetraoctyl ammonium bromide as the phase transfer reagent and reducing the metal ions at the organic-aqueous interface using sodium borohydride. Thiol-derivatization of the particles is simply achieved by the addition of required amount of the thiol to toluene. Let us first discuss the various preparations carried out using the first method.

Thiol-derivatized Au nanoparticles A hydrosol containing nanoparticles of Au was first prepared by the reduction of 2.0 ml of a solution of HAuCl₄ solution (25 mM) using partially hydrolyzed tetrakis(hydroxymethyl) phosphonium chloride (THPC) as the reducing agent [32], having prepared the reagent by the addition of 1 ml of a fresh solution of THPC (50 mM) in water to 47 ml of 6.38 mM NaOH solution. To the dark brown Au sol obtained, 100 ml of a 0.25 mM solution of dodecanethiol in toluene (Au:S = 2:1) was added, to obtain immiscible layers consisting of the transparent organic phase containing the thiol on the top and the colored hydrosol at the bottom. To this biphasic mixture, 125 ml of conc. HCl was added under stirring. This resulted in a remarkably swift movement (within 3 min) of the Au nanoparticles to the hydrocarbon layer containing the thiol. Clearly, the gold particles have an inherent attraction to the thiol molecules. This could be seen vividly by the complete transfer of color across the

interface as shown in Fig. 2. 7. The gold sol in toluene was shaken with water several times to remove traces of HCl and evaporated to around 2 ml in a rotary evaporator. The excess thiol was removed by the addition of 350 ml of ethanol (95%). The dark brown solid thus obtained was filtered, washed with ethanol and dispersed in 10 ml toluene. In order to prepare Au particles of different sizes, the above procedure was repeated with hydrosols obtained using different amounts of HAuCl₄ solution. The color of the hydrosol and also that of the toluene sol varied from light brown to reddish brown as the initial amount of HAuCl₄ solution was increased from 1.8 ml to 2.2 ml.

Gold nanoparticles prepared using citric acid as the reducing agent have also been thiol-derivatized. In this method of preparation, 5 ml of 1% citric acid solution is added to a boiling solution of 1 ml of 30 mM HAuCl₄ in 94 ml water. The formation of sol was marked by a change in the color to purple-blue. Thiol-derivatization is then carried out in the same manner as described in the above process.

Thiol derivatized Pt nanoparticles Initially, a Pt hydrosol was prepared using NaBH₄ as the reducing agent. A 0.01 M solution of NaBH₄ (aged for 3 h) was added dropwise upto 0.5 ml to a beaker containing 100 ml of the stock solution of 2.6 mM H₂PtCl₆ under vigorous stirring. The Pt solution became yellowish grey due to the formation of the metal sol. To this hydrosol, 1.668 mM

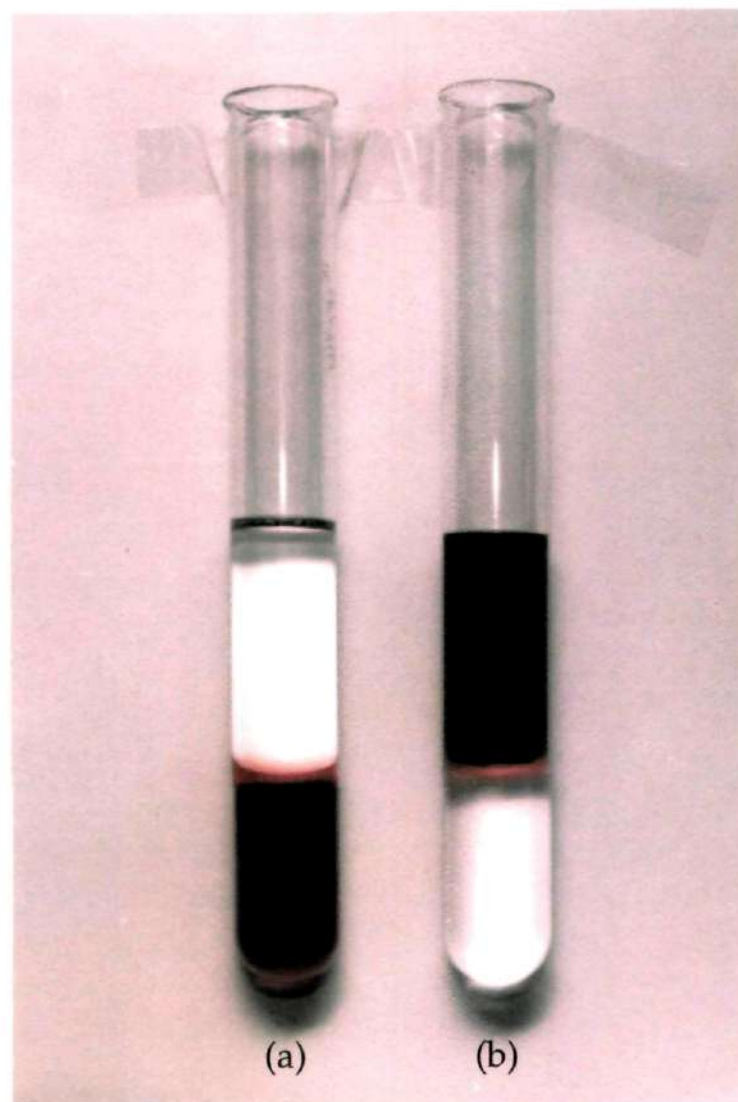


Fig. 2. 7. Immiscible layers of (a) the gold hydrosol (at the bottom) and the clean toluene solution containing the thiol (top) (b) Thiol-derivatized Au sol in toluene (on top) and the clean aqueous solution at the bottom.

dodecanethiol solution was added resulting in a biphasic mixture. Around 1.0 ml of conc.HCl was added dropwise under stirring to the mixture resulting in the transfer of the nanoparticles to the toluene layer, as evidenced by the color change.

In a recent report [22], the preparation of regular cubic Pt nanoparticles using sodium polyacrylate as a stabilising agent has been described. We have adopted a variant of this procedure to prepare hexagonal nanoparticles of platinum. In our procedure, 2.1 mg of K_2PtCl_6 was dissolved in 50 ml of water containing 8.4 mg of sodium polyacrylate (M.W 2100, Aldrich). Pure argon was bubbled through this solution for 20 min, followed by H_2 gas for 5 min. The glass vessel was sealed and left undisturbed for 12-14 h. The resulting light golden sol containing the Pt sol was mixed with 20 ml of 1.668 mM toluene solution of the thiol to yield a milky solution. To this solution, 0.01 M $NaBH_4$ solution was added dropwise followed by vigorous shaking, to obtain a thin yellow layer containing thiol-derivatized Pt nanoparticles floating above the milky layer. The sol was washed with an excess of $NaBH_4$ solution.

Thiol-derivatized Ag nanoparticles We have also prepared Ag hydrosol using the $NaBH_4$ reduction method. A 0.5 ml of $NaBH_4$ solution was added to 100 ml of 0.29 mM $AgNO_3$ stock solution under vigorous stirring. The resulting Ag solution turned light yellow on formation of the sol. Thiol derivatization was

carried out using conc. HCl as described in the case of the Pt-NaBH₄ sol. No special precaution to maintain oxygen free atmosphere seemed necessary.

We have also thiol-derivatized silver nanoparticles, which were initially coated with polyvinylpyrrolidone (PVP) [12]. To a 20 ml of bright yellow Ag-PVP sol in a separating funnel, 10 ml of the 1.668 mM thiol solution in toluene was added. To this resulting medium, a fresh aqueous solution of NaBH₄ (0.01M) was added in excess. A thin yellow layer of the thiol-derivatized Ag sol formed on the turbid solution. The bottom layer was drained out and the yellow layer was repeatedly washed with the NaBH₄ solution.

Thiol-derivatization of organosols This second method has been applied to thiol-derivatization of Au and Pt nanoparticles. In this method, chloroauric ions from 3 ml of a 30 mM HAuCl₄ solution were phase transferred to toluene using 8 ml of 80 mM n-tetraoctyl ammonium bromide solution. To this organic layer, 2.5 ml of 0.4 M NaBH₄ aqueous solution was added under vigorous stirring which resulted in a deep red Au sol. Similarly, a Pt sol was prepared by adding 0.6 ml of 0.02 mM NaBH₄ to toluene containing the Pt ions stabilised by n-tetraoctyl ammonium bromide. We have also carried out an incomplete reduction of Pt by using 0.2 ml of 0.02 mM NaBH₄ with an intention that the resulting sol would possibly contain very small Pt particles. This sol was orange

in color. Thiol-derivatization of the nanoparticles was achieved by simply adding the required amount of the thiol (Au:S = 2:1), to the organosols.

2.3.3 Superlattices of metal and metal-semiconductor nanoparticles

The procedure used for the deposition of successive layers of metal nanoparticles using 1,10-decanedithiol as spacer molecules is briefly discussed here. Initially a gold substrate was dipped in a 50 mM 1,10-decanedithiol solution for approximately an hour. This would result in the adsorption of dithiol molecules onto the gold substrate. The excess dithiol molecules were washed away using excess toluene. The dithiol-coated substrate was then dipped into one of the Pt organosols, whose preparations are described in the experimental section. This would facilitate the migration of the Pt nanoparticles from the sol onto the Au substrate via thiol attachment. It is worth noting that the deposition of the particles is highly selective and takes place irrespective of other reagents present. After an hour, the Au substrate bearing the adsorbed Pt particles was removed from the organosol and was dipped in toluene. In order to stack layers of the Pt nanoparticles on the Au substrate, we have repeated the above steps in many cycles and after each deposition, various measurements - XPS, XRD, STM, UPS were carried out. The above procedure was also applied to obtain successive depositions of the Au particles on silver substrate. We have also extended the study to incorporate alternate layers of two different metals (Au and Pt nanoparticles) as well as semiconductor-metal heterostructures. A

schematic describing the layer by layer deposition of successive layers of Pt nanoparticles (metal-metal layers) and heterostructure consisting of metal (Pt) – semiconductor (CdS) nanoparticles is shown schematically in Fig. 2. 8. We have characterised the size of the nanoparticles in the organosols using TEM. The mean dia of the Au and the Pt particles were found to be 6 and 5 nm respectively. The TEM imaging of the Pt organosol prepared with lesser amount of the reducing agent was not possible due to the co-presence of unreduced metal salt. However, our STM studies on the multilayer system prepared using this organosol particle helped us to obtain the mean diameter of the particles ~2 nm, the details of which will be discussed later. Semiconductor nanoparticles of CdS were prepared by inverse micellar solution method [105] involving AOT (sodium bis(2-ethylhexyl)sulfosuccinate)/*n*-heptane. In this method, two solutions - 0.4 M Cd(ClO₄) (*aq*)/0.2 M AOT/*n*-heptane is added under inert and dark conditions to a solution of 0.3 M Na₂S.9H₂O (*aq*)/0.2 M AOT/*n*-heptane over a time period of 1 h. The mean dia of the CdS particles so obtained was 2.4 nm as determined by absorption spectroscopy.

2.3.4 Au-polyoctylthiophene blends

Organosols of gold was prepared as described in Sec 2.3.2. Polymer polyoctylthiophene, P3OT was obtained from Aldrich Inc., and was dissolved in *p*-xylene in a weight-volume ratio of 2.0 mg per ml. Blends of Au-P3OT with two different ratios, S1 & S2, were obtained by the addition of polymer solution to the

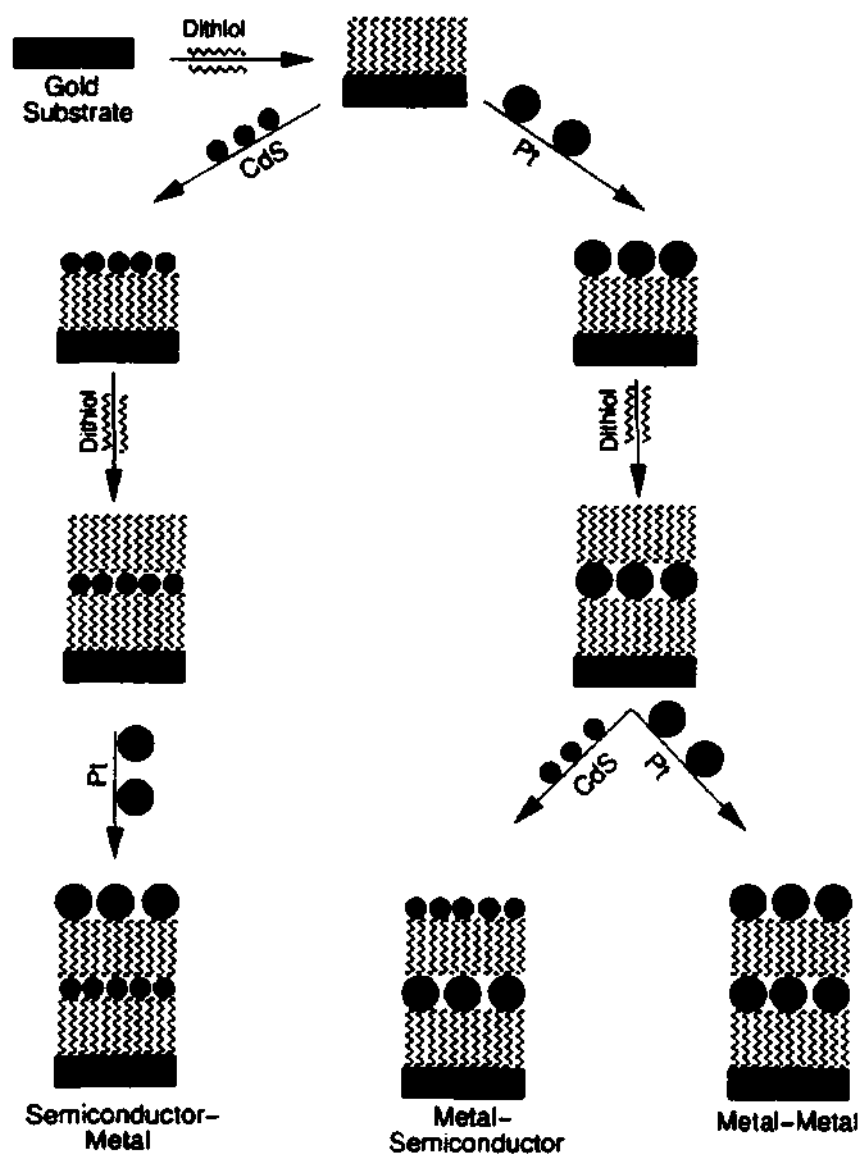


Fig. 2. 8. Schematic drawing describing the layer-by-layer deposition of Pt nanoparticles onto a Au substrate, the layers being separated by dithiol molecules. Also shown is the formation of a heterostructure consisting of alternate layers of semiconductor and metal nanoparticles.

Au sol (0.8 ml and 1.6 ml of P3OT per ml of Au organosol). The resulting homogenous solution was stable over a period of several days with no phase separation visible due to aggregation/coagulation of the nanoparticles. In order to prepare smaller Au nanoparticles, the above quantity of reducing agent was reduced by a factor of five. Thin films on pre-cleaned glass substrates were deposited by spin coating and casting methods.

2.3.5 Characterization

Thiol-derivatized metal nanoparticles were characterized by several techniques. X-ray diffraction (XRD) patterns of the films of the thiol-derivatized metal particles obtained by vacuum drying of the concentrated toluene sols on glass substrates, were recorded with a Seifert 3000TT instrument using $\text{CuK}\alpha$. Transmission electron microscopy (TEM) images were recorded with a JEOL-3010 microscope operating at 300 keV. For this purpose, samples were prepared by placing a drop of the sol containing thiol-derivatized metal nanoparticles on a holey carbon grid (dia - 3 mm). The solvent was evaporated before introducing the grid into the microscope. Histograms of particle size distributions were obtained using Quantimat image analyzer. X-ray photoelectron spectroscopic (XPS) measurements were carried out using ESCALAB MKIV (VG Scientific) instrument. A few drops of the toluene containing thiol-derivatized metal nanoparticles were evaporated on amorphized graphite substrate before

recording the spectrum. AlK_{α} (1486.6 eV) radiation was used as the source. Ultraviolet Photoelectron Spectroscopic (UPS) measurements were carried out using an OMICRON instrument, employing He-I radiation. The Au and Ag metal substrates required in some of these experiments were obtained by resistive evaporation of the metals and subsequent deposition onto stainless steel stubs under UHV conditions.

Ultraviolet-Visible absorption spectroscopic measurements of the thiol coated metal sols were carried out on a Pye-Unicam SP8-100 spectrophotometer in the double beam mode between 800-300 nm in 1 cm quartz cuvettes. Fourier transform infrared spectroscopy (FT-IR) was performed in diffuse reflectance mode with a BRUKER 66V/S. IR measurements were carried out in the range of 4000 cm^{-1} to 400 cm^{-1} . A few drops of the metal colloid were thoroughly mixed with KBr before the diffuse reflectance spectrum of the pellet was recorded.

Scanning tunneling microscopy (STM) images were recorded with a Nanoscope (II) of Digital Instrument by employing Pt-Ir tips. Samples for STM were prepared by evaporating the sols of the thiol-derivatized metal nanoparticles on freshly cleaved highly oriented pyrolytic graphite (HOPG) surface. Far-field optical microscopy was performed using an Olympus model B2020 microscope in epi-fluorescence mode. For NSOM measurements, a Witec-Alpha/2 instrument was used. A fiber tip with a 100 nm aperture was used to

excite the sample with ~ 10 nW of light at 457 nm from an Ar* laser. Scattered light was collected with a high numerical aperture microscope objective in the transmission mode. NSOM tip height regulation in the near field is achieved completely by electronic shear-force detection [112]. A long-pass filter along with an avalanche photodiode were used for fluorescence imaging. Near-field spectra were obtained with a cooled CCD detector at the output of a 0.3 m spectrometer.

2.4 RESULTS AND DISCUSSION

2.4.1 Metal colloids by the polyol process

TEM images were employed to characterize the particles of nanometer dimensions, while SEM was employed to characterize particles of sub-micron dimensions. In Fig. 2. 9, we show the TEM images of typical colloids of nanometer dimensions of Au, Ag, Pt and Ru prepared by the polyol process. The average diameters of these colloids are in the 7-20 nm range. In Fig. 2. 10, we show typical SEM images of sub-micron colloids of Au and Ag. These colloids of Au and Ag have average diameters of 0.38 μm and 0.8 μm respectively. The size distributions of the colloids obtained in these preparations were generally quite narrow. In Table 2. 2, we list the average particles diameters of the various metal colloids prepared in the present study.

In order to characterize the surfaces of colloids, we employed core-level x-ray photoelectron spectroscopy. Typical spectra in the case of Au colloids are shown in Fig. 2. 11. The binding energies of the different core-levels were fixed with respect to the binding energy of the bulk metal core-level. The oxygen, nitrogen and carbon signals confirm the presence of PVP and possibly ethylene glycol on the surface of the colloids. In Table 2. 3, we list the binding energies of the C(1s), N(1s) and O(1s) core-levels due to the surface coatings on the metal colloids.

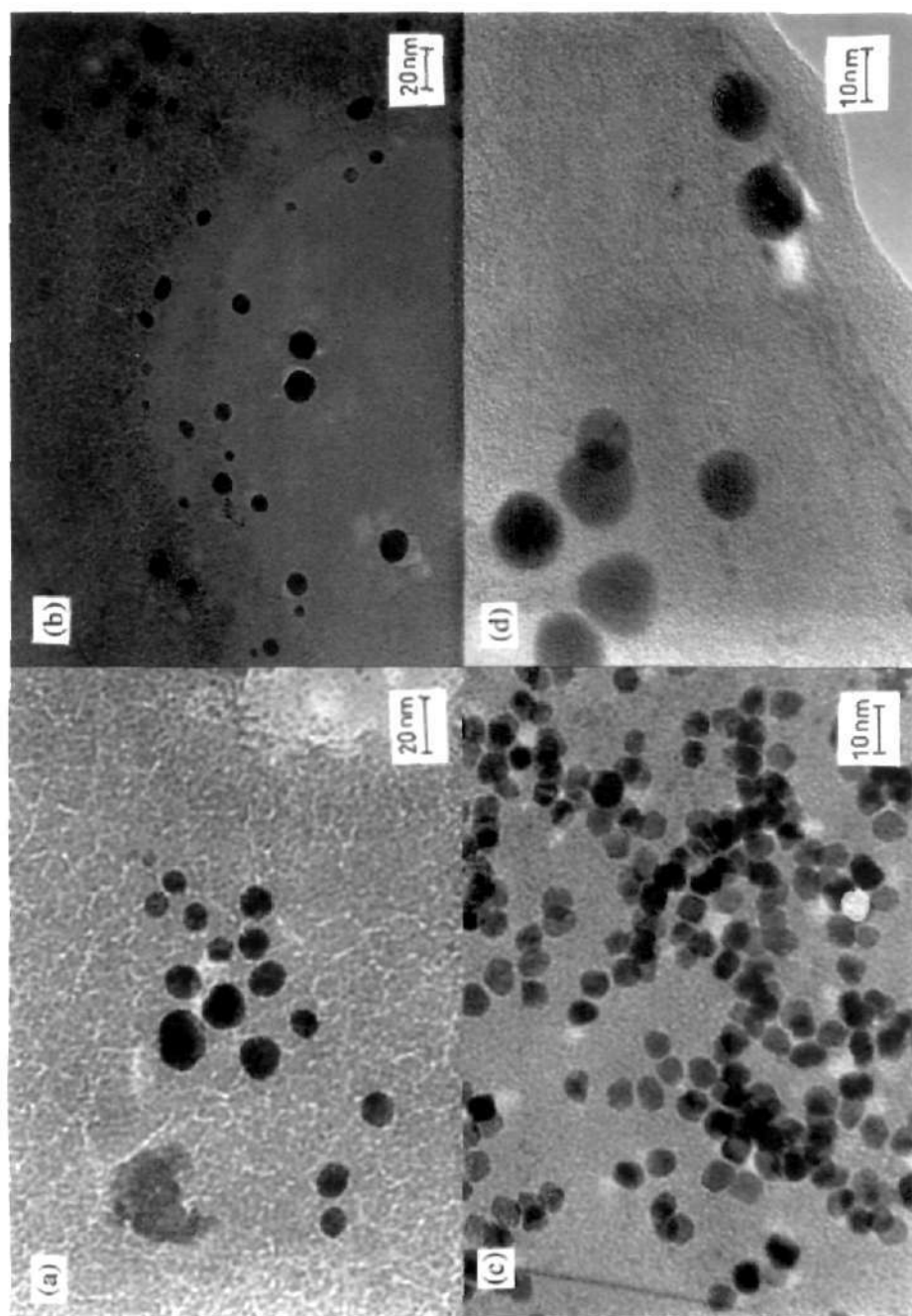


Fig. 2. 9. TEM images depicting nanoparticles of (a) Au (b) Ag (c) Pt and (d) Ru as synthesized by polyol process.

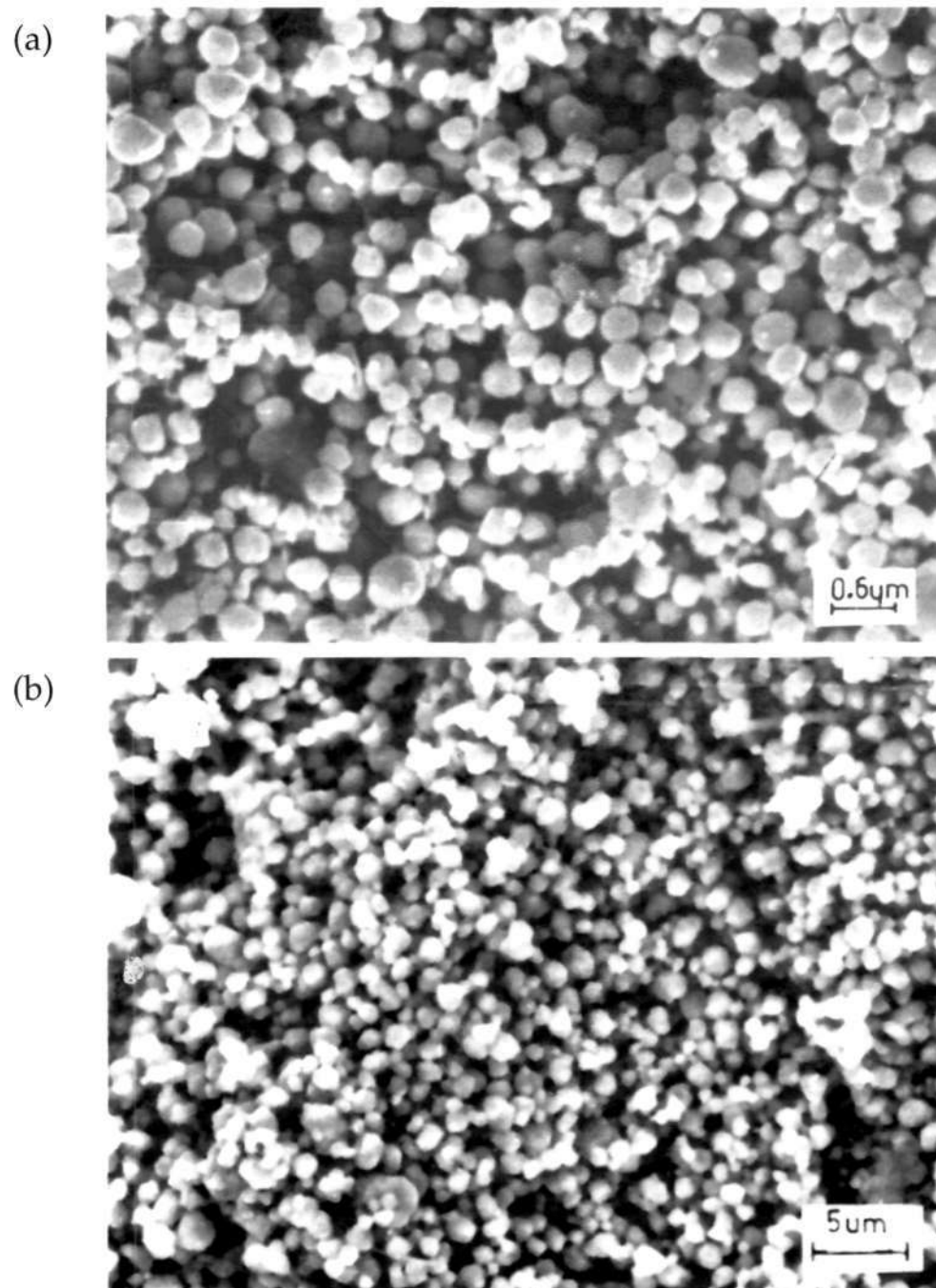


Fig. 2. 10. SEM images depicting sub-micron particles of (a) Au and (b) Ag sol prepared by polyol process.

Table 2.2 Average diameters of the metal colloids.

Metal	Nanoparticles* (nm)	Submicron particles † (μm)
Au	15.0	0.38
Ag	20.1	0.8
Pt	6.5	----
Pd	----	0.4
Ru	16.9	----

* As determined by TEM studies

† As determined by SEM studies

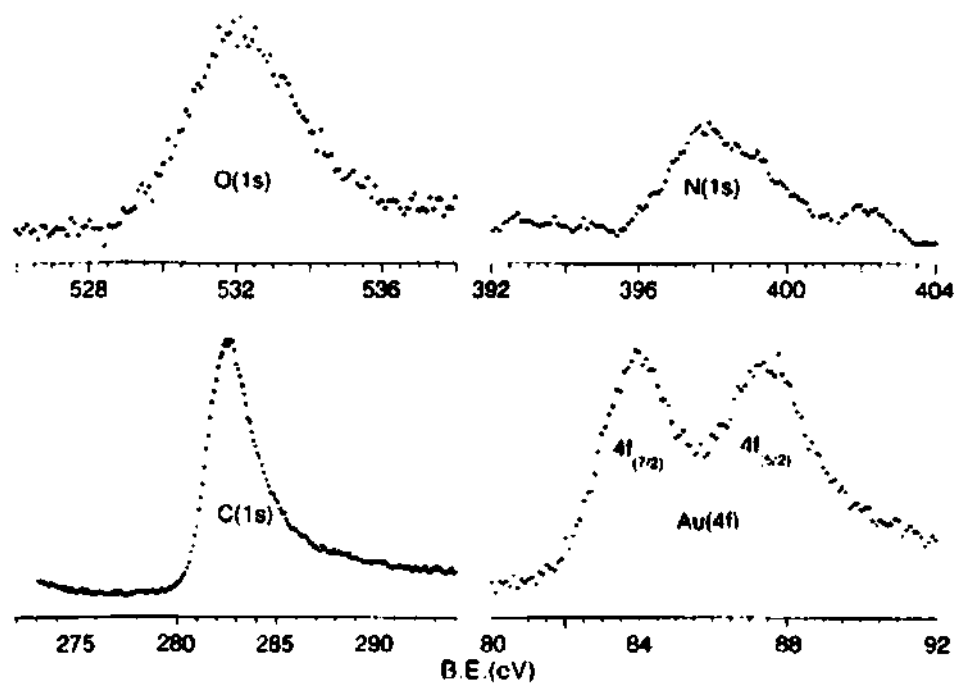


Fig. 2. 11. X-ray photoelectron spectra of Au colloid with mean dia of 0.38 μm.

The figure shows core-level spectra in O(1s), N(1s), C(1s) and Au(4f) regions.

Table 2. 3 Core-level binding energies of surface coating on the metal colloids.

Metal	Particle diameter	O(1s) (eV)	N(1s) (eV)	C(1s) (eV)
Au	0.38 μ m	532.0	398.0	282.4
Pt	6.5nm	531.9	397.9	282.7
Pd	0.4 μ m	532.0	397.9	282.8

Diffuse reflectance FT-IR spectra of the metal colloids were compared with the spectra of EG and PVP that were employed in the synthesis. The spectra show that the -OH stretching band shifts to higher frequencies after the formation of the colloids suggesting a decrease in hydrogen bonding in the glycol medium after formation of the colloid. This is because the hydroxy group of the glycol is directly involved in reducing the metal compounds to the metallic colloids. More interestingly, the carbonyl region of spectra shows distinct changes. In Fig. 2. 12, we see typical diffuse reflectance IR spectra to illustrate the nature of changes in the carbonyl-stretching band. Sub-micron sized colloids generally show a positive C=O frequency shift, while the nanometric colloids show negative shifts. It is known from the infrared spectra of metal complexes of amides, ureas and related compounds [113] that a positive shift of the C=O stretching band implies co-ordination of the nitrogen atom to the metal while a negative shift implies coordination of the carbonyl group to the metal. It seems therefore possible that the coordination of the PVP to the metal colloids depends on the size of the colloid particle. In the case of sub-micron sized particles, the nitrogen-containing heterocyclic ring of the PVP may coordinate more strongly than the carbonyl group whereas the opposite may occur in the case of nanometer size particles.

Since ethylene glycol acts as a reducing agent, it was interesting to find out how it transforms in the reduction process. In order to understand this

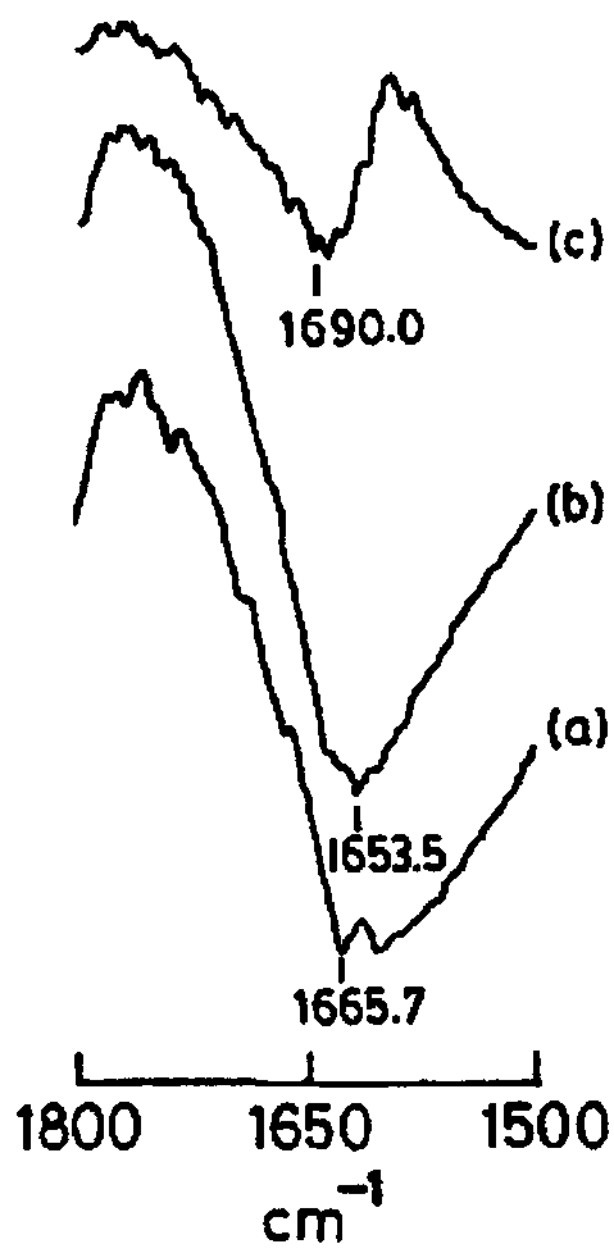


Fig. 2. 12. FT-IR diffuse reflectance spectra in the region of 1500-1900 cm⁻¹ for (a) ethylene glycol; ethylene glycol oxidation after formation of (b) Pt (c) Pd and (d) Ru nanoparticles.

transformation, we recorded the IR spectra of the reaction mixture after carrying out the reduction of the metal compound in the absence of the polymer. We show typical spectra in the carbonyl region in Fig. 2. 13 corresponding to the reduction of Pt, Pd and Ru compounds by EG. The reduction of the metal salt is accompanied by the appearance of a carbonyl-stretching band between 1730 cm^{-1} and 1750 cm^{-1} characteristic of aldehydes and ketones. This observation suggests that ethylene glycol gets oxidized during the reduction process, as expected. Clearly, as ethylene glycol reduces the metal compound, it undergoes oxidation to a carbonyl compound.

2.4.2 Two-dimensional arrays of metal nanoparticles capped by alkanethiols

The simple procedure of transferring the metal nanoparticles from an aqueous medium to a toluene medium containing the thiol, described in the experimental section, has enabled us to obtain thiol-derivatized Au nanoparticles of different size distributions. In Fig. 2. 14 we show TEM images of thiol-derivatized Au nanoparticles of three size distributions, prepared from hydrosols containing different concentrations of HAuCl_4 . The particle size dependence on the concentration of HAuCl_4 is evident from the figure. The particles are near spherical and the size distributions are reasonably narrow with the mean

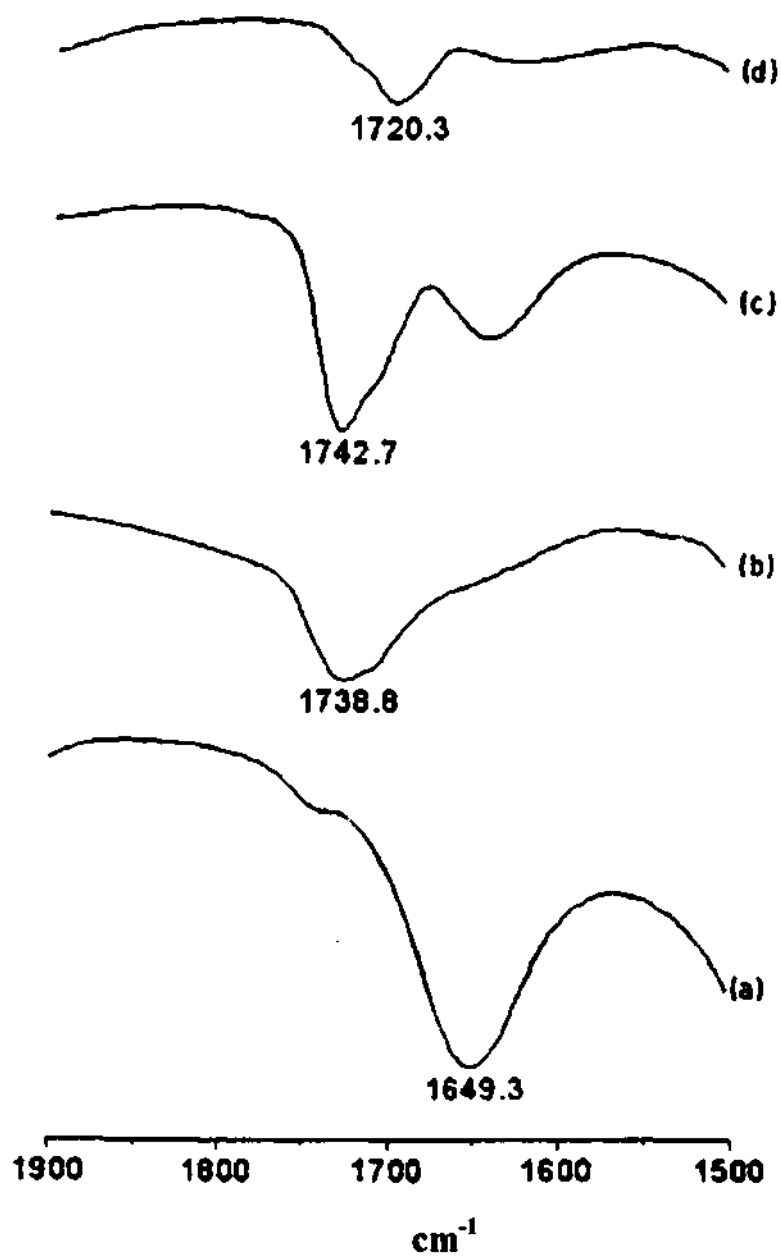


Fig. 2. 13. FT-IR diffuse reflectance spectra in the region of 1500-1800 cm⁻¹ of (a) ethylene glycol (b) Pt colloid (c) Pd and (d) Ru colloid.

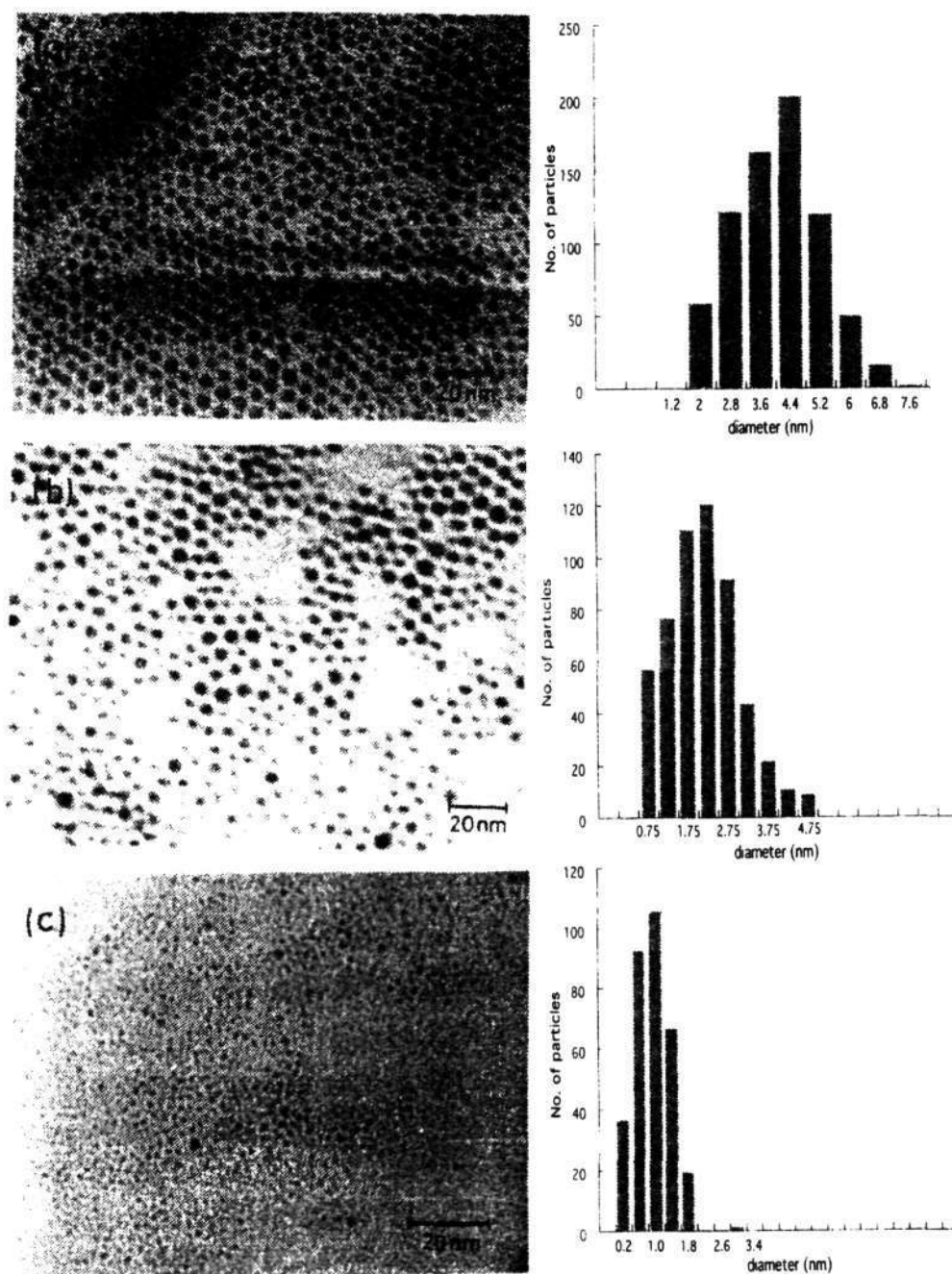


Fig. 2. 14. TEM images of the thiol-derivatized Au nanoparticles. The particle size distributions are shown in the form of the histograms alongside the TEM images. The nanoparticles in (a) (b) and (c) were obtained using 2.2, 2.0 and 1.8 ml of the 25 mM HAuCl_4 solution, respectively.

diameters of the particle arrays in (a) (b) and (c) is 4.2, 2.1 and 1.0 nm respectively.

The TEM images in Fig. 2. 14 reveal that thiol-derivatized particles readily form nanocrystalline arrays over tens of nm with regular spacing (~ 1 nm) between the particles. Particles with the mean diameter of 4.1 nm form a close-packed structure, while the smaller particles of mean diameters of 2.1 nm and 1.0 nm form superstructure islands, with voids in between. All of them however show characteristic XRD patterns. In Fig. 2. 15, we show the XRD patterns obtained with the nanoparticles with the mean diameters of 4.2, 2.1 and 1.0 nm, giving low angle peaks corresponding to d -spacings of 5.0, 4.5 and 3.8 nm respectively. These diffraction peaks are likely to result from the nanocrystalline arrays revealed in the TEM images, in particular due to the (110) spacing of the BCC structure [72]. We do not see higher angle peaks due to the limited thickness of the films. Accordingly, the XRD feature is more intense in the case of bigger nanoparticles and broader in the case of the small 1.0 nm particles. The distance between the nanoparticles deduced from the d -spacings is somewhat smaller than the expected value. Thus, in the case of the 4.1 nm particles, the d -spacing of 5.0 nm gives an inter particle distance of 0.8 nm, which is smaller than the estimated surfactant layer thickness of ~ 1.5 nm. It appears that there is a significant overlap (or close-packing) of the passivating layers of the thiol molecules on the neighboring particles.

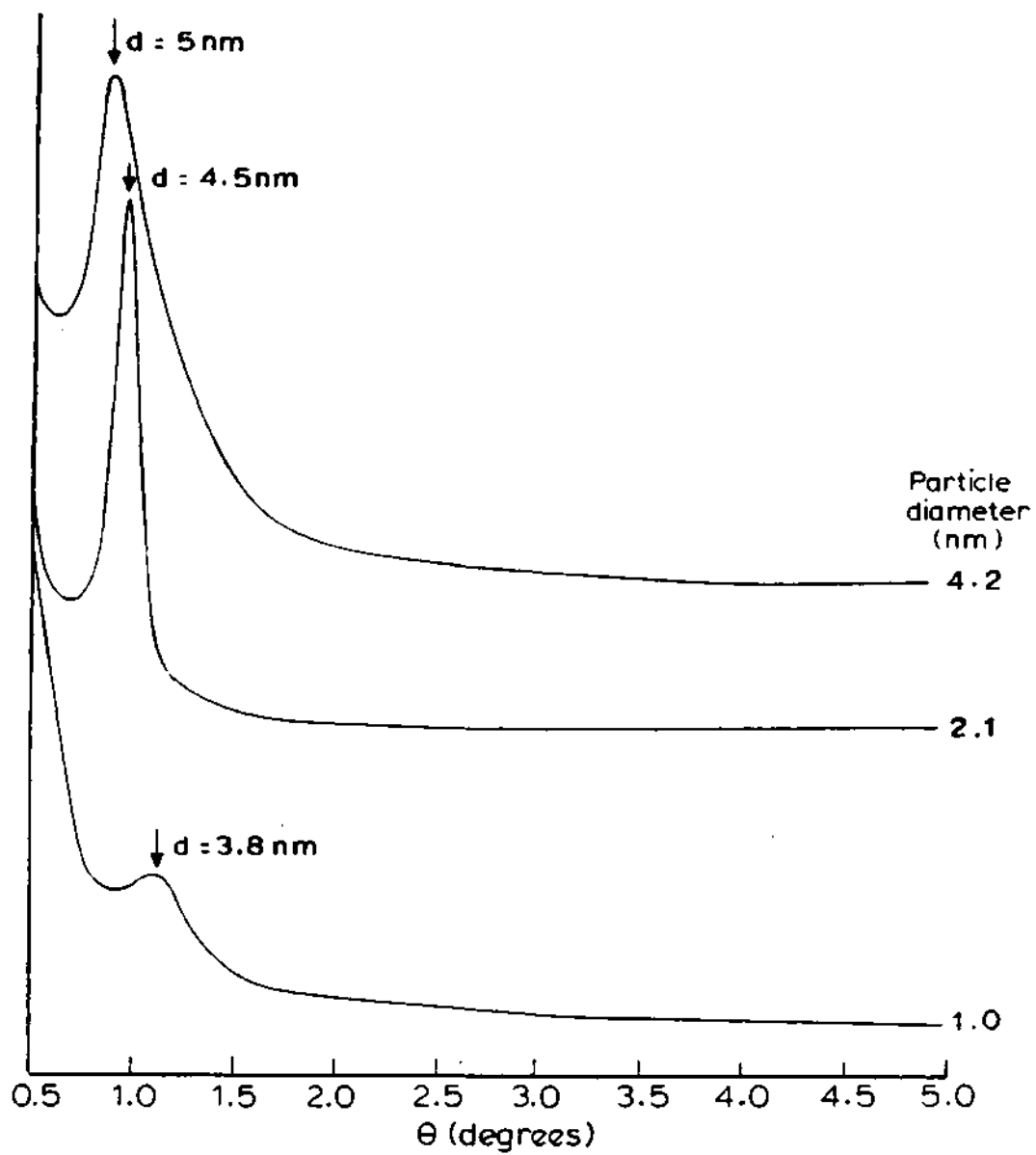


Fig. 2. 15. X-ray diffraction patterns from the nanocrystalline arrays of Au particles of different diameters (4.2, 2.1 and 1.0 nm).

Scanning tunneling microscopy (STM) images of thiol-derivatized Au nanoparticles of 4.1 nm diameter are shown in Fig. 2. 16. The STM image in top view (Fig. 2. 16a) shows a large number of particles arranged into a lattice of a crystallite extending over 50 nm. We find that the image yield a diameter of the nanoparticle which is close to the value estimated from the TEM image. The image in a smaller scan shown in Fig. 2. 16b provides certain details. On each of the particles, there is a large number of high contrast features ascribable to the chemisorbed thiol molecules. By counting the features on the corrugated portion, we obtain an average value for the number of thiol molecules on the 4.1 nm particles to be around 250.

We have sought to examine the crystallinity of the Au nanoparticles by making use of the Moiré patterns obtained from the nanoparticles on thin flakes of MoSe₂. In Fig. 2. 17, we show a TEM image collected in a region where the Au nanoparticles showed strong interference with the support lattice of MoSe₂. The figure distinctly shows Moiré patterns in the background of the MoSe₂ lattice. The Moiré pattern associated with each particle is uniform with a spacing of 0.55 nm, conforming that each of them is a nanocrystallite. The observed lattice spacing of MoSe₂ is 0.34 nm corresponding to the (006) planes. It is likely that the diffraction pattern due to Au (111) planes (0.24 nm) of the nanocrystallites, (which are faintly visible in some of the particles) interfere with that from the

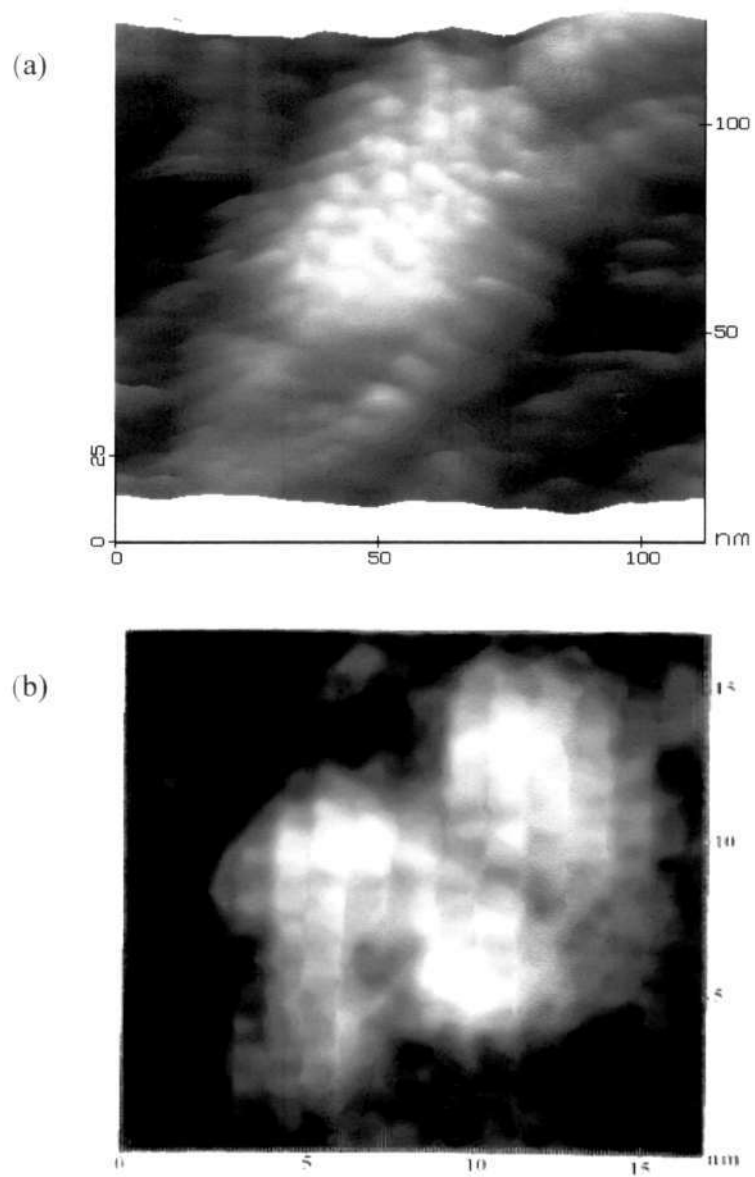


Fig. 2. 16. STM images of (a) a portion of a crystallite formed by thiol-derivatized Au nanoparticles of ~ 5 nm diameter. (b) Low-scan image of Au nanoparticles of the crystallite in (a); we ascribe the several small features seen on the particles to the chemisorbed thiol molecules.

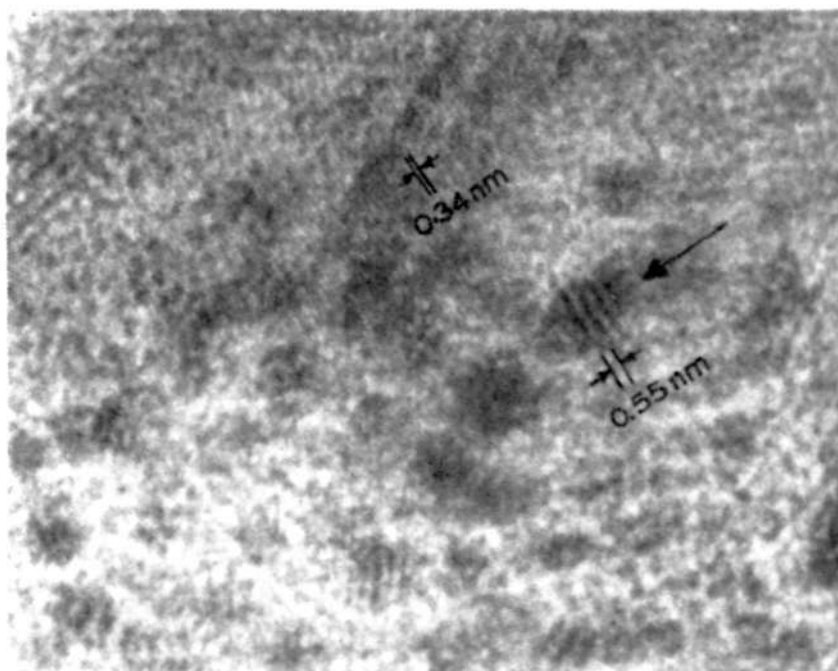


Fig. 2. 17. TEM image obtained with Au nanocrystallites deposited on a MoSe₂ flake. The prominent fringes (shown by an arrow) with a regular spacing of 0.55 nm are due to Moiré interference.

MoSe₂ (006) planes, to produce the Moiré fringes. For instance, with the particle indicated by an arrow in Fig. 2. 17, the angle between the two interfering lattices is around 20, close to that estimated from the Moiré formula.

The UV-VIS absorption spectra of the toluene gold sols (Fig. 2. 18) show a distinct plasma band centered around 525 nm in the case of the 4.2 and 2.1 nm particles, the intensity of the band being higher with the bigger particles. We hardly see any feature in the 525 nm region in the case of the 1.0 nm particles. It is possible that such small particles are truly not metallic. There is evidence to show that Au nanoparticles of 1.0 nm diameter or less, prepared by different methods, are non-metallic [87].

We have examined the electronic nature of the nanoparticles using XPS as well. Interestingly, we found that the Au(4f_{7/2}) binding energy was identical to the value of the bulk metal (84 eV), irrespective of the particle size. This is not expected since the core-level binding energy of metals is known to increase with the decrease in particle or cluster size, specially when the diameter is smaller than 1 nm [87,114,115]. The invariance in binding energy with respect to the bulk metal value found here, could either be due to the effect of the thiol molecules or due to the formation of the nanocrystalline arrays shown in Fig. 2. 14. In order to test this, we measured the Au(4f) binding energy of gold clusters

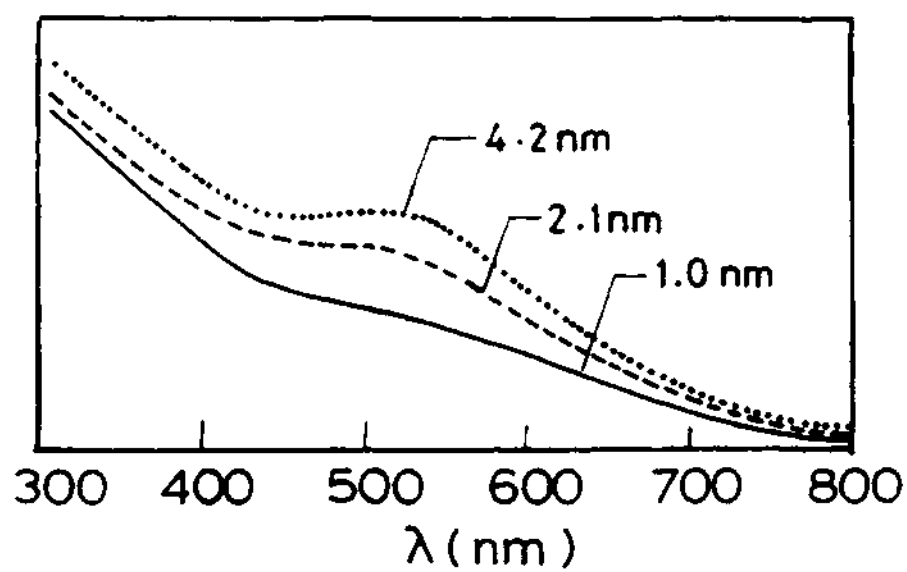


Fig. 2. 18. UV-Vis absorption spectra of Au toluene sols showing characteristic plasmon band at 525 nm. The mean diameter of the particles are indicated.

of various sizes deposited on amorphized graphite substrate by the resistive evaporation of gold in the UHV chamber of the electron spectrometer [87], before and after the passivation of clusters by dodecanethiol. The measurement showed that in the absence of thiol, gold clusters do indeed show the variation as reported in the literature [114,115]. Upon thiol-derivatization, the binding energy of the Au(4f_{7/2}) core-level of all the clusters is around 84 eV, irrespective of the particle size as shown in Fig. 2. 19. These experiments suggest that the thiol molecules may donate electrons to the small Au clusters (1.5 nm dia) and compensate for the cluster size effect.

We have also used XPS to find out the composition of the surface. As shown in Fig. 2. 20, we see a feature at 163.5 eV due to S(2p) showing that the thiol molecules were chemisorbed on the surface of the Au particles. There was no evidence of a feature due to P(2p) from the THPC reagent in the spectrum unlike particles from the hydrosol which showed a feature at ~ 133 eV (see inset of Fig. 2. 20). The C(1s) spectrum showed a peak centred at 285.0 eV, characteristic of methyl species in hydrocarbons. Based on the relative intensities of the Au(4f_{7/2}) and S(2p) peaks we have been able to quantify the number of thiol molecules on Au surface, as in the case of STM studies. The results are shown in Table 2. 4. It may be noted that the thiol coverage obtained by us (~ 20 Å²/molecule) compares well with the reported value on plane Au surfaces (~ 21 Å²/molecule).

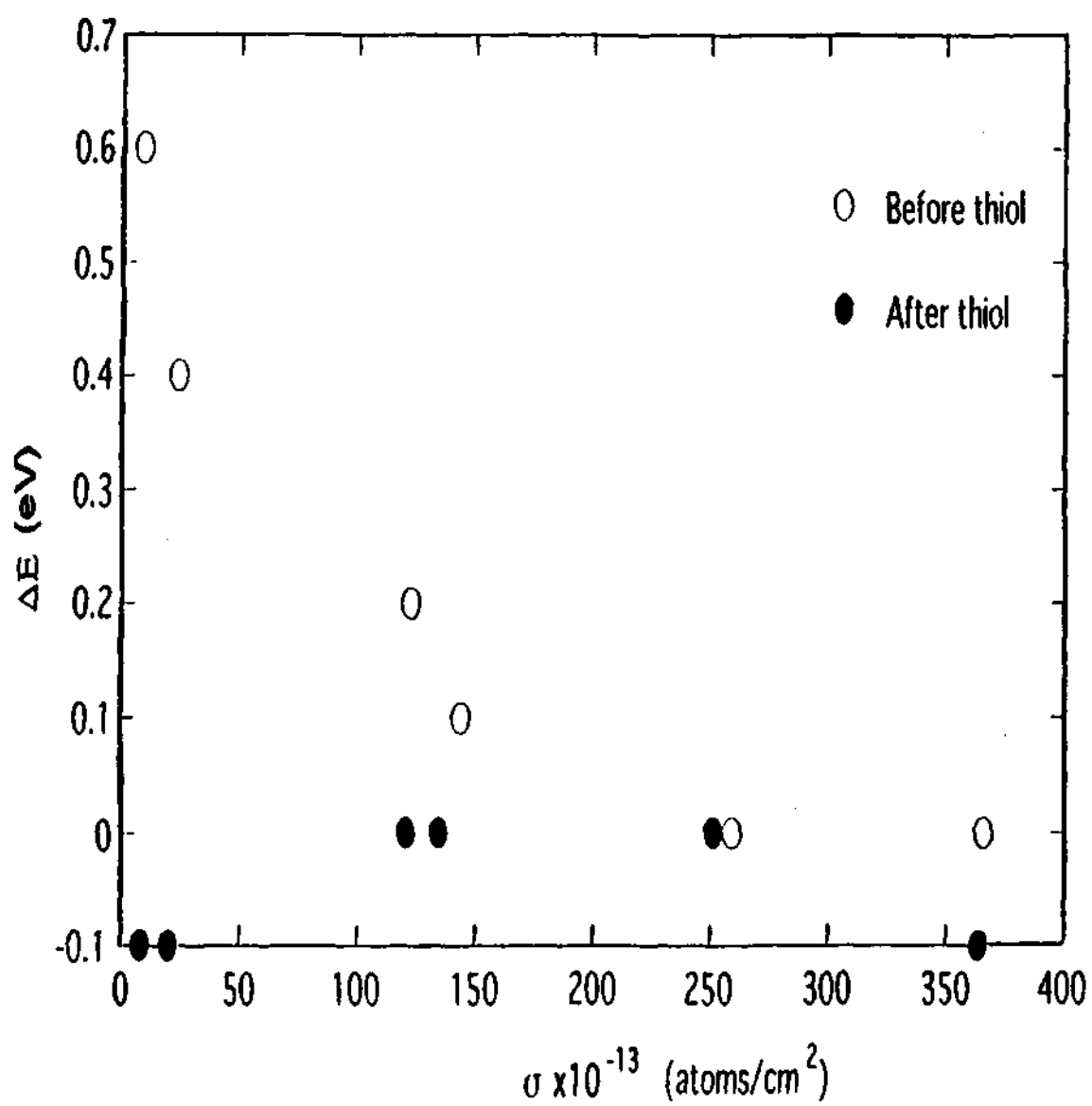


Fig. 2. 19. Variation in the binding energy of Au(4f_{7/2}) with respect to bulk value as a function of gold coverage before and after thiol adsorption.

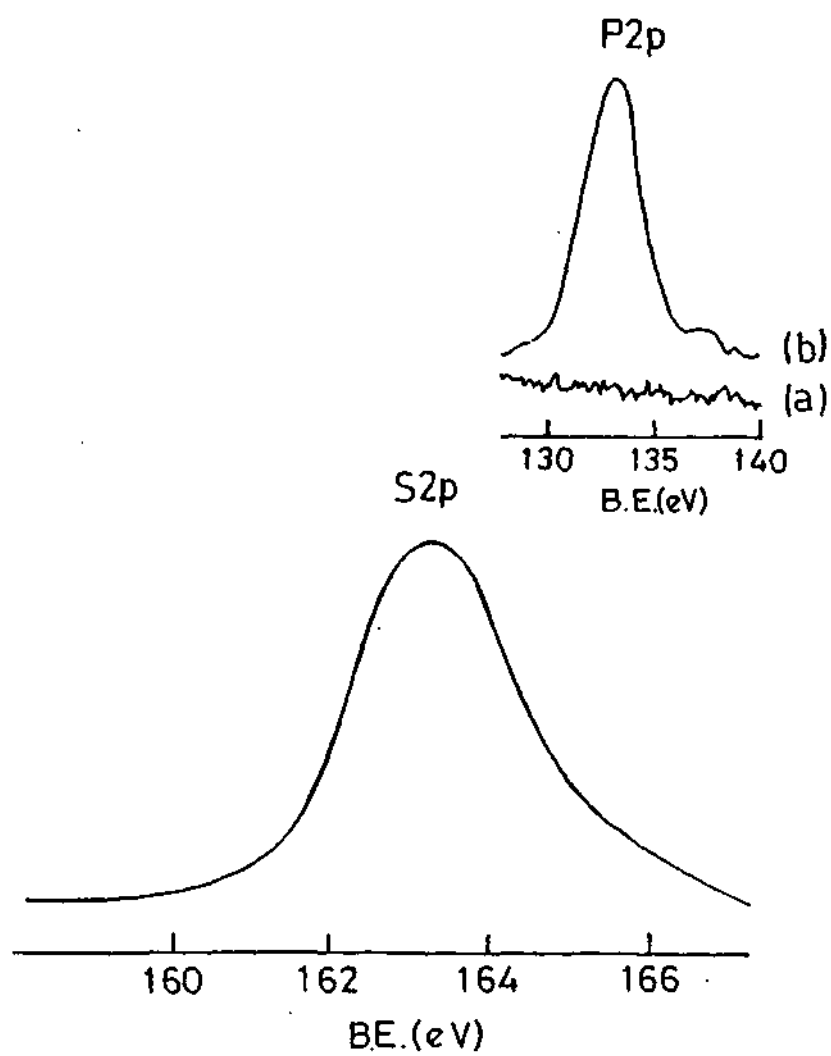


Fig. 2. 20. X-ray photoelectron spectrum in the S(2p) region of thiol-derivatized Au sol. (Inset) X-ray photoelectron spectrum in the P(2p) region of the Au hydrosol from THPC method (a) after thiol derivatization (b) before thiol derivatization.

Table 2. 4 Thiol coverage on Au nanoparticles.

Particle size (Å)	STM (Area/Thiol molecule) (Å ²)	XPS (Area/Thiol molecule) (Å ²)
42	19	20
21	-	31
10	-	63

In Fig. 2. 21, we show a TEM image of the thiol-derivatized Pt nanoparticles obtained by NaBH_4 reduction. The particles are spherical with a mean diameter of 4.1 nm. There is a clear evidence for the formation of a nanocrystalline array. The STM image of the Pt particles shown in Fig. 2. 21 confirms the spherical shapes. The line profile given next to the STM image provides a measure of the particle size, which is comparable to that from TEM.

In Fig. 2. 22, we show a TEM image of the Pt nanoparticles obtained by using sodium polyacrylate. We distinctly see that the particles have a hexagonal shape, forming close-packed structures resembling honeycomb pattern, each honeycomb representing a nanoparticle. This is to be contrasted with the spherical shape of the particles in Fig. 2. 21 prepared in the absence of sodium polyacrylate. This is the first observation of hexagonal particles of Pt arranged into a nanocrystalline array. The honeycomb structures in Fig. 2. 22 have a mean diameter of around 8 nm. The wiggly pattern in the TEM image, is due to the second layer of the honeycomb structure sitting over the first layer in a AB type packing. Particles which are not well formed hexagons are left out in the packing, as evidenced in the image. The STM image (top view) in Fig. 2. 22 is consistent with the hexagonal shape. The image shows the well-defined edges of the central nanoparticles.

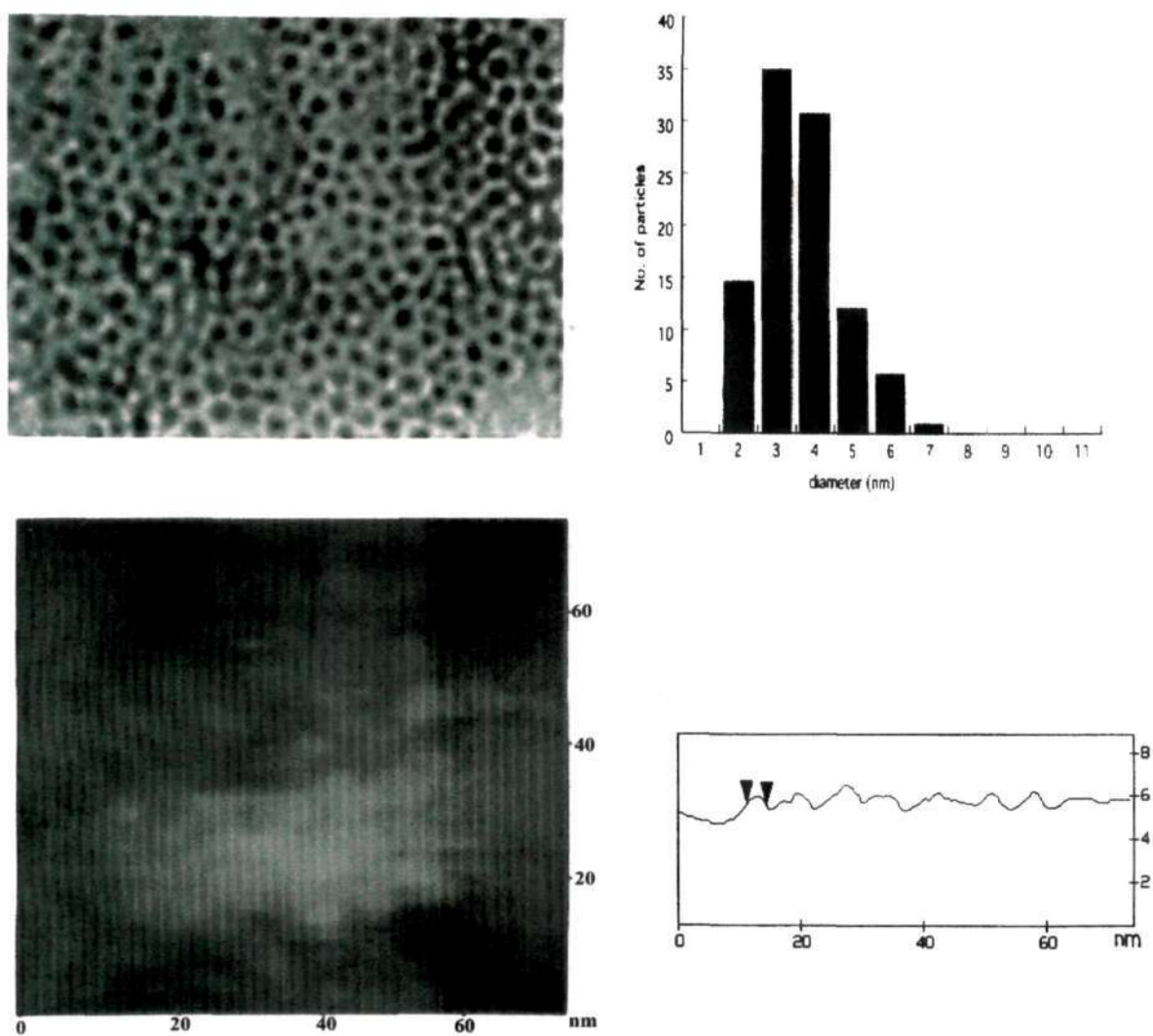


Fig. 2. 21. (a) TEM image of thiol-derivatized Pt nanoparticles prepared by NaBH_4 reduction (b) The histogram shows the particle size distribution (mean diameter = 4.1 nm) (c) STM image of a crystallite formed by spherical nanoparticles (d) The line profile of a crystallite in (c) with the two arrows marking the diameter of the particle.

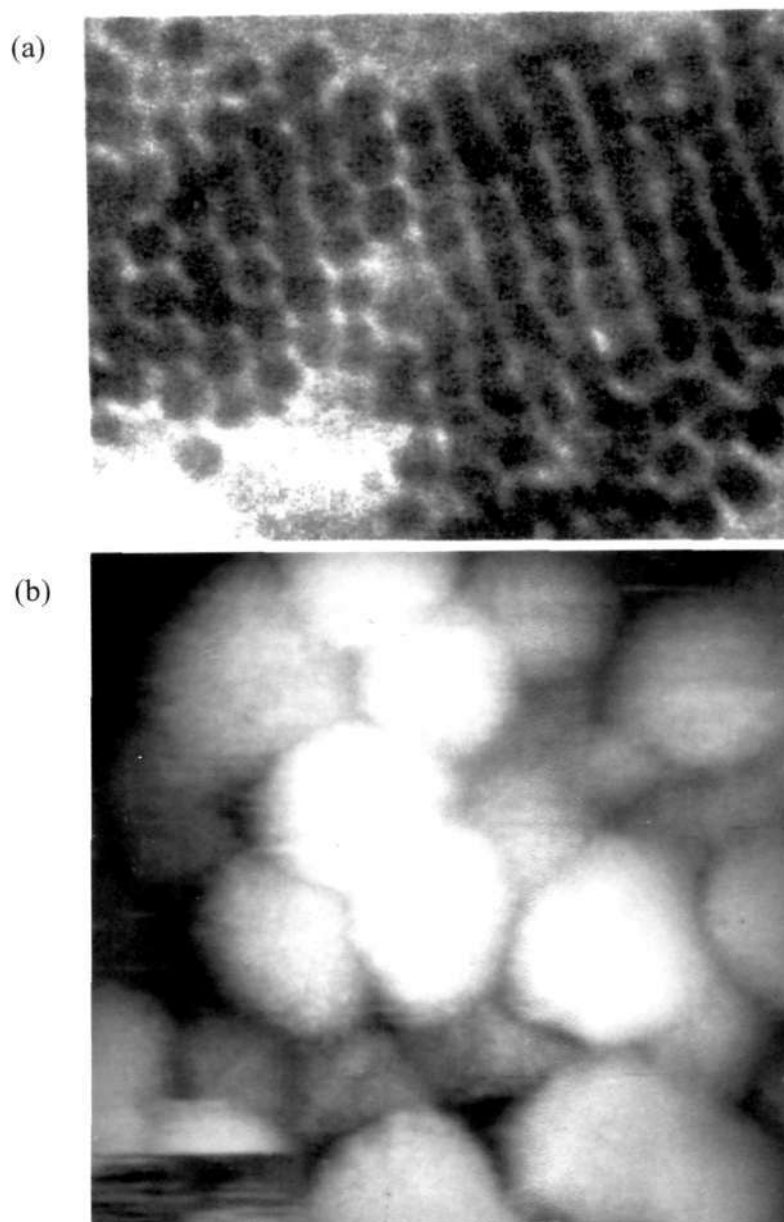


Fig. 2. 22. (a) TEM image thiol-derivatized Pt particles (mean dia ~ 8 nm) prepared by the sodium polyacrylate method. Hexagonal nanocrystallites forming a honeycomb structure are seen (b) STM image ($45 \times 45 \mu\text{m}$) of hexagonal Pt nanocrystallites. The hexagonal stacking of the top three layers is clearly seen.

In Fig. 2. 23, we show the TEM image of the thiol-derivatized Ag nanoparticles obtained by the NaBH_4 reduction. The particle shape is not always spherical, but the size distribution is fairly narrow and the mean diameter is 4.1 nm. Here again we see a nanocrystalline array formed by the particles. Similar nanocrystalline arrays of thiol-derivatized Ag particles have been prepared by vacuum evaporation technique [72].

In the above discussion, we have shown how particles of various metals form arrays extending over hundreds of nanometers. The most common feature of these 2D structures is that each nanocrystallite is in the centre of a hexagon formed by neighbours and an interparticle distance close to the length of the thiol molecule (~ 1.5 nm). Such structures are observed to form if the particle size distribution is relatively narrow regardless of shape. It is likely that the nanoparticles in these arrays are held by attractive forces due to van der Waals interaction balanced by incompressibility and chain-chain repulsion among the surfactant thiol molecules. The arrays are therefore very fragile. If the shapes and sizes of the particles are very large (> 25 nm), the arrays will not form. For instance, the thiol derivatized colloidal particles from the citrate method occur in various shapes – triangular, quadrilateral, pentagon, rod like etc –and sized (10-50 nm) but they do not form an ordered as seen from TEM image shown in Fig. 2. 24. Also shown is the STM image obtained from the thiolized sol which show

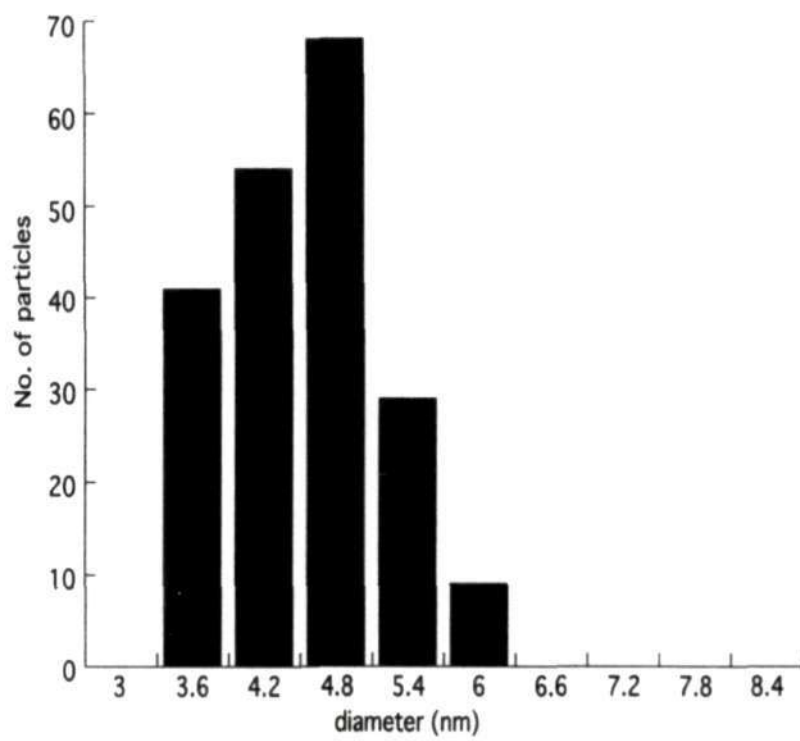
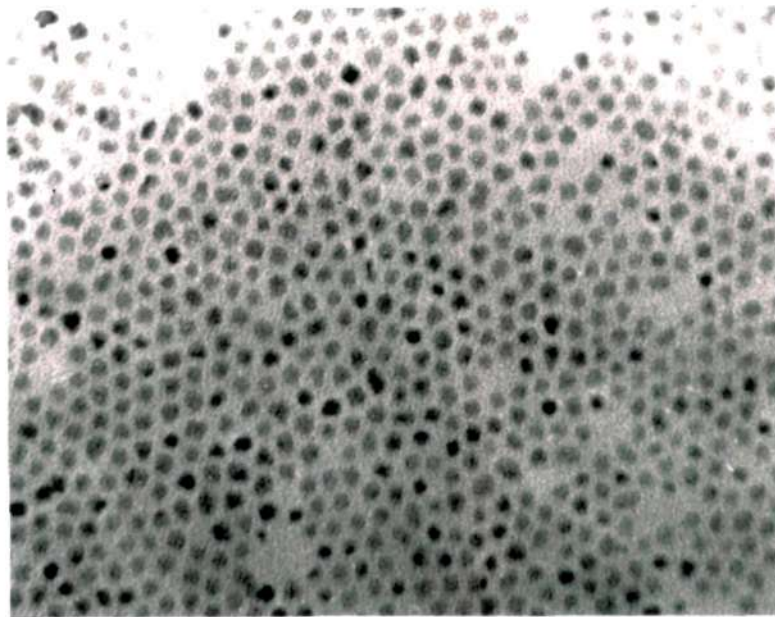


Fig. 2. 23. TEM image of the thiol-derivatized Ag particles prepared by NaBH_4 reduction. The histogram depicts the mean diameter (4.2 nm) of the particles.

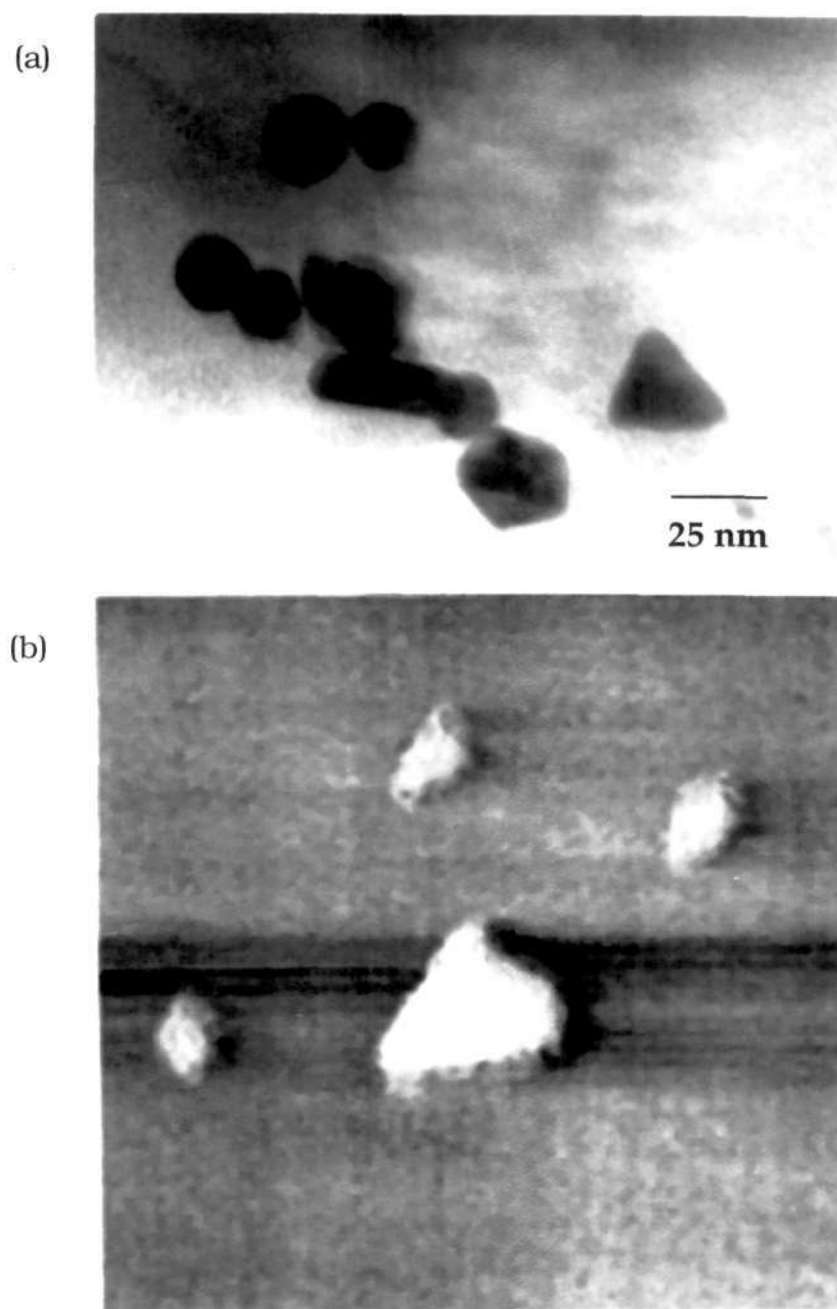


Fig. 2. 24 (a) TEM image and (b) STM image of thiol-derivatized Au nanoparticles prepared from citrate reduction.

correlates with observed behavior from TEM studies. We have used this study to emphasize that the particle morphology is well preserved subsequent to the transfer of the particles across the aqueous-organic interface and the adsorption of thiol molecules.

2.4.3 Superlattices of metal nanoparticles

In the previous section, we presented the synthesis and characterization of nanocrystalline two-dimensional arrays of metal nanoparticles. These metal nanoparticles, also known as quantum dots, exhibit properties that lie between the atomic and the bulk state. We therefore, considered it important to further elucidate the electronic structure of small metal particles using photoelectron spectroscopic techniques having already seen the changes in the plasmon absorption as a result of particle size. The nanocrystalline arrays described in the previous section are in fact ideal for the measurement of electronic band structure of nanoparticles. The usefulness of these systems is that the particles are held apart by the relatively inert chains of the thiol molecules thereby preventing coagulation and growth of the particles during the measurements. Moreover, nanometric dimensions of the spacer thiol molecules enhance the conductivity of the system through tunneling. In what follows, we have used dithiol molecules as spacers (instead of monothiol molecules) with a feasibility of building multilayers of nanocrystallites on a metal substrate. An artistic impression of the same is shown in Fig. 2. 25. Such stacked nanocrystalline arrays

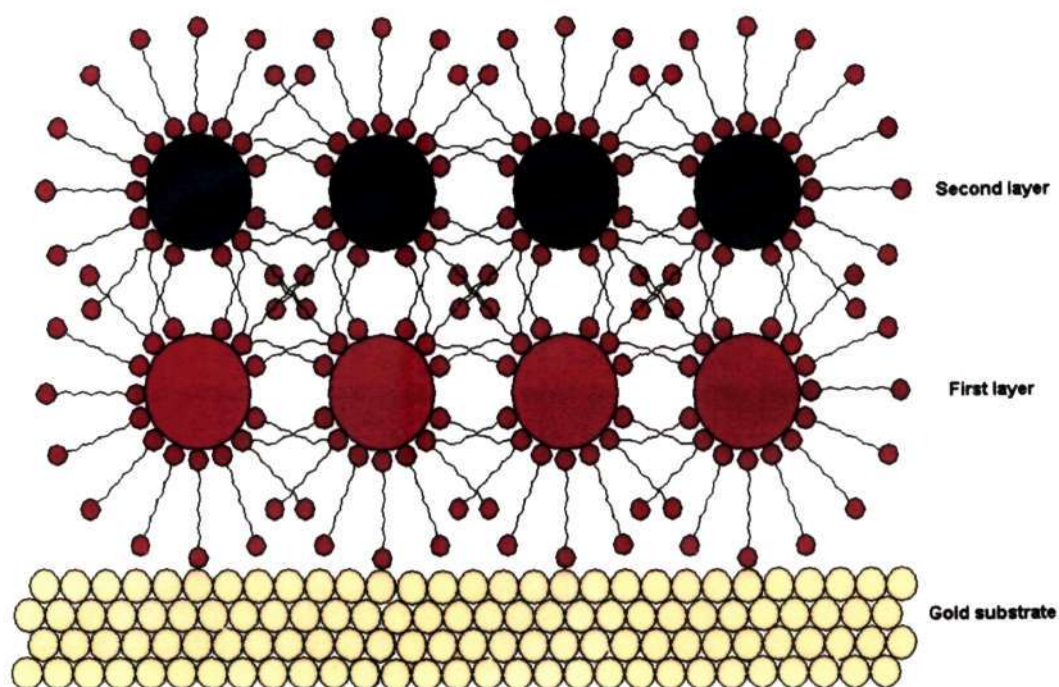


Fig. 2. 25. Schematic representation of successive depositions of metal nanoparticles forming layers separated by dithiol molecules as spacer molecules.

would in fact serve as models in nanoscale architecture as vertical self-organized systems.

In Fig. 2. 26, we show typical XRD patterns of lattices formed by Pt nanoparticles of a mean diameter of 5 nm (as determined by TEM) after the first, third and fifth depositions on a gold substrate. We see a low-angle peak with a d -spacing of 7.2 nm corresponding to a centre-to-centre distance between two adjacent particles in an array. XRD patterns of such lattices obtained from the deposition of Pt and Au nanoparticles of different sizes reveal that the d -spacing of the low-angle feature increases with mean diameter of the nanoparticle as shown in the inset of Fig. 2. 26. The intercept on the y -axis (~ 2 nm) approximately gives the spacing between two adjacent particles.

Scanning tunneling microscopy (STM) has been employed in order to visualise the packing and the growth mode of the layers after each deposition. The study after the first layer deposition of 5 nm Pt particles showed arrays extending over 300 nm, corresponding to a typically flat terrace of the substrate. In Fig. 2. 27, we show the magnified region of $\sim 40 \times 40 \mu\text{m}$ showing Pt nanoparticles of ~ 5 nm in diameter. Moreover a regular spacing of ~ 2 nm was obtained between these particles. In order to visualise the growth pattern, we have chosen Pt(1.5nm)/Au system since larger number of particles can be imaged for a given scan size. A typical STM image obtained in an area of 100×100

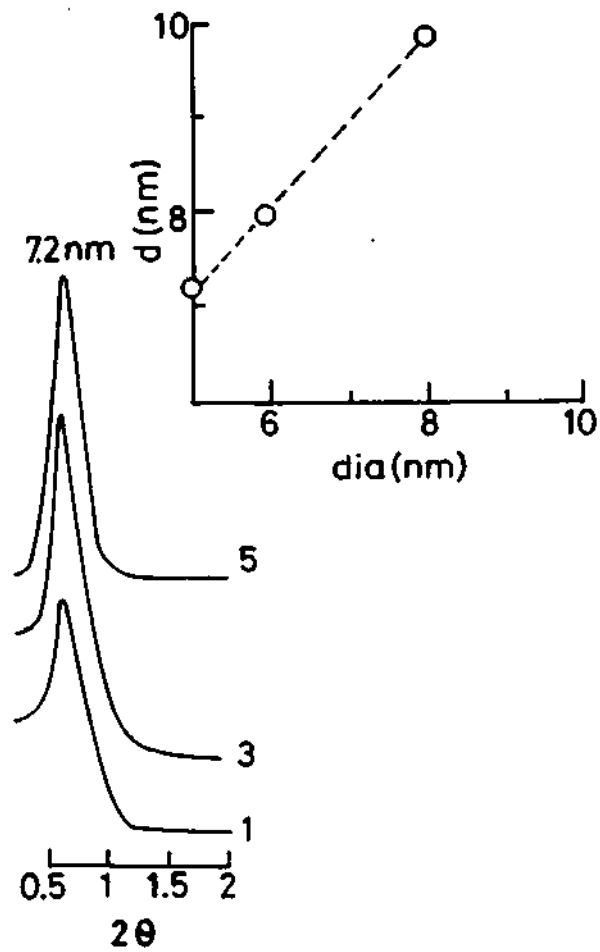


Fig. 2. 26. X-ray diffraction patterns of nanocrystalline arrays of 5 nm Pt depositions. The inset shows the variation in the d -spacing due to nanocrystalline arrays formed by the particles of different diameters. Layers of Pt 1.5 nm particles did not give a XRD pattern.

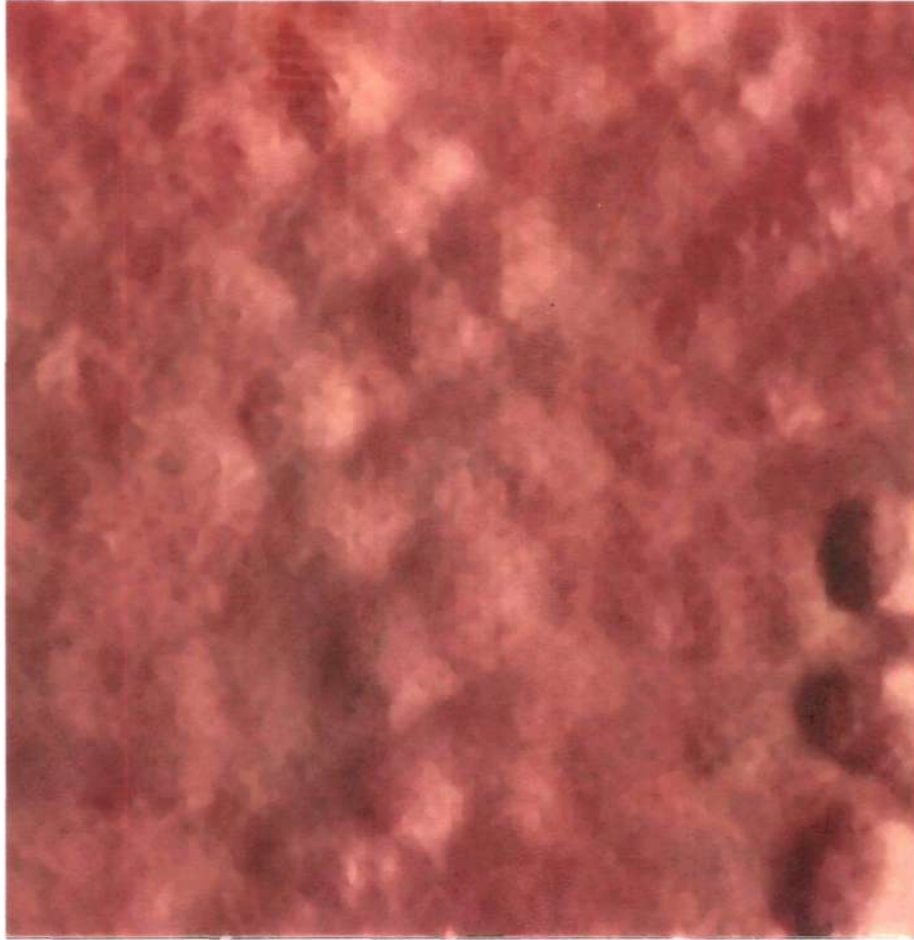


Fig. 2. 27. STM image of Pt (5nm)/Au system after the first deposition of Pt nanoparticles. Each sphere seen is approximately 5 nm in diameter.

nm after the first deposition is shown in Fig. 2. 28a. We see a large number of particles with diameter in a narrow range centred around 1.5 nm. After examining over 100 particles, we have obtained the mean dia of the particles to be 1.5 nm. We also noted that the particles are separated by a nearly constant distance of 20 Å due to the dithiol molecules. However we see no long range ordering of the particles unlike that are seen with the nanocrystalline arrays obtained using monothiols. The STM image obtained after the second deposition is shown in Fig. 2. 28b. An interesting feature of this image is that the layers obtained after the first and the second depositions are seen as varying corrugation in the image. The depth profile analysis was therefore carried out and is displayed in Fig. 2. 29. Markers are used to indicate the shallow regions and the high regions. The values shown indicate the clear formation of the second layer. As an example, the profile in Fig. 2. 29 shows an average height of ~ 2.5-3.0 nm. Now, the length of a dithiol bonded to a metal atom is ~ 1.4 nm and this added to the diameter of the cluster of 1.5 nm give a height of 2.9 nm, which is close to the observed value. In Fig. 2. 28c, we see an image of 85 x 85 nm after the third deposition. We see clearly big spherical structures of dia ~ 30 nm. Unlike the first layer, which has a metal substrate as its support, the third layer is entirely held by highly conformal 1,10-decanedithiol molecules. Possibly, the particles assemble into dense structures stabilized by the dithiol molecules.

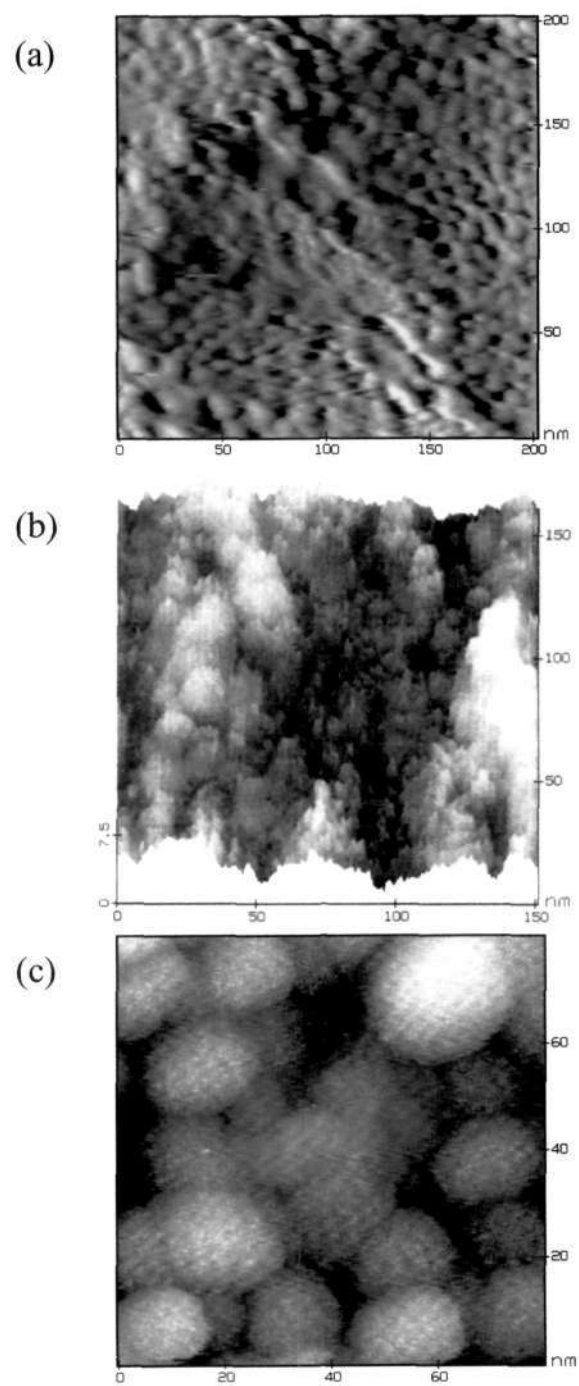


Fig. 2. 28. STM image of the Pt(1.5nm)/Au system after the (a) first (b) second and the (c) third depositions of the Pt nanoparticles.

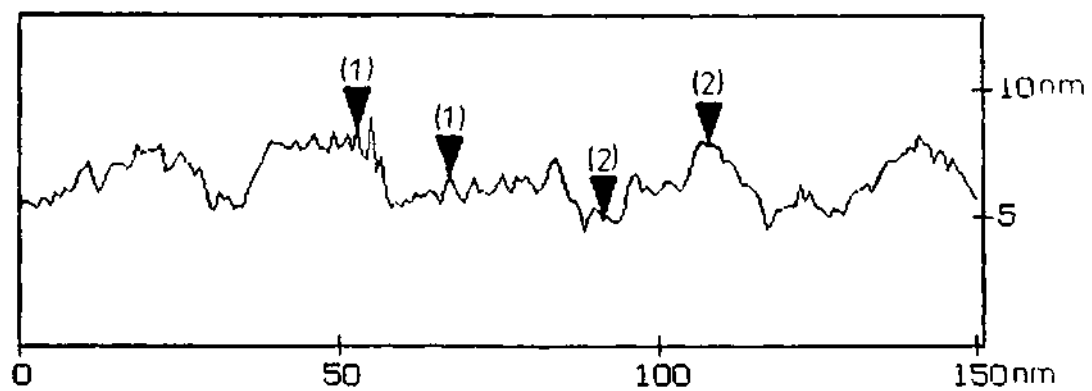


Fig. 2. 29. Depth profile analysis of the STM image shown in Fig. 2. 28b.

The core-level intensities of both the substrate and the metal nanoparticles have been monitored in XPS as a function of deposition. In Fig. 2. 30 we show the Pt(4f) and the Au(4f) spectra after each deposition for the Pt(1.5nm)/Au multilayer system. We clearly see that the Pt(4f) spectrum increases in intensity with deposition and that of the Au4f decreases simultaneously indicating that the substrate is increasingly shadowed due to the limited escape depth of the photoelectrons. We discontinued at the fifth deposition since the substrate Au(4f) intensity became negligible. The core-levels of the carbon and sulfur (C(1s) and S(2p)) have also been monitored (see Fig. 2. 31). At zero deposition, no measurable signal was observed in the carbon and the sulfur regions. After the first deposition, we observe the C(1s) and the S(2p) peaks, where the former was found to be much higher in intensity. Both the peaks grew with successive depositions until the fourth and saturate thereafter.

As regards the binding energies of the different core-levels, the Au(4f_{7/2}) and the Pt(4f_{7/2}) showed the same values as in the bulk that is 84.0 and 71.3 eV respectively, characteristic of the zero oxidation state in the metal nanoparticles. The binding energies of the C(1s) and S(2p) was found to be 285.0 and 163.6 eV similar to the values obtained with chemisorbed monothiols (see Sec 2.4.2).

Similar measurements were carried out on the Pt(5nm)/Au system. As shown in Fig. 2. 32, the intensity of the Pt(4f) spectrum increases with successive

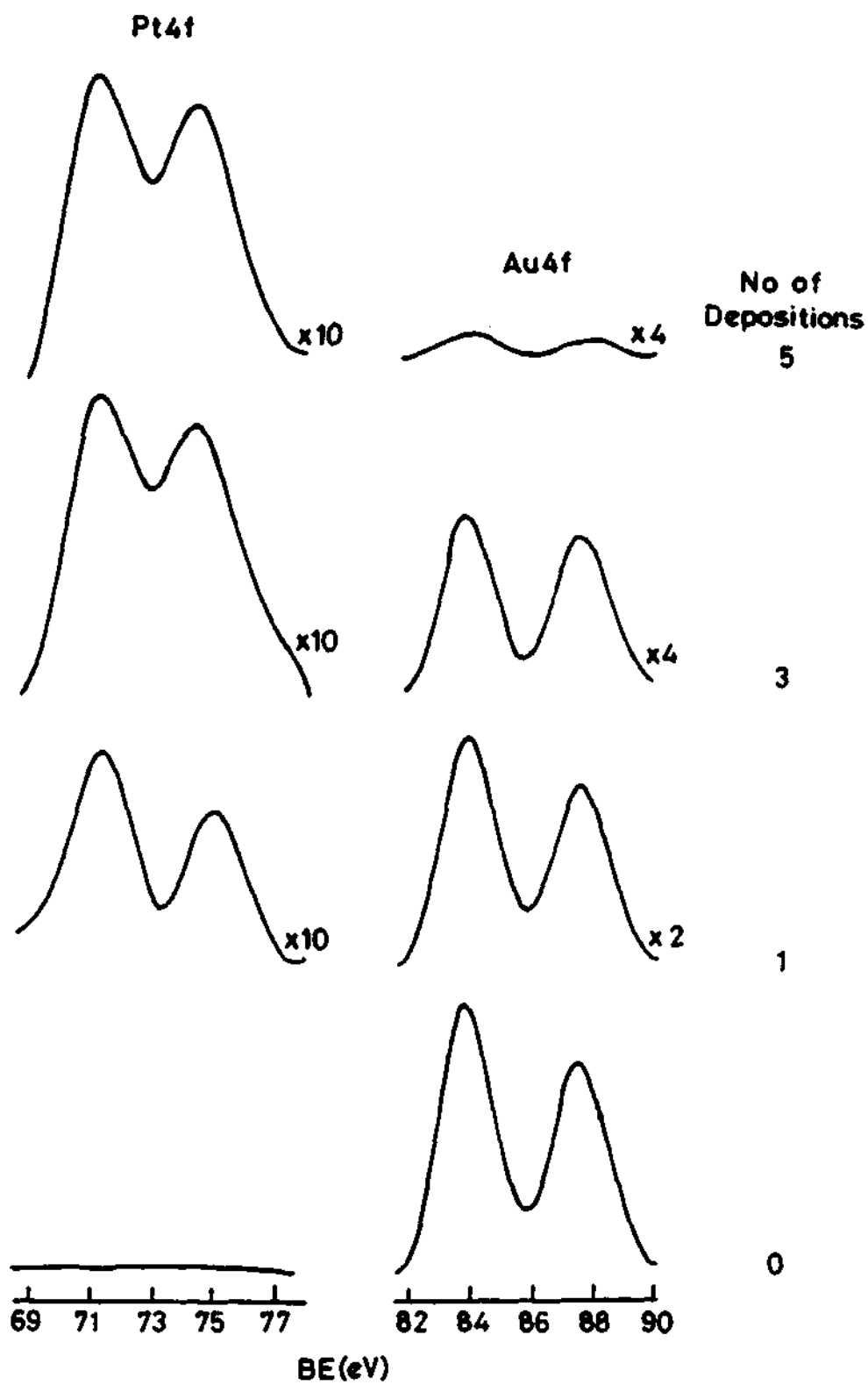


Fig. 2. 30. X-ray photoelectron spectrum in the Pt(4f) and the Au(4f) regions for the Pt(1.5nm)/Au system.

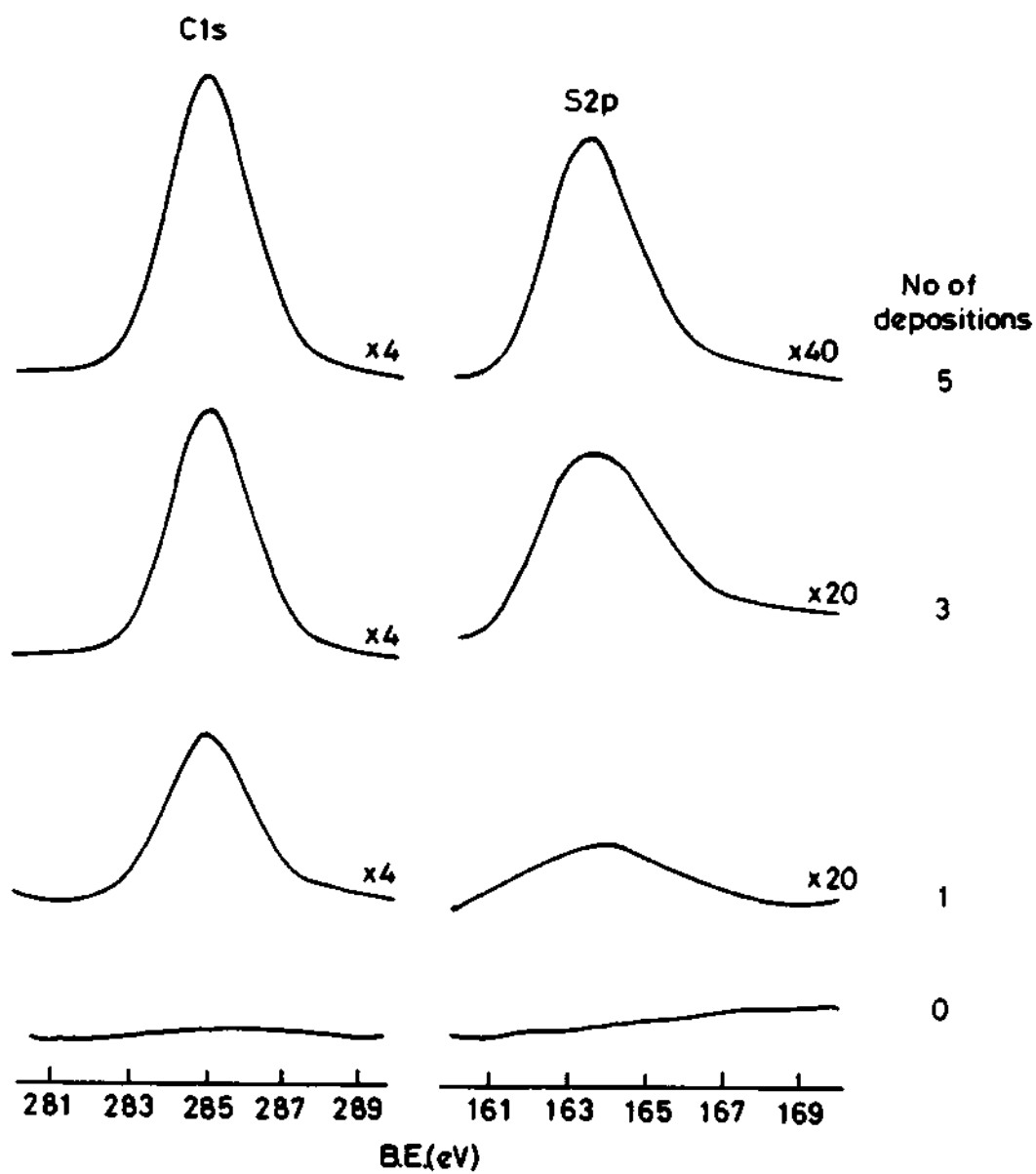


Fig. 2. 31. X-ray photoelectron spectrum in the C(1s) and the S(2p) regions for the Pt(1.5nm)/Au system.

depositions and that of the Au(4f) decreases similar to the behavior observed in the case of the Pt(1.5nm)/Au system. However, the Pt intensity appears much higher in the Pt(5nm)/Au system than that containing the 1.5 nm particles for similar depositions. This can be rationalised as due to the increase in mass per deposition where the particles are bigger. The C(1s) and S(2p) spectra for the Pt(5nm)/Au system are shown in Fig. 2. 33. We find a similar trend as in the Pt(1.5nm)/Au system (Fig. 2. 31).

In order to have a quantitative comparison of the different species, we have normalized the area under the XPS peaks with respect to the spectra of the bulk obtained under similar conditions. In Fig. 2. 34 we show the normalized intensities of the Au(4f_{7/2}), Pt(4f_{7/2}), C(1s) and S(2p) core-levels as a function of deposition for the Pt(1.5nm)/Au system. From Fig. 2. 34a, it can be seen that the visibility of the gold substrate in XPS decreases with successive depositions whereas the Pt intensity reaches saturation. The surface concentration of the carbon and sulfur species varies nearly linear at lower depositions and appears to reach saturation values at the fifth deposition. Similar curves were obtained for the Pt(5nm)/Au system (see Fig. 2. 35).

In another experiment, the Au nanoparticles have been deposited on a silver substrate using a similar procedure and the depositions have been monitored using XPS. The core-level spectra in the Au(4f) and Ag(3d) regions are shown in

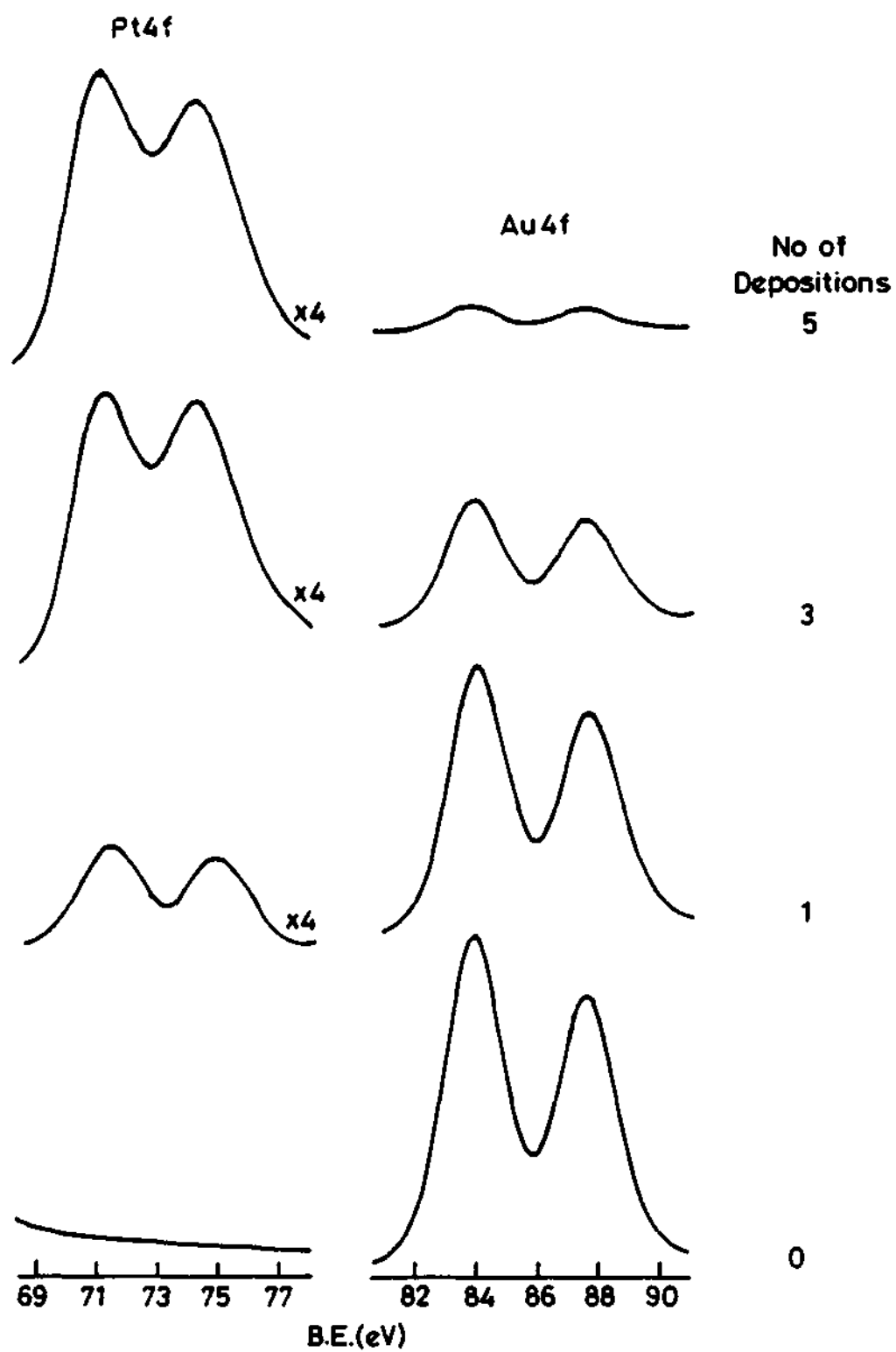


Fig. 2. 32. X-ray photoelectron spectrum in the Pt(4f) and the Au(4f) regions for the Pt(5nm)/Au system.

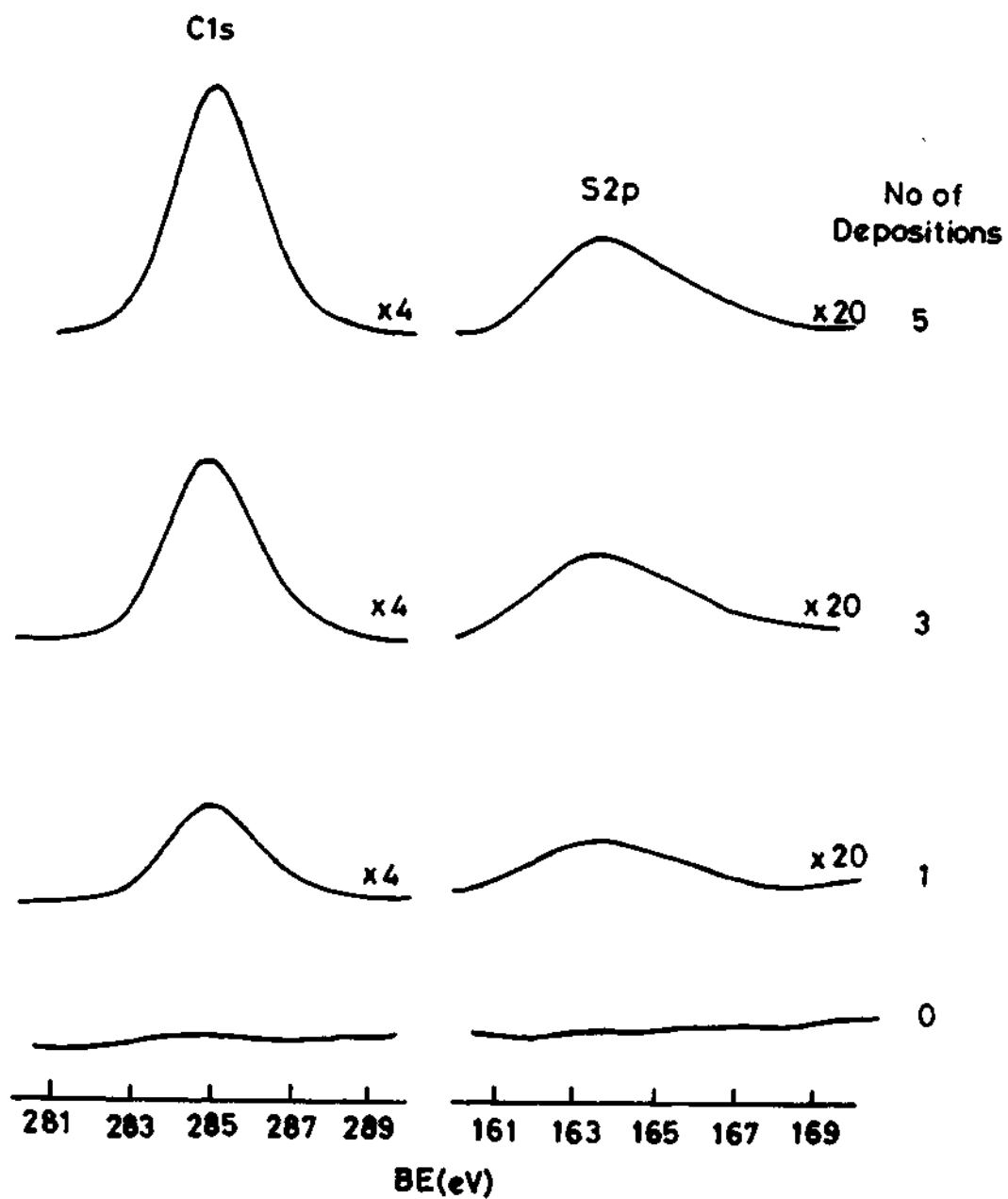


Fig. 2. 33. X-ray photoelectron spectrum in the C(1s) and S(2p) regions for the P(5nm)/Au system.

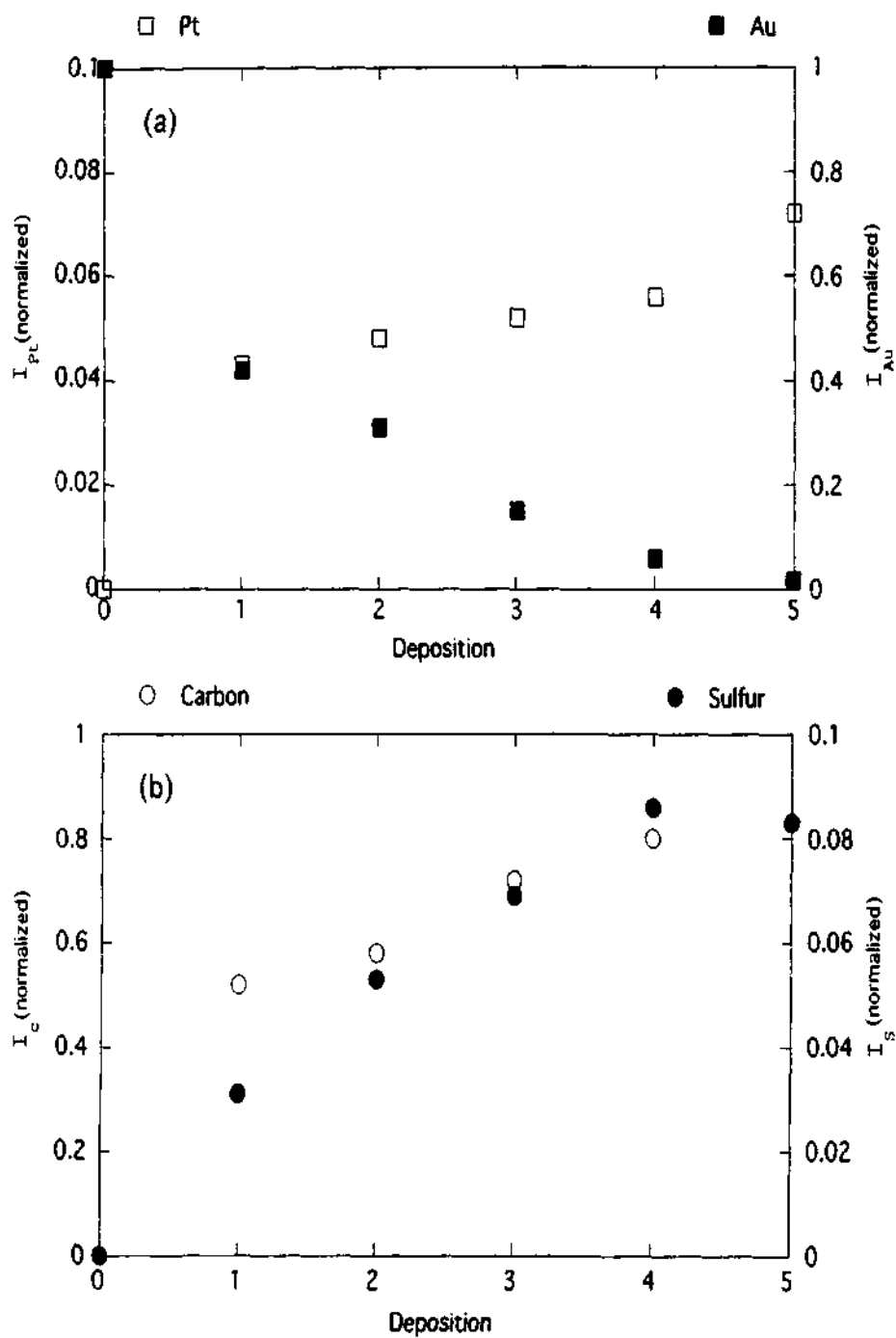


Fig. 2. 34. Normalized intensities of the photoelectron spectra as a function of deposition for the Pt(1.5nm)/Au system (a) Pt(4f) and Au(4f) (b) C(1s) and S(2p).

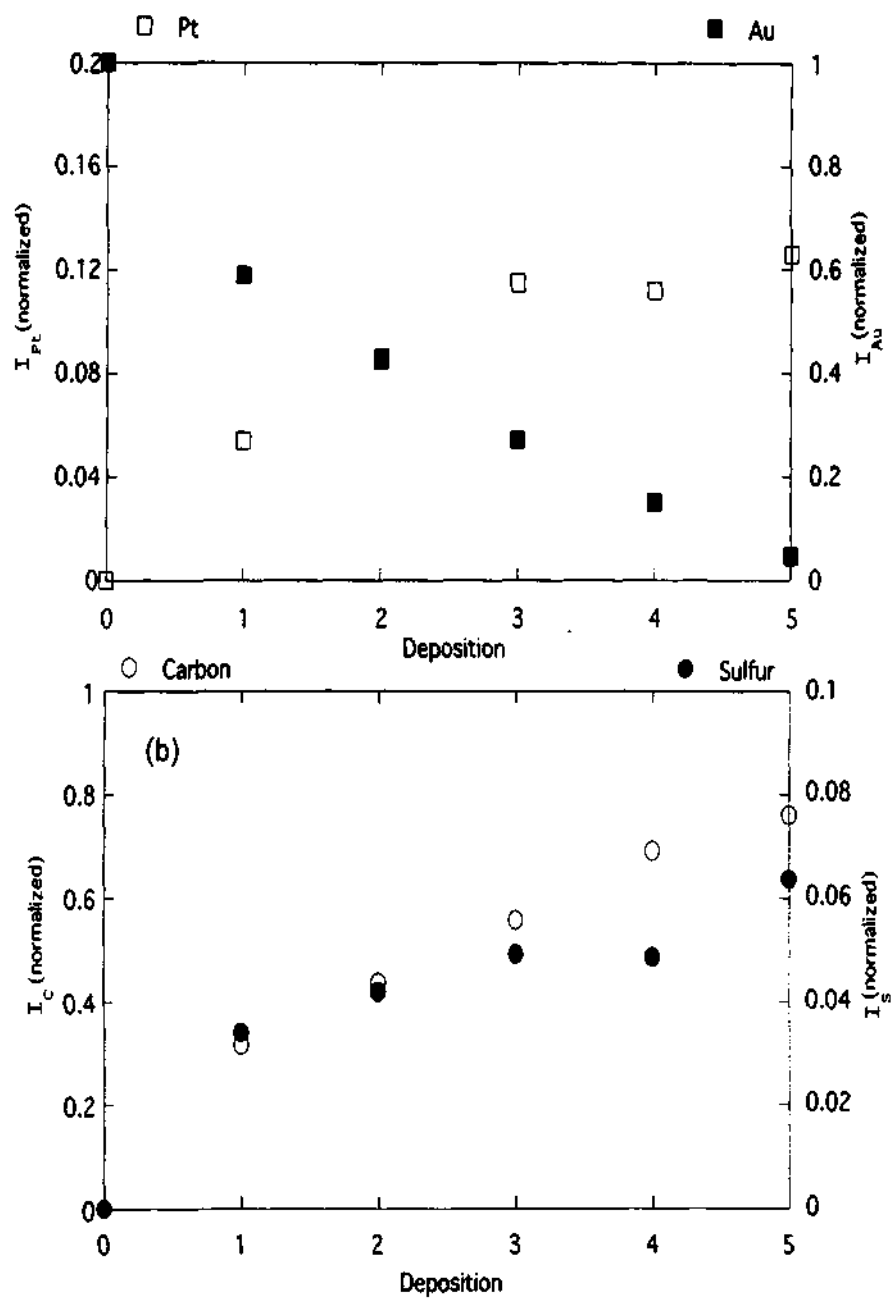


Fig. 2. 35. Normalized intensities of the photoelectron spectra as a function of deposition for the Pt(5nm)/ Au system (a) Pt(4f) and Au(4f) (b) C(1s) and S(2p).

Fig. 2. 36 for the first and the third depositions. The inset of the figure shows normalized intensities of the core-levels. It is seen that the substrate signal becomes negligible by the third deposition.

We have investigated the formation of bimetallic superlattice by alternate depositions of 6 nm Au particles and 5 nm Pt particles on a Ag substrate, the particulate layers being separated by decanedithiol molecules. In Fig. 2. 37, we show the core level spectra in the Ag(3d), Au(4f) and Pt(4f) regions. There is a decrease in the intensity of the Ag(3d) level with successive depositions, while the Au(4f) intensity appears after the first deposition and decreases after the deposition of Pt nanoparticles in the second layer. This demonstrates the formation of superlattices of arrays of metal nanoparticles by the technique developed by us.

In view of the above confirmation with regard to the growth of superlattices, we have been able to prepare heterostructures consisting of alternate layers of semiconductor and metal nanoparticles. For this purpose, we have deposited a first layer of 5 nm Pt particles on a dithiol-covered Au substrate. Above this another layer of dithiol molecules was grown. This system was finally dipped into an inverse micellar solution of AOT capped CdS nanoparticles for 12 h in order to obtain a CdS-Pt heterostructure. XPS evidence

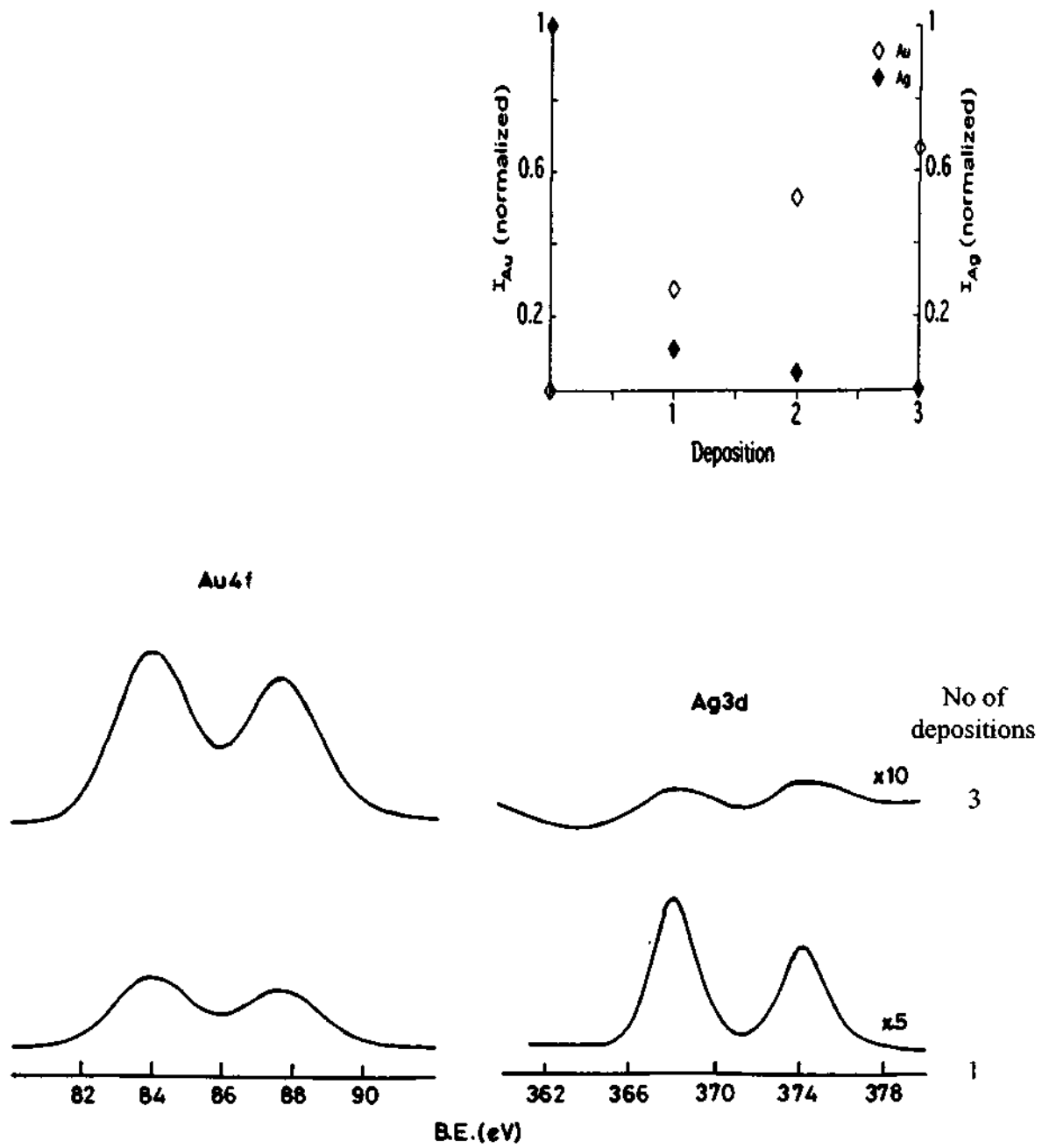


Fig. 2. 36. X-ray photoelectron spectrum in the Au(4f) and Ag(3d) regions for the Au(6nm)/Ag system. (Inset) Normalized intensities of the photoelectron spectra as a function of deposition for Au(4f) and Ag(3d).

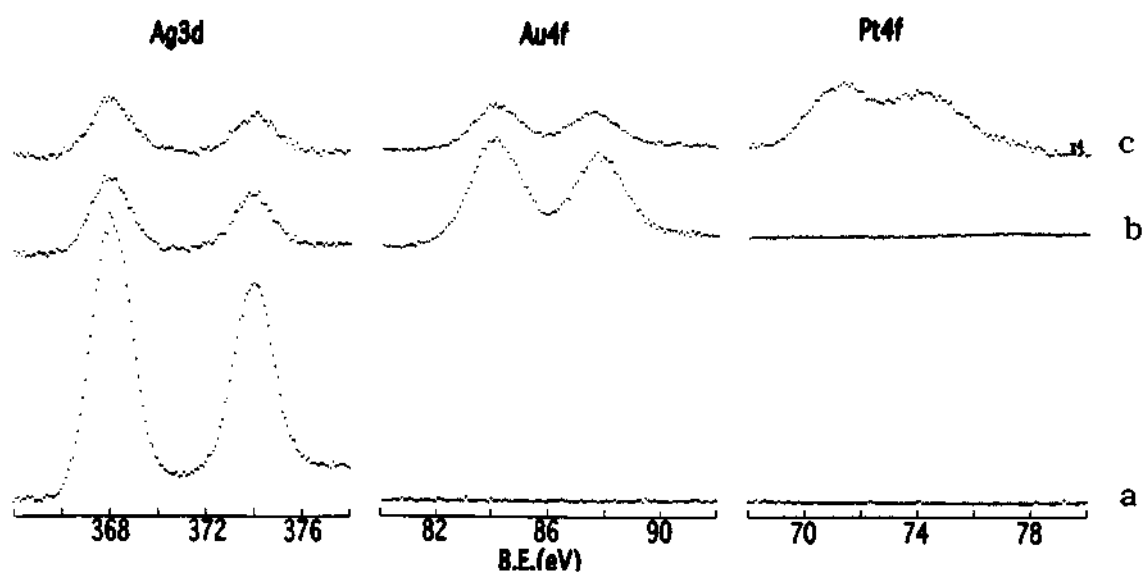


Fig. 2. 37. X-ray photoelectron spectra in the Ag(3d), Au(4f) and Pt(4f) regions for the Pt/Au/Ag system: (a) clean Ag substrate (b) after the deposition of 6 nm Au particles in the first layer and (c) after the deposition of the 5 nm Pt particles in the second layer.

for such a growth is shown in Fig. 2. 38. The intensity pattern is similar to the bimetallic system. The Cd(3d) core level is seen after the second layer deposition.

We now report our results on the Ultraviolet photoelectron spectroscopic (UPS) measurements of the multilayer systems discussed above. In Fig. 2. 39, we have shown He-I UPS spectra of Pt(1.5nm)/Au after the first and the fifth deposition along with those of the gold substrate before and after the thiol adsorption. The clean gold substrate exhibits a small intensity at the Fermi level (E_F) and two prominent 5d peaks at approximately 4.5 and 6.0 eV and a shoulder feature at ~ 2.5 eV. The spectrum resembles closely with that reported for polycrystalline Au. We notice significant changes after the dithiol adsorption. The intensity of the spectral region near E_F , the shoulder feature at ~ 2.5 eV and the 5d band at 4.5 eV show considerable decrease in intensity after dithiol adsorption and the maximum of the spectrum occurs as a broad feature around 6.0 eV. It is reported in the literature [116] that the thiolate species exhibit features approximately at 4.0 and 6.5 eV due to the π and the σ bonding with the metal atoms respectively. In the case of the dithiol attachment on a metal substrate as in our systems, the σ bonding probably dominates. We therefore conclude that the dithiol covered Au substrate exhibits the metal features along with that of the thiolate species. The spectrum obtained after the first deposition of the 1.5 nm Pt particles do not show any feature due to the substrate, which indicates that the particle coverage is continuous and complete. This was

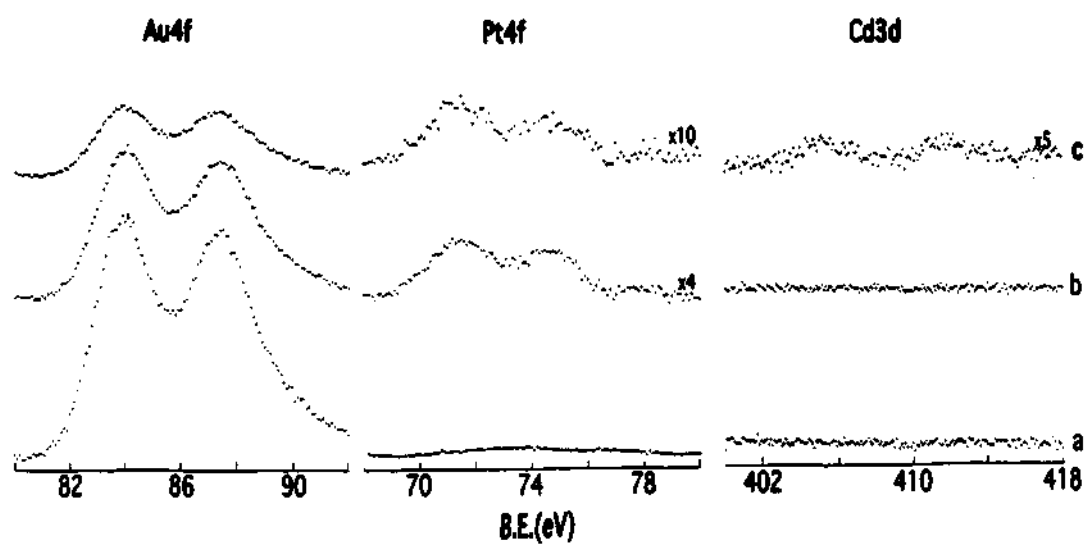


Fig. 2. 38. X-ray photoelectron spectra in the Cd(3d), Pt(4f) and Au(4f) regions for the CdS/Pt/Au system: (a) clean Au substrate (b) after the deposition of the 5 nm Pt particles in the first layer and (c) after the deposition of the 2.4 nm CdS particles in the second layer.

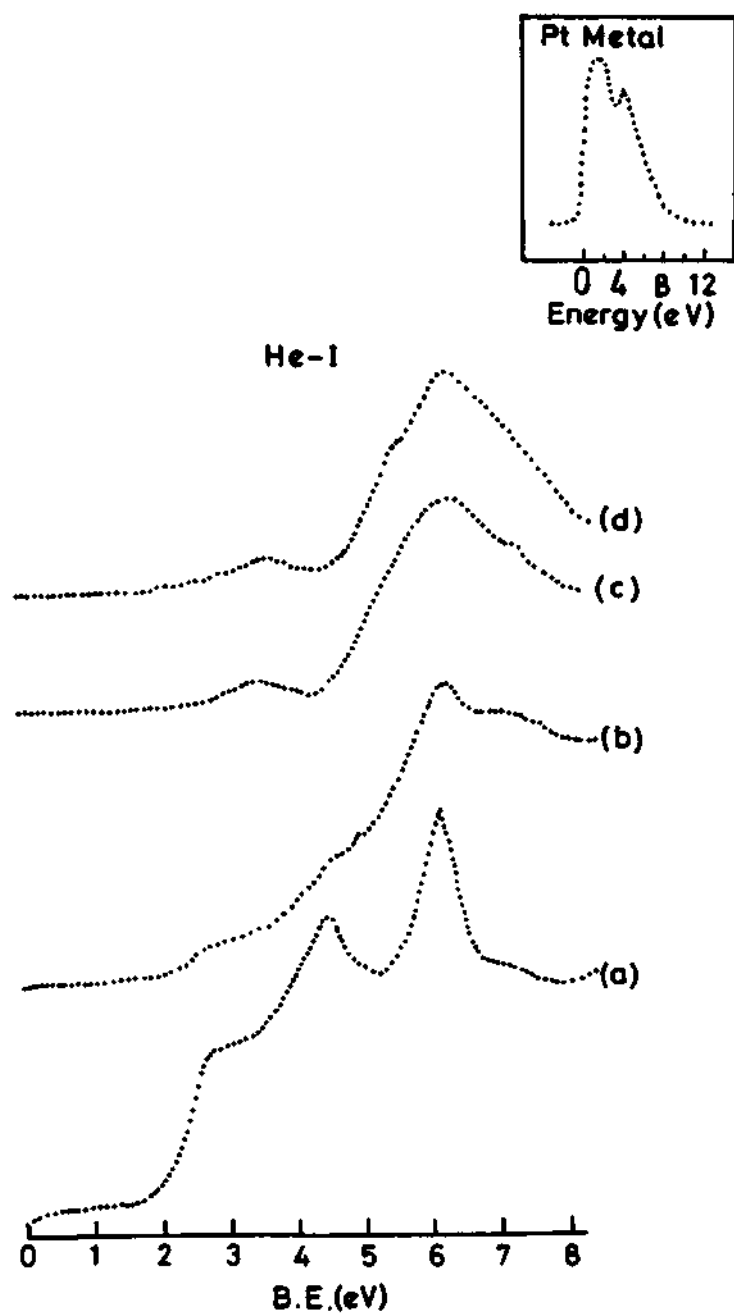


Fig. 2. 39. He-I UPS of (a) polycrystalline Au substrate (b) the Au substrate after the dithiol adsorption (c) Pt(1.5nm)/Au after the first deposition and (d) after the fifth deposition. (Inset) Polycrystalline Pt foil.

substantiated using the spectrum obtained after the fifth deposition. We observe two peaks at approximately 4.0 and 6.5 eV respectively in both the spectra. As mentioned before, the 6.0 eV feature arises due to a bonding between the metal and the thiol group. The feature at 4.0 eV is seen prominently in the polycrystalline Pt (see inset of the Fig. 2. 39) spectrum and can therefore be concluded to arise from the Pt metal. It is interesting to note that there is negligible intensity at the Fermi-level in the case of these particles, whereas the bulk Pt shows a sharp onset at E_F .

We have extended our UPS studies to the Pt(5nm)/Au and the Au(6nm)/Ag systems. In Fig. 2. 40a, we show the ultra-violet photoelectron spectra after the fifth deposition of 5 nm Pt particles on Au substrate. The features seen in the spectrum are comparable to those obtained from a similar deposition on the Pt(1.5nm)/Au system. In addition to the feature at 4.0 and 6.0 eV seen in both the spectra, two additional peaks low in intensity are seen at 0.5 and 2.5 eV. The feature at 0.5 eV is ascribable to the onset of the density of states at the Fermi level as this is also seen in the bulk polycrystalline Pt (Inset of Fig. 2. 39). The feature at 2.5 eV is also due to the Pt cluster. This is established by noting that a similar feature was observed in the He-I spectra of bare Pt clusters at low coverages by Garrett and co-worker [117].

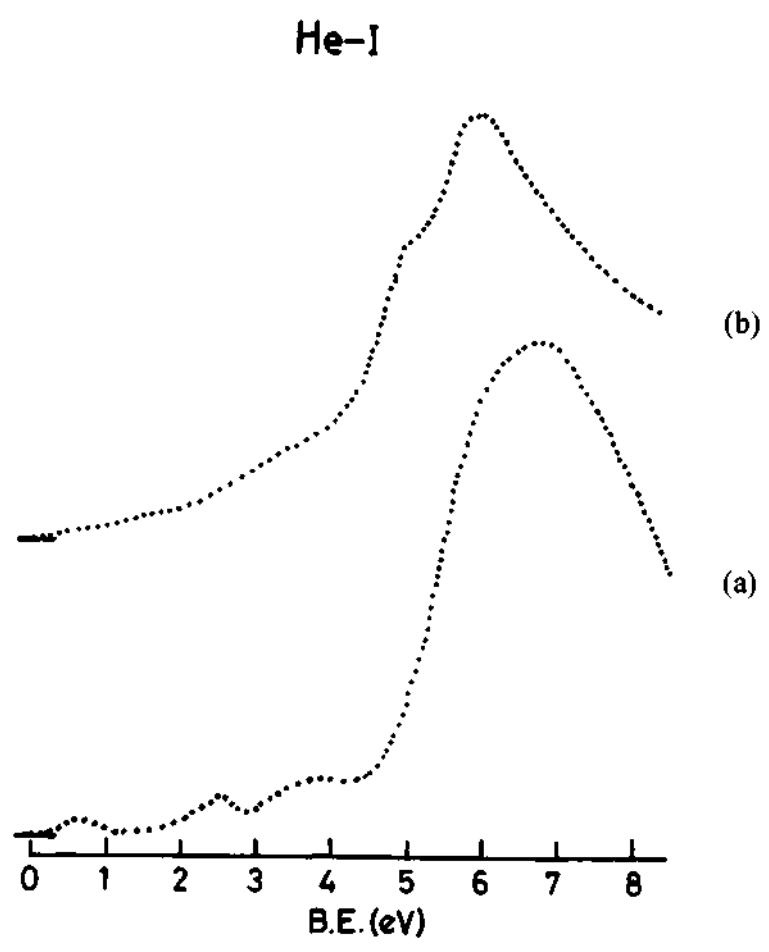


Fig. 2. 40. He-I UPS of (a) Pt(5nm)/Au after the fifth deposition (b) Au(6nm)/Ag after the third deposition.

In Fig. 2. 40b we see the spectrum obtained after the third deposition of Au(6nm)/Ag system. The spectrum compares well with that obtained from the bare gold substrate covered with dithiol, indicating that there are no features arising from the silver substrate.

In conclusion, our UPS measurements reveal the non-metallic nature of sub nanometer metal particles. We observe very low intensity for the density of states near E_F in the case of Pt particles with mean diameter 1.5 nm. On the other hand, the UP spectra of bigger particles of Au and Pt resemble that of bulk. Features due to the interaction of the thiol with the metal surfaces are also observed.

2.4.4 Au nanoparticle-polymer blends

A typical confocal fluorescence image of the Au-P3OT, (S1), blended film is shown in Fig. 2. 41a. Randomly distributed circular features with sharp intensity contrast are present throughout the film, indicating distinct phases. The circular features are essentially a signature of the differences in the evaporation/dewetting rates of the two systems during the film formation, resulting in the creation of local domains. The emission of these circular regions resembled the emission from a pristine polymer film which has a PL maximum centred at ~ 700 nm. As the proportion of polymer is increased (S2), the size of

the circular regions increases and the contrast between the bright and dark regions decreases as can be seen in Fig. 2. 41b.

In Fig. 2. 42a and Fig. 2. 42b we show the near-field scanning optical microscopic (NSOM) image in the topographic mode and also the simultaneously obtained fluorescence image, respectively. The fluorescence image showing polymer strand structures, with spatial resolution better than 200 nm were also obtained, with no corresponding topographic feature, thereby indicating that the optical images were free from topographic artefacts. It is also to be noted that these polymer/Au-nanoparticle film patterns, as shown in Fig. 2. 40, are obtained only with polythiophene derivatives, P3AT such as P3OT and P3HT (polyhexylthiophene). The PPV based polymers, such as MEHPPV, do not show such distinct macroscopic structural patterns.

SEM observations provide further quantitative insight of the phase distribution. Fig. 2. 43 shows the SEM images of Au-P3OT blend where the polymer concentration is high. The average diameters of the circles are shown in the histogram, corroborating our observations made in the optical studies. In Fig. 2. 44a and Fig. 2. 44b the TEM micrographs of two blended Au-P3OT samples with Au nanoparticles of mean diameter corresponding to 4.1 and 7.0 nm are shown. The common feature observed in both micrographs is the circular structure, with a prominent periphery. TEM imaging was repeated on different

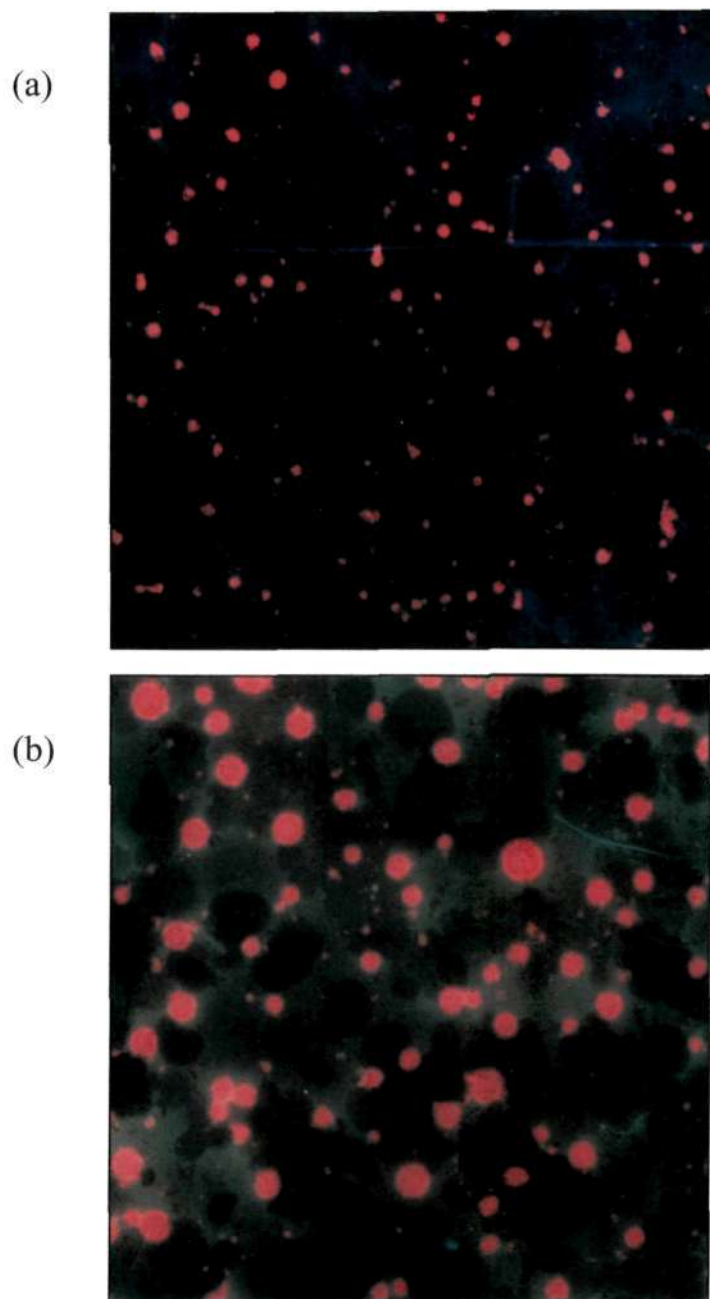


Fig. 2. 41. Optical microscope images of nanoparticle-polymer films with two different ratios of Au:P3OT are shown, wherein the ratio of polymer to that of Au nanoparticles is higher by a factor of three in going from (a) to (b).

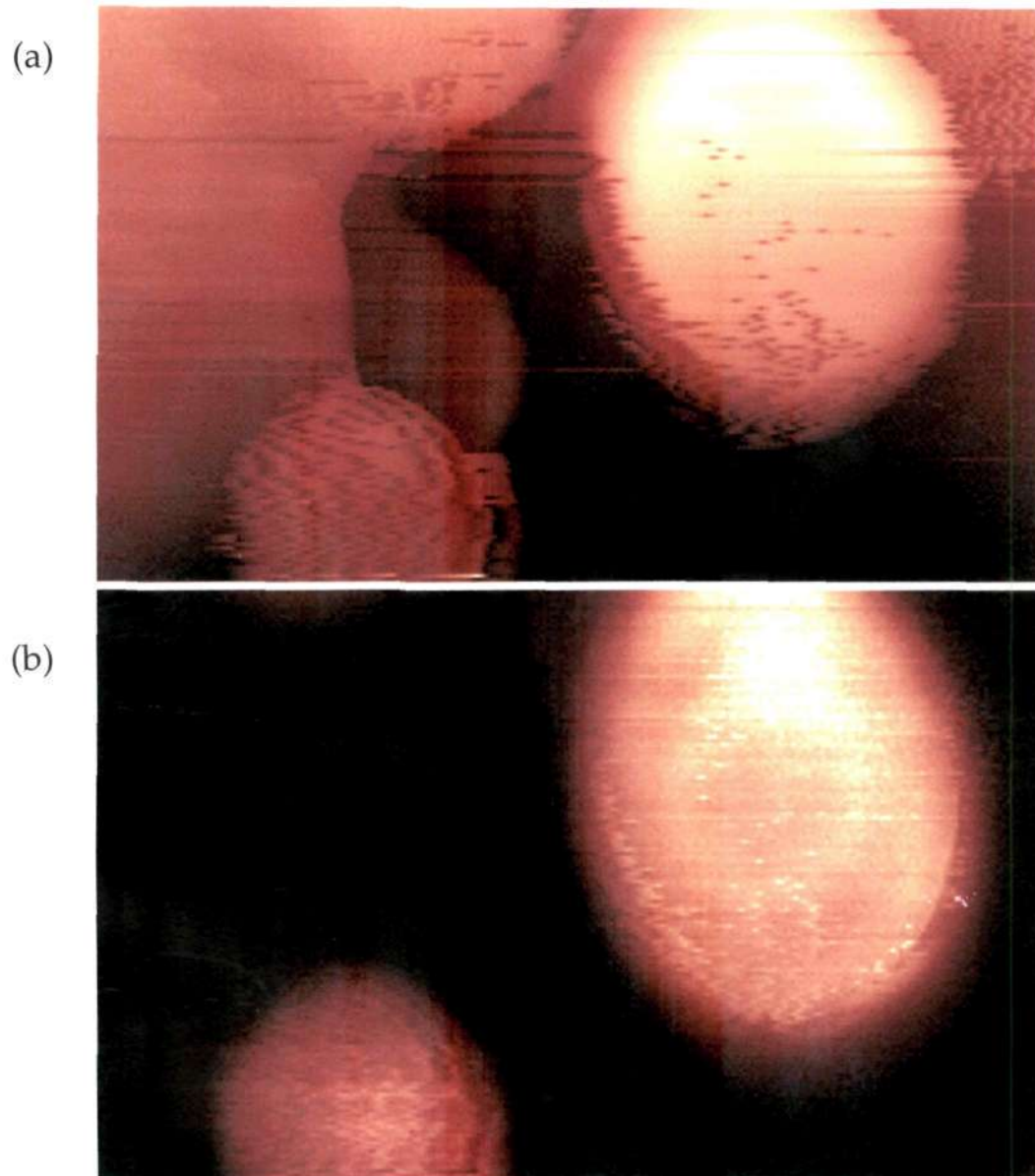


Fig. 2. 42. $6 \times 6 \mu\text{m}$ NSOM image depicting (a) topographic image and (b) fluorescence image.

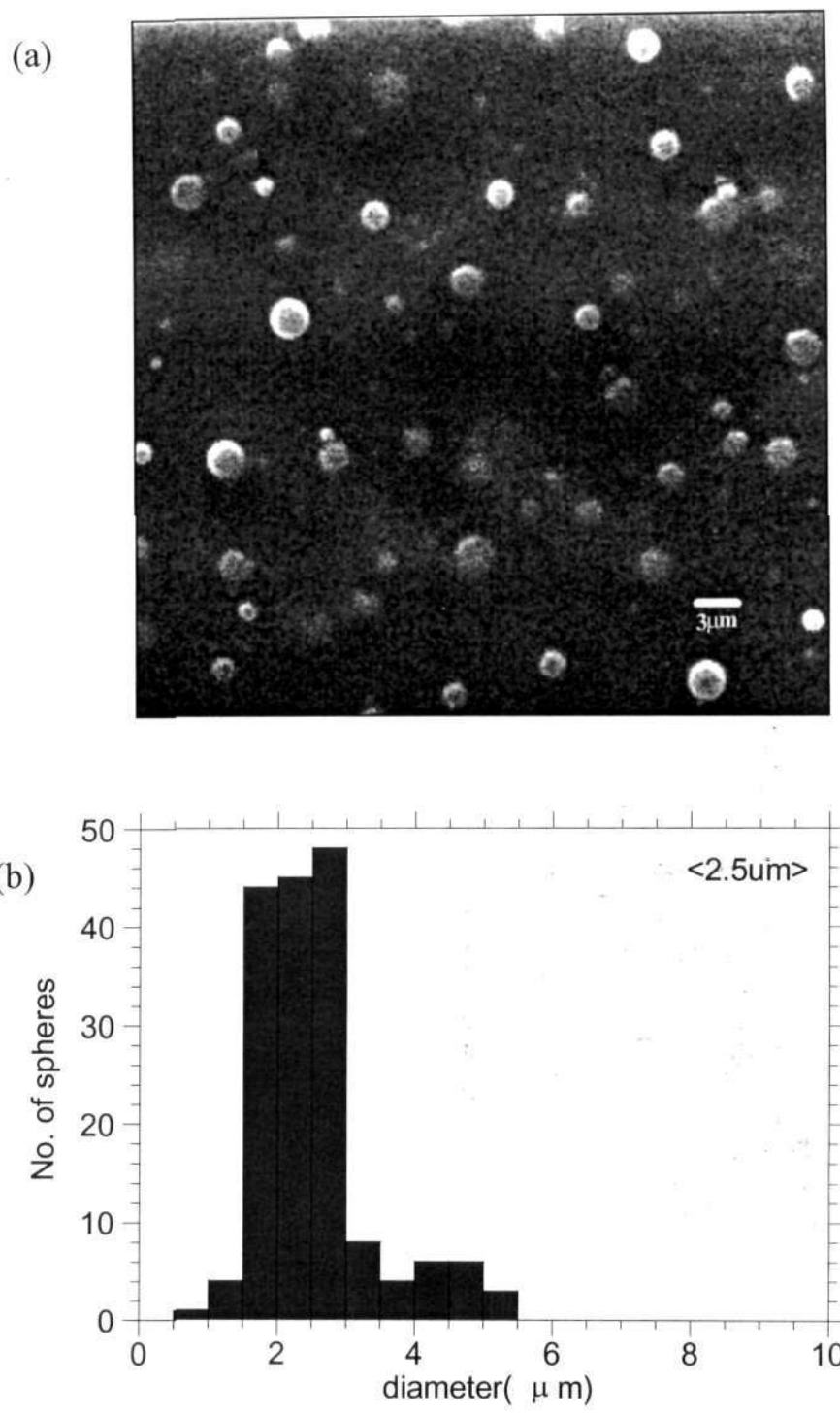


Fig. 2. 43. (a) SEM images of Au-P3OT film showing circular features. (b) The variation in the diameters is depicted in the histogram shown.

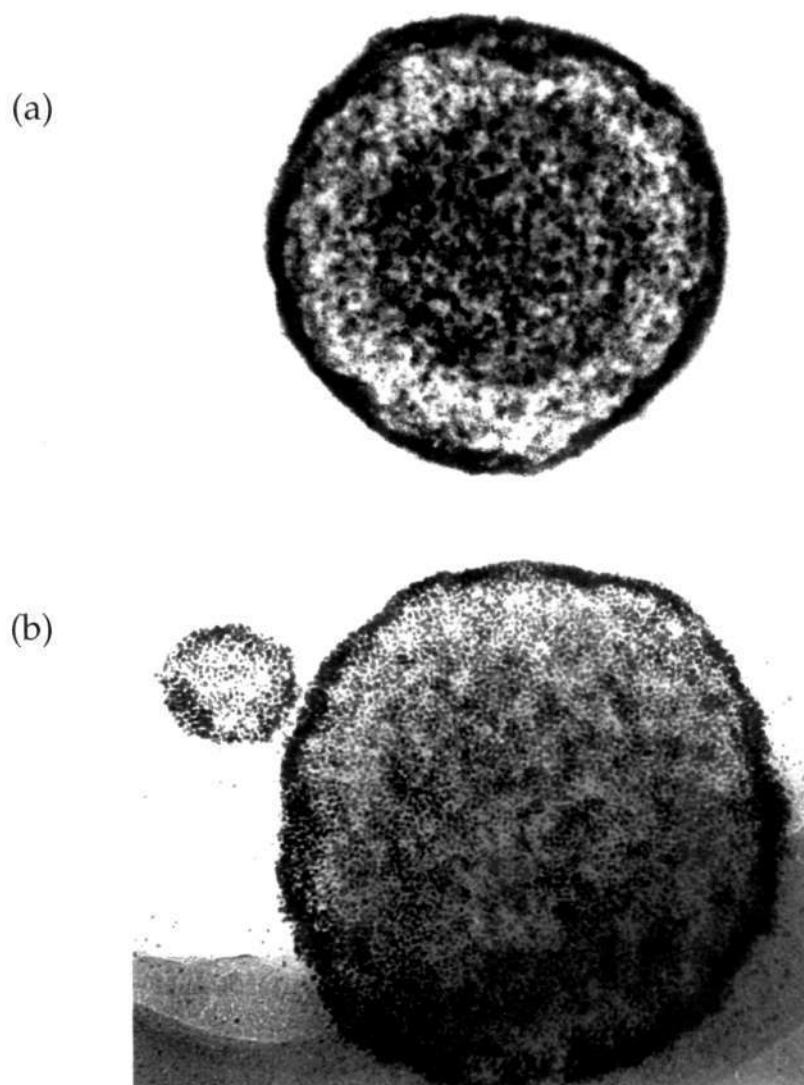


Fig. 2. 44. TEM image of a film made from P3OT blended with Au-nanoparticles of diameters: (a) 4 nm and (b) 7 nm.

samples to discount any interpretation on the basis of artefacts. Previous results have shown that metal nanoparticles encapsulated in a block co-polymer polymer matrix tend to assemble into well-ordered two-dimensional structures or be dispersed in a random manner in polymers, such as polyvinylpyrrolidone (PVP). The present structure is unusual in this respect. The high density of the nanoparticles in the periphery can be explained by the non-uniform evaporation rate and a finite mobility of the nanoparticles, which become pinned at the rim. Another factor which comes into play is the aggregation of polymer chains, which can act as an effective drag on the nanoparticle motion during the drying process, giving rise to the inhomogeneous radial distribution of the nanoparticle. The ring-like structures have been observed in alkanethiol-coated Au nanoparticles [118]. The nanoparticle mobility in that case was high enough to allow most particles to accumulate in the ring during the process of receding of the contact line, i.e. the interface between the solvent and the substrate. Hence, a well-formed perimeter was observed, with a near empty hole in it [118].

Spatially-resolved photoluminescence (PL) spectra are obtained with the fibre tip held at several positions in the vicinity of a typical fluorescent center of the blended system. Fig. 2. 45 depicts the emission spectra from different regions. Spectra are blue-shifted as the tip moved from the center towards the periphery. The centre spot has predominantly a response with a maximum at ~ 700 nm. The spectrum obtained at the center spot is similar to the NSOM spectrum of a

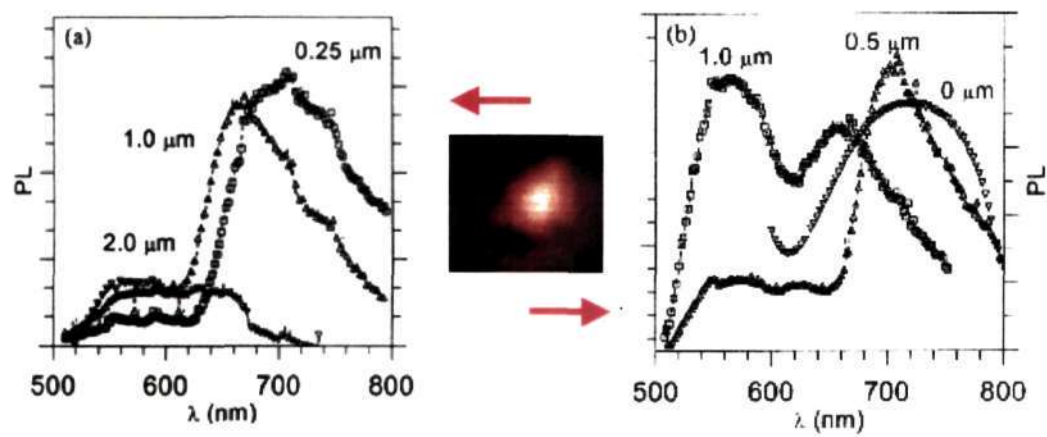


Fig. 2. 45. Near-field PL spectra using NSOM of a fluorescent region (shown between (a) and (b)) in the Au-P3OT film at different positions of the tip. The centre of the region corresponds to $\sim 0 \mu\text{m}$ and (a) and (b) represent the left- and right-hand direction with respect to centre respectively.

pristine P3OT film, which does not change with spatial variation of the fiber tip. The 700 nm peak decreases in intensity, with a corresponding increase in the 565 nm peak, as the fibre tip traverses radially. The PL profile from the centre spot is similar to an NSOM PL response from a homogeneous pristine P3OT film. The periphery emits with a predominant PL-response peaking at ~ 565 nm. However, it is noticed that PL intensity from the center gradually decreases over several minutes with constant exposure to the excitation source, while the emission away from the centre is more stable. The emission outside the circular spots predominantly emits with a maxima at 565 nm. A recent report on NSOM measurements on conjugated polymers, indicates the photobleaching process due to the high aeral power densities of ~ 2 kW/cm² (for aperture diameter of 150 nm and emitted power of 300 nW) [119]. A lower incident power (10 nW) was used in the present studies to minimise the bleaching process and the spectral scans were performed at different regions to ascertain the spatially varying PL characteristics. Upon correlating the positionally varying NSOM spectral profiles with TEM observation, the blue-shift of the PL spectra appear to be controlled by the Au nanoparticle distribution.

The spatially-dependent spectral features have their signature in the far-field PL. Apart from the photobleaching process, which occurs at high incident light flux, a low-light level, photoinduced spectral shift of the PL is also present in these blended systems. Fig. 2. 46 shows the PL response from a thin film of the

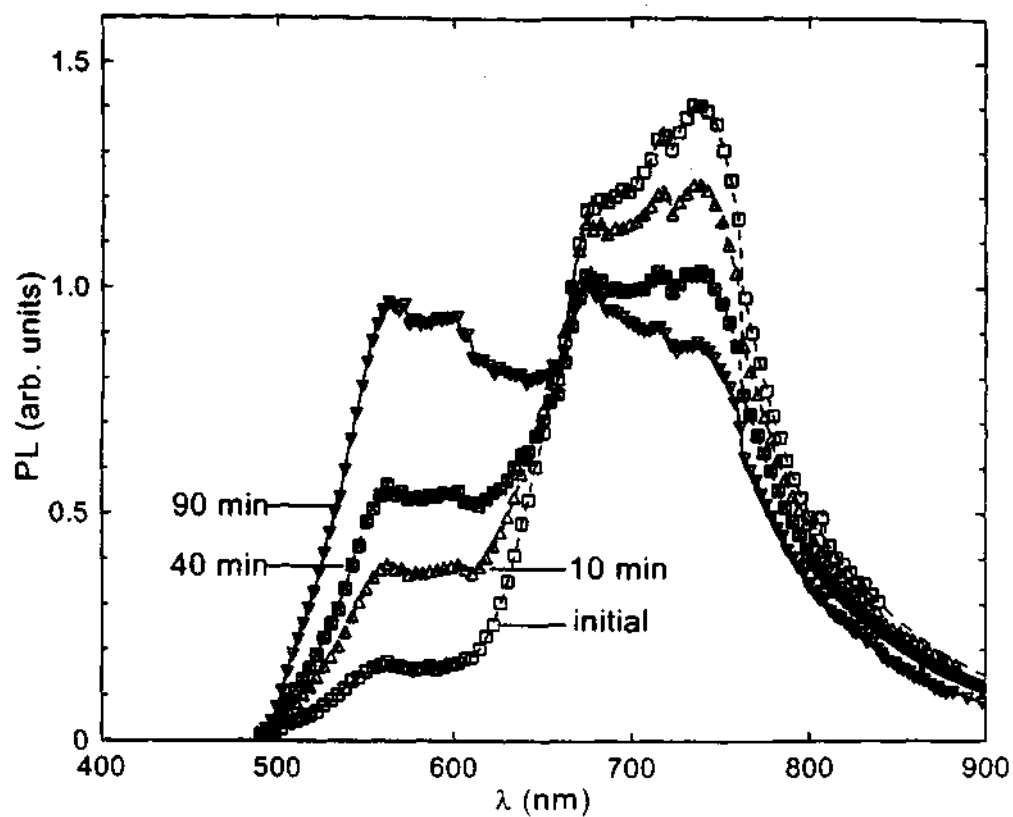


Fig. 2. 46. PL emission in the far field of a thin film of the blended system with excitation at 473 nm after different exposure duration. The sample is kept exposed to the excitation source ($\sim 100 \mu\text{W}$) during the entire duration.

blended system at different intervals after irradiation (473 nm, CW, < 1 mW/cm²). The PL response originally (t=0) resembled the pristine polymer film with a maximum at 700 nm accompanied by vibronic features. A gradual blue-shift in the PL spectra is observed, with the maximum shifting to 565 nm as a function of time, under constant exposure to the excitation source. It is also noticed that the total emission, as measured from the area under the curve, varies marginally, indicating that the changes are not a photodegradation process. The pristine polymer film does not show this blue-shift effect at such a low level of irradiation. Photo-induced degradation processes have been observed in thiophene-based polymers only after exposing to UV light in an oxygen atmosphere over a period of several hours, resulting in quenching of the emission [120]. The degradation process is also observed in these Au nanoparticle/polyoctylthiophene blended systems with sufficient exposure to UV light and is indicated by the appearance of carbonyl defects seen in infrared spectroscopy (FTIR). The changes induced by the low-level blue light exposure are different from the UV-induced changes. The NSOM PL response with the fiber tip positioned on such a pre-irradiated fluorescent region also has responses with the maximum at 565 nm. These results suggest that the PL emission feature of 565 nm is specific to the hybrid blended system, and represents the more prevalent form of the fluorescent polymer in the film.

The PL from these fluorescent centers of the blended film can be interpreted in terms of a crystalline (PL maximum ~ 700 nm) and an amorphous phase (PL maximum ~ 565 nm) of the polymer. The presence of Au nanoparticles drastically alters the crystallinity of the pristine polymer, as indicated from the X-ray observations. This is because in the pristine polymer, a low angle peak corresponding to 21 \AA is observed, representing the orderly arrangement in regio-regular P3ATs [121] whereas this is not observed after the blend is formed. Previous results on thermochromism in P3ATs have indicated the routes to the amorphous phase upon heating via a quasi-ordered intermediate phase, or directly to the disordered phase, depending upon the degree of regioregularity and side chain length [122]. The resultant feature of the disordered phase is a decrease in the effective conjugation length, with a reduced delocalization compared to the crystalline phase, leading to a blue-shifted emission. In the Au-blended samples, the spatially resolved NSOM results reveal the existence of these different phases of the polymer. An interesting feature of the blended system, which is not observed in the pristine system, is the phase conversion upon a low level excitation at room temperature, as shown in Fig. 2. 46. The results may be governed by the diffusion dynamics of the Au nanoparticles interspersed in the polymer matrix which can effectively lower the barrier for a crossover to a structurally disordered phase. Another question which needs to be determined is whether these spectral changes are exclusive to Au-blended P3AT systems. Preliminary studies of P3AT blends with other nanoparticles, such as

SiO₂ and TiO₂ do not result in films with such properties. An important issue which needs to be resolved is to determine whether the electronic structural changes of the polymer in the blended system are secondary effects, caused by nanoparticle-induced physical processes such as rearrangement of the polymer chains or a primary nanoparticle-specific effect with the weak metal polymer interaction which acts as the driving factor for the appearance of different phases.

In conclusion, novel spectral and morphological features are observed in blends of P3OT and Au nanoparticles. Spatially-resolved fluorescence spectroscopy reveals the nanoparticle modified PL responses from different regions of the film and is correlated with the features in the far-field emission.

REFERENCES

- [1] W. P. Halperin, *Rev. Mod. Phys.*, **58** (1986) 532.
- [2] C. N. R. Rao; G. U. Kulkarni; P. J. Thomas and P. P. Edwards, *Chem. Soc. Rev.*, **29** (2000) 27.
- [3] J. H. Fendler, *Nanoparticles and Nanostructured Films* (Ed), Wiley VCH (1998) Weinheim.
- [4] Juncher, *Conspectus chemiae theoreticopracticae*, Magdenburg, **1** (1730) 82.
- [5] M. Faraday, *Philos. Trans. R. Soc. London*, **147** (1857) 145.
- [6] G. Schmid, *Chem. Rev.*, **92** (1992) 1709-1727.
- [7] W. A. deHeer, *Rev. Mod. Phys.*, **65** (1993) 611.
- [8] J. Turkevich; P. C. Stevenson and J. Miller, *Discuss. Faraday. Soc.*, **11** (1951) 55.
- [9] R. Hernández; G. Díaz; A. Vázquez; J. Reyes-Gasga and M. José-Yacamán, *Langmuir*, **7** (1991) 1546-1549.
- [10] C. Larpent and J. Patin, *J. Mol. Catal.*, 1988, **44**, 191.
- [11] S. Ayyappan; R. G. Gopalan; G. N. Subbanna; and C. N. R. Rao, *J. Mater. Res.*, **2** (1997) 398.
- [12] F. Fieret; J. P. Lagier and M. Figlarz, *MRS Bull.*, (1989) 29.
- [13] F. Fievet; L. B. Blin; B. Beaudoin and M. Figlarz, *Solid State Ionics*, **32/33** (1989) 198.
- [14] R. Seshadri and C. N. R. Rao, *Mat. Res. Bull.*, **29** (1994) 795.
- [15] S. Ayyappan; G. N. Subbanna; R. G. Gopalan and C. N. R. Rao, *Solid State Ionics*, **84** (1996) 271-281.

- [16] R. Krasnansky; S. Yamamura and J. K. Thomas, *Langmuir*, **7** (1991) 881.
- [17] V. Arcolego and V. T. Liveri, *Chem. Phys. Lett.*, **258** (1996) 223.
- [18] J. Tanori and M. P. Pileni, *Langmuir*, **13** (1997) 639.
- [19] J. Turkevich and G. Kim, *Science*, **169** (1970) 873.
- [20] L. D. Rampino and F. F. Nord, *J. Am. Chem. Soc.*, **63** (1941) 2741.
- [21] D. N. Furlong; A. Launikonis and W. H. F. Sasse, *J. Chem. Soc., Faraday Trans. 1.*, **80** (1984) 571.
- [22] T. S. Ahmadi; Z. L. Wang; A. Henglein and M. A. El-Sayed, *Chem. Mater.*, **8** (1996) 1161.
- [23] G. P. Zach and R. M. Penner, *Adv. Mater.*, **12** (2000) 878.
- [24] T. P. Martin; T. Bergmann; H. Gohlich and T. Lange, *J. Phys. Chem.*, **95** (1991) 6421.
- [25] D. H. Rapoport; W. Vogel; H. Cölfen and R. Schlögl, *J. Phys. Chem.*, **B101** (1997) 4175.
- [26] G. Schmid; G. R. Pfeil; R. Boese; F. Bandermann; S. Mayer; G. H. M. Calis and J. W. A. Vander Velden, *Chem. Ber.*, **114** (1981) 3634.
- [27] G. Schmid and W. Huster, *Z. Naturforsch.*, **41b** (1981) 1028.
- [28] G. Schmid, *Aspects Homogenous Catal.*, **7** (1990) 1.
- [29] M. N. Vargaftik; V. P. Zagorodnikov; I. P. Stolyarov; I. I. Moiseev; V. A. Likholobov; D. I. Kochubey; A. L. Chuvilin; V. I. Zaikovsky; K. I. Zamaraev, and G. I. Timofeeva, *J. Chem. Soc., Chem. Commun.*, (1985) 937.

- [30] M. N. Vargaftik; I. I. Moiseev; D. I. Kochubey and K. I. Zamaraev, *Faraday Discuss.*, **92** (1991) 13-29.
- [31] G. Schmid; B. Morun and J. -O. Malm, *Angew. Chem., Int. Ed. Engl.*, **28** (1989) 778.
- [32] D. G. Duff, A. Baiker and P. P. Edwards, *J. Chem. Soc., Chem. Commun.*, (1993) 96.
- [33] K. -L. Tsai and J. L. Dye, *J. Am. Chem. Soc.*, **113** (1991) 1650.
- [34] J. L. Dye, and K. -L. Tsai, *Faraday Discuss.*, **92** (1991) 45.
- [35] G. Schmid, *Polyhedron*, **7** (1988) 2321.
- [36] K. L. Muetterties, *J. Organometal. Chem.*, **200** (1980) 177.
- [37] P. Chini, *J. Organometal. Chem.*, **200** (1980) 37-61.
- [38] A. I. Kirkand; P. P. Edwards; D. A. Jefferson and D. G. Duff, *Faraday Discuss.*, **92** (1991) 247.
- [39] A. Henglein; P. Mulvaney and T. Linnert, *Faraday Discuss.*, **92** (1991) 31.
- [40] R. P. Andres; R. S. Averback; W. L. Brown; L. E. Brus; W. A. Goddard III; A. Kaldor; S. G. Louie; M. Moscovits; P. S. Peercy; S. J. Riley; R. W. Siegel; F. Spaepen and Y. Wang, *J. Mater. Res.*, **4** (1989) 704.
- [41] G. Schmid, *Clusters and Colloids. From Theory to Applications* (1994) Weinheim, VCH.
- [42] P. P. Edwards, and C. N. R. Rao, (Eds), *The Metallic and Nonmetallic States of Matter*. Taylor and Francis (1985) London.
- [43] Matijevic', E., *Faraday Discuss.*, 1991, **92**, 229-239.

- [44] R. G. Nuzzo and D. L. Allara, *J. Am. Chem. Soc.*, **105** (1983) 4481.
- [45] T. P. Jr Beebe; T. E. Wilson; F. Ogletree; J. E. Katz; B. M. B. Salmerson and W. J. Siekhaus, *Science*, **240** (1989) 370.
- [46] P. E. Laibinis; G. M. Whitesides; D. L. Allara; Y. -T. Tao; A. N. Parikh and R. G. Nuzzo, *J. Am. Chem. Soc.*, **113** (1991) 7152.
- [47] M. A. Hines; J. A. Todd and P. Guyot-Sionnest, *Langmuir*, **11** (1995) 493.
- [48] C. D. Bain and G. M. Whitesides, *Adv. Mater. (Angew. Chem, 28(4))*, (1989) 506.
- [49] J. Y. Gui; D. A. Stern; D. G. Frank; F. Lu; D. C. Zapien and A. T. Hubbard, *Langmuir*, **7** (1991) 955.
- [50] H. -J. Himmel; Ch. Wöll; R. Gerlach; G. Polanski and H. -G. Rubahn; *Langmuir*, **13** (1997) 602.
- [51] M. Buck; M. Grunze; F. Eisert; J. Fischer and F. Trager, *J. Vac. Sci. Technol. A.*, **10**, (1992) 926.
- [52] C. D. Bain; H. A. Biebuyck and G. M. Whitesides, *Langmuir*, **5** (1989) 723.
- [53] R. G. Nuzzo; F. A. Fusco and D. L. Allara, *J. Am. Chem. Soc.*, **109** (1987) 2358.
- [54] H. Rieley; N. J. Price; R. G. White; R. I. R. Blyth and A. W. Robinson, *Surface Science*, **331-333** (1995) 189.
- [55] A. -S. Duwez; S. Di Paolo; J. Ghijsen; J. Riga; M. Deleuze and J. Delhalle, *J. Phys. Chem., B.*, **101** (1997) 884.
- [56] P. Fenter; P. Eisenberger; J. Li; N. Camillone III; S. Bernasek; G. Scoles; T. A. Ramanarayanan and K. S. Liang, *Langmuir*, **7** (1991) 2013.

- [57] N. Camillone III, C. E. D. Chidsey, G. Liu and G. Scoles, *J. Phys. Chem.*, **98** (1993) 4234.
- [58] E. Delamarche; B. Michel; H. A. Biebuyck and G. Gerber, *Adv. Mater.*, **8** (1996) 719.
- [59] J. A. M. Sondag-Huethorst; C. Schonenberger and L. G. J. Fokkink, *J. Phys. Chem.*, **98** (1994) 6826.
- [60] R. Heinz and J. P. Rabe, *Langmuir*, **11** (1995) 506.
- [61] D. -F. Yang; C. P. Wilde and M. Morin, *Langmuir*, **13** (1997) 243-249.
- [62] A. Badia, R. Back and R. B. Lennox, *Angew. Chem., Int. Ed. Engl.*, **33** (1994) 2332.
- [63] K. Bandyopadhyay, M. Sastry; V. Paul and K. Vijayamohanan, *Langmuir*, **13** (1997) 866.
- [64] R. G. Nuzzo; E. M. Korenic and L. H. Dubois, *J. Chem. Phys.*, **93** (1990) 67.
- [65] M. Brust; M. Walker; D. Bethell; D. J. Schiffrin and R. Whyman, , *J. Chem. Soc., Chem. Commun.*, (1994) 801.
- [66] D. V. Leff; P. C. Ohara; J. R. Heath and W. M. Gelbart, *J. Phys. Chem.*, **99** (1995) 7036.
- [67] P. C. Ohara; D. V. Leff; J. R. Heath and W. M. Gelbart, *Phys. Rev. Lett.*, **75** (1995) 3466.
- [68] M. Brust, D. Bethell; D. J. Schiffrin and C. J. Kiely, *Adv. Mater.*, **7** (1995) 795.
- [69] R. P. Andres; J. D. Bielefeld; J. I. Henderson; D. B. Janes; V. R. Kolagunta; C. P. Kubiak; W. J. Mahoney and R. G. Osifchin, *Science*, **273** (1996) 1690.

- [70] R. L. Whetten; J. T. Khoury; M. M. Alvarez; S. Murthy, I. Vezmar; Z. L. Wang; P. W. Stephens; C. L. Cleveland; W. D. Ludtke and U. Landman, *Adv. Mater.*, **8** (1996) 428.
- [71] S. A. Harfenist; Z. L. Wang; M. M. Alvarez; I. Vezmar and R. L. Whetten, *J. Phys. Chem.*, **100** (1996) 13904.
- [72] S. A. Harfenist; Z. L. Wang, R. L. Whetten; I. Vezmar and M. M. Alvarez, *Adv. Mater.*, **9** (1997) 817.
- [73] C. S. Weisbecker, M. V. Merritt and G. M. Whitesides, *Langmuir*, **12** (1996) 3763.
- [74] C. J. Kiely; J. Fink; M. Brust; D. Bethell and D. J. Schiffrin, *Nature*, **396** (1998) 444.
- [75] C. J. Kiely; J. Fink; J. G. Zheng; M. Brust; D. Bethell and D. J. Schiffrin, *Adv. Mater.*, **12** (2000) 640.
- [76] P. J. Thomas; G. U. Kulkarni and C. N. R. Rao; *Chem. Phys. Lett.*, **11/12** (2000) 333.
- [77] C. Petit and M. Pileni, *Appl. Surf. Sci.*, **162-163** (2000) 519.
- [78] L. F. Chi; S. Rakers; T. Drechsler, M. Hartig; H. Fuchs and G. Schmid, *Thin Solid Films*, **329** (1998) 520.
- [79] S. R. Johnson; S. D. Evans; S. W. Mahon and A. Ulman, *Langmuir*, **13** (1997) 51.
- [80] D. V. Leff; L. Brandt and J. R. Heath, *Langmuir*, **12** (1996) 4723.
- [81] S. P. Spatz; St. Mößner and M. Möller, *Chem. Eur. J.*, **2** (1997) 1552.

- [82] J. P. Spatz; A. Roescher and A. M. Moller, *Adv. Mater.*, **8** (1996) 337.
- [83] M. T. Reetz; M. Winter and B. Tesche, *J. Chem. Soc., Chem. Commun.*, (1997) 147.
- [84] S. Horiuchi, M. I. Sarwar and Y. Nakao, *Adv. Mater.*, **12** (2000) 1507.
- [85] C. A. Mirkin; R. L. Letsinger; R. C. Mucic and J. J. Storhoff, *Nature*, **386** (1996) 607.
- [86] H. Biebuyck; C. D. Bain and G. M. Whitesides, *Langmuir*, **10** (1994) 1825.
- [87] C. N. R. Rao; V. Vijayakrishna; H. N. Aiyer; G. U. Kulkarni and G. N. Subbanna, *J. Phys. Chem.*, **97** (1993) 11157.
- [88] B. Badia; S. Singh; L. Demers; L. Cuccia; G. R. Brown and R. B. Lennox, *Chem. Eur. J.*, **2** (1996) 359.
- [89] R. G. Terrill; T. A. Postlethwaite; C. Chen; C. D. Poon; A. Terzis; A. Chen; J. E. Hutchison; M. R. Clark; G. Wignall; J. D. Londono; R. Superfine; M. Falvo; C. S. Jr. Johnson; E. T. Samulski and R. W. Murray, *J. Am. Chem. Soc.*, **117** (1995) 12537.
- [90] G. Schmid and A. Lehnert, *Angew. Chem. Int. Ed. Engl.*, **28** (1989) 780.
- [91] M. Dorogi; J. Gomez; R. G. Osifchin; R. P. Andres and R. Reifenberger, *Phys. Rev.*, **B52** (1995) 9071.
- [92] P. J. Thomas; G. U. Kulkarni and C. N. R. Rao, *J. Phys. Chem.*, **B104** (2000) 8138.
- [93] J. G. A. Dubois; J. W. Gerritsen; S. E. Shafranjuk; E. F. G. Boon; G. Schmid and H. Van Kempen, *Europhys. Lett.*, **33** (1996) 279.

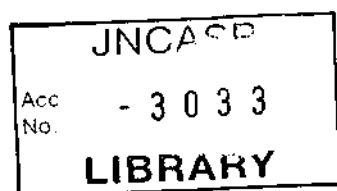
- [94] C. P. Collier; R. J. Saykally; J. J. Shiang; S. E. Henrichs and J. R. Heath, *Science*, **277** (1997) 1978.
- [95] U. Simon; G. Schön and G. Schmid, *Angew. Chem., Int. Ed. Engl.*, **32** (1993) 250.
- [96] G. Schmid, and G. L. Hornyak, *Current Opinion in Solid State & Materials Science*, **2** (1997) 204.
- [97] M. A. Hayat (Ed.), *Colloidal Gold: Principles, Methods and Applications*, **1 & 2**, (1989).
- [98] Y. Xia; D. Qin and G. M. Whitesides, *Adv. Mater.*, **8** (1996) 1015.
- [99] Kumar, A. and Whitesides, G. M., *Science*, 1994, **263**, 60.
- [100] J. Heinze, *Angew. Chem., Int. Ed. Engl.*, **32** (1993) 1268.
- [101] J. Küther and W. Tremel, *J. Chem. Soc., Chem. Commun.*, (1997) 2029.
- [102] S. Sun; C. B. Murray; D. Weller; L. Folks and A. Moser, *Science*, **287** (2000) 1989.
- [103] V. L. Colvin; M. C. Schlamp and A. P. Alivisatos, *Nature*, **370** (1994) 354.
- [104] C. B. Murray; C. R. Kagan and M. G. Bawendi, *Science*, **270** (1996) 1335.
- [105] T. Nakanishi; B. Ohtani and K. Uosaki, *J. Phys. Chem.*, **B102** (1998) 1571.
- [106] M. Brust; R. Etchenique; E. J. Calvo and G. J. Gordillio, *Chem. Commun.*, (1996) 1949.
- [107] J. H. Burroughs; D. C. Bradley; A. R. Brown; R. N. Marks; K. Mackay; R. H. Friend; H. Burn and A. B. Holmes, *Nature*, **347** (1990) 539.
- [108] N. Tessler, N. T. Harrison and R. H. Friend, *Adv. Mater.*, **10** (1998) 64.

- [109] U. Kreibig and M. Vollmer, *Optical Properties of Metal Clusters*, (1995) Springer Series in Materials Science-25.
- [110] L.C. III Brousseau; J. P. Novak; S. M. Marniakos and D. P. Feldheim, *Adv. Mater.*, **11** (1999) 447.
- [111] H. Bässler in: N. S. Saricifiti (Ed), *Primary Photoexcitations in Conjugated Polymers: Molecular Exciton versus Semiconductor Band Model*, World Scientific (1997) Singapore.
- [112] R. Brunner; A. Biettsch; O. Hollricher and O. Marti, *Rev. Sci. Instrum.*, **68** (1997) 1769.
- [113] K. Nakamoto, *Infrared and Raman Spectra of Inorganic and Co-ordination Complexes*, John Wiley (1978) New York.
- [114] V. Vijayakrishnan and C. N. R. Rao, *Surf. Sci.*, **255** (1991) L516.
- [115] V. Vijayakrishnan; A. Chianani; D. D. Sarma and C. N. R. Rao, *J. Phys. Chem.*, **96** (1992) 8679.
- [116] J. Gopalakrishnan; T. Murugesan; M. S. Hegde and C. N. R. Rao, *J. Phys. C: Solid State Phys.*, **12** (1979) 5255.
- [117] V. Murugai; S. Raaen; M. Strongin and R. F. Garrett, *Phys. Rev.*, **B33** (1986) 4345.
- [118] P. C. Ohara; J. R. Heath and W. M. Gelbart, *Angew. Chem., Int. Ed. Engl.*, **36** (1997) 1077.
- [119] R. Stevenson; M. Granstrom and D. Richards, *Appl. Phys. Lett.*, **75** (1999) 1574.

[120] M. S. A. Abdou and S. Holdcroft, *Macromolecules*, **26** (1997) 2954.

[121] T. -A. Chen, X. Wu and R. D. Rieke, *J. Am. Chem. Soc.*, **117** (1998) 233.

[122] C. Yang, F. P. Orfino and S. Holdcroft, *Macromolecules*, **29** (1996) 6510.



620.1892
P02

Handwritten text in black ink, consisting of two lines: '620.1892' and 'P02'.